

Predicting scale effects on floating offshore wind turbines

A numerical analysis of model- and full-scale wind turbines using a RANS CFD solver

M.K.P. Make

Predicting scale effects on floating offshore wind turbines

**A numerical analysis of model- and full-scale wind
turbines using a RANS CFD solver**

MASTER OF SCIENCE THESIS

M.K.P. Make

April 28, 2014

Supervisor:
dr.ir. G.N.V.B. Vaz
prof.dr.ir. T.J.C. van Terwisga

Thesis Committee:
prof.dr.ir. T.J.C. van Terwisga
dr.ir. G.N.V.B. Vaz
dr.ir. M.I. Gerritsma
dr.ir. H.J. de Koning Gans
dr.ir. A.C. Viré
ir. F.J. Savenije

Faculty of Mechanical, Maritime and Materials Engineering (3mE) · Delft University of
Technology

Abstract

Floating wind turbines are becoming fashionable within the Renewable Energy world. In the last years MARIN has been involved in an increasing number of projects for the offshore wind industry. Model tests are often used for validating and optimizing the floater design before construction starts. A key point of model testing floating wind turbines is that wind and waves are presented simultaneously in the basin. This makes it possible to study the complex motions and interactions between the rotating turbine and the moving platform.

However the experiments are done using smaller scaled models. While for the underwater loads Froude scaling laws are used successfully in the Offshore industry, the same should not be done for the aerodynamic loads. Due to the strong Reynolds scale effects, the flow regime on the blades is critical or even sub-critical, and therefore laminar-turbulent transition and flow-separation effects play an important role. The traditional potential-flow based tools used for design and analysis of turbines (Blade-Element-Momentum-Theory BEMT) were not intended to work in these regimes, nor the inviscid-viscous (Boundary-Element-Method BEM) tools, like XFOIL, used to obtain the turbine sections $C_l/C_d/C_m$ input for the BEMT calculations.

The complete simulation of a full-scale free-floating wind turbine under waves and winds using viscous-flow (Unsteady-Reynolds-Averaged-Navier-Stokes URANS) CFD codes is still nowadays very costly, if not impossible. However these CFD theoretically more accurate methods, can be used in an efficient way for aerodynamic analysis. And they can be used rather to generate 2D input for the BEMT design tools or for the real complete analysis of the wind turbine. In the present work CFD URANS code ReFRESCO is used for both purposes, having in mind the design of the new MARIN Stock (not Floating) Wind Turbine (MSWT), based on the 5MW NREL full-scale turbine. Only open-water constant wind, fixed platform conditions are considered here.

The objectives of the work presented are therefore threefold: 1) the NREL 5MW baseline turbine is calculated using ReFRESCO both in full-scale and model-scale (Froude-scaling) conditions and the scale-effects studied and quantified; 2) the MSWT designed for thrust and performance-scaling is analyzed using CFD and validation against available MARIN experimental data is done; 3) in order to possibly further improve the MSWT design, the

aerodynamic characteristics of its sections/foils are scrutinized by means of a full numerical study using ReFRESCO.

The poor performance of the NREL 5MW turbine is due to a fully separated flow over the full range of tip speed ratios. Additionally decambering laminar separation bubbles are observed at the pressures side of the blades, further decreasing the aerodynamic performance of the turbine. Although laminar separation bubbles are not observed for the model-scale MSWT, separation does occur over the full span of the suction side of the blades. For the performance-scaled MSWT, however, an attached flow region is observed at the blade tips for the higher tip speed ratios, resulting in increased C_P / C_T values and performance. Flow separation at full-scale conditions is present only for the heavily loaded operating conditions. These separated regions show large radial velocity components, which contradict the assumed 2D flow in BEMT models.

The separated flow is also observed for the flow over the 2D airfoil sections of the MSWT. Even for small angles of attack at model-scale Reynolds numbers, separation occurs and URANS computations are necessary for larger angles of attack. For the full-scale Reynolds number regime the flow remains attached up to larger angles of attack and URANS computations are needed only for the extreme angles of attack ($AoA > 14deg$). The 2D flow phenomena at model- and full-scale are in line with those observed for the flow over the 3D turbine.

Although the MSWT has already greatly improved model-scale performance characteristics, the present research indicate that more improvements are perhaps possible. An alternative pitch angle distribution can be considered in order to reduce flow separation for even lower TSRs. Furthermore the present work showed the challenge of obtaining accurate numerical solutions for the complex unsteady flow over a wind turbine at these critical Reynolds numbers, which requires: domain studies, grid and time-step studies, good iterative convergence and an adequate turbulence model. All of these aspects were studied in this thesis.

Table of Contents

Acknowledgements	xiii
1 Introduction	1
1-1 Motivation	1
1-2 Background	4
1-3 Objectives	7
1-4 Report Outline	7
2 Theoretical Background	9
2-1 Geometry and Coordinate System	9
2-1-1 Three-Dimensional Wind Turbine	9
2-1-2 Two-Dimensional Airfoil	12
2-2 Scaling Methodology	12
2-3 Wind Turbine Aerodynamics	13
2-3-1 Theory of Wing Sections	14
2-3-2 Blade Element Momentum Theory	20
2-4 Governing Equations	29
2-4-1 Navier-Stokes Equations	29
2-4-2 Reynolds-Averaged Navier-Stokes (RANS) Equations	31
2-4-3 Unsteady Reynolds-Averaged Navier-Stokes (URANS) Equations	32
2-4-4 Turbulence Modeling	33
2-5 Verification and Validation	37
2-5-1 Verification	37
2-5-2 Validation	42

3 Numerical Background	45
3-1 Numerical Tools	45
3-1-1 HEXPRESS	45
3-1-2 ReFRESCO	47
3-2 Discrete Governing Equations	47
3-2-1 Discretization of integrals	48
3-2-2 Defining the Cell Geometry	48
3-2-3 Time Discretization	50
3-2-4 Gradients	50
3-2-5 Convective Terms	51
3-2-6 Diffusive Terms	53
3-2-7 Source Terms	54
3-2-8 Eccentricity	54
3-3 Solution Process	54
3-3-1 Under-Relaxation	55
3-3-2 Pressure Correction	57
3-4 Note on Unsteady Computations	57
4 Numerical Setup	59
4-1 Two-Dimensional Airfoil	59
4-1-1 Domain Dimensions	59
4-1-2 Boundary Conditions	60
4-1-3 Grid Topology	63
4-1-4 Calculation Overview	64
4-1-5 Post-Processing	67
4-2 Three-Dimensional Turbine	67
4-2-1 Domain Dimensions	69
4-2-2 Turbine motion modeling	69
4-2-3 Boundary Conditions	71
4-2-4 Grid Topology	72
4-2-5 Calculation Overview	74
4-2-6 Post-Processing	74
5 Numerical Study on a Two-Dimensional Wing Section	77
5-1 General Results	77
5-2 Domain Size Variation	85
5-2-1 Steady Flow Calculations	85
5-2-2 Unsteady Flow	89
5-2-3 Final Remark	92
5-3 Numerical Uncertainty Study	93
5-3-1 Geometric Similarity	93
5-3-2 Grid Characteristics	95
5-3-3 Iterative Error	96
5-3-4 Discretization Error	96
5-3-5 Final Remarks	105
5-4 Turbulence Modeling	106
5-4-1 Final Remarks	110

6 Numerical Study on MARIN Stock Wind Turbine (MSWT) at Model-Scale	117
6-1 Domain Size Variation	117
6-2 Numerical Uncertainty Study	120
6-2-1 Iterative Error	121
6-2-2 Discretization Error	122
6-2-3 Final Remarks	126
6-3 Turbulence Modeling	126
6-3-1 Result Summary	127
6-4 Validation procedure	127
6-5 General Flow Characteristics	135
7 Comparison of NREL 5MW and MSWT Scaling Effects	143
7-1 Scaling Effects on the NREL 5MW Baseline Turbine	143
7-2 Scaling Effects on the MARIN Stock Wind Turbine	145
7-3 Comparing the overall performance of the model-scale MSWT and full-scale NREL 5MW baseline turbine	149
7-4 Comparing the full-scale BEMT and RANS results	155
8 Conclusions and Recommendations	157
8-1 Two-dimensional study	157
8-2 Three-dimensional study	158
8-3 Scaling effects of the MSWT and NREL 5MW	160
8-4 Wind Turbine Analysis Using CFD	161
Bibliography	163
Glossary	169
List of Acronyms	169
List of Symbols	170

List of Figures

1-1	Three Floating Offshore Wind Turbine (FOWT) design concepts.	3
1-2	Environmental loads working on FOWTs.	3
1-3	Effect of change in lift and drag on thrust and torque.	5
1-4	Foil sections of both Drela AG04 and Drela AG04-Modified (double thickness). .	6
2-1	Drela AG04 foil sections	11
2-2	Coordinate system for the 3D wind turbine.	11
2-3	Pressure, shear stress, resulting force, and moment on the airfoil.	14
2-4	Resultant force decomposed in lift and drag.	15
2-5	Velocity profiles for laminar and turbulent boundary layers	16
2-6	Effects of a negative and positive pressure gradient on a boundary flow.	18
2-7	Reynolds number effects on laminar boundary layer.	19
2-8	Lift curves for varying airfoil geometries obtained using XFOIL at $Re = 5 \cdot 10^6$. .	20
2-9	Energy extraction over the stream-tube of an actuator disc.	21
2-10	Trajectory of an air particle in a wake-field.	24
2-11	Blade element swept area and airflow over rotor blade.	25
2-12	Blade element velocities and forces.	26
2-13	Reynold decomposition of a time fluctuating velocity signal.	31
2-14	Time averaging for non stationary turbulence.	33
3-1	Hanging nodes at boundary of grid refinement region	46
3-2	Unit vectors used for determination of orthogonality.	46
3-3	Geometric representation of volume element and volume face.	49
3-4	Schematic overview of two-dimensional structured grid.	52
3-5	Schematic of solution process used by ReFRESCO.	56

4-1	Coordinate system for the 2D airfoil computations	59
4-2	Boundary conditions on the airfoil domain	60
4-3	XY -plane view of the airfoil domain	61
4-4	Autodetect geometry.	62
4-5	Refinement box around airfoil.	63
4-6	Viscous layer refinement.	64
4-7	Dimensions of the hub at model-scale.	69
4-8	Dimensions of the 3D domain.	70
4-9	Boundary conditions on the 3D turbine domain.	72
4-10	Detail of the 3D grid.	73
5-1	Flow field characteristics for MS Reynolds number regime. $Re = 10^4, AoA = 0 \text{ deg}$	79
5-2	Flow field characteristics for FS Reynolds number regime. $Re = 10^6, AoA = 6 \text{ deg}$	80
5-3	Convergence history of L_∞ residual norms and C_l and C_d	81
5-4	Vorticity $\bar{\omega}$ for $Re = 10^4, AoA = 20 \text{ deg}$, for different time instants.	82
5-5	Vorticity $\bar{\omega}$ for $Re = 10^6, AoA = 20 \text{ deg}$, for different time instants.	83
5-6	Time trace of lift, drag and moment coefficients for model- and full-scale.	84
5-7	Time trace of lift, drag and moment coefficients for model-scale at $AoA = 20 \text{ deg}$	85
5-8	C_l and C_d for varying domain size.	86
5-9	Domain dependence C_l and C_d for varying Re and AoA	87
5-10	Domain dependence drag components for various flows.	90
5-11	Development of lift, drag and moment coefficients for $Re = 10^6, AoA = 20 \text{ deg}$	92
5-12	Domain dependence of C_l and C_d for unsteady computations with $AoA = 20$	93
5-13	Coarse and fine grid at the airfoil trailing edge (TE).	94
5-14	Coarse and fine grid at the viscous layer refinement.	94
5-15	y^+ of the grid set for $Re = 10^6$	95
5-16	Grid uncertainty for C_l , C_d and C_m at $AoA = 0 \text{ deg}$, $Re = 10^4, 10^6$	100
5-17	Grid uncertainty for C_l , C_d and C_m at $AoA = 4 \text{ deg}$, $Re = 10^4, 10^6$	101
5-18	Distribution of cell volumes and typical grid cell size based on various methods.	102
5-19	Numerical uncertainty estimation for unsteady flow $AoA = 20 \text{ deg } Re = 10^4$	104
5-20	Pressure coefficient along the surface of the airfoil	107
5-21	C_l and C_d curves of the AG04 modified foil for various turbulence models ($Re = 10^6$).	108
5-22	Normalized turbulence viscosity $\bar{\mu}_t = \mu_t/\mu$ for $AoA = 4, 10^4$	109
5-23	Flow field and shear stress over an airfoil for various turbulence models.	111
5-24	Trailing edge detail of the normalized turbulence viscosity.	112
5-25	Effect of turbulence model choice on C_P in the flow domain.	113
5-26	Effect of turbulence model choice on C_P in the flow domain.	113
5-27	Normalized turbulence viscosity $\bar{\mu}_t = \mu_t/\mu$ for $AoA = 4, 10^6$	114

6-1	Normalized velocity fields, slice at $z = 0$	119
6-2	Domain size dependency.	120
6-3	Iterative convergence plots of the L_2 -norm and C_T and C_P for grid 5.	121
6-4	Pressure residuals in the wake of the blade root and root vortex.	122
6-5	Numerical uncertainty for $V_{wind} = 2.47 \text{ m/s}$ and $TSR = 7.0$	124
6-6	Power and thrust coefficient as percentage of finest grid.	124
6-7	Limiting streamlines for model-scale MSWT for various grid refinements.	125
6-8	Limiting streamlines for two turbulence models	128
6-9	Turbulence viscosity over the turbine blade using two turbulence models.	129
6-10	Iso-surface of the turbulence viscosity in the wake-field of the turbine.	130
6-11	C_T curves of model-scale MSWT including uncertainties.	133
6-12	C_P curves of model-scale MSWT including uncertainties.	134
6-13	Limiting streamlines for model-scale MSWT at various TSR.	136
6-14	Pressure distribution on a turbine blade and in the domain at $TSR = 7.0$	137
6-15	Normalized velocities over the turbine at $TSR = 7.0$	139
6-16	Normalized Q -factor and vorticity $\bar{\omega}_y$ in the wake-field at $TSR = 7.0$	140
6-17	C_T and C_P curve of MSWT experiments and numerical simulations at model-scale.	141
7-1	Turbulence viscosity along the blade for NREL 5MW baseline turbine at MS/FS. .	144
7-2	Limiting streamlines for MS/FS scale NREL 5MW wind turbine at various TSR. .	146
7-3	Radial velocity and limiting streamlines at the turbine blade for $TSR = 7.0$	147
7-4	C_T and C_P as function of TSR for MS/FS NREL 5MW baseline wind turbine. .	148
7-5	Turbulence viscosity at various sections along the blade span for MSWT at MS/FS.	150
7-6	Limiting streamlines for model-scale and full scale MSWT at various TSR.	151
7-7	C_T and C_P as function of TSR for MS/FS MARIN stock wind turbine.	152
7-8	Limiting streamlines for MS MSWT and FS NREL 5MW turbine at various TSR.	153
7-9	C_T and C_P as function of TSR for FS NREL 5MW and MS MSWT.	154
7-10	C_T and C_P as function of TSR for FS NREL 5MW BEMT and RANS results. . .	156

List of Tables

2-1	Properties of the full scale and model scale NREL 5MW Baseline Wind Turbine.	10
4-1	MSWT flow properties at model-scale operating condition, $TSR = 7.0$.	65
4-2	Overview of performed computations on 2D airfoil.	66
4-3	Non-dimensional geometry of the MARIN Stock Wind Turbine 5MW turbine.	67
4-4	Non-dimensional geometry of the NREL 5MW turbine.	68
4-5	Overview of performed computations on the MS/FS MSWT and NREL 5MW turbine.	75
5-1	Periodic characteristics at $AoA = 20 \text{ deg}$.	84
5-2	Domain size variation for various angles of attack and Reynolds number.	88
5-3	Lift components for domain size variation.	90
5-4	Drag components for domain size variation.	91
5-5	2D unsteady domain size computations.	91
5-6	Average lift, drag and moment coefficients for the computed unsteady flow.	92
5-7	Grid properties of grid refinement study.	96
5-8	Iterative convergence and error.	97
5-9	Average lift of the final 5 cycles for $AoA = 20 \text{ deg}$ and $Re = 10^4$.	98
5-10	lift drag and moment coefficients for analyzed flow cases	99
5-11	Typical grid cell size h_i/h_1 obtained using alternative methods.	103
5-12	Uncertainty estimation for various typical grid cell size definitions.	103
5-13	Grid set and timesteps used for unsteady uncertainty study.	105
5-14	Uncertainty estimation for $AoA = 20 \text{ deg}$, $Re = 10^4$ case.	105
5-15	Lift drag and moment coefficients for three turbulence models	107
6-1	Overview domains used and corresponding dimensions.	118
6-2	C_T and C_P for varying domain size.	118

6-3	Grid properties of grid refinement study	120
6-4	Iterative convergence and error	123
6-5	Numerical uncertainty estimation for the MSWT model-scale computations.	123
6-6	Power and thrust coefficients for two turbulence models	126
6-7	MSWT MS experimental results including 2.5% uncertainty	131
6-8	MSWT MS $U\phi$ using relative difference of two finest grids and LS method.	132
6-9	MSWT MS U_{val} using relative difference of two finest grids and LS method.	132
6-10	Absolute comparison error $ E $ for both C_T and C_P	135
6-11	C_T and C_P of experiments and ReFRESCO calculations of the MSWT at MS . .	138

Acknowledgements

The work presented in this thesis is the final task in achieving a Master's degree in Ship Hydromechanics at the Technical University of Delft. It is the result of a study performed at the Maritime Research Institute Netherlands (MARIN) in Wageningen. Without the availability of proper guidance and tools, performing this study would have been impossible. Therefore I would like to express my gratitude towards the following people.

Dr.ir. Guilherme Vaz, who guided me during my stay at MARIN. Whenever needed, I could always count on his support both professional and personal. Prof.dr.ir Tom van Terwisga, who gave me the opportunity to perform my thesis work at MARIN in the first place and was always willing to give advice regarding my research topic.

I would like to thank MARIN in general for providing me with the proper tools, expertise, a pleasant working atmosphere, not to mention the endless amounts of computer power. I consider the time I spend at both MARIN and Wageningen as very satisfying.

Finally I would like to thank my girlfriend, parents and friends for their support during this period.

Wageningen, MARIN
April 28, 2014

M.K.P. Make

“In the future, airplanes will be flown by a dog and a pilot. And the dog’s job will be to make sure that if the pilot tries to touch any of the buttons, the dog bites him.”

— *Scott Adams*

Chapter 1

Introduction

In this chapter a general introduction related to floating offshore wind turbines is given. In section 1-1 a motivation is given which includes a description of previous and future developments in the wind energy market. The relevant developments of previous studies are explained in section 1-2. In section 1-3 the importance of the continuation of the work and the related objectives of this thesis is described. Finally an outline of the thesis is given in section 1-4.

1-1 Motivation

The growing demand for energy worldwide and the continuously increasing fossil fuel prices create a bright future for the development of clean and sustainable alternatives to fossil fuels [1, 2]. An alternative, both clean and renewable, is wind energy. The global production of wind energy at the end of 2012 was 282.5 GW, with a growth rate over the last decade of about 22% [3]. The total amount of potential wind energy generated worldwide is estimated at 72 TW, more than enough to supply all the world's energy needs [4].

Onshore wind energy technology has already been used with success over the past decades. Although this technology is clean and renewable it also has its limitations. Offshore wind installations are an alternative with a number of advantages.

The size of onshore turbines is constrained by capacity limitations of the available transportation and erection equipment. Transportation and erection problems are mitigated in offshore, where the size and lifting capacities of marine shipping and handling equipment still exceeds the installation requirements for multi-megawatt wind turbines. Onshore, particularly in Europe or on the East Coast of the United States, the visual appearance of massive turbines in populated areas start to be undesirable. At a sufficient distance from the coast, visual intrusion is minimized and wind turbines can be larger, thus increasing the overall installed capacity per unit area. Similarly, less attention needs to be devoted to reduce turbine noise emissions offshore, which adds significant costs to onshore wind turbines. Also, the wind tends to blow faster and more uniformly at sea than on land due to the absence topographical constraints such as mountains and buildings. A higher, steadier wind means

less wear on the turbine components and more electricity generated per square meter of swept rotor area. Onshore turbines are often located in remote areas, where the electricity must be transmitted by relatively long power lines to densely populated regions, but offshore turbines can be located close to high-value urban load centers.

The disadvantage of offshore development is that, investment costs are higher and accessibility is restricted, resulting in higher capital and maintenance costs. Also, environmental conditions at sea are more severe: more corrosion from salt water and additional loads from waves and ice. And finally offshore construction is more complicated.

Despite the difficulties of offshore development, it holds great promise for expanding wind generation capacity, however extracting wind energy offshore still is a daunting challenge [5].

The Floating Offshore Wind Turbine Concept The last decades bottom-founded offshore wind installations already have been in operation with success. Water depth however is a limiting factor in the deployment of these systems. One way to tackle this problem is to install wind turbine installations on top of floating structures.

A recent report by the European Wind Energy Association (EWEA) stated that reliable offshore wind turbine designs are necessary to unlock the promising offshore market potential in the Atlantic, Mediterranean and deep North Sea waters. Potentially the energy produced by wind turbines in deep waters in the North Sea alone could meet the total EU electricity consumption four times over. Although these statements are very positive, the technology is still at a very early stage of development, and in order to achieve commercial and large-scale deployment, the sector must overcome technical, economic and political challenges. The EWEA estimates that if these challenges are overcome, the first deep sea offshore wind farms could be installed and grid connected by 2017 [6]. Comparable findings follow from an assessment done by the National Renewable Energy Lab (NREL) for the United States [7]. Both EWEA and NREL reports also state that reliable modeling tools are key in the future for further improvement of FOWT designs.

In the past several different FOWT design concepts have been published (see figure Figure 1-1). Furthermore a number of FOWTs have been deployed with success. In 2009 the first full-scale FOWT installation called Hywind spar-buoy was deployed with success in Norway with a 2.3 MW turbine [6]. In 2011 a FOWT called WindFloat was deployed with a 2 MW turbine in Aguçadoura Portugal. Another one-to-eight scale FOWT named VolturnUS 1:8 was deployed off the coast of Maine (US) in 2013 for data collection. This particular design was based on the NREL 5 MW baseline turbine, the subject of study in this thesis [8].

With the arrival of FOWTs several technical challenges arose. In addition to the loads to which land based wind turbine structures are exposed, FOWTs are subject to an even more complex loading. Additional loads such as irregular wave loads, ice loads, collision impact, ocean currents and many others (see figure Figure 1-2) are to be dealt with. In addition, fluid structure interaction has an important role due to the large and slender bodies (blades and tower) of these installations [10]. Modeling the fully coupled aeroelastic and hydrodynamic response is therefore highly complex.

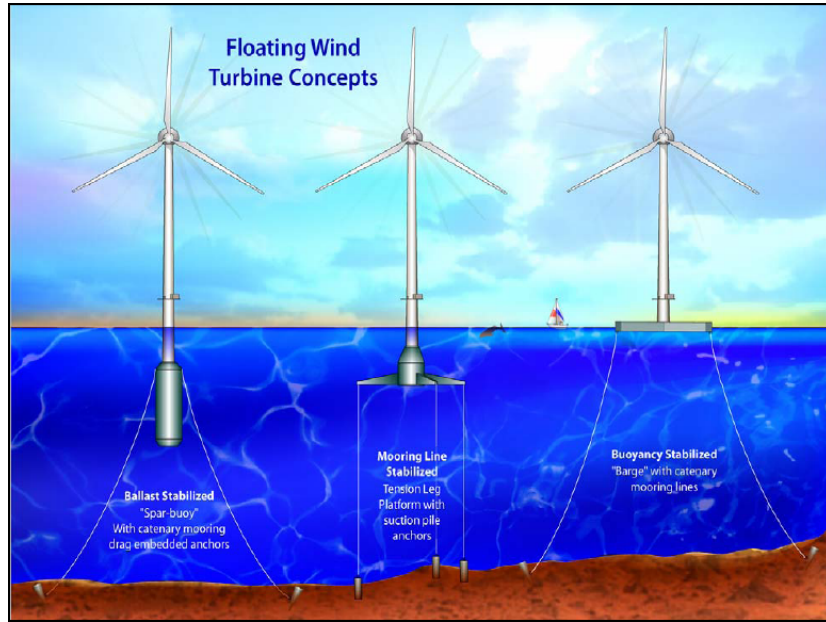


Figure 1-1: Three FOWT design concepts from left to right: **Left:** Ballast stabilized “Spar buoy” (Spar), **Center:** Mooring line stabilized “Tension leg platform” (TLP) **Right:** Buoyancy Stabilized “Barge” With catenary mooring lines (BG) [9]

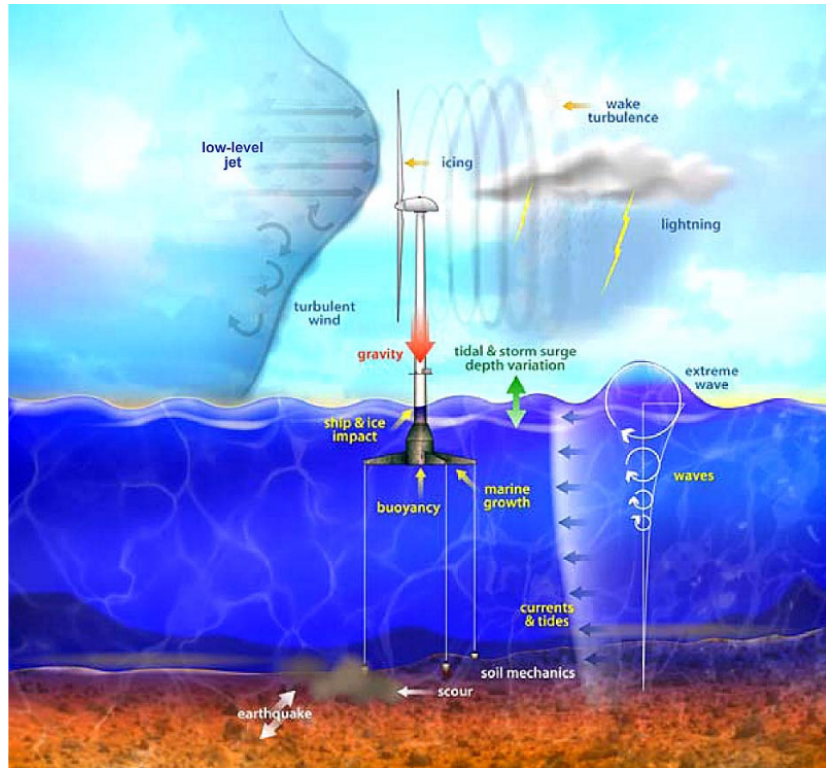


Figure 1-2: Environmental loads working on FOWTs [9].

1-2 Background

The need for comprehensive modeling tools capable of modeling the fully coupled response of floating offshore wind turbines led to design tools such as FAST [11]. The aerodynamic model used by these tools is based on Blade Element Momentum Theory (BEMT) in which it is assumed that the forces on a blade element can be calculated by means of two dimensional airfoil characteristics. In addition this model implements empirical knowledge to account for other effects, not described well by the BEMT, which will be explained in more detail in chapter 2 [12, 13].

The advantage of using the modified BEMT model instead of more advanced tools such as CFD codes lies in the fact that it is fast, cheap, and relatively easy to implement, which makes it ideal for the early stage of concept design. In addition this aerodynamic model is applied as part of a more complex model in which many factors need to be considered (see figure 1-2), this would result in very complex calculations when using CFD analysis. Although these relatively simple BEMT tools show good results for some situations their limitations, drawbacks, and disadvantages have to be understood. Furthermore validation is needed.

The commercial floating wind turbines deployed today, such as the Hywind spar-buoy, are equipped with instruments to collect valuable data, unfortunately the collected information is often not publicly available. Other data for the Hywind spar-buoy platform is available, however they are derived from wave basin model-scale testing [14].

Model-Scale Testing Proper model testing of FOWTs subject to combined wind and wave loads is desired for the validation of FOWT design tools and to better understand the complex underlying physics. Once accurately capturing real data of the rigid body motions and loads by means of model testing is possible, the data can be compared with numerical model results coming from the design tools available. These modeling tools can then be used with a much greater degree of confidence in the design process for commercial development of floating offshore wind turbines.

Although several model tests have been performed on FOWTs, e.g. [15–17], only one model experiment to date has made the effort to create the high-quality wind environment required for simulating proper wind turbine performance in a combined wind/wave test [17].

These model experiments were performed at the MARIN offshore basin where Froude scaling was applied in order to correctly model the combined loads on these structures (both hydro- and aerodynamic). The Froude scaling method showed good results for the structure's response. Unfortunately it led to significantly lower wind loads on the model-scale turbine when compared to both model- and full-scale estimations available from numerical modeling tools (FAST).

Reynolds Similitude The difference in wind loading was caused by Reynolds dissimilitude when Froude scaling was applied [17]. While the full-scale Reynolds number for the operating condition was 11×10^6 at 70% blade radius, the model-scale Reynolds number was found to be 35.7×10^3 . This difference in Reynolds number resulted in a laminar flow field at model-scale while the flow was fully turbulent for the full-scale case. In addition wind turbines and also current turbines are mostly operating at high AoA and therefore high loads, very

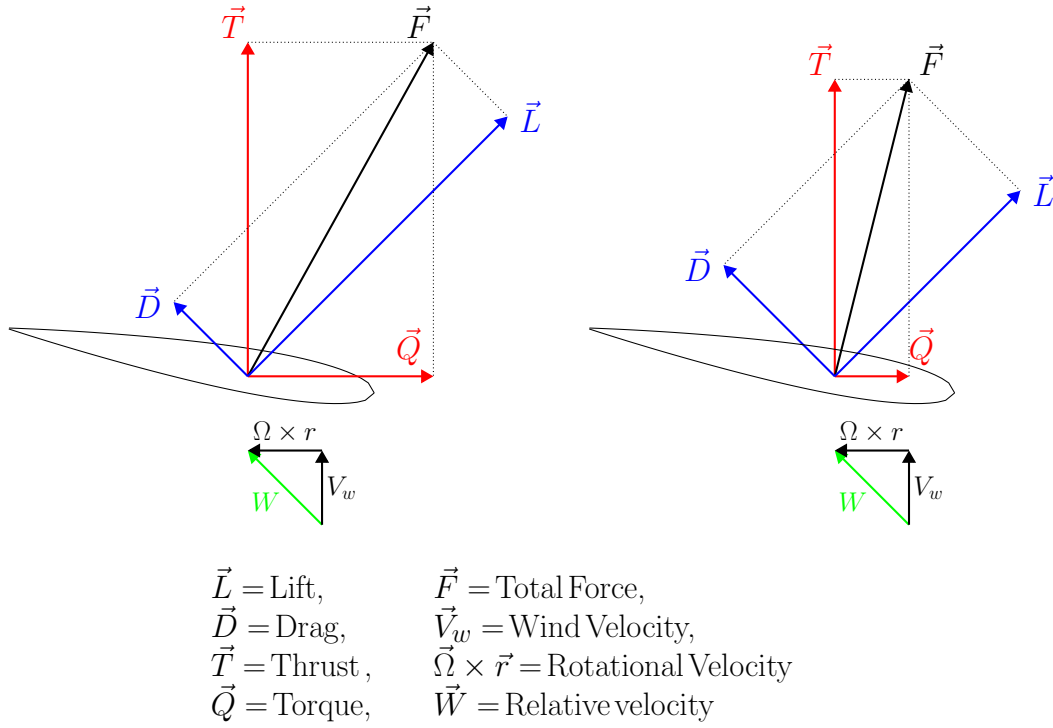


Figure 1-3: Effect of change in lift and drag on thrust and torque. **Left:** turbulent case **Right:** laminar case.

close to stall. Separation occurs often, and for low Reynolds numbers even more often. The laminar/turbulent difference between model and full-scale in combination with the presence of flow separation has a major impact on both C_l and C_d (C_T and C_P). The effect of Reynolds dissimilitude has previously been described and studied using CFD for axial marine current turbines [18].

For the lower Reynolds number regime at model-scale, the C_l values were significantly lower than for the high Reynolds number full-scale flow. On the contrary C_d was larger for the low Reynolds numbers at model-scale. The combined effect of the altered C_l and C_d for the low Reynolds numbers result in significantly lower aerodynamic loading especially the power coefficient C_P as can be seen in figure 1-3. Additionally Reynolds dissimilitude also has an effect on tower loading where vortex-induced vibration phenomena might occur.

Model-Scale Turbine Improvement Since the aerodynamic loads measured during model experiments were unsatisfactory, it was decided to improve the turbine aerodynamics while maintaining all other dynamic loads such as centrifugal forces generated by the turbine rotor. Several improvements have been proposed each with varying results [17, 19].

A blade section specially designed for low Reynolds numbers was proposed to improve the model-scale turbine performance i.e. C_P and C_T . The new rotor blade was designed based on the Drela AG04 airfoil section [20]. The idea was to obtain similar C_T for model- and full-scale conditions, since this axial force is the most important quantity for the floating behavior of the turbine and platform construction. The performance of the new turbine design was

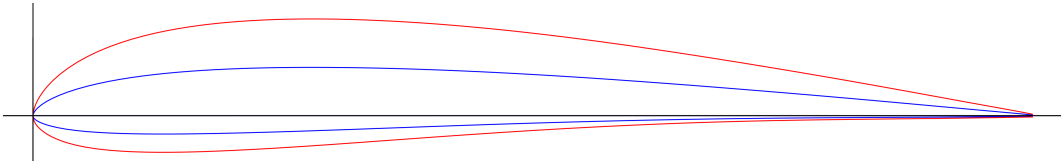


Figure 1-4: Foil sections of both Drela AG04 and Drela AG04-Modified (double thickness).

predicted using the BEMT based turbine dedicated design tool PropID [21] and showed a significant improvement of both the thrust and power coefficient (C_T and C_P respectively). For the performance predictions done using PropID 2D C_l , C_d values coming from XFOIL¹ computations were used.

Despite the improved rotor characteristics, manufacturing of such a thin turbine blade at model scale is not feasible while maintaining adequate structural integrity. As an alternative an increase in foil thickness was proposed as seen in figure 1-4. The effect of the increased blade thickness on rotor performance was studied using the BEMT based turbine dedicated design tool PropID [21] using two-dimensional C_l and C_d values coming from XFOIL. Based on the PropID results it was decided to further use this geometry for the new model-scale design [23]. The turbine was built and tested afterwards. This new model was further referred to as the MARIN Stock Wind Turbine (MSWT) [19].

Results After MSWT Improvement Next, the new turbine design was tested in MARIN's offshore basin, and calculations were done using PropID. Both the experiment and calculation data showed an improvement in the C_T values. The improved turbine also showed a better match with the estimated full-scale turbine performance. Despite the improvements in C_T (the objective) the results were still unsatisfactory in terms of C_P .

Implementing CFD Tools Since PropID makes use of a relatively simple aerodynamic BEMT model [21], it was desired to compare the results using a more advanced numerical model.

The use of a Computational Fluid Dynamics (CFD) tool was the next step in validating the data already obtained. MARIN's in-house Unsteady Reynolds Averaged Navier Stokes (URANS) code ReFRESCO was used to validate the previous results. 3D calculations were performed on the improved design to compare with the model-scale experiments, model-scale calculations by PropID, and eventually full-scale BEMT (FAST) estimates.

CFD Results The results of PropID and ReFRESCO agreed reasonably well for C_T at the design TSR= 7.0. However, for the lower TSR values the results start to deviate. When C_P is considered, the differences between the two methods (PropID, ReFRESCO) were significant. Since PropID makes use of 2D section data it might be that the 3D effects are not well predicted with these type of programs (BEMT) [19, 23].

¹XFOIL is an interactive program for the design and analysis of subsonic isolated airfoils. Given the coordinates specifying the shape of a 2D airfoil, Reynolds and Mach numbers, XFOIL can calculate the pressure distribution on the airfoil and hence lift and drag characteristics [22].

The results of the 3D ReFRESCO calculations showed a good agreement with the model experiments for both C_T and C_P while the PropID results show larger deviations, again, especially for C_P [19].

Since the full-scale prediction was based on the same modeling tool PropID, a full-scale CFD ReFRESCO analysis of the NREL 5MW baseline turbine would be of interest. In this way the full-scale predictions of the NREL wind turbine of both PropID and ReFRESCO can be compared. It is expected that this also provides better knowledge on the scaling effects present.

1-3 Objectives

The aim of the present thesis work is to predict the scale-effects on floating offshore wind turbines by means of a numerical analysis of model- and full-scale wind turbines using a RANS CFD solver.

Based on the previous work presented, the tasks of the thesis can be summarized as follows:

1. The research previously done by MARIN must be critically evaluated to provide a clear starting point for the remaining tasks.
2. A numerical study considering the 2D low Reynolds number airfoils, used for the MSWT design must be performed. This, to check the sensitivity to domain-size and turbulence model, and to determine the numerical uncertainty. The results can be used to further improve the turbine design, and to illustrate the scale effects. Furthermore, the results can be used as a guideline for the generation of BEMT input data by means of 2D low Reynolds number CFD calculations.
3. A numerical study considering the model-scale MSWT must be performed in order to check the sensitivity to domain-size and turbulence model. Furthermore a V&V study is performed to validate the numerical results against experimental measurement data. The results will provide the following; 1) more insight in the complex physics behind the observed scale effects, 2) provide a guideline for future wind-turbine analysis using CFD, 3) depending on the results suggestions can be proposed to further improve the MSWT design.
4. The MSWT and NREL 5MW baseline turbine must be analyzed for full-scale and model-scale conditions. The numerical settings for this analysis follow from the numerical studies on the 2D airfoils and MSWT. The results will provide insight in the scale effects present for both geometries. Additionally the results can be compared with the predicted full-scale performance coming from the BEMT-based design tools.

1-4 Report Outline

The remaining chapters of this report will provide a detailed description of the study and the relevant theory. In chapter 2 the theoretical background applicable to the study is presented.

Topics such as wind turbine aerodynamics, scaling laws, and the equations governing fluid flows will be covered.

The numerical theory is discussed in chapter 3. In this chapter more information is given on the numerical tools used, especially the CFD code ReFRESCO is described in detail.

Chapter 4 is devoted to the numerical setup of both two- and three-dimensional models. The geometry of the domains, grid topologies, and imposed boundary conditions are discussed in this chapter.

The results are split into three parts, each presented separately in chapters 5 to 7. First the study focusing on the numerical computations of the 2D airfoil is discussed in chapter 5. The study considering the flow over the three-dimensional MSWT at model-scale is given in chapter 6. The scaling effects for both NREL 5MW baseline turbine and MSWT are discussed in chapter 7.

An overall conclusion and recommendations regarding the complete study are provided in chapter 8.

Chapter 2

Theoretical Background

The required theoretical background necessary for the completion of this research is presented in this chapter. First the applied coordinate systems are presented in section 2-1. Next the scaling methodology is discussed in section 2-2. The relevant theory on wind turbine aerodynamics is presented in section 2-3. Finally the mathematical formulation of the flow is discussed in section 2-4 followed by an introduction on verification and validation procedures for numerical computations in section 2-5.

2-1 Geometry and Coordinate System

In this section the geometries of both the two and three-dimensional geometries will be discussed and additionally the respective coordinate systems will be explained. Since the two-dimensional model is based on the full three-dimensional wind turbine geometry, the three dimensional model will be discussed first.

2-1-1 Three-Dimensional Wind Turbine

Within this study two different turbines will be analyzed i.e. the NREL 5MW baseline and the modified MARIN Stock Wind Turbine (MSWT).

NREL 5MW geometry In support of concept studies which are aimed at assessing offshore wind technology, NREL developed the specifications of a representative utility-scale multi-megawatt turbine known as the "NREL offshore 5MW baseline wind turbine". This wind turbine is a conventional three-bladed upwind variable-speed variable blade-pitch-to-feather-controlled turbine. To create the model, NREL obtained some broad design information from the published documents of turbine manufacturers. Because detailed data was unavailable, the publicly available properties from various projects were also used. From this data a composite was created by extracting the best available and most representative specifications.

The NREL 5MW model is now commonly used as a reference by research teams throughout the world [24].

The general particulars of the NREL 5MW relevant for this study as given by [24] are presented in the second column of table 2-1.

Table 2-1: Properties of the full scale and model scale ($\lambda = 50$ + Froude scaling) NREL 5MW Baseline Wind Turbine [24].

Property	Full Scale	Model Scale	Units
Rated Power	5	5.7	[MW]/[W]
Rotor Diameter	126	2.52	[m]
Hub Diameter	3	-	[m]
Hub Height (above sea level)	90	1.80	[m]
Cut-In Rotor Speed	6.9	48.81	[RPM]
Rated Rotor Speed	12.1	85.6	[RPM]
Cut-In Wind Velocity	3	0.42	[m/s]
Rated Wind Velocity	11.4	1.6	[m/s]
Cut-Out Wind Velocity	25	3.54	[m/s]
Rated Tip Speed	80	11.31	[m/s]
Reynolds no. @ 0.7 Radius	11.5×10^6	35.7×10^3	[–]

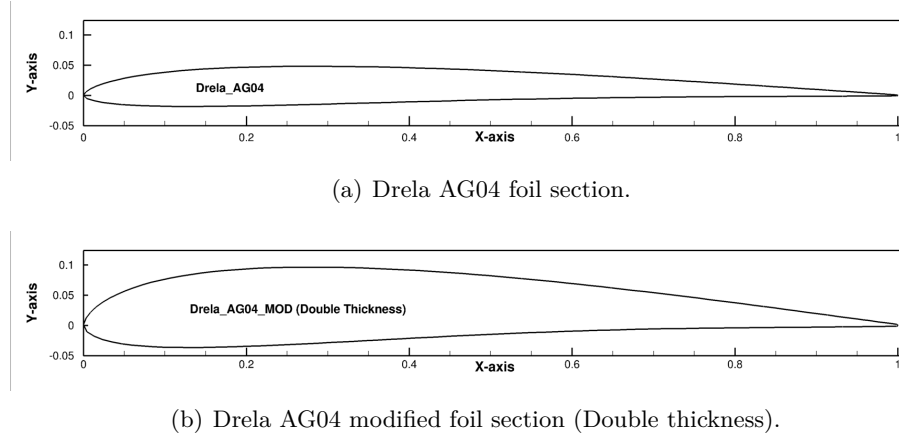
To perform experimental measurements at the MARIN offshore basin, the NREL 5MW model was scaled using Froude scaling and geometric similarity, with a scaling parameter of $\lambda = 50$. More details on the scaling methodology is given in section 2-2. The model scale properties of the NREL 5MW turbine are presented in the third column of table 2-1.

The rotor blade design of the NREL 5MW turbine consists of a varying section along the span of the blade. Near the root of the blade cylindrical sections are used, near the blade tip a NACA 64-618 foil is used and in the intermediate region a series of sections form the DU series is implemented. A detailed description of the blade geometry can be found in [14, 24], or in section 4-2 of this thesis.

MARIN Stock Wind Turbine As explained before, a modified wind turbine model was proposed to improve model-scale turbine performance. A new blade design was obtained based on a specially designed low Reynolds number foil section i.e. the Drela-AG04. A graphical presentation of the Drela AG04 airfoil section is given in figure 2-1(a).

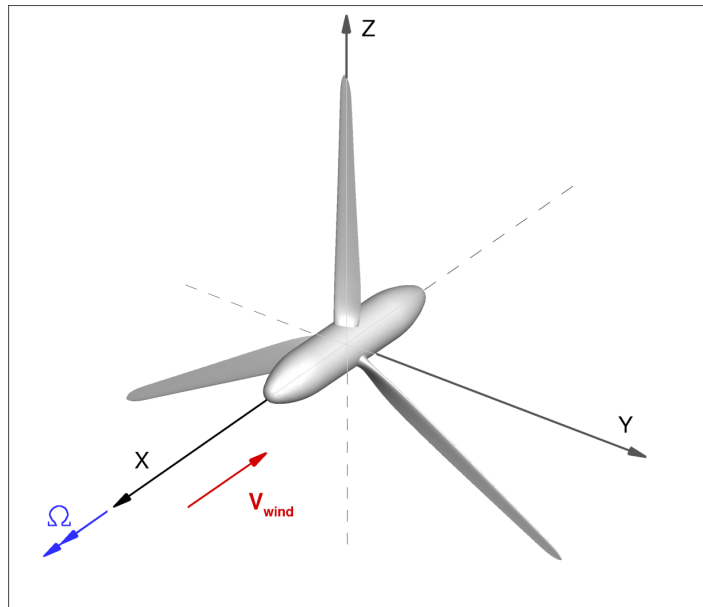
Despite the Drela AG04 being suitable for use in sub-critical flow regimes, manufacturing a wind turbine blade using such thin airfoil sections while maintaining adequate structural integrity is simply not feasible [14, 23]. To solve this problem the thickness of the Drela AG04 was doubled resulting in a foil section as presented in figure 2-1(b). The modified foil section will be further referred to as the *Drela AG04-Modified*.

For the redesign of the turbine blade the Drela AG04-Modified airfoil is employed over the complete length of the blade, in which the structural twist of the NREL 5MW turbine blade is mimicked. Furthermore the relative chord distribution is maintained from the NREL 5MW blade, but the chord length is uniformly increased by 25% in order to compensate for the

**Figure 2-1:** Drela AG04 foil sections

slightly lower lift coefficient allowing for production of the appropriate thrust forces under Froude-scaled wind [17]. Furthermore the pitch distribution is altered using large pitch angles. The redesigned wind turbine is further referred to as MSWT.

Coordinate System The origin of the coordinate system used for both the NREL 5MW and the MSWT designs is located at the intersection of the rotating axis and the swept plane of the rotor. From the origin the x -axis is pointing in forward direction, i.e. in opposite direction to the wind direction. The positive z -axis is pointing in vertical upward direction. Finally the y -axis is pointing in horizontal direction resulting in a positive Cartesian coordinate system as presented in figure 2-2. In this figure also the wind velocity and the rotational direction of the turbine is indicated by vectors \mathbf{V}_{wind} and $\boldsymbol{\Omega}$ respectively.

**Figure 2-2:** Coordinate system for the 3D wind turbine.

2-1-2 Two-Dimensional Airfoil

The study of the two-dimensional sections are all done on the modified version of the low Reynolds number Drela-AG04 airfoil as described in the previous section.

For these computations the x -axis is pointing from Leading Edge (LE) to Trailing Edge (TE). The y -axis is pointing upward perpendicular to the chord line of the foil. The origin of the coordinate system is located at the LE of the foil. The coordinate system is fixed to the airfoil geometry and will translate along with the airfoil for different angles of attack. A graphical presentation of the axis system is also given in figure 4-1 in chapter 4, where the numerical setup is discussed.

2-2 Scaling Methodology

To perform accurate model-scale experiments it is of importance to properly scale the dynamic environment and behavior of the system considered. Within this report the scaling methodology applied during tests previously performed at MARIN is used. In this section only a brief description of the method is presented, for a full detailed presentation see e.g. [14, 17].

Froude Similitude The Froude number, denoted by Fr , is the dimensionless parameter which quantifies the ratio between gravitational and inertial forces of waves. Froude's scaling law in combined with geometric similarity, is the most appropriate scaling method for free and moored floating structure tests, since the gravitational effect of the water with a free surface predominates. The effects of other factors, such as viscosity and surface tension are often small such that they can be neglected [25].

The Froude number is given by equation (2-1) where V represents the characteristic velocity, g the gravitational constant, and L the characteristic dimension,

$$Fr = \frac{V}{\sqrt{gL}}. \quad (2-1)$$

When Froude-scaling is used, the Froude numbers for both the prototype and the model are remained, this results in the following relationship,

$$\frac{V_p}{\sqrt{gL_p}} = \frac{V_m}{\sqrt{gL_m}}, \quad (2-2)$$

in which the subscripts p and m in equation (2-2) represents the prototype and model respectively. By combining geometric similarity, a scaling factor $\lambda = L_p/L_m$, and equation (2-2), other quantities can be scaled in terms of the scaling factor λ . Note that for the model tests described by [14, 17] a scaling factor of $\lambda = 50$ was used.

By implementing Froude scaling most properties of interest, which influence the global dynamic response of the system, are scaled accurately, except for the aerodynamic wind loads, as will be discussed later [14]. Additional information on Froude-scaling can be found in [26].

Tip Speed Ratio The Tip Speed Ratio (TSR) is the ratio between the angular velocity multiplied by the radius of the turbine rotor and the inflow wind velocity [27]. The TSR is given by equation (2-3), where Ω is the angular velocity, R the blade tip radius of the rotor, and V the wind inflow velocity,

$$TSR = \frac{\Omega R}{V}. \quad (2-3)$$

Maintaining the TSR between prototype and model will ensure that the rotational speed and the corresponding excitation frequencies caused by aerodynamic effects are scaled correctly. Other quantities such as the thrust and torque of the turbine are scaled accurately when a small Reynolds number dependency is assumed for the lift and drag coefficients of the turbine blades [14].

Reynolds Similitude Although many quantities are scaled correctly when using the Froude scaling method, there are complications due to Reynolds number effects. The Reynolds number, often denoted by Re quantifies the ratio between the viscous and inertial forces of fluid flows and is given by equation (2-4) in which ρ represents the density, V the wind velocity, L a characteristic dimension and μ the dynamic viscosity.

$$Re = \frac{\rho V L}{\mu} \quad (2-4)$$

While the Froude number is the primary scaling parameter in hydrodynamic model tests, the Reynolds number effects are not scaled properly for large scaling factors. The Reynolds number for a Froude scaled model is in fact smaller than the full-scale Reynolds number by a factor of $\lambda^{1.5}$, which for the experiments here considered result in a model-scale Reynolds number which is 354 times smaller(!) than the full-scale Reynolds number (for $\lambda = 50$) [25].

The consequence of this difference in Reynolds numbers is that if the flow at full scale may be fully turbulent $\mathcal{O}(10^7)$, at model-scale the flow maybe fully laminar $\mathcal{O}(10^4)$. The effects of these low Reynolds numbers on aerodynamic performance is discussed in section 2-3-1

Additional Quantities Other quantities not related to the Reynolds number such as gyroscopic and mass properties are normally not scaled correctly when Froude scaling is applied, however these are not relevant to the aerodynamic analysis of the turbine considered in the present study. Additionally, from the performed experiments it was shown that these quantities were scaled with reasonable accuracy for this specific experiment [14].

2-3 Wind Turbine Aerodynamics

To analyze the performance of wind turbines a good understanding of the relevant concepts of wind-turbine aerodynamics is desired. In this section the basic required concepts and terminology are introduced. Additionally the basic theory of both the Blade Element Method and Blade Element Momentum Theory (BEMT) are presented in section 2-3-2.

2-3-1 Theory of Wing Sections

Although the airflow around wind turbines is three dimensional, some of the theory to describe wind-turbine performance relies mainly on two dimensional wing section data. Additionally the 2D theory is applied in the studies presented in chapter 5. Therefore the main concepts of 2D wing sections is given in this section.

Non Dimensional Parameters Three important parameters commonly used to describe the aerodynamic performance of an airfoil section are the lift, drag, and the moment generated by an airflow around a foil. A flow of air over an airfoil section creates a pressure P working perpendicular to the airfoil surface. This pressure is generated by the rate of change of momentum of the air molecules impacting on the airfoil surface. Additionally the frictional property of the airflow generates a shear stress τ tangential to the surface of the airfoil as can be seen in figure 2-3(a).

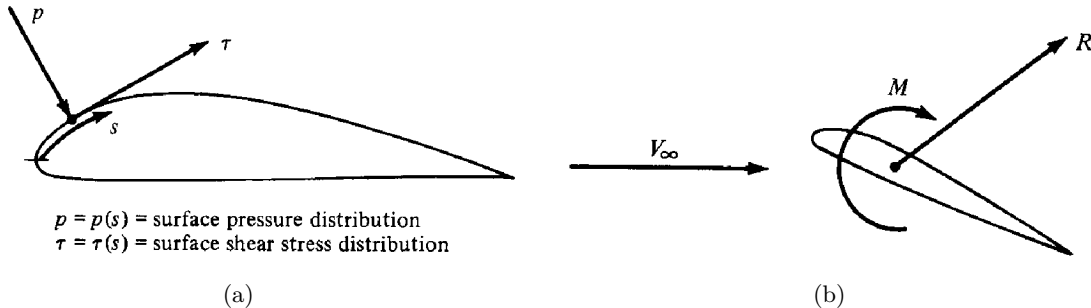


Figure 2-3: Left Pressure and shear stress on the airfoil surface. Right Resultant aerodynamic force and moment on the airfoil [28].

The combined net shears-stress and pressure integrated over the airfoil surface result in a net resultant force R and moment M working in a certain direction as can be seen in figure 2-3(b).

When the resultant force R is decomposed in the direction parallel and perpendicular to the flow direction, the lift and drag forces are obtained. By definition the lift force L is working perpendicular to the flow direction and the drag force D is working parallel to the flow direction. In figure 2-4 a graphical presentation of this decomposition is given where α represents the angle of attack. The lift force mainly consists of pressure contributions while the drag is dominated mainly by the frictional forces (i.e. at small angles of attack at which the flow is fully attached).

Both the lift and drag forces as well as the moment can be non-dimensionalized using a reference area S , a reference length l , and the free-stream dynamic pressure which is given by

$$q_\infty \equiv \frac{1}{2} \rho_\infty V_\infty^2, \quad (2-5)$$

where the subscript ∞ represent the properties of the flow far upstream. The resulting dimensionless coefficients are the lift, drag, and moment coefficients given by,

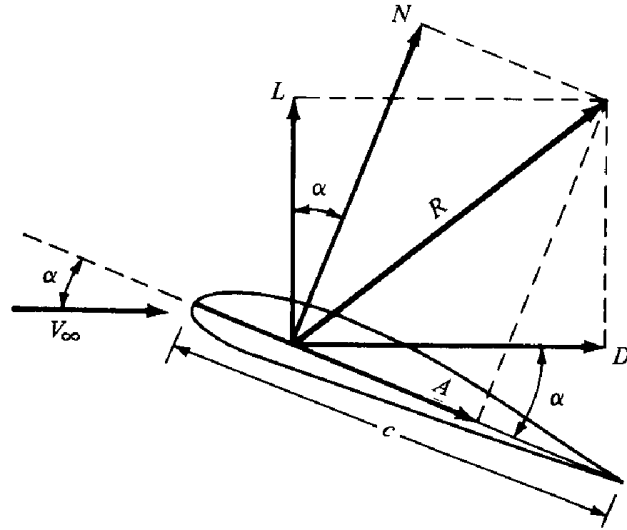


Figure 2-4: Resultant force decomposed in lift and drag [28].

$$C_L \equiv \frac{L}{q_\infty S}, \quad (2-6)$$

$$C_D \equiv \frac{D}{q_\infty S}, \quad (2-7)$$

$$C_M \equiv \frac{M}{q_\infty S l}. \quad (2-8)$$

These expressions are valid for three-dimensional airfoils. For considering two-dimensional sections the reference area is reduced to only the chord length c of the foil. When the reference length is also set to the chord length the following expressions will be as follows,

$$C_l \equiv \frac{L'}{q_\infty c}, \quad (2-9)$$

$$C_d \equiv \frac{D'}{q_\infty c}, \quad (2-10)$$

$$C_m \equiv \frac{M'}{q_\infty c^2}. \quad (2-11)$$

Note that the two-dimensional coefficients described by (2-9) to (2-10) are per unit span. These coefficients describe important characteristics of a wing section and are dependent of various variables such as Reynolds number and angle of attack.

Commonly the efficiency of an airfoil is described by the lift to drag ratio given by equation (2-12).

$$\frac{L}{D} = \frac{q_\infty S C_L}{q_\infty S C_D} = \frac{C_L}{C_D}. \quad (2-12)$$

As an addition to the lift drag and moment coefficients the pressure coefficient C_p is often used to describe the pressure in a non-dimensional way. This is done by dividing manually the pressure by the dynamic pressure of the free-stream flow or,

$$C_p = \frac{P - P_\infty}{q_\infty}, \quad (2-13)$$

where q_∞ is given by equation (2-5).

Boundary Layer The boundary layer is located close to the surface of the body where the viscous effects of the fluid are significant. The thickness of the boundary layer can vary and is either laminar or turbulent. Laminar flow is smooth and regular and fluid elements move smoothly along the stream-lines. In turbulent flow the streamlines break up and fluid elements move in a random, irregular, and tortuous fashion.

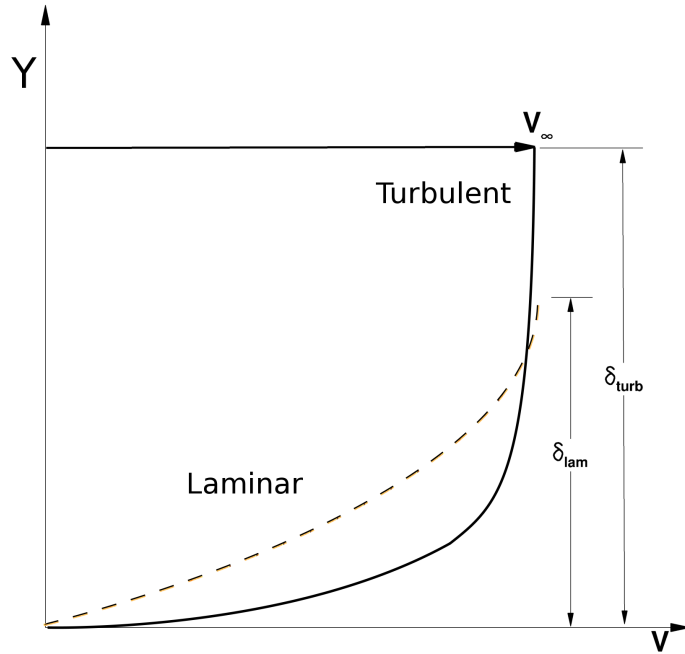


Figure 2-5: Velocity profiles for laminar and turbulent boundary layers. Note the difference in thickness between the laminar and turbulent layers

The difference between laminar and turbulent flow is dramatic and can have a major impact on the aerodynamics. From figure 2-5 it can be seen that the turbulent velocity profile is “fatter”, or fuller, than the laminar profile. For the turbulent profile, from the outer edge to a point near the surface, the velocity remains reasonably close to the free-stream velocity; it then rapidly decreases to zero at the surface. In contrast, the laminar velocity profile gradually decreases to zero from the outer edge to the surface. When the velocity gradients at the wall for both turbulent and laminar flows are compared in figure 2-5 it follows:

$$\left(\frac{dV}{dy} \right)_{y=0} \text{laminar} < \left(\frac{dV}{dy} \right)_{y=0} \text{turbulent} \quad (2-14)$$

Hence it follows from $\tau_w = \mu(dV/dy)$ (where τ_w is the surface shear stress), that the frictional forces at the surface are larger when the boundary layer is turbulent [28], i.e.,

$$(\tau_w)_{laminar} < (\tau_w)_{turbulent} \quad (2-15)$$

The change from a laminar to turbulent flow is called transition. The exact location at which transition takes place, known as the *transition point*, depends on a large number of variables such as the velocity of the flow and the roughness of the surface. The value of x along the airfoil surface where transition takes place is the critical value X_{cr} . Additionally the critical Reynolds number, $Re_{x_{cr}}$, is given by

$$Re_{X_{cr}} = \frac{\rho_\infty V_\infty x_{cr}}{\mu_\infty}. \quad (2-16)$$

Using the Reynolds number and the boundary layer thickness, the skin-friction coefficient can be estimated based on flat-plate theory for both laminar and turbulent flow as follows [28];

$$\text{Laminar flow : } C_{f_{lam}} \approx \frac{1.328}{\sqrt{Re}}, \quad \delta_{lam} \approx \frac{5.0x}{\sqrt{Re_x}}, \quad (2-17)$$

$$\text{Turbulent flow : } C_{f_{turb}} \approx \frac{0.074}{Re^{1/5}}, \quad \delta_{turb} \approx \frac{0.37x}{Re_x^{1/5}}, \quad (2-18)$$

where δ is the boundary layer thickness at a certain location x along the airfoil surface, Re_x the Reynolds number at location x from the leading edge of the surface.

An adverse pressure gradient i.e. an increasing pressure in the flow direction occurs when the velocity is decreasing in the flow direction. The magnitude of this gradient has major influence on the behavior of the boundary layer [29]. An increasing pressure gradient in the flow direction could, depending on the curvature of the geometry, result in a negative velocity in the boundary layer which may eventually cause separation as illustrated in figure 2-6.

The state of the boundary layer, whether laminar or turbulent, also has a significant effect on the performance of an airfoil. The laminar boundary layer for instance is highly sensitive for separation when adverse pressure gradients are present (typically towards the trailing edge of an airfoil). It is susceptible to destabilization and transition to turbulent flow. The stability of a laminar boundary layer is affected by both pressure gradients and Reynolds number [29]. Depending on the Reynolds number the laminar boundary layer reacts to adverse pressure gradients in three different ways as can be seen in figure 2-7.

The viscous phenomena in the boundary layer work against the development of lift. The desired lift is obtained only as long as the boundary layer can remain attached when subject to the lift producing pressure gradients about the airfoil. Once boundary layer separation occurs, loss of lift results and the loss increases with the extent of separation. The boundary layer also produces drag through both friction forces and pressure forces when separation occurs. The Reynold number serves as an indicator of certain boundary layer characteristics.

As mentioned in section 2-2 the Reynolds number regime for the particular problems (turbine/foils) at model-scale is extremely low. As a result the flow around the turbine blades is likely to be laminar and thus resulting in degraded airfoil performance i.e. decreased C_l and increased C_d due to early flow separation.

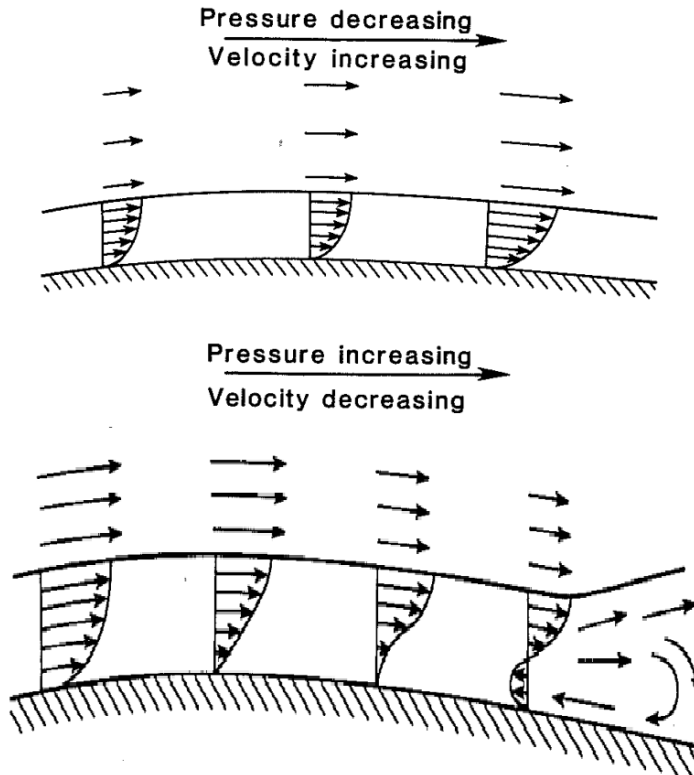
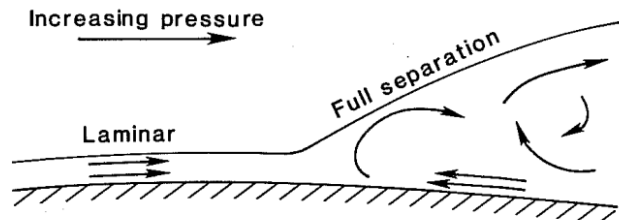


Figure 2-6: Effects of a negative and positive pressure gradient on a boundary flow [29].

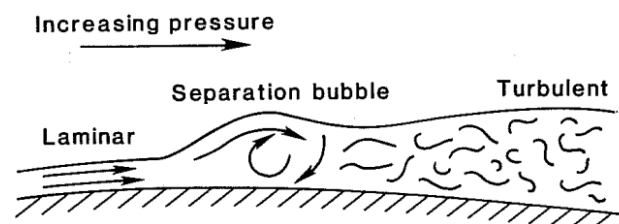
Foil Thickness Within the linear range of a lift curve, the inviscid lift curve slope of an airfoil will benefit from increased thickness as can be seen in figure 2-8(a). With increasing section thickness an increase of lift curve slope of 10 percent over the thin airfoil value of $2\pi\alpha$ can be obtained. At high Reynolds numbers ($Re \geq 10^6$) viscous effects will decrease the lift curve slope, which results in lift curve slopes of typically 5% to 10% below the slope obtained from thin airfoil theory. This is not the case for the extremely low Reynolds number regime (typically $Re = 10^4$) [30].

For very low Reynolds numbers, where the flow is fully laminar, increasing the maximum airfoil thickness has a negative effect on both the lift and drag properties of the airfoil. The drag is increased due to larger pressure recovery caused by the increased thickness. Although this negative effect is present for a wide range of Reynolds numbers (both laminar and turbulent) the order of magnitude is much larger for the low Reynolds number case (typically $Re < 10^6$) resulting in a decrease in lift to drag ratio and hence a lower efficiency [30].

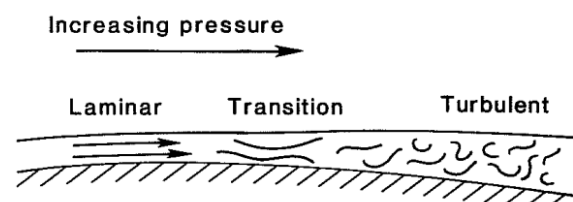
For these low Reynolds numbers the growth of the boundary layer is dominating the effect of increasing thickness by a significant decrease in lift curve slope in the linear range of the lift curve. Additionally, increased boundary layer thickness has a decambering effect on the effective airfoil geometry, which grows with increasing thickness. The decambering of the effective geometry will cause a rapid reduction of the lift curve slope in the non-linear region. The increase of thickness also causes separation to happen for lower angles of attack. The separated regions will then result in a large displacement of flow within the aft boundary



(a) Low Reynolds numbers: full separation and stall



(b) Medium Reynolds numbers: separation and reattachment as turbulent.



(c) High Reynolds numbers: transition to turbulent.

Figure 2-7: Reynolds number effects on laminar boundary layer subject to adverse pressure gradient [29].

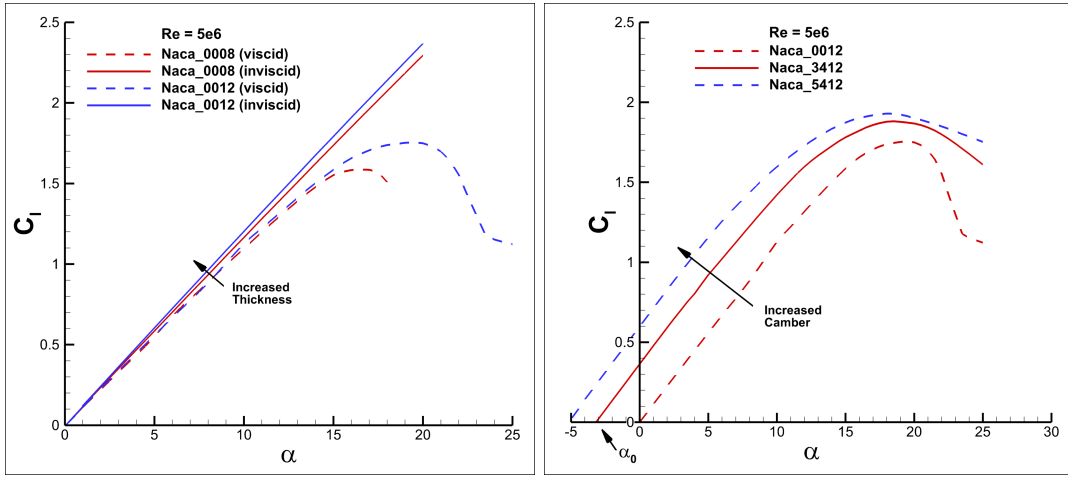


Figure 2-8: Lift curves for varying airfoil geometries obtained using XFOIL at $Re = 5 \cdot 10^6$.

layer, increasing the decambering effect even more and resulting in larger reductions in lift compared to fully attached flows [30].

It is obvious that increasing the thickness of airfoil geometries has a great effect on the performance of the foil. Especially for the low Reynolds number regime, increasing the thickness can have negative effects. Meaning, that for attaining a specific lift at low Reynolds numbers, it is better to have thinner airfoils with an increased amount of camber, to account for the decambering effect.

2-3-2 Blade Element Momentum Theory

A common method to predict the performance of wind turbines is the Blade Element Momentum Theory (BEMT). This method is based on the actuator disc concept which describes the energy extraction process of the turbine by an energy extracting disc i.e. the “actuator disc”. The basic BEMT and all the necessary derivations are presented in this section (for a full detailed derivation see e.g. [27]).

Actuator Disc Theory The actuator concept assumes that the affected mass of air remains separate from the air which does not pass through the rotor disc and no air flows across the boundary of the stream-tube (see figure 2-9). From these assumptions it follows that the mass flow rate of the air flowing along the stream-tube will be constant for all stream-wise positions along the stream-tube. When the air flows through the rotor disc a drop in static pressure exists such that the air is below the atmospheric pressure behind the rotor. The energy extraction and therefore wind-velocity and pressure drop over the actuator disc causes the stream-tube to expand as can be seen in figure 2-9.

The power of the actuator disc theorem lies in the fact that it does not require any specific turbine design because only the energy extraction process is considered. As a consequence it

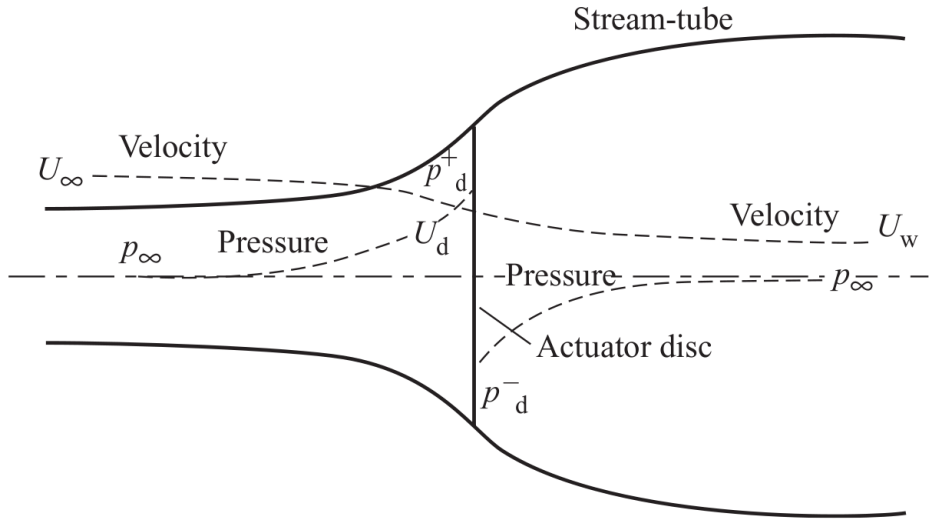


Figure 2-9: Energy extraction over the stream-tube of an actuator disc [27].

does in no way explain what happens to that energy; it may well be put to useful work but some may be spilled back into the wind as turbulence and eventually be dissipated as heat.

The mass flow rate must be the same everywhere along the stream-tube and is given by $\rho A U$ where ρ is the air density, A the swept area of the rotor, and U is the inflow velocity of the wind. Along the stream-tube the mass flow rate can be written as follows,

$$\rho A_\infty U_\infty = \rho A_d U_d = \rho A_w U_w, \quad (2-19)$$

where the subscripts ∞ , d , and w refer to the undisturbed conditions far upstream, the conditions at the actuator disc, and the conditions in at the wake-field respectively. When the velocity variation induced by the actuator disc is superimposed on the inflow velocity U_∞ , the velocity at the disc can be written in terms of a constant as follows,

$$U_d = U_\infty(1 - a), \quad (2-20)$$

where the constant a is known as the *axial-flow induction factor*.

Momentum Theory The air passing through the actuator disc as discussed previously, undergoes a change in velocity i.e. $U_\infty - U_w$, and a rate of change of momentum which is equal to the change of velocity multiplied by the mass flow rate. This can be written as follows,

$$\text{Rate of change of momentum} = (U_\infty - U_w)\rho A_d U_\infty(1 - a). \quad (2-21)$$

This change of momentum is caused by the pressure difference across the disc and results in a net force. When the pressure difference is multiplied by the swept area of the rotor the following can be written,

$$(P_d^+ - P_d^-)A_d = (U_\infty - U_w)\rho A_d U_\infty (1 - a), \quad (2-22)$$

where P_d^+ and P_d^- represent the up and downstream pressure at the actuator disc respectively. To find the pressure difference between the upstream and downstream flow, Bernoulli's equation is used to both the upstream and downstream sections of the stream-tube. Two separate equations are necessary because the amount of energy upstream of the actuator disc differs from the amount downstream. Under steady conditions Bernoulli's equation states the following,

$$\frac{1}{2}\rho U^2 + P + \rho gh = \text{constant}, \quad (2-23)$$

where P is the pressure and h is the height. It then follows from equation (2-23) that,

$$\frac{1}{2}\rho_\infty U_\infty^2 + p_\infty + \rho_\infty g h_\infty = \frac{1}{2}\rho_d U_d^2 + p_d^+ + \rho_d g h_d. \quad (2-24)$$

Similarly for the downstream case,

$$\frac{1}{2}\rho_w U_w^2 + p_w + \rho_w g h_w = \frac{1}{2}\rho_d U_d^2 + p_d^- + \rho_d g h_d. \quad (2-25)$$

When subtracting equation (2-24) and (2-25) and assuming the flow to be incompressible and horizontal i.e. $\rho_\infty = \rho_d = \rho_w$ and $h_\infty = h_d = h_w$ then,

$$(P_d^+ - P_d^-) = \frac{1}{2}\rho(U_\infty^2 - U_w^2). \quad (2-26)$$

Substitution of this equation into (2-22) will give,

$$\frac{1}{2}\rho(U_\infty^2 - U_w^2)A_d = (U_\infty - U_w)\rho A_d U_\infty (1 - a), \quad (2-27)$$

and hence,

$$U_w = (1 - 2a)U_\infty. \quad (2-28)$$

Power and Thrust Coefficients A common method to describe the performance characteristics of a wind turbine is by the power and thrust coefficients which are derived next.

The force generated by the rotor on the air is given by equation (2-22). Since this force is working at the actuator disc the rate of work can be expressed using the air velocity at the location of the actuator disc,

$$\begin{aligned} Power &= FU_d = U_\infty(1-a)2\rho A_d U_\infty^2 a(1-a) \\ &= 2\rho A_d U_\infty^3 a(1-a)^2. \end{aligned} \quad (2-29)$$

The power can be made dimensionless by dividing it with the power available in the free-stream airflow, resulting in the following expression,

$$\begin{aligned} C_P &= \frac{Power}{\frac{1}{2}\rho A_d U_\infty^3}, \\ &= \frac{2\rho A_d U_\infty^3 a(1-a)^2}{\frac{1}{2}\rho A_d U_\infty^3}, \\ C_P &= 4a(1-a)^2. \end{aligned} \quad (2-30)$$

The thrust coefficient is obtained when the force given by (2-22) is non-dimensionalized by the thrust available in the free-stream flow and the swept area of the rotor. The resulting expression for the thrust coefficient is given by,

$$\begin{aligned} C_T &= \frac{Thrust}{\frac{1}{2}\rho U_\infty^2 A_d}, \\ &= \frac{2\rho A_d U_\infty^2 a(1-a)}{\frac{1}{2}\rho U_\infty^2 A_d}, \\ C_T &= 4a(1-a). \end{aligned} \quad (2-31)$$

Betz Limit When the power coefficient is given by (2-30) it follows that the maximum value of C_P occurs when the following is true,

$$\frac{dC_P}{da} = 4(1-a)^2 - 8a(1-a) = 0. \quad (2-32)$$

This is satisfied when $a = \frac{1}{3}$. Substitution of $a = \frac{1}{3}$ back into equation (2-30) will give the maximum achievable power coefficient,

$$C_{P_{max}} = 4 \cdot \frac{1}{3}(1 - \frac{1}{3})^2 = \frac{16}{27} \approx 0.5926. \quad (2-33)$$

This maximum achievable power coefficient is referred to as the Betz limit, named after the German physicist who published the Betz limit in 1919. Until today no wind turbines have been designed capable of exceeding this limit [27].

Angular Momentum Theory The exertion of a torque on a rotor disc by the air passing through it requires an equal and opposite torque to be imposed upon the air. As a consequence the air in the wake-field will rotate in the opposite direction to that of the rotor. This means the air behind the rotor gains angular momentum. The angular and axial momentum of the air in the wake-field result in an air particle trajectory given in figure 2-10

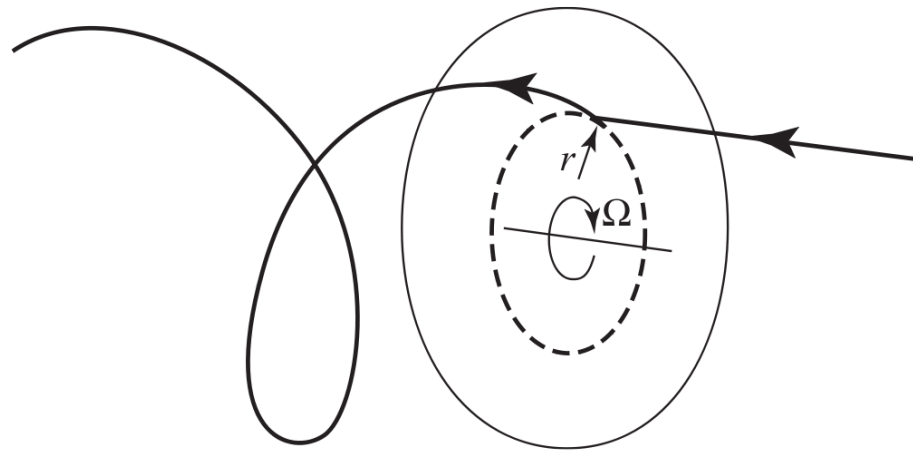


Figure 2-10: Trajectory of an air particle in the wake-field of a rotor disc [27].

The change in tangential velocity is expressed in terms of a *tangential flow induction factor* a' . The tangential velocity is assumed to be zero upstream of the rotor and $2\Omega r a'$ downstream of the rotor opposite to the rotor motion. The tangential induction factor is given by the following expression [27],

$$a' = \frac{a(1-a)}{\gamma_r^2}, \quad (2-34)$$

where γ_r is the local tip speed ratio.

Blade Element Theory The blade element theory assumes that the aerodynamic lift and drag forces on the span-wise elements of radius r and length δr of the rotor blades are responsible for the rate of change of both axial, and angular momentum of the air passing through the annulus swept by these blade elements as can be seen in figure 2-11.

The theory assumes that the forces on a blade element can be calculated by means of two-dimensional airfoil characteristics such as C_l and C_d using an angle of attack determined from the incident resultant velocity in the cross-sectional plane of the element. Both the span-wise velocity component and other three-dimensional effects are ignored within this theory.

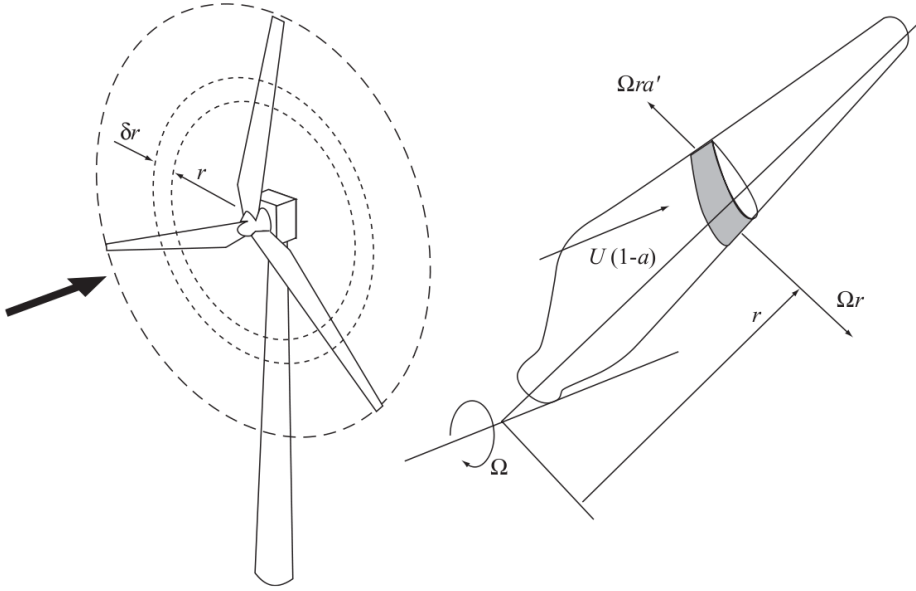


Figure 2-11: Blade element swept area and airflow over rotor blade [27].

The angle of attack used for each blade element follows from the wind speed, the induction factors a and a' , and the rotational velocity of the rotor. The lift and drag forces can then be calculated using the two-dimensional lift and drag coefficients, the apparent angle of attack, and the induction factors.

From the angular velocity Ωr , the tangential velocity in the wake, and the inflow velocity U_∞ , the relative velocity at the blade element can be determined. First the angular velocity and tangential velocity are combined resulting in the tangential flow velocity at the blade given by $(1 + a')\Omega r$. The relative velocity W at the blade is then as follows,

$$W = \sqrt{U_\infty^2(1 - a)^2 + \Omega^2 r^2(1 + a')^2}. \quad (2-35)$$

This relative velocity acts at an angle ϕ relative to the rotor plane, as can be seen in figure 2-12. The relative velocity angle ϕ can be obtained using the following expressions,

$$\sin \phi = \frac{U_\infty(1 - a)}{W} \quad \text{and} \quad \cos \phi = \frac{\Omega r(1 + a')}{W}. \quad (2-36)$$

The lift and drag forces on the blade element of length δr relative to the direction of W are then given by,

$$\delta L = \frac{1}{2}\rho W^2 c C_l \delta r, \quad (2-37)$$

$$\delta D = \frac{1}{2}\rho W^2 c C_d \delta r, \quad (2-38)$$

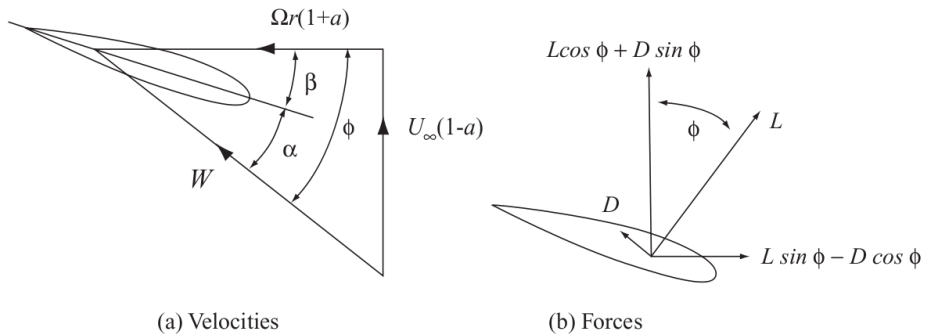


Figure 2-12: Blade element velocities and forces [27].

The resulting forces parallel and perpendicular to the rotor plane can then be derived as shown in figure 2-12.

The magnitude of the relative velocity angle ϕ greatly influences the effect of lift and drag (C_l and C_d) on both thrust and torque (C_T and C_P). For a large relative velocity angle, the drag of the foil is the main contributor to the total thrust force, while the lift force is the main contributor to the torque. When the relative velocity angle is small the opposite is true, i.e. lift is mainly contributing to the thrust force while drag is mainly contributing to the total torque. Note that for small ϕ the drag is contributing negatively to the total amount of generated torque.

Blade Element Momentum Theory All the previously discussed theorems can be combined resulting in the Blade Element Momentum Theory (BEMT), which is generally attributed to Betz and Glauert [12]. The theory assumes that the force of a blade element is only responsible for the change in momentum of the air passing through the swept area of a blade element. It is also assumed that there is no interaction between the single blade element flows in radial direction. Although in theory this is only the case when the axial induction factor is constant in radial direction this assumption gives good results. Especially for long aspect ratio blades this is true, which is the case for wind turbine blades (flow is almost two-dimensional) [27].

The aerodynamic force component in axial direction generated by N blade elements is given by,

$$\delta L \cos \phi + \delta D \sin \phi = \frac{1}{2} \rho W^2 N c (C_L \cos \phi + C_d \sin \phi) \delta r. \quad (2-39)$$

The rate of change of axial momentum of the air passing through the swept area of a single blade element is given by,

$$\rho U_\infty (1-a) 2\pi r \delta r 2a U_\infty = 4\pi \rho U_\infty^2 a(1-a)r \delta r. \quad (2-40)$$

The pressure drop in the wake field caused by the rotational velocity induced by the rotor generates an additional axial force on the annulus given by

$$\begin{aligned} F_{wake} &= P_{wake} \cdot Area \\ &= \frac{1}{2} \rho (2a' \Omega r)^2 2\pi r \delta r. \end{aligned} \quad (2-41)$$

Combining the axial force contributions given by equation (2-40) and (2-41) will give the total axial force generated by N blade elements,

$$\frac{1}{2} \rho W^2 N c (C_l \cos \phi + C_d \sin \phi) \delta r = 4\pi \rho [U_\infty^2 a(1-a) + (a' \Omega r)^2] \delta r, \quad (2-42)$$

$$\frac{W^2}{U_\infty^2} N \frac{c}{R} (C_l \cos \phi + C_d \sin \phi) = 8\pi (a(1-a) + (a' \gamma \zeta)^2) \zeta. \quad (2-43)$$

where R is the radius of the wind turbine, γ the tip speed ratio, and ζ the non-dimensional radial position given by $\zeta = r/R$,

The axial rotor torque caused by aerodynamic forces on the rotor blade elements is given by,

$$(\delta L \sin \phi - \delta D \cos \phi) r = \frac{1}{2} \rho W^2 N c (C_l \sin \phi - C_d \cos \phi) r \delta r. \quad (2-44)$$

The rate of change of angular momentum of the air passing through the swept annulus of the blade element is

$$\rho U_\infty (1-a) \Omega r 2a' r 2\pi r \delta r = 4\pi \rho U_\infty (\Omega r) a' (1-a) r^2 \delta r. \quad (2-45)$$

When combining equation (2-44) and (2-45) the result is as follows,

$$\begin{aligned} \frac{1}{2} \rho W^2 N c (C_l \sin \phi - C_d \cos \phi) r \delta r &= 4\pi \rho U_\infty (\Omega r) a' (1-a) r^2 \delta r, \\ \frac{W^2}{U_\infty^2} N \frac{c}{R} (C_l \sin \phi - C_d \cos \phi) &= 8\pi \gamma \zeta^2 a' (1-a). \end{aligned} \quad (2-46)$$

The expressions for the angular and axial forces (equations (2-43) and (2-46)) can now be used to find both the induction factors a and a' . This is an iterative process that makes use of the following expressions,

$$\frac{a}{1-a} = \frac{\sigma_r}{4 \sin^2 \phi} \left[C_x - \frac{\sigma_r}{4 \sin^2 \phi} C_y^2 \right], \quad (2-47)$$

$$\frac{a}{1-a'} = \frac{\sigma_r C_y}{4 \sin \phi \cos \phi}, \quad (2-48)$$

here σ is the total blade area divided by the rotor disc area and is a parameter used to determine the rotor performance. Chord solidity σ_r is defined as the chord length divided by the circumferential length at that radius or,

$$\sigma_r = \frac{N c}{2\pi r} = \frac{N c}{2\pi \zeta R}. \quad (2-49)$$

The variables C_x and C_y are given by the following expressions,

$$C_x = C_l \cos \phi + C_d \sin \phi, \quad (2-50)$$

$$C_y = C_l \sin \phi - C_d \cos \phi. \quad (2-51)$$

again finding the induction factors is an iterative process. Often an initial value is chosen for both a and a' from which the final values will be determined.

Corrections to the Blade Element Momentum Theory In addition to the classic BEMT several corrections are commonly used to improve the accuracy of this theory. These corrections include tip- and hub-loss models that account for vortices that are shed at these respective locations, Glauert correction to account for large induced velocities, and a skewed wake correction model to model air inflow which is non-perpendicular to the rotor plane. The codes available today can often be distinguished by the difference in implementation of these corrections.

These models are applied commonly in BEMT-based design-tools. The corrections mentioned above are described in detail in [12], where a brief description of the BEMT itself is also included.

Common Codes Used As of today BEMT-tools are being used either commercially or in-house for a wide range of engineering fields. A number of commonly used BEMT codes applicable to wind turbine design are listed below,

- **FAST** This is a widely used wind turbine design tool using BEMT and developed by National Renewable Energy Lab (NREL). Aside from modeling the aerodynamics, FAST is also capable of modeling the structure of a wind turbine by a combination of rigid and flexible bodies [13].
- **Propid** This is a computer program for the design and analysis of horizontal axis wind turbines which allows for inverse design. The program varies user specified parameters to achieve a desired peak rotor power [21].
- **Qblade** This is an open source, cross-platform simulation software for wind turbine blade design and aerodynamic simulation. This code was developed at the technical university of Berlin [31].
- **CCBlade** This is a blade element momentum code designed for efficient use in optimization applications. The solution algorithm is provably convergent, and analytic gradients are provided for all outputs. Developed by the National Wind Technology Center [32].

Blade Element Momentum Theory Limitations As mentioned before, the theory is strictly only applicable if the circulation of the blades is uniform, i.e., if the induction factor a is uniform. If a is non-uniform there exists a radial interaction between the elements and an exchange of momentum is present. This is a three-dimensional effect which is neglected by the BEMT.

Additionally an important assumption is that the calculations are purely steady, it is assumed that the flow field around the airfoil is always in equilibrium and the flow passing the airfoil is accelerated instantaneously.

Another effect not accounted for is the large deflection of the blades when subject to large aerodynamic loading. BEMT assumes that the momentum is balanced in the rotor plane, any deflections of the rotor will lead to errors in the aerodynamic model. Heavy blade loading also effects the amount of span-wise pressure variation which will deteriorate the accuracy of the theorem since it assumes that there is no span-wise interaction between the two-dimensional blade elements [12].

Finally, one very important limitation is the fact that BEMT-methods require 2D airfoil characteristics which are not always available for the desired airfoil geometry or Reynolds number.

Keeping these limitations in mind, the BEMT can be a powerful tool in wind turbine performance prediction, and early stage of turbine design.

2-4 Governing Equations

In this section the equations which govern viscous flows will be presented. The fluid considered is Newtonian, incompressible and isothermal. The fluid velocity is given by the velocity vector $\mathbf{V} = (u, v, w)^T$ in which u , v , and w represent the velocity components in the x , y , and z direction respectively. The density, static pressure, and dynamic viscosity are denoted ρ , p , and μ respectively. Additionally a fixed spatial Cartesian coordinate system is assumed in this chapter.

2-4-1 Navier-Stokes Equations

Only the important equations and derivations of the Navier-Stokes (NS) equations are presented in this sections, for a full detailed derivation see e.g. [28, 33]. The governing equations of fluid flows consist of the equations for the conservation of mass and momentum given by the following expressions respectively,

$$\frac{\partial \rho}{\partial t} + \nabla \cdot (\rho \mathbf{V}) = 0, \quad (2-52)$$

$$\frac{\partial(\rho \mathbf{V})}{\partial t} + \nabla \cdot (\rho \mathbf{V} \mathbf{V}) = \nabla \cdot \mathbf{T} + \rho \mathbf{B}, \quad (2-53)$$

in which \mathbf{B} is the body force vector and \mathbf{T} the stress tensor which given by,

$$\mathbf{T} = \left(p + \frac{2}{3}\mu\nabla \cdot \mathbf{V} \right) \mathbf{I} + 2\mu\mathbf{D}, \quad (2-54)$$

where \mathbf{I} is the identity matrix and \mathbf{D} the deformation tensor given by,

$$\mathbf{D} = \frac{1}{2} \left(\nabla \mathbf{V} + \nabla \mathbf{V}^T \right). \quad (2-55)$$

Equations (2-52) and (2-53) combined are known as the Navier-Stokes equations.

Incompressibility For incompressible flows it is assumed that the fluid density is constant hence $\rho = c$. When incompressibility is assumed the mass conservation equation (2-52) can be written as follows,

$$\nabla \cdot \mathbf{V} = 0. \quad (2-56)$$

Analogously the conservation of momentum equation can be written as

$$\rho \left(\frac{\partial \mathbf{V}}{\partial t} + \nabla \cdot (\mathbf{V}\mathbf{V}) \right) = \nabla \cdot \mathbf{T} + \rho \mathbf{B}, \quad (2-57)$$

although air is compressible, in general for aerodynamic problems where the velocities are much lower than the speed of sound c (typically $\mathbf{V} < c/3$) the fluid is assumed incompressible. Within this research the problems considered all deal with incompressible flow, following the incompressibility assumption mentioned above.

Reynolds Decomposition The fluid properties can be split into a mean time independent value and fluctuating part as shown in figure 2-13. For the velocity component in the x direction this yields \bar{u} and u' , or,

$$u_i = \bar{u}_i(x, y, z) + u'_i(x, y, z, t). \quad (2-58)$$

Note that the over-bar ($\bar{\cdot}$) represents the mean value. For the mean and time fluctuating variables in equation (2-58) the follow must hold:

$$\bar{u}' = 0, \quad \bar{u} = \bar{u}, \quad \text{and} \quad \bar{f}\bar{g} = \bar{f}\bar{g} \quad (2-59)$$

This method of decomposing flow quantities is used in the derivation of the Reynolds Averaged Navier Stokes (RANS) equations and is referred to as Reynolds decomposition. More information on this matter can be found in [34].

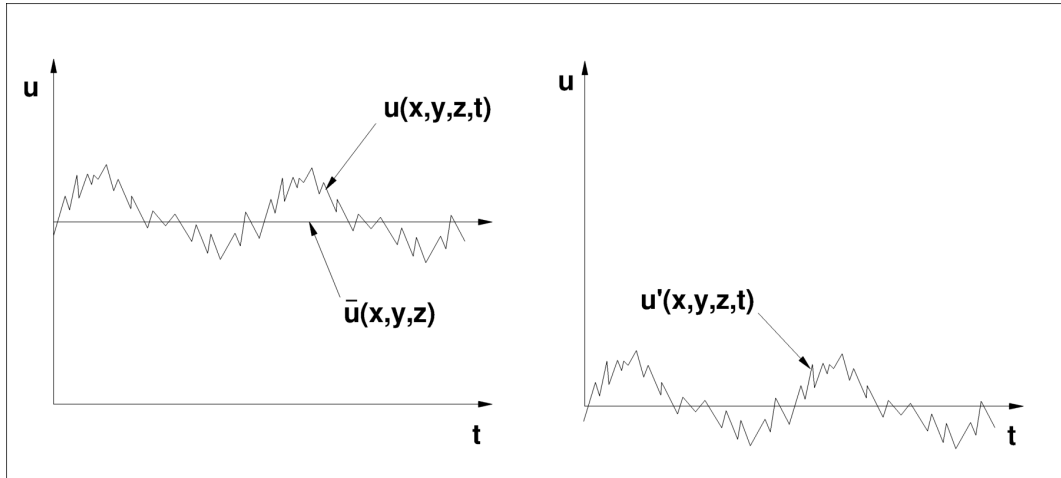


Figure 2-13: Reynold decomposition of a time fluctuating velocity signal.

Turbulence As mentioned before, the flow around an object can be characterized by two different flow regimes i.e. laminar and turbulent flow. The laminar regime is characterized by a steady flow where streamlines are smooth. Perturbations present in laminar flow are damped by viscous forces in the fluid.

Turbulent flows can be characterized by a chaotic flow where the fluid particles move randomly. For turbulent flows the inertia forces present in the fluid dominate, and the viscous forces are no longer able to dampen perturbations in the fluid flow.

As described in section 2-2 the definition of the Reynold number gives the ratio between inertia and viscous forces in a fluid. It is therefore an important parameter in describing laminar, turbulent, and transition in fluid flows.

Two common ways to describe the turbulence in a fluid flow is by the turbulence intensity and the turbulence kinetic energy per unit mass. Both quantities are given below where T_i represents the turbulence intensity and k the mean turbulence kinetic energy per unit mass,

$$T_i = \frac{\sqrt{\frac{2}{3}k}}{\bar{V}} \quad (2-60)$$

$$k = \frac{1}{2} (\bar{u'^2} + \bar{v'^2} + \bar{w'^2}) \quad (2-61)$$

The turbulence kinetic energy is associated with eddies in the turbulent flow and characterized by the RMS of the velocity fluctuations.

2-4-2 Reynolds-Averaged Navier-Stokes (RANS) Equations

Simulating turbulent flow using the full NS equations requires a fine spatial and temporal discretization to capture the small scales in the turbulent flow and as a consequence very fine grids and time steps to properly model small perturbations present in the flow. This high grid resolution and small time-step requires large amounts of CPU power.

In many practical engineering problems one is only interested in the mean flow phenomena, therefore a more feasible modeling approach is used in which Reynolds decomposition is used. When Reynolds decomposition is applied to the NS equations the so-called Reynolds Averaged Navier Stokes (RANS) can be derived. The mass conservation equation given by (2-56) can then be written as follows,

$$\nabla \cdot \bar{\mathbf{V}} = 0, \quad \text{and}, \quad (2-62)$$

$$\nabla \cdot \mathbf{V}' = 0. \quad (2-63)$$

Note that both the mean flow and the time fluctuating velocity field are divergence free [35]. Equation (2-62) is known as the mean continuity equation. The momentum conservation equation given by (2-57) can be rewritten as follows,

$$\rho \frac{\partial \bar{V}_i}{\partial t} + \rho \frac{\partial \bar{V}_i \bar{V}_j}{\partial x_j} = \rho \bar{f}_i + \frac{\partial}{\partial x_j} \left[\bar{p} \delta_{ij} + \mu \left(\frac{\partial \bar{V}_i}{\partial x_j} + \frac{\partial \bar{V}_j}{\partial x_i} \right) - \rho \bar{V}'_i \bar{V}'_j \right]. \quad (2-64)$$

Equations given by (2-64) are known as the Reynolds equations and is the same as the NS-equations given by (2-57) except for an extra set of terms in the Reynolds equation given by $\rho \bar{V}'_i \bar{V}'_j$, which are known as the Reynolds stresses [34, 35]. Note that here the Einstein notation is used where the indices $i, j = 1, 2, 3$ refer to the x , y , or z direction.

The Closure Problem For a statistically three-dimensional flow, there are four independent governing equations describing the mean velocity field, i.e. the three components of the Reynolds equations given by (2-64) and the mean continuity equation given by (2-62). However these four equations combined contain more than four unknowns i.e. the mean velocities components of \bar{V} , the mean pressure \bar{p} , and additionally the Reynolds stresses.

When a set of equations contain more unknowns than there are equations it is said to be unclosed. The Reynolds equations are unclosed i.e. they cannot be solved unless the Reynolds stresses are somehow determined [34]. The closure problem is where turbulence modeling comes to play a role. More on turbulence modeling is presented in section 2-4-4.

2-4-3 Unsteady Reynolds-Averaged Navier-Stokes (URANS) Equations

For some types of flows the mean flow contain slow variations with time that are not turbulent in nature. A good example is vortex shedding of an airfoil in low Reynolds number flows [36], or flows around rotating machinery (wind turbine), imposed motions, free motions, etc.. The decomposition of flow properties e.g. given by equation (2-58) is then replaced by the following expression,

$$u_i = \bar{u}_i(x, y, z, t) + u'_i(x, y, z, t). \quad (2-65)$$

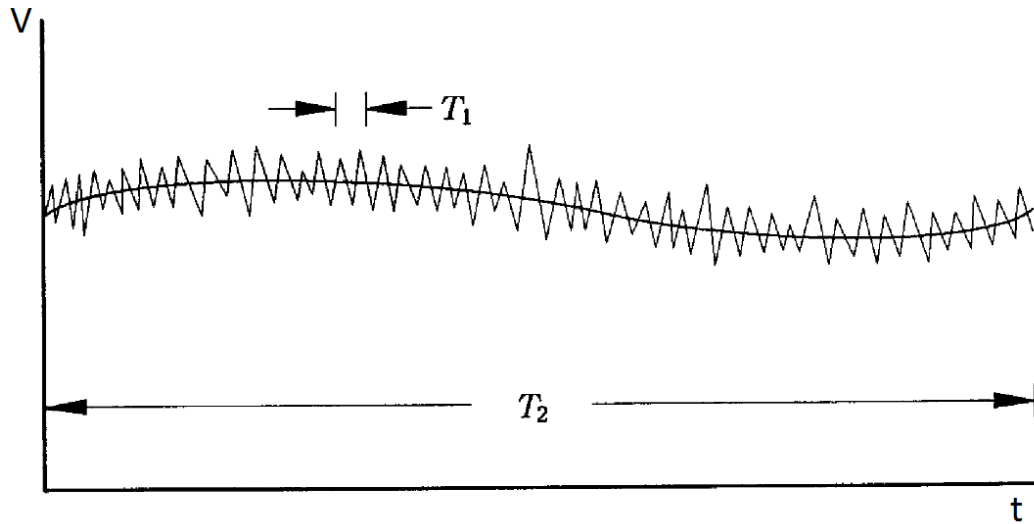


Figure 2-14: Time averaging for non stationary turbulence [36]

Note that in this expression the mean value is now also time dependent as can be seen in figure 2-14. In this case the time scale of the cyclic variation is not related to turbulence and must be significantly larger than the time scale of the turbulence, i.e. $T_1 \ll T_2$ in figure 2-14.

Application of this averaging approach to the RANS equations is sometimes referred to as Unsteady Reynolds Averaged Navier Stokes (URANS) and in general requires increased amounts of CPU time when compared to RANS computations. This is due to the inclusion of the variation of the solution in time.

Equation (2-65) cannot be used when no clear distinction is found between the time scale of the imposed unsteadiness and the turbulence time scale. That is, when $T_1 \ll T_2$ is not satisfied.

2-4-4 Turbulence Modeling

In order to solve the RANS equations turbulence models are introduced to “close” the problem. These models are used to solve the Reynolds equations for the mean velocity field. As of today numerous models have been proposed with a variety of modeling methods and fields of application.

One class of turbulence models is based on the turbulence-viscosity hypothesis first introduced by Boussinesq in 1877. In this approach the Reynolds stresses are related to the mean rate of strain of a fluid element as follows,

$$-\rho \overline{V'_i V'_j} = \mu_t \left(\frac{\partial \bar{V}_i}{\partial x_j} + \frac{\partial \bar{V}_j}{\partial x_i} \right) - \frac{2}{3} \rho k \delta_{ij}, \quad (2-66)$$

In this expression a new scalar known as the *turbulence viscosity*, μ_t is introduced (sometimes referred to as *eddy viscosity*). Expression (2-66) is analogous to the stress-rate-of-strain

relation for a Newtonian fluid (see (2-64)) [34].

The models used in this study are based on this hypothesis and are of one-, and two-equation type. The one-, or two-equation models refer to number of turbulence quantities for which the model transport equations are solved. A total of three models are used in this research, i.e. the Spalart-Allmaras model, and two variations of the $k - \omega$ shear stress model.

Spalart-Allmaras This one-equation model is specially developed for aerodynamic applications, and solves a single model transport equation for the turbulence viscosity μ_t . The model of Spalart-Allmaras (SA) offers a considerable improvement with respect to the algebraic models (i.e. models that do not require the solution of any additional equations, and are calculated directly from the flow variables) while still being a simple alternative to the 2-equation models [34].

The SA defines the turbulence viscosity by means of an auxiliary viscosity $\tilde{\nu}$ and an auxiliary function f_{v1} as follows:

$$\nu_t = \tilde{\nu} f_{v1}, \quad (2-67)$$

Note that the turbulence viscosity in this case is given by the kinematic turbulence viscosity, $\nu_t = \mu_t / \rho$. The auxiliary viscosity $\tilde{\nu}$ obeys the following transport equation,

$$\begin{aligned} \frac{\partial \rho \tilde{\nu}}{\partial t} + \underbrace{\frac{\partial}{\partial x_j} (\rho \tilde{\nu} U_j)}_{\text{Convection}} &= \underbrace{c_{b1}(1 - f_{v1}) \rho \tilde{S} \tilde{\nu}}_{\text{Production}} + \cdots \\ &+ \underbrace{\frac{1}{\sigma} \left\{ \frac{\partial}{\partial x_j} \left[\rho(\nu + \tilde{\nu}) \frac{\partial \tilde{\nu}}{\partial x_j} \right] + c_{b2} \rho \frac{\partial \tilde{\nu}}{x_j} \frac{\partial \tilde{\nu}}{x_j} \right\}}_{\text{Dissipation}} + \cdots \\ &- \underbrace{\left(c_{w1} f_w - \frac{c_{b1}}{\kappa^2} f_{t2} \right) \rho \left(\frac{\tilde{\nu}}{d} \right)^2}_{\text{Destruction}}. \end{aligned} \quad (2-68)$$

The terms in the right hand side represent the production, the dissipation, and the destruction related term respectively. The coefficients and auxiliary functions are based on basis models for shear flows, boundary layer flow models and transition flow models. The coefficients are as follows:

$$\begin{aligned} c_{b1} &= 0.1355, \quad c_{b2} = 0.622, \quad \sigma = \frac{2}{3}, \quad \kappa = 0.41, \\ c_{w1} &= \frac{c_{b1}}{\kappa^2} + \frac{1 + c_{b2}}{\sigma}, \quad c_{w2} = 0.3, \quad c_{w3} = 2, \\ f_{t2} &= c_{t3} \exp(-c_{t3} \chi^2), \quad c_{t3} = 1.2, \quad c_{t4} = 0.5. \\ r &= \min \left(10, \frac{\tilde{\nu}}{\tilde{S} \kappa^2 d^2} \right), \quad g = r + c_{w2}(r^6 - r), \quad f_w = g \left(\frac{1 + c_{w3}^6}{g^6 - c_{w3}^6} \right)^{1/6} \end{aligned}$$

The auxiliary functions which are related to the flow close to walls are given by,

$$\begin{aligned}\tilde{S} &= S + \frac{\tilde{\nu}}{\kappa^2 d^2} f_{v2}, \quad S = \sqrt{2S_{ij}S_{ji}}, \quad \mathcal{X} = \frac{\tilde{\nu}}{\nu}, \\ f_{v1} &= \frac{\mathcal{X}^3}{\mathcal{X}^3 + c_{v1}^3}, \quad f_{v2} = 1 - \frac{\mathcal{X}}{1 + \mathcal{X}f_{v1}}, \quad c_{v1} = 7.1,\end{aligned}$$

A more detailed description of the Spalart-Allmaras model can be found in [37].

k – ω SST (1994) Until today many two-equation models have been proposed, of which many use the turbulence kinetic energy k as one of the variables while often different choices are made for the second variable such as the widely used $k – \varepsilon$ model [38]. This particular model makes use of the turbulence dissipation ω . For the $k – \omega$ model, first introduced by Wilcox [36], the turbulence dissipation rate ω is used, which is given by $\omega = \varepsilon/k$.

The $k – \varepsilon$ model is known to perform well far away from walls, whereas the $k – \omega$ model is more suitable for near boundary modeling. An improved model in which both the $k – \varepsilon$ and $k – \omega$ model are combined was introduced by Menter (1994). This model is the $k – \omega$ Shear Stress Transport (SST) model, which is a blend between the $k – \omega$ model near walls, and $k – \varepsilon$ model far from walls [34].

For the standard $k – \omega$ SST model the turbulent viscosity is given by,

$$\mu_t = \frac{\rho k / \omega}{\max(1, \Omega F_2 / (a_1 \omega))}, \quad \text{where } a_1 = 0.31. \quad (2-69)$$

In this equation Ω represents the magnitude of the vorticity defined by $\Omega = \sqrt{2\omega_{ij}\omega_{ij}}$. The auxiliary function F_2 is defined by means of the wall distance d as follows,

$$F_2 = \tanh \left\{ \left[\max \left(2 \frac{\sqrt{k}}{0.09d\omega}, \frac{500\mu}{\rho d^2 \omega} \right) \right]^2 \right\}. \quad (2-70)$$

The transport equations for both the turbulent kinetic energy k and the dissipation rate ω are then given by the following equations,

$$\frac{\partial \rho k}{\partial t} + \frac{\partial}{\partial x_j} \left[\underbrace{\rho U_j k}_{\text{Convection}} - \underbrace{\mu + \sigma_k \mu_t}_{\text{Dissipation}} \frac{\partial k}{\partial x_j} \right] = \underbrace{\tilde{P}}_{\text{Production}} - \underbrace{\beta^* \rho \omega k}_{\text{Destruction}}, \quad (2-71)$$

and,

$$\frac{\partial \omega k}{\partial t} + \frac{\partial}{\partial x_j} \left[\underbrace{\rho U_j \omega}_{\text{Convection}} - \underbrace{(\mu + \sigma_\omega \mu_t) \frac{\partial \omega}{\partial x_j}}_{\text{Dissipation}} \right] = \underbrace{\gamma \rho \tilde{P}}_{\text{Prod.}} - \underbrace{\beta \rho \omega^2}_{\text{Destr.}} + \underbrace{2(1 - F_1) \frac{\rho \sigma_\omega \kappa}{\omega} \frac{\partial k}{\partial x_j} \frac{\partial \omega}{\partial x_j}}_{\text{Blending}}. \quad (2-72)$$

The auxiliary function F_1 is given by the following expression,

$$F_1 = \tanh \left\{ \left[\min \left[\max \left(2 \frac{\sqrt{k}}{\beta^* d\omega}, \frac{500\mu}{\rho d^2 \omega} \right), \frac{4\rho \sigma_\omega \kappa}{CD_{k\omega} d^2} \right] \right]^4 \right\}, \quad (2-73)$$

where,

$$CD_{k\omega} = \max \left(\frac{2\rho \sigma_\omega \kappa}{\omega} \frac{\partial k}{\partial x_j} \frac{\partial \omega}{\partial x_j}, 10^{-20} \right), \quad (2-74)$$

and β^* and κ are given by,

$$\beta^* = 0.09, \quad \kappa = 0.41.$$

The production \tilde{P} is limited to prevent the build-up of turbulence in stagnation regions:

$$\tilde{P} = \min(\tau_{ij} S_{ij}, 20 \cdot \beta^* \rho k \omega) \quad (2-75)$$

The remaining coefficients, i.e. β , γ , σ_k and σ_ω are defined by a blending between the coefficients of the original $k - \omega$ model and a $k - \varepsilon$ transformed model. Both models are denoted by 1 or 2 respectively. The blending of both constants is defined by,

$$\phi = F_1 \phi_1 + (1 - F_1) \phi_2, \quad \phi = \{\beta, \gamma, \sigma_k, \sigma_\omega\}. \quad (2-76)$$

The values of the coefficients are as follows,

$$\begin{aligned} \sigma_{k1} &= 0.85, \quad \sigma_{\omega 1} = 0.50, \quad \beta_1 = 0.075, \quad \gamma_1 = \frac{\beta_1}{\beta^*} - \frac{\sigma_{\omega 1} \kappa^2}{\sqrt{\beta^*}} = 0.553, \\ \sigma_{k2} &= 1.00, \quad \sigma_{\omega 2} = 0.856, \quad \beta_2 = 0.0828, \quad \gamma_2 = \frac{\beta_2}{\beta^*} - \frac{\sigma_{\omega 2} \kappa^2}{\sqrt{\beta^*}} = 0.440. \end{aligned}$$

In the remainder of the thesis this turbulence model is referred to as the $k - \omega$ SST (Standard) model. A more detailed description of the model can be found in [39].

$k - \omega$ SST (2003) The third turbulence model is similar to the $k - \omega$ SST (Standard) model however small modifications are applied based on several years of experience. The major change in the formulation is that the strain rate, S instead of the vorticity is used in equation 2-69. Hence $\Omega = \sqrt{2\omega_{ij}\omega_{ij}}$ is replaced by $S = \sqrt{2S_{ij}S_{ij}}$, i.e. the invariant measure of the strain rate instead of the vorticity. The resulting expression is as follows,

$$\mu_t = \frac{\rho k / \omega}{\max(1, SF_2 / (a_1 \omega))}. \quad (2-77)$$

Additionally the limiter to prevent the build-up of turbulence in stagnation regions is altered where a factor 10 instead of 20 is used in 2-71,

$$\tilde{P} = \min(\tau_{ij} S_{ij}, 10 \cdot \beta^* \rho k \omega) \quad (2-78)$$

A more detailed description of the $k - \omega$ SST (2003) model can be found in [40].

2-5 Verification and Validation

In order to determine whether the results of the numerical computations are accurate (validation) and reliable (verification), it is necessary to perform both verification and validation studies. Verification and Validation (V&V) are distinct activities; verification is a purely mathematical exercise consisting of both code and solution verification while validation is a science/engineering activity meant to show that the selected model is a good representation of “reality” [41].

2-5-1 Verification

In any numerical calculation there are errors which have to be controlled, and if possible quantified. The three errors generally present in numerical calculations are the *round-off*, *iterative*, and *discretization error*.

The round-off error, sometimes referred to as the truncation error, is due to the finite precision of computers, and by using double or quadruple precision can be considered low [42]. The importance of the round-off error tends to increase with grid refinement, however, in this study all calculations are done in double-precision in order to decrease its influence. Hence it is assumed that the round-off error is negligibly small and therefore not considered.

The iterative error stems from the non-linearity of the mathematical equations solved by the CFD solver. In principle the iterative error should be reduced to the same order as the round-off error. However, for complex CFD calculations this can be very time consuming or even impossible due to low-quality grids, complex flows or non-robust codes [41, 42].

The discretization error stems from the approximations made within the applied numerical scheme, which discretize the partial differential RANS equations to a set of algebraic equations. It is generally the largest source of numerical uncertainty. However refinement of

the grid or time-step will in theory reduce the discretization error. Performing a refinement and/or time-step study will provide insight in the discretization error of a specific problem [43]. The remainder of this section is used to describe the iterative and discretization error for both steady and unsteady computations.

Iterative Error for Steady Flows A qualitative measure of the iterative error can be obtained from the convergence history of a specific simulation. In this study the L_2 - and L_∞ -norm of the non-dimensional residuals of the flow quantities are used to analyze the iterative error. The L_2 -norm is defined as the RMS over the whole domain of the absolute change of the residuals of a given variable between successive iterations, or,

$$L_2(res_\phi) = \sqrt{\frac{\sum_{i=1}^{n_p} (|res_{\phi_i}|^2)}{n_p}}, \quad (2-79)$$

where res_ϕ is the non-dimensional change of the residual of a given variable, and n_p the total number of grid cells. The L_∞ -norm of the residuals is defined as the maximum absolute change in the whole domain of the residuals of a given variable between iterations ($L_\infty(res_\phi)$).

The flow quantities analyzed are the velocity components in the x , y , and z direction, the pressure p , and the turbulence quantities such as the turbulent kinetic energy k . These quantities are non-dimensionalized using undisturbed flow properties.

For the iterative error to be negligible the residuals must be two to three orders below the discretization error, but preferably as low as possible [41, 42].

Other than the convergence of the residuals it is of importance that the integral quantities such as the monitored lift drag and moment coefficients are converged sufficiently. For the two-dimensional analysis, the fluctuation of C_l , C_d , and C_m are monitored for the last 200 iterations. These are then quantified as a percentage of the final iterative value,

$$U_\phi = 100 \times \max \left(\frac{|\phi_i - \phi_{end}|}{|\phi_{end}|} \right), \quad (2-80)$$

where ϕ_i is a specific local integral quantity at iteration i , e.g. C_l , C_d , and C_m respectively. The resulting percentage must be at least two to three orders below the discretization uncertainty which will be discussed next. A similar approach applied to the thrust and power coefficient, C_T and C_P , is applied to the turbine cases.

Discretization Error for Steady Flows For steady computations the remaining error, i.e. the discretization error is due to the finite number of grid cells. The numerical uncertainty related to this error can be obtained by a so-called verification procedure.

The aim of solution verification is to estimate the numerical uncertainty U_ϕ of a solution, ϕ_i , for which the exact solution, ϕ_{exact} , is unknown. As of today several methods are available to determine the numerical uncertainty in CFD [42]. For this study the method described in [41] will be used.

The goal of the uncertainty study is to define an interval that contains the exact solution with a 95% confidence, or,

$$\phi_i - U_\phi \leq \phi_{exact} \leq \phi_i + U_\phi. \quad (2-81)$$

Within this approach the numerical uncertainty for an arbitrary integral flow quantity ϕ is described by,

$$U_\phi = F_s |\varepsilon|, \quad (2-82)$$

where F_s represents a safety factor and ε the estimated discretization error. The uncertainty estimation procedure is based on Richardson extrapolation (RE), and the discretization error ε is determined by,

$$\varepsilon \simeq \delta_{RE} = \phi_i - \phi_0 = \alpha h_i^p, \quad (2-83)$$

where ϕ_0 is the estimate for the exact solution, ϕ_i represents any integral of local quantity, α is a constant, h is the typical cell size, and p is the observed order of accuracy.

The definition of h is a geometrical problem (grid generation problem). A single parameter is used to define the typical cell size of the grids. This requires that the grids must be geometrically similar, i.e. the grid refinement ratio must be constant in the complete domain and the grid properties (deviations from orthogonality or skewness) independent of the grid refinement. Unfortunately any small deviation from this constraint may have severe consequences for the error estimation (and for the estimation of p) [44].

To determine ε , this approach requires the determination of ϕ_0 , α , and p , which is done in the least square sense using the solution from at least four grids. Since the determination of p is extremely sensitive to perturbations alternative error estimators are being applied, i.e.,

$$\delta_{RE}^{02} = \phi_i - \phi_0 = \alpha_{01} h^2, \quad (2-84)$$

$$\delta_{RE}^{12} = \phi_i - \phi_0 = \alpha_{11} h + \alpha_{12} h^2, \quad (2-85)$$

and,

$$\delta_{\Delta_M} = \frac{\Delta_M}{\left(\frac{h_{ng}}{h_1}\right) - 1}, \quad (2-86)$$

where the ratio h_{ng}/h_1 is known as the *relative step-size*, and Δ_M is the data range given by,

$$\Delta_M = \max(|\phi_i - \phi_j|) \quad 1 \leq i, j \leq n_g, \quad (2-87)$$

where n_g represents the total number of grids. The relative step size is given by equations (2-88) and (2-89) for two- and three-dimensional grids respectively.

$$\frac{h_1}{h_i} = \sqrt{\frac{n_i}{n_1}} \quad (2-88)$$

$$\frac{h_1}{h_i} = \sqrt[3]{\frac{n_i}{n_1}} \quad (2-89)$$

Note that for an increase in grid resolution the relative step size will decrease to unity for the finest grid. As for equation (2-83), the error estimators, δ_{RE}^{02} and δ_{RE}^{12} are determined in the least squares sense.

By using equation (2-82), and the error estimator ε the numerical uncertainty can be obtained. Depending on the value of p the uncertainty can be determined using the following conditions,

- $0.95 \leq p \leq 2.05$: $U_\phi = 1.25\delta_{RE} + U_s$,
- $p \leq 0.95$: $U_\phi = \min(1.25\delta_{RE} + U_s, 3\delta_{RE}^{12} + U_s^{12})$,
- $p \geq 2.05$: $U_\phi = \max(1.25\delta_{RE} + U_s, 3\delta_{RE}^{02} + U_s^{02})$,
- For oscillatory convergence: $U_\phi = 3\delta_{\Delta_M}$,
- For anomalous behavior: $U_\phi = \min(3\delta_{\Delta_M}, 3\delta_{RE}^{12} + U_s^{12})$,

in which U_s , U_s^{02} and U_s^{12} are the standard deviations of the least squares fits and 1.25 and 3 represent the safety factors. These safety factors are according to the procedure proposed by Eça & Hoekstra, who tested several flow problems and manufactured solutions regarding this matter [44].

Iterative Error for Unsteady Flows In statistically unsteady flows, an extra contribution for the iterative error, which is related to the influence of the initial conditions is present. In periodic flows, the solution will only become periodic once the influence of the initial conditions has become negligible. For quantification of the iterative error for unsteady flows it is therefore important to monitor both the iterative error per time step and the error due to the influence of the initial conditions [45]. The iterative error per time step is obtained in similar way as the iterative error for steady flow problems previously discussed. The iterative error caused by the influence of the initial condition will be obtained by computing the averaged value of integral quantities such as the lift and drag coefficients. For this study the iterative error introduced by the influence of the initial conditions is considered negligible when the change per period of the averaged integral quantities is two to three orders lower than the discretization error.

Discretization Error for Unsteady Flows In statistically periodic flows, time-averaging must be replaced by ensemble-averaging. In that case, time-derivatives of the mean flow quantities are included in the RANS equations. Therefore the numerical solution of the RANS equations requires both time and spatial discretization techniques. In such case the convergence properties of the discretization error becomes more challenging [45]. The power series expansion given by (2-90) will now include a term to account for the time discretization present for unsteady RANS computations.

$$\varepsilon \simeq \delta_{RE} = \phi_i - \phi_0 = \alpha_x h_i^{P_x} + \alpha_t \tau_i^{p_t} \quad (2-90)$$

In this expression τ_i is the time step, p_t the observed order of accuracy with respect to the time discretization, and α_t is a constant.

Typical Cell Size Definition Implementing the uncertainty analysis described previously requires a set of geometrically similar grids, a requirement that is hard to satisfy when using unstructured grids. As an alternative several methods to describe the typical grid cell size are proposed [46].

As used before the typical cell size h_i is defined by the inverse of the number of cells in a grid,

$$h_i = \left(\frac{1}{N_{cells}} \right)^{\frac{1}{n}}, \quad (2-91)$$

where n is the space dimension of the grid (1, 2, or 3). Alternatively h_i can be defined by the average size of the cells (Λ_1), the root mean square of the cells (Λ_2), or the mode of the cell size, i.e. the cell size that occurs more often in the cell size distribution (Λ_m). Λ_1 and Λ_2 are expressed as follows,

$$\Lambda_1 = h_i = \left(\frac{\sum_{i=1}^{N_{cells}} \Lambda_i}{N_{cells}} \right)^{\frac{1}{n}}, \quad (2-92)$$

$$\Lambda_2 = h_i = \left(\sqrt{\frac{\sum_{i=1}^{N_{cells}} \Lambda_i^2}{N_{cells}}} \right)^{\frac{1}{n}}. \quad (2-93)$$

The method using the mode of the cell size requires a number of intervals, which are than used to generate a cell volume histogram. The choice must be large enough to obtain a good estimate of the mode.

The different methods to express h_i can be graphed as a function of the grid index (n_i). For geometrically similar grids these graphs should be identical. Additionally a Probability Density Function (PDF), used to compute the mode of the cell volumes, can be graphed. For geometrically similar grids the PDFs for different grids in a grid-set must coincide, which does not have to be the case for non-geometrically similar grids [46].

The implementation of different typical cell size definitions can be a valuable tool in evaluating the numerical uncertainty for unstructured grids.

2-5-2 Validation

The aim of the verification exercise is to estimate the error/uncertainty of the numerical calculations for which the exact solution is not known. Validation on the other hand aims at identifying the modeling error of a given mathematical model in relation to a given set of experimental data (physical model). The validation procedure used in [42] is discussed next.

This procedure compares the validation uncertainty U_{val} and the comparison error E given by equations (2-94) and (2-95) respectively.

$$U_{val} = \sqrt{U_\phi^2 + U_{inp}^2 + U_{exp}^2} \quad (2-94)$$

$$E = \phi_i - \phi_{exp} \quad (2-95)$$

In these equations U_{inp} is the input uncertainty, i.e. uncertainties in the fluid properties, flow geometry and boundary conditions. U_{exp} is the experimental uncertainty and ϕ_{exp} the experimental value.

The outcome of the validation exercise is determined from a comparison of $|E|$ and U_{val} as follows:

- $|E| > U_{val}$, the comparison error is likely to be dominated by the modelling error, hence the model must be improved.
- $|E| < U_{val}$, the modeling error is within the “noise level” imposed by the three uncertainties.

The last case can mean two things, if E is considered sufficiently small, the model and its solution are validated with U_{val} precision against the given experiment. When this is not the case the quality of the numerical solution and/or the experiment should be improved in order to draw conclusions on the validity of the mathematical model.

Experimental Uncertainty For a proper validation assessment, the experimental uncertainty U_{exp} is needed. However this is uncertainty is rarely assessed, and the available experimental data for model-scale wind turbines is very limited. In this study all experimental data is subject to an uncertainty of 2.5% in thrust and torque, which is based on in-house studies taking into account reproducibility for different test runs, manufacturing tolerances and uncertainties of the measurement hardware.

Numerical Uncertainty The numerical uncertainty follows from the previously discussed round-off, iterative, and discretization error. Applying the presented approach, in which round-off and iterative errors are assumed negligible, the discretization error is the main contribution of the numerical uncertainty. Note this only holds when the iterative errors are two to three orders below the discretization error [41, 42]

Input Uncertainty The input uncertainty is caused by assumptions and simplifications made in the numerical model. The important simplifications for the model are:

- Uniform inflow,
- No blockage effects,
- The flow is quasi-steady, which in a RANS perspective means that the flow is considered unsteady on a turbulence time scale only.

These simplifications hold for both two- and three-dimensional steady computations. Additionally there is an uncertainty contribution caused by concessions in model geometry: e.g. only the turbine rotor, using a simplified hub geometry is considered.

Additionally the numerical computations are performed without taking into account the effects of surface imperfections and roughness of the turbine geometry used during the experiments. It is expected that these effects could have a significant effect on the separated region due to the laminar operating conditions.

Chapter 3

Numerical Background

In this chapter the numerical background of the two- and three-dimensional studies are presented. First the required tools used to perform the numerical computations are discussed in section 3-1. A detailed description of the discretization methods used in the CFD code *ReFRESCO* is given in section 3-2, and finally the solution procedure is presented in section 3-3.

3-1 Numerical Tools

During the course of this study a number of software tools are used such as *HEXPRESS* for grid generation, and *ReFRESCO* for (U)RANS computations. In this section the basic concepts of these tools are presented.

3-1-1 HEXPRESS

The grids for this study are generated using *HEXPRESS* [47]. This is an automatic unstructured hexahedral mesh generator software. It generates unstructured grids which only contain hexahedral elements and implements hanging nodes for refinements. The advantage of this tool is the ease of use for the user. Compared to grid generator tools for structured grids the amount of working time spent is significantly lower [48]. This is preferred for this study since numerous grids have to be generated.

As a disadvantage, the grid quality is generally lower, especially when high aspect ratio cells are required. This implies that a relatively large number of cells is required to obtain an adequate grid quality [18]. Additionally, grids generated using *HEXPRESS* contain hanging nodes which are commonly located at edges where refinements are implemented as can be seen in figure 3-1. These hanging-nodes decrease the quality of the grid (and of the numerical calculations) due to additional geometric eccentricity (see section 3-2-8).

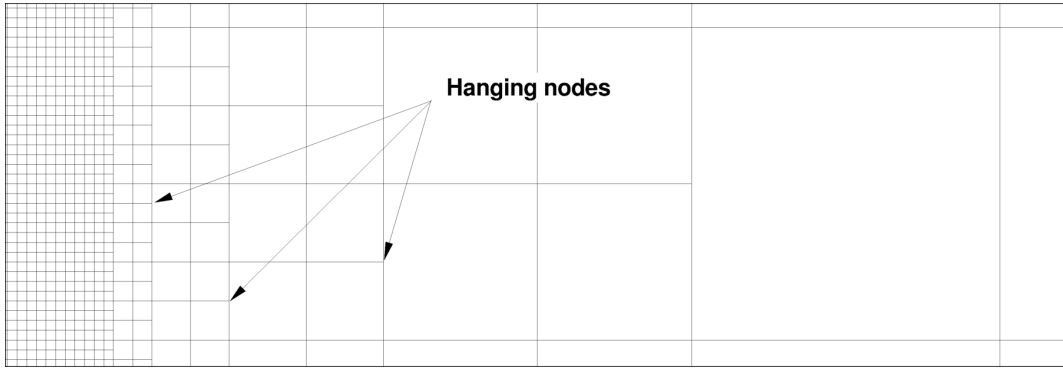


Figure 3-1: Hanging nodes at boundary of grid refinement region

Grid quality To judge whether the quality of the grid is sufficient, a number of grid characteristics can be calculated. Two important parameters are the *orthogonality* and the *equi-angular skewness*. These parameters are calculated within *HEXEXPRESS* according to the following expressions,

$$\text{Equiangular skewness} = \max \left(\frac{(T_{\max} - T_e)}{180 - T_e}, \frac{(T_e - T_{\min})}{T_e} \right), \quad (3-1)$$

$$\text{Orthogonality} = 90 - \text{acos}(\min(\Gamma_{ijk})), \quad (3-2)$$

where T_{\min} and T_{\max} are the minimum and maximum angle of a face or cell respectively. T_e is the angle of an equiangular face cell, i.e. 60 degrees for a triangular face, and 90 for a quadrilateral face or hexahedral cell. Γ_{ijk} is given by equation (3-3) which is the mixed product of the unit vectors which link the centroids of two opposite faces of a hexahedral cell, as presented in figure 3-2.

$$\Gamma_{ijk} = h_i \cdot (h_j \times h_k), \quad \text{for } i \neq j \neq k. \quad (3-3)$$

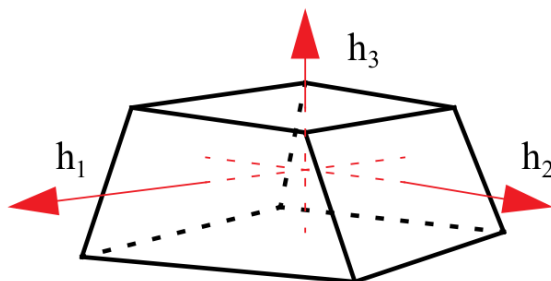


Figure 3-2: Unit vectors used for determination of orthogonality [48].

The grids used within the three-dimensional study have a minimum orthogonality of 10 degrees and maximum equiangular skewness of 0.9, whereas for the two-dimensional case a minimum orthogonality and equiangular skewness of 35 degrees and 0.7 was achieved.

3-1-2 ReFRESCO

ReFRESCO is a viscous-flow CFD code that solves multiphase (unsteady) incompressible flows with the RANS equations, complemented with turbulence models, cavitation models and volume-fraction transport equations for different phases [49]. The equations are discretized using a finite-volume approach with cell-centered collocated variables. The equations are discretized in strong-conservation form and a pressure-correction equation based on the SIMPLE algorithm is used to ensure mass conservation [50]. Time integration is performed implicitly with first or second-order backward schemes. At each implicit time step, the non-linear system for velocity and pressure is linearized with Picard's method and rather a segregated or coupled approach is used. In the latter, the coupled linear system is solved with a matrix-free Krylov subspace method using a SIMPLE-type preconditioner [50]. A segregated approach is always adopted for the solution of all other transport equations. The implementation is face-based, which permits grids with elements consisting of an arbitrary number of faces (hexahedrals, tetrahedrals, prisms, pyramids, etc.), and if needed h-refinement (hanging nodes). State-of-the-art CFD features such as moving, sliding and deforming grids, as well automatic grid refinement are also available in the code. For turbulence modeling, RANS/URANS, SAS, DES approaches can be used (PANS and LES are being currently studied). The code is parallelized using MPI and subdomain decomposition, and runs on Linux workstations and HPC clusters. ReFRESCO is currently being developed, verified and validated at MARIN (in the Netherlands) [42, 51–56] in collaboration with IST (in Portugal) [57], USP-TPN (University of São Paulo, Brasil) [58], TU Delft (Technical University of Delft, the Netherlands) [50], RuG (University of Groningen, the Netherlands) [59] and recently at UoS (University of Southampton, UK) [60].

The implemented methods for the discretizing and solving the governing equations are presented in next.

3-2 Discrete Governing Equations

The general conservation equation for an arbitrary quantity ϕ in integral form is given by equation (3-4). All equation (except mass conservation), being the momentum equations and turbulence equations are solved using this general equation. Replacing the arbitrary quantity ϕ with the velocity vector V results in three momentum equations for u , v , and w (for the three-dimensional case). To solve the turbulence models discussed in section 2-4-4, ϕ is replaced by either $\tilde{\nu}$ (Spalart-Allmaras one-equation model) or k and ω ($k - \omega$ SST two-equation models) solving equation (3-4) either one or two times depending on the number of variables.

$$\underbrace{\frac{\partial}{\partial t} \int_V \rho \phi dV}_{\text{Time dependent term}} + \underbrace{\int_S \rho \phi \mathbf{V} \cdot \mathbf{n} dS}_{\text{Convective term}} = \underbrace{\int_S \Gamma \nabla \phi \cdot \mathbf{n} dS}_{\text{Dissipation terms}} + \underbrace{\int_V q_\phi dV}_{\text{Source term}} . \quad (3-4)$$

In this equation ρ is the density, \mathbf{n} the normal outward unit vector, Γ the diffusive coefficient (viscosity μ in case of the momentum equation), and q_ϕ represents a source or sink term.

Each of the terms in equation (3-4) can be discretized using different methods. The following sections are used to present the discretization methods used for all these terms.

3-2-1 Discretization of integrals

Because *ReFRESCO* allows for general polyhedral grids, the discretization is designed for cells with an arbitrary number of cell faces. The integral form of the momentum equations given by equation (3-4) contains volume and surface integrals. For the approximation of the volume integrals, the variable values at the cell centers are considered as a proper average of the cell volume. The volume integral is therefore approximated using a second-order mid-point rule,

$$\int_V \phi \, dV \approx \phi_c \Delta V, \quad (3-5)$$

where ϕ_c is the integrand value at the cell center and ΔV is the cell volume. Accordingly the surface integrals are approximated using the following expression,

$$\int_S \phi \, dS \approx \sum_{i=1}^{N_f} \phi_{f_i} S_{f_i}, \quad (3-6)$$

where ϕ_{f_i} is the integrand value at the surface obtained by interpolation of the neighboring cell center values. S_{f_i} is the surface area of the respective cell face and N_f is the number of cell faces of the cell considered. The method used to obtain the cell volume and face surface areas are presented next.

3-2-2 Defining the Cell Geometry

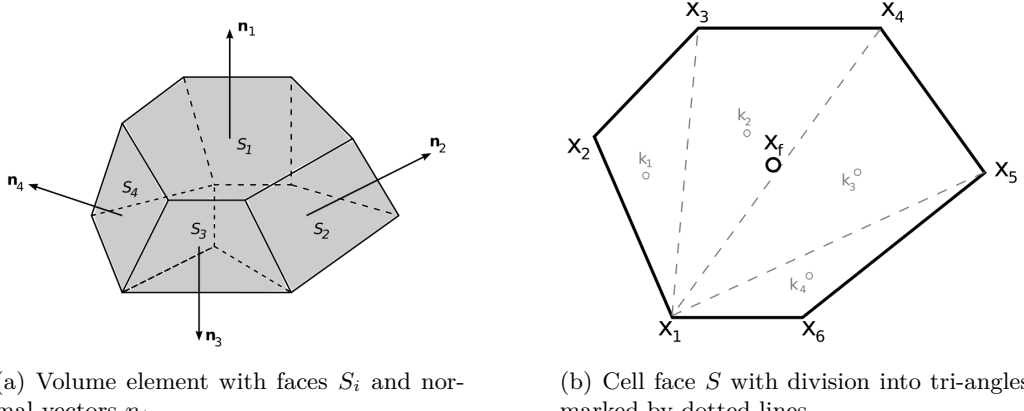
As explained, for each cell the volume, the location of the center, and the face surfaces are needed. In this section the method to obtain these quantities is explained. Consider an arbitrary three-dimensional polyhedral volume element with N_f cell faces (see figure 3-3(a)).

Each cell face S_f is generated by v line segments N_v that connect the vertices. The face center \mathbf{x}_f is defined by dividing the face surface in $p = N_v - 2$ triangles (see figure 3-3(b)). Each triangle denoted by k_p , consists of three vertices i.e. $\mathbf{x}_1, \mathbf{x}_i$ and \mathbf{x}_{i-1} (with $i = 3, \dots, N_v$ and $N_v \geq 3$). The area and the area centroid are calculated using equations (3-7) and (3-8).

$$A_k = \frac{1}{2} |(\mathbf{x}_i - \mathbf{x}_1) \times (\mathbf{x}_{i-1} - \mathbf{x}_1)| \quad (3-7)$$

$$\mathbf{x}_k = \frac{1}{3} (\mathbf{x}_1 + \mathbf{x}_i + \mathbf{x}_{i-1}) \quad (3-8)$$

The face center can now be obtained as the average of the centers of each triangle weighted by the area of the triangle:



(a) Volume element with faces \$S_i\$ and normal vectors \$n_i\$

(b) Cell face \$S\$ with division into tri-angles marked by dotted lines

Figure 3-3: Geometric representation of volume element (left) and its face (right) [61].

$$\mathbf{x}_f = \frac{\sum_{k=1}^{N_k} A_k \mathbf{x}_k}{\sum_{k=1}^{N_k} A_k} = \frac{1}{3} \frac{\sum_{i=3}^{N_v} |(\mathbf{x}_i - \mathbf{x}_1) \times (\mathbf{x}_{i-1} - \mathbf{x}_1)| (\mathbf{x}_1 + \mathbf{x}_i + \mathbf{x}_{i-1})}{\sum_{i=3}^{N_v} |(\mathbf{x}_i - \mathbf{x}_1) \times (\mathbf{x}_{i-1} - \mathbf{x}_1)|}. \quad (3-9)$$

Additionally the surface vector of the cell faces is given by the sum of the triangle areas \$A_k\$ or,

$$S_f = \frac{1}{2} \sum_{i=3}^{N_v} |(\mathbf{x}_i - \mathbf{x}_1) \times (\mathbf{x}_{i-1} - \mathbf{x}_1)|. \quad (3-10)$$

The Magnitude and the location of the surface vector can be used to define the face unit normal vector as given in equation (3-11). The volume of a cell can than be calculated using the divergence theorem given by (3-12), which results in equation (3-13).

$$\mathbf{n}_f = \frac{S_f}{|S_f|}, \quad S_f = \mathbf{n}_f |S_f| \quad (3-11)$$

$$\Delta V = \int_V dV = \frac{1}{3} \int_V \nabla \cdot \mathbf{x} dV = \frac{1}{3} \int_S \mathbf{x} \cdot \mathbf{n} dS \quad (3-12)$$

$$\Delta V \approx \frac{1}{3} \sum_{i=1}^{N_f} \mathbf{x}_{f_i} \cdot S_{f_i}, \quad (3-13)$$

Finally the location of the cell center is determined as the average of the face centers weighted by the area of each face or:

$$\mathbf{x}_c \approx \frac{\sum_{i=1}^{N_f} \mathbf{x}_{f_i} S_{f_i}}{\sum_{i=1}^{N_f} S_{f_i}}. \quad (3-14)$$

Now the expressions for the cell characteristics such as volume and cell-center, and the expressions for surface and volume integrals from section 3-2-1 are known. The next step is to discretize the terms in the integral equation (3-4) which will be presented in the following sections.

3-2-3 Time Discretization

ReFRESCO allows for a number of discretization methods to discretize the time derivative in the time dependent term. The time derivative term for a control volume \mathcal{V} is given by,

$$\frac{\partial}{\partial t} \int_S \rho \phi dV, \quad (3-15)$$

where the control volume \mathcal{V} is assumed constant in time. The discretization method applied is known as the *implicit backward approximation scheme* given by:

$$\frac{\partial}{\partial t} \int_S \rho \phi dV \approx \frac{[c_1(\rho_c \phi_c \Delta \mathcal{V})^n + c_2(\rho_c \phi_c \Delta \mathcal{V})^{n-1} c_3(\rho_c \phi_c \Delta \mathcal{V})^{n-2}]}{\Delta t}, \quad (3-16)$$

where n represents the time level and Δt the time step. Note that the subscript c represents the value at the cell center. The choice of the coefficients c_1 , c_2 , and c_3 determine the discretization method to be used, where choosing,

$$c_1 = 1.0; \quad c_2 = -1.0; \quad c_3 = 0.0, \quad (3-17)$$

will result in the *first-order backward Euler scheme*, and,

$$c_1 = 1.5; \quad c_2 = -2.0; \quad c_3 = 0.5, \quad (3-18)$$

will result in the *second-order backward scheme*. Note that for the first and second order schemes the choice of coefficients result in two or three time steps in the discretization respectively. In this study all unsteady calculations are done using the second order backward scheme.

3-2-4 Gradients

For the spatial discretization of equation (3-4) we will need to refer not only to the variable quantities at the cell centers, but also to the gradients of these quantities. The gradients of an arbitrary quantity ϕ can be determined from the cell surfaces by using the divergence theorem given by:

$$\int_V \nabla \phi \cdot dV = \int_S \phi \cdot \mathbf{n} \, dS, \quad (3-19)$$

this results in equation (3-20), where ϕ_{f_i} is an arbitrary quantity at a cell face.

$$(\nabla \phi)_c \approx \frac{1}{\Delta V} \sum_{i=1}^{N_f} \phi_{f_i} S_{f_i}. \quad (3-20)$$

3-2-5 Convective Terms

The convective term from equation (3-4) is given below, which describes the convection of flow property ϕ . For high Reynolds number flows the convective term is much more dominant than the diffusive term, therefore it is of importance that discretization of this term is done while keeping the discretization error as small as possible.

To discretize the convective term the flow property ϕ and the velocity \mathbf{V} are needed at the cell faces as well as the areas of the cell faces S_{f_i} . Before continuing it must be noted that although the grids used in this study contain hanging-nodes, for simplicity the discretizations presented in the present work are all for structured grids. The discretization of the convective term in equation (3-4) can be written as follows,

$$\int_S \rho \phi \mathbf{V} \cdot \mathbf{n} dS \approx \sum_{i=1}^{N_f} \rho \phi_{f_i} (\mathbf{V}_{f_i} \cdot \mathbf{n}) S_{f_i}, \quad (3-21)$$

where f_i denotes the specific value at the cell faces i . Note that \mathbf{n} included in S_{f_i} according to equation (3-11). Since the flow variables are defined at the cell centers an interpolation must be performed to obtain the flow variables at the cell faces; in this context this is called a “convection scheme”.

Various convection schemes are available, each with a different level of accuracy, stability conditions and computational efficiency. The four interpolation methods commonly used in CFD codes will be discussed here, i.e. the central difference scheme, the upwind difference scheme, the blending scheme, and the Quadratic Upstream Interpolation for Convective Kinetics (QUICK) scheme.

Convection Schemes In the following paragraphs the four interpolation schemes will be demonstrated using a two-dimensional structured grid given in figure 3-4, where C_{uu} represents the second upstream cell centroid, C_u the first upstream cell centroid, and C_d the downstream cell centroid. The distance from the cell-centers to the face f is given by S .

The Central Difference Scheme (CDS) makes use of the flow variable upwind and downwind from the respective cell-face. To do so first an interpolation coefficient λ is defined as follows,

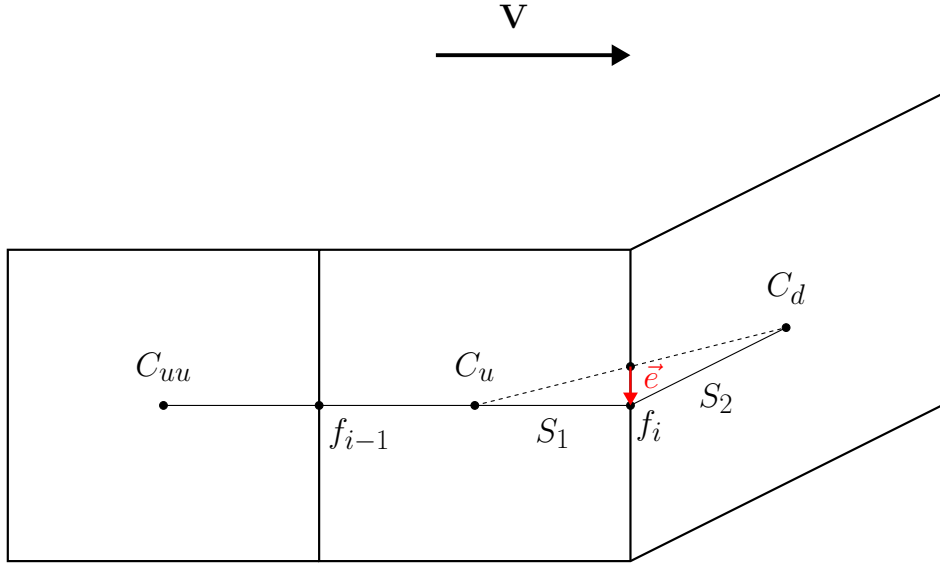


Figure 3-4: Non-uniform structured grid with flux from left to right where C_{uu} represents the second upstream cell centroid, C_u the first upstream cell centroid, and C_d the downstream cell centroid.

$$\lambda = \frac{S_2}{S_1 + S_2}. \quad (3-22)$$

The variable value ϕ_{f_i} at the face centroid, using CDS is then given by,

$$\phi_{f_i} = \lambda\phi_u + (1 - \lambda)\phi_d. \quad (3-23)$$

CDS is based on Taylor series expansion and is second order accurate [62]. The Upwind Difference Scheme (UDS) given next is less involved than the CDS and is of first order accuracy. The face value of the variable is given by the value upwind from the face as follows,

$$\phi_{f_i} = \phi_u. \quad (3-24)$$

In order for this method to work, first the flow direction needs to be found to determine which of the neighboring cells is the upwind cell.

The blending scheme, as the name suggests, is a blending of two schemes i.e. CDS and UDS. A linear combination is constructed of both methods in order to express the flow properties at the cell face. The blending scheme is described as follows,

$$\phi_{f_i} = \beta\phi_{f_i}^{CDS} + (1 - \beta)\phi_{f_i}^{UDS}, \quad (3-25)$$

in which β is the *blending coefficient* which can be chosen between 0 and 1. β , in this case, is nothing more than a coefficient which describes the blending between both methods. For $\beta = 0$ the CDS term will vanish resulting in a fully upwind discretization. Accordingly if β is chosen 1, the discretization is of the CDS type. The blending scheme is of first order accuracy unless β is chosen one (in which case the central differencing scheme results).

The last convection scheme to be discussed is the QUICK scheme, which is a parabolic interpolation method. This convection scheme is given by,

$$\phi_{f_i} = \phi_u \lambda \left[S_f^2 (\phi_d - \phi_u) + S_f (1 - S_f) \nabla \phi_u \cdot d_{du} \right]. \quad (3-26)$$

The four methods discussed are discussed extensively in [63].

3-2-6 Diffusive Terms

The diffusive term presented in equation (3-4) will be discretized next. This term is a surface integral describing the gradient at the surface i.e. face of the cells. The gradient is discretized analogous to the method used in section 3-2-4, where a linear interpolation using the two neighboring cell center values is applied. This results in the following discretization,

$$\int_S \Gamma \nabla \phi \cdot \mathbf{n} dS \approx \sum_{i=1}^{N_f} \Gamma_{f_i} (\nabla \phi \cdot \mathbf{n})_{f_i} \mathbf{S}_{f_i} \approx \sum_{i=1}^{N_f} \Gamma_{f_i} (\nabla \phi_{f_i} \cdot \mathbf{S}_{f_i}). \quad (3-27)$$

As can be seen from equation (3-27) the gradients at the face-centers are needed. ReFRESCO can calculate the gradients either by interpolation of the gradients at the neighboring cell-centers (equation (3-28)), or by dividing the difference of the variable values at the neighboring cell-centers by their distance $|d_f|$ (equation (3-29)).

$$(\nabla \phi)_{f_i} = \alpha_f (\nabla \phi)_{C_u} + (1 - \alpha_f) (\nabla \phi)_{C_d}, \quad (3-28)$$

$$(\nabla \phi)_{f_i} = \frac{\phi_{C_d} - \phi_{C_u}}{|d_f|}. \quad (3-29)$$

Note that equation (3-28) must be solved iteratively due to the face based data structure of ReFRESCO. In non-orthogonal grids, the above approaches may compute the gradients in a direction which deviates from the unit normal vector of the cell-face. This difference introduces a constant error which will not vanish with grid refinements. Extra measures have to be taken to reduce this error. ReFRESCO has two types of correction methods which are not discussed here. More information on the correction methods can be found in [63]

3-2-7 Source Terms

The final term in (3-4) describes the effect of a source q_ϕ in integral form. The source is working on the volume of the cell considered. The integral can therefore be expressed as the source at the cell center multiplied by the volume of the specific cell as follows,

$$\int_V q_\phi dV \approx q_{\phi_c} \Delta V. \quad (3-30)$$

3-2-8 Eccentricity

The discretization of the governing equations, implemented in ReFRESCO uses the second-order mid-point rule, which for the surface integrals requires the integrand values at the cell faces ϕ_f . In addition, variable values at the cell faces are needed to compute gradients at the cell centroid (see section 3-2-4). In general ϕ_f is computed using linear interpolation between two neighboring cell centers. However, for non-orthogonal grids the position of the computed face variable deviates from the location of the face centroid (see figure 3-4). This deviation is the so-called eccentricity, which, if not corrected, affects the numerical solution by introducing a constant numerical error.

The error introduced by the eccentricity can be corrected for by moving the point of the interpolated value \mathbf{x}_e to the location of the face centroid \mathbf{x}_f . This results in an extra term to the linear interpolation of ϕ_f ,

$$\phi_f = \phi_e + (\nabla \phi_e \cdot \mathbf{e}_f), \quad (3-31)$$

where \mathbf{e}_f is the eccentricity vector defined by,

$$\mathbf{e}_f = \mathbf{x}_f - [\alpha_f \mathbf{x}_u + (1 - \alpha_f) \mathbf{x}_d] = \mathbf{x}_f - \mathbf{x}_e, \quad (3-32)$$

and α_f is the interpolation factor. Note that when applied to the calculation of gradients at the cell center, the eccentricity correction is an iterative process. Since the gradient depends on the variable at the face centroid, which in turn depends on the gradient at the cell center.

Although not discussed in the present work, the interpolation factor α_f can be determined in several ways. More information on determining the interpolation factor is given in [63].

3-3 Solution Process

The flow problem to be solved is described by a coupled system of equations, i.e. the dominant variable of each equation occurs in some of the other equations. ReFRESCO allows for two methods to solve these systems of equation in discrete form, i.e. a coupled and segregated

method. The coupled method solves the system of equations for all variables simultaneously, the segregated approach solves each equation for its dominant variable, treating the other variables as known. An iterative procedure is then used until the solution of the coupled system is obtained. In this study only the segregated method is used and therefore the coupled solver will not be treated here.

The non-linearities and higher-order corrections, e.g. the discretized convective term of the momentum equation given by,

$$\sum_{i=1}^{N_f} \rho V_{f_i} (\mathbf{V}_{f_i} \cdot \mathbf{S}_{f_i}), \quad (3-33)$$

needs to be solved iteratively. This iterative process is performed within the so-called outer-loop (see figure 3-5), which for equation 3-33 results in,

$$\sum_{i=1}^{N_f} \rho V_{f_i}^k (\mathbf{V}_{f_i} \cdot \mathbf{S}_{f_i})^{k-1}, \quad (3-34)$$

where the subscripts k and $k - 1$ represent the current and previous outer-loop iteration respectively. Higher-order corrections such as the eccentricity correction discussed in 3-2-8 are also solved within the outer-loop.

Next a linear system of equations for each variable, i.e. u , v , w , and the required variables of the turbulence model are solved in a number of so-called inner-loops. The three velocity components are first obtained after which the pressure is corrected (see section 3-3-2). After the pressure correction procedure the turbulence quantities are solved. Depending on the number of quantities used within the turbulence model, this is done in one or two extra inner-loops. After solving the turbulence model transport equations the whole process is repeated (outer-loop).

Both the inner- and outer-loops are stopped when a user defined maximum number of iterations is reached, or when the solution reached the required level of convergence. Convergence criteria are based on the L_2 - or L_∞ -norm of the residuals (see e.g. section 2-5). A schematic presentation of the solution process is given in figure 3-5. More information on the applied solution methods can be found in [64].

3-3-1 Under-Relaxation

To improve the convergence stability of the solution it is necessary to limit the change in each variable from one outer iteration to the next. This is because a change in one variable changes the coefficients in the next equations to be solved, which may slow down or prevent convergence. Controlling the change in variables from one iteration to the next is done by implementing under-relaxation. This can be done either explicit or implicit. By implementing explicit under-relaxation a flow variable to be solved is expressed as a function of both the old and new solution given by,

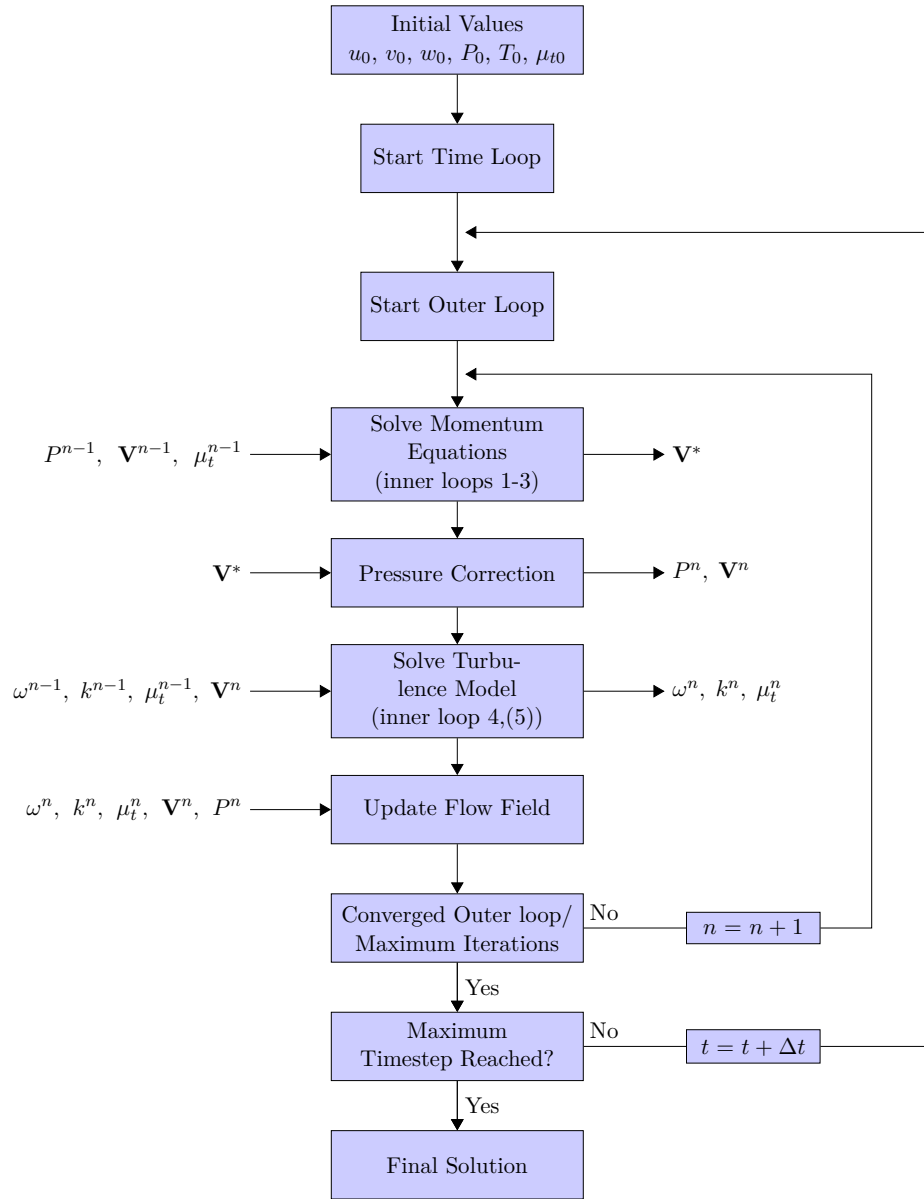


Figure 3-5: Schematic of solution process used by ReFRESCO.

$$\phi = \phi^{old} + \beta(\phi^{new} - \phi^{old}) \quad (3-35)$$

In which the variable β can be chosen $0 \leq \beta \leq 1$. When $\beta = 1$ the solution consists of only the new solution ϕ^{new} , hence no under-relaxation is implemented. On the other hand when $\beta = 0$ the solution consists of only the old solution, which results in no progress towards convergence. Selecting the correct value for β and thus the amount under-relaxation is largely empirical, however it is obvious that choosing $\beta = 1$ or $\beta = 0$ is somewhat useless [64]. Choosing β close to zero results in steady convergence but decreased convergence rate.

3-3-2 Pressure Correction

When the momentum equations are solved sequentially, i.e. using the decoupled approach, the set of algebraic equations for each component of the momentum is solved in turn, treating the grid point values of its dominant velocity component as the sole set of unknowns. The pressure field used in these iterations is obtained from the previous outer-loop iteration (see figure 3-5), hence the velocities computed do not normally satisfy the discretized continuity equation. To ensure the continuity condition, the velocities need to be corrected, i.e. the pressure field needs to be modified. This is done using the so-called Semi Implicit Method for Pressure Linked Equation (SIMPLE) method, which is an iterative method designed for a "collocated" variable arrangement.

This method makes use of the Poisson equation for the pressure given by,

$$\frac{\partial^2 P}{\partial x_i^2} = -\rho \frac{\partial}{\partial x_i} \left[\frac{\partial \mathbf{V}_j \mathbf{V}_i}{\partial x_j} \right], \Rightarrow . \quad (3-36)$$

The sequence of steps of the SIMPLE method, which are performed each outer-loop, is three-fold:

- Step A: Solve momentum equations using an initial (\mathbf{P}_0 at the first step) or a previously computed pressure field \mathbf{P}^{n-1} . This results in an initial prediction of the velocity field \mathbf{V}^*
- Step B: Solve the Poisson equation (3-36) using \mathbf{V}^* to compute the pressure correction \mathbf{P}' at the new iteration step.
- Step C: Correct the velocity field using the corrected pressure ($\mathbf{P} = \mathbf{P}^{n-1} + \mathbf{P}'$).

3-4 Note on Unsteady Computations

When performing unsteady computations the time step size Δt needs to be defined. For the two-dimensional computations the time step is based on the shedding frequency of the airfoil and constraints regarding the CFL number. A Strouhal number of $St = 0.20$ is used to estimate the shedding frequency, following the theory on flow around circular cylinders [65].

The corresponding shedding period T is used to obtain an initial value for Δt by choosing $\Delta t = T/100$. Additionally the CFL number must be kept around 100. Both the choice of $\Delta t = T/100$ and $CFL = 100$ are based on previous studies [58, 66] and result in sufficient resolution to properly capture the flow.

Note that considering the *CFL* number only by itself is not sufficient in choosing the time-step, since it only describes the ratio between the time-step and grid-cell size.

Chapter 4

Numerical Setup

In this chapter the numerical setup used all computations is presented. The chapter is split into two sections: first a section on the two-dimensional setup used for the calculations on the 2D foils, followed by a section on the three-dimensional setup used for the computations on the turbine rotor (section 4-1 and 4-2 respectively).

4-1 Two-Dimensional Airfoil

4-1-1 Domain Dimensions

The two-dimensional computational domain consists of the airfoil geometry located at the center of a circular domain. The origin of the coordinate system is located at the Leading Edge (LE) of the airfoil (see figure 4-1).

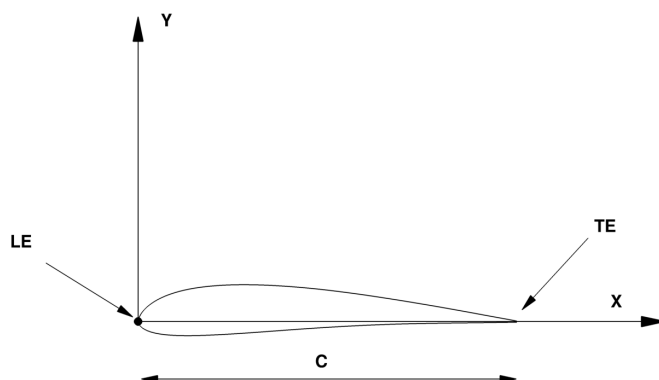


Figure 4-1: Coordinate system for the 2D airfoil computations

The choice for the circular domain follows from the various angles of attack to be analyzed. By correctly altering the boundary condition a single grid can be used for different angles of attack.

Even though the analysis of the airfoil is two-dimensional the domain is modeled with a finite thickness in the third (z) dimension (see figure 4-2). The NS-equations however are only solved in the x - and y -direction. This is required since the discretization is face based as explained in section 3-2-2.

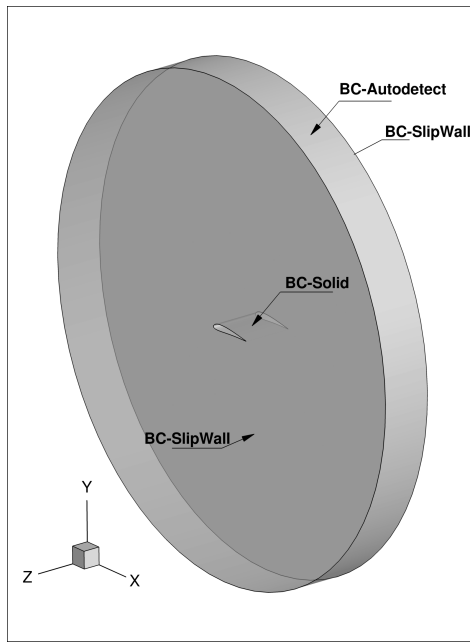


Figure 4-2: Boundary conditions on the airfoil domain

Because of this finite thickness in the z -direction the airfoil has a non-zero span. For simplicity both the chord and the span of the airfoil are unity. By doing so quantities such as the lift and drag coefficients, given by equations (2-9) and (2-11), remain unchanged (hence two-dimensional). The diameter D of circular boundary of the domain is be expressed in terms of the airfoil chord, i.e. $D = 2 \times R/c$. Figure 4-3 shows an xy -plane section of the domain.

To assure that the influence of the outer wall on the solution is negligibly small, an optimum domain diameter study is presented in section 5-2.

4-1-2 Boundary Conditions

In order to obtain a numerical solution a number of boundary conditions need to be imposed at the domain walls. In figure 4-2 the names of the imposed boundary conditions are presented.

When a solid surface is subject to a flow it is impossible for the flow to penetrate the surface. Additionally, when the flow is viscous, the interaction between the surface and the flow creates a zero velocity at the surface as can be seen from figure 2-5. Mathematically this can be imposed onto the airfoil wing by prescribing the normal and tangential velocities to be zero or $\mathbf{V} = \vec{0}$ at the airfoil surface. Furthermore the turbulence variables for the Spalart-Allmaras and $k-\omega$ SST models are given by, $\tilde{\nu}_{wall} = 0$, $k_{wall} = 0$, and $\omega_{wall} = 60 \cdot \mu / \rho \beta_1 (\Delta d)^2$.

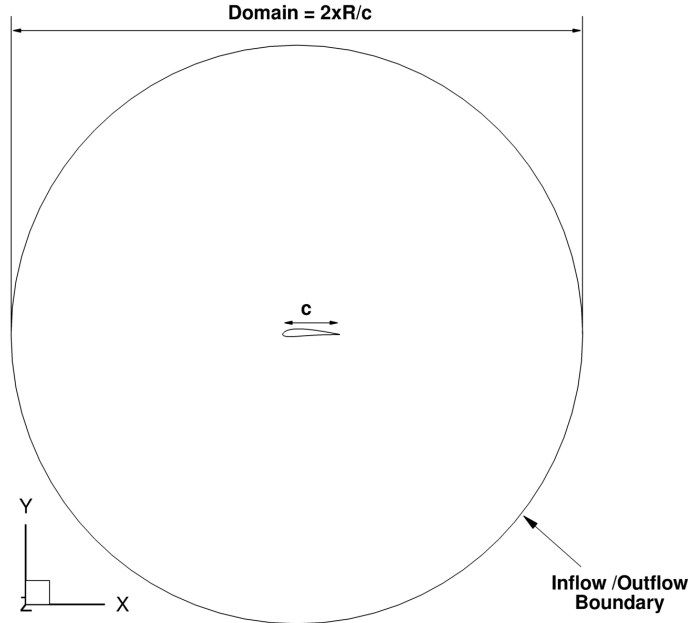


Figure 4-3: XY-plane view of the airfoil domain

These boundary conditions combined are referred to as the BCWALL boundary condition within *ReFRESCO*.

Since the problem to be solved is two-dimensional the sides of the domain are treated separately. A slip wall boundary condition is imposed at the sides of the domain to maintain the 2D character of the flow. Mathematically this is obtained by setting the velocity normal to the boundary to zero,

$$\mathbf{V} \cdot \vec{n} = \frac{\partial \mathbf{V}}{\partial \vec{n}} = 0, \quad (4-1)$$

where \vec{n} is the normal unit vector. Although the normal velocity components are set to zero it has no influence on the solution since the RANS equations are not solved in the z -direction. Note however that by implementing this boundary condition the tangential velocity is not prescribed at the wall. This boundary condition is prescribed by implementing BCSLIPWALL within *ReFRESCO*.

The third boundary condition is imposed at the outer circular wall and is known as the BCAUTODETECT boundary conditions (see figure 4-2). This boundary condition automatically prescribes the inflow, outflow, and pressure boundary regions by means of a prescribed velocity vector and two angles α and β . The velocity vector is used to determine the in and outflow regions and α and β are used to determine the size of the pressure boundary. This method is a “trick” of ReFRESCO that permits to save a lot of computational time. A graphical presentation of the BCAUTODETECT boundary condition is given in figure 4-4. The effect of α and β on the numerical solution is outside the scope of the work presented in this report, however a detailed study previously performed is presented in [67]. For this study, α and β were set to the default values of 75 and 105 degrees respectively.

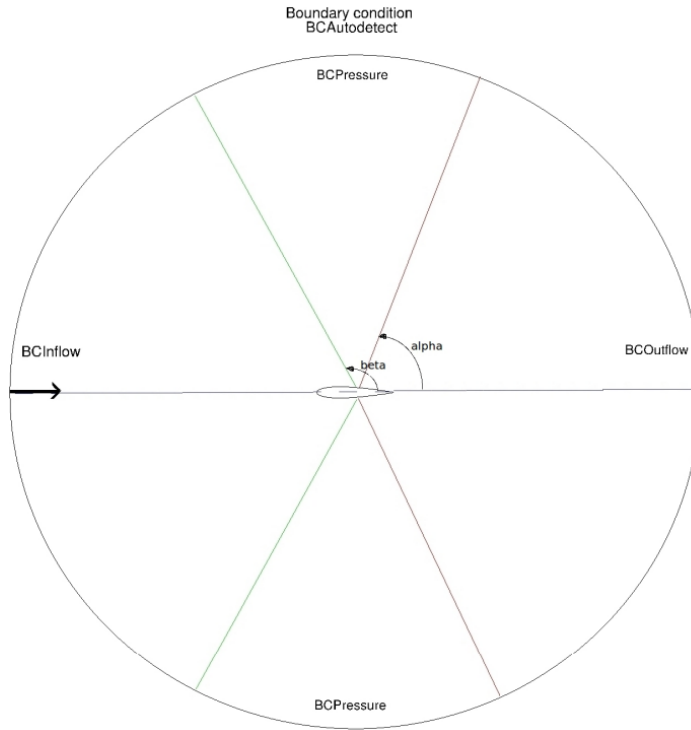


Figure 4-4: Geometry of the autodetect boundary conditions [67].

At the inflow boundary region determined by `BCAUTODETECT` the velocity is prescribed by means of the velocity vector \mathbf{V} . The pressure regions are prescribed by means of setting the pressure at these boundaries to atmospheric pressure. At the remaining boundary region an outflow condition is prescribed, for which Neumann boundary conditions are applied to the flow variables, i.e. the normal gradients are zero for,

$$\frac{\partial \mathbf{V}}{\partial \vec{n}} = \frac{\partial P}{\partial \vec{n}} = \frac{\partial \tilde{\nu}}{\partial \vec{n}} = \frac{\partial k}{\partial \vec{n}} = \frac{\partial \omega}{\partial \vec{n}} = 0, \quad (4-2)$$

where \vec{n} is the outward normal unit vector. Having boundaries close to the airfoil or turbine will influence the solution, e.g. blockage-effects due to the imposed boundary conditions can alter the airfoil or turbine performance. To study the effect of the boundary conditions on the numerical solution a domain study must be performed, which is part of the present study (for both 2D and 3D turbine).

Additionally the turbulence variables of the turbulence models need to be prescribed at the inflow boundary, which will determine the level of turbulence entering the domain. The choice of the inflow turbulence variables is especially important for the unsteady low Reynolds number flows considered in this thesis. The values of the turbulence variables at the inflow are equal for all computations, and set such that a laminar inflow is obtained.

4-1-3 Grid Topology

The domain, as previously discussed, is discretized using *HEXPRESS*. Since the calculations are two-dimensional only one cell is modeled in the z -direction. In the xy -plane a uniform mesh is generated as a starting point for the grid generation process.

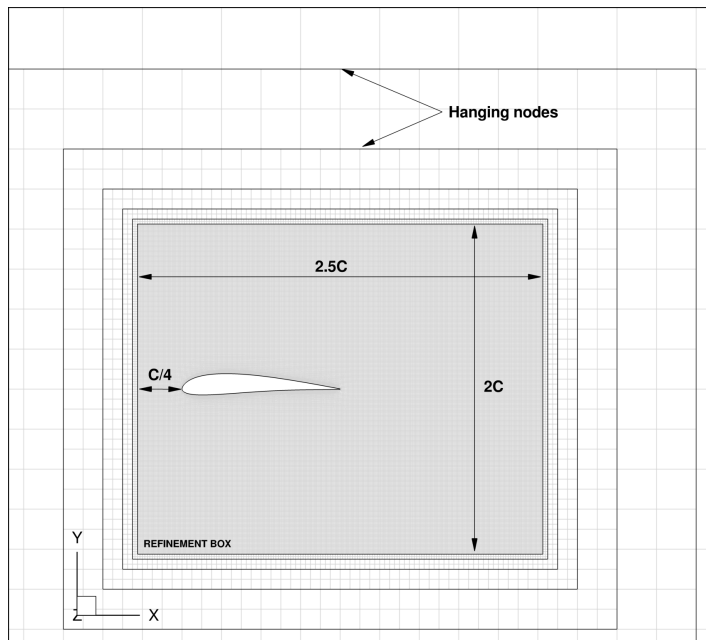


Figure 4-5: Refinement box around airfoil.

To avoid hanging nodes in the vicinity of the airfoil a refinement box is introduced in which the airfoil geometry is contained as shown in figure 4-5. The refinement of the cells within refinement box is such that the desired grid resolution at the airfoil is obtained. The size and location of the refinement-box is given in figure 4-5 and is chosen such that the important flow phenomena e.g. flow separation are captured within the refined area. Note that the refinement box dimensions are such that the flow phenomena are captured for the full range of angles of attack considered, as will be discussed later.

Because the calculations are executed without the use of wall functions, an additional refinement, called “viscous layer”, has to be imposed near the airfoil surface. This is done to guarantee sufficient grid resolution to accurately compute the large gradients present in the boundary layer. The resolution of this refinement is based on the dimensionless wall distance y^+ . $y^+ < 1$ refers to the viscous sublayer where the Reynolds shear stress is negligible compared to the viscous stress. Based on this y^+ the initial cell size at the airfoil surface is determined using the following expression,

$$\Delta S = \frac{y^+ \mu}{\rho V_{fric}}. \quad (4-3)$$

ΔS and a stretching ratio can than be used as input for *HEXPRESS* to determine the amount of refinements needed. Figure 4-6 shows the viscous layer refinements around the airfoil surface with a detailed view at the bottom right corner. These refinements follow directly from ΔS

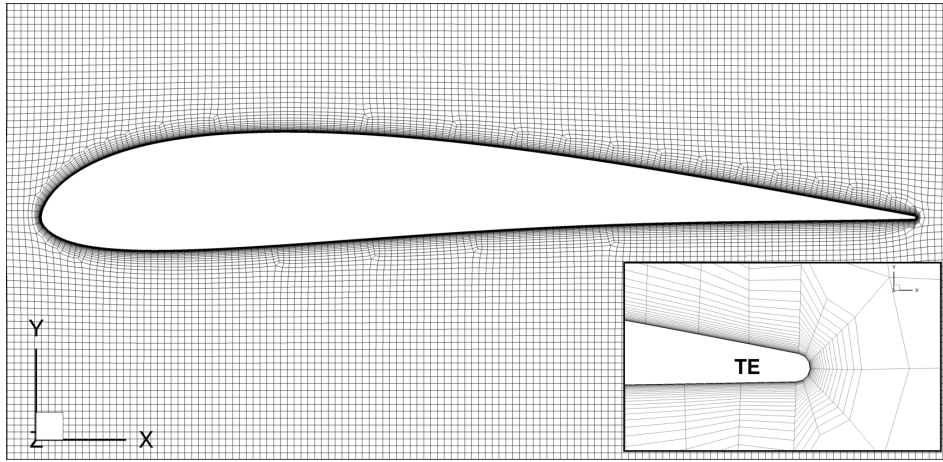


Figure 4-6: Viscous layer refinement with detailed view of TE.

4-1-4 Calculation Overview

The analysis for the two dimensional study consists of computations where both angle of attack and Reynolds number are varied. The range of these parameters follow from a number of reasons. First; the local tip speed ratio ($\gamma_r = \Omega r / V_{wind}$) is non uniform in radial direction, causing the radial velocity Ωr to vary with increasing radius r . As a result the direction of the relative velocity, and therefore the angle of attack, varies over the span of the blade (see equations (2-35) and (2-36)). A non-uniform pitch angle of the rotor blade in radial direction also contributes to the need for a wide range of angles of attack to be computed. Second; the turbine is analyzed using two different scales, hence different wind velocities. As a consequence the Reynolds number will vary.

The final reason follows directly from the range of tip speed ratios to be analyzed. Despite the fact that the operating condition of the NREL 5MW turbine is at a tip speed ratio of 7 (see table 2-1), a range of various tip speed ratios is analyzed. By doing so the overall performance of the turbine is obtained. The range of TSRs to be analyzed also requires numerous computations in which Reynolds number and angles of attack are varied.

The local angle of attack and Reynolds number along the radius of the MSWT and NREL 5MW turbine are presented in table 4-1. Note that the data for the MSWT is presented for model-scale conditions while the data for the NREL 5MW turbine is presented for full-scale conditions. The data presented in these tables correspond to the operating conditions specified in table 2-1.

From the given data the flow properties for the initial studies (i.e. domain size and grid refinement study) are as follows:

- 2x Reynolds numbers; $10^4, 10^6$;
- 2x Angles of attack; 0 and 20 degrees.

Based on the above, a number of computations are performed, as presented in table 4-2.

Table 4-1: MSWT flow properties at model-scale operating condition, $TSR = 7.0$.

Radius r/R [−]	Chord Length c/r [−]	Pitch Angle β [deg]	Angular vel. Ωr [m/s]	Local AoA [deg]	Apparent Velocity [m/s]	Re_{local} [−]
Marin Stock Wind Turbine at model-scale ($V_{wind} = 2.0$ [m/s])						
0.1	0.076	31.18	1.13	23.60	1.96	$12.1 \cdot 10^3$
0.2	0.090	16.39	2.26	18.92	2.77	$20.3 \cdot 10^3$
0.3	0.088	8.50	3.39	16.78	3.75	$26.9 \cdot 10^3$
0.4	0.082	5.50	4.52	14.00	4.79	$32.0 \cdot 10^3$
0.5	0.074	3.80	5.65	12.02	5.87	$35.4 \cdot 10^3$
0.6	0.068	2.50	6.78	10.78	6.96	$38.6 \cdot 10^3$
0.7	0.060	1.67	7.91	9.77	8.07	$39.5 \cdot 10^3$
0.8	0.052	1.00	9.04	9.04	9.18	$38.9 \cdot 10^3$
0.9	0.046	0.40	10.16	8.54	10.29	$38.6 \cdot 10^3$
1	0.028	0.05	11.29	8.01	11.41	$26.0 \cdot 10^3$
NREL 5MW Turbine at full-scale ($V_{wind} = 11.4$ [m/s])						
0.05	0.056	13.26	3.99	57.45	12.08	$27.7 \cdot 10^5$
0.15	0.069	13.26	11.97	30.33	16.53	$46.3 \cdot 10^5$
0.25	0.073	11.70	19.96	18.04	22.98	$68.0 \cdot 10^5$
0.35	0.070	9.66	27.94	12.53	30.18	$86.2 \cdot 10^5$
0.45	0.064	7.65	35.92	9.96	37.69	$98.2 \cdot 10^5$
0.55	0.057	5.79	43.91	8.76	45.36	$10.5 \cdot 10^6$
0.65	0.050	4.11	51.89	8.28	53.13	$10.9 \cdot 10^6$
0.75	0.046	2.60	59.87	8.18	60.95	$11.3 \cdot 10^6$
0.85	0.040	1.31	67.85	8.23	68.80	$11.3 \cdot 10^6$
0.95	0.029	0.31	75.84	8.24	76.69	$90.4 \cdot 10^5$

Table 4-2: Overview of performed computations on 2D airfoil.

AoA [deg]	Re no. [-]	Std./Unstd. [-]	Radius (r/R) [-]	N_{cells} [-]	Turbulence model [-]
Domain Size Study					
0	10^4	Steady	10 - 200	22.3k	$k - \omega$ SST (2003)
4	10^4	Steady	10 - 200	22.3k	$k - \omega$ SST (2003)
0	10^6	Steady	10 - 200	22.3k	$k - \omega$ SST (2003)
4	10^6	Steady	10 - 200	22.3k	$k - \omega$ SST (2003)
20	10^4	Unsteady	10 - 100	22.3k	$k - \omega$ SST (2003)
20	10^6	Unsteady	10 - 100	22.3k	$k - \omega$ SST (2003)
Refinement Size Study					
0	10^4	Steady	100	36.3k - 1.4M	$k - \omega$ SST (2003)
4	10^4	Steady	100	36.3k - 1.4M	$k - \omega$ SST (2003)
0	10^6	Steady	100	36.3k - 1.4M	$k - \omega$ SST (2003)
4	10^6	Steady	100	36.3k - 1.4M	$k - \omega$ SST (2003)
20	10^4	Unsteady	100	36.3k - 739.4k	$k - \omega$ SST (2003)
20	10^6	Unsteady	100	36.3k - 739.4k	$k - \omega$ SST (2003)
Turbulence modeling Study					
0	10^4	Steady	100	739.4k	Spalart-Allmaras
0	10^4	Steady	100	739.4k	$k - \omega$ SST (Standard)
0	10^4	Steady	100	739.4k	$k - \omega$ SST (2003)
4	10^4	Steady	100	739.4k	Spalart-Allmaras
4	10^4	Steady	100	739.4k	$k - \omega$ SST (Standard)
4	10^4	Steady	100	739.4k	$k - \omega$ SST (2003)
0	10^6	Steady	100	739.4k	Spalart-Allmaras
0	10^6	Steady	100	739.4k	$k - \omega$ SST (Standard)
0	10^6	Steady	100	739.4k	$k - \omega$ SST (2003)
4	10^6	Steady	100	739.4k	Spalart-Allmaras
4	10^6	Steady	100	739.4k	$k - \omega$ SST (Standard)
4	10^6	Steady	100	739.4k	$k - \omega$ SST (2003)

4-1-5 Post-Processing

From the results the correct data needs to be generated. From the two-dimensional computations the total forces on the airfoil in x - and y -direction relative to the coordinate system explained previously (see figure 4-1) are obtained. Additionally the total moment about the origin of the coordinate system is generated. The total x and y forces can be decomposed into a drag and lift component using the following expression,

$$L = F_y \cos \alpha - F_x \sin \alpha \quad (4-4)$$

$$D = F_y \sin \alpha - F_x \cos \alpha \quad (4-5)$$

Where L and D are the lift and drag force respectively, and α is the angle of attack. The lift, drag, and moment coefficients are made non-dimensional using equations (2-9) to (2-11) from chapter 2. Note that the moment coefficient C_m is defined at the leading edge i.e. C_{mLE} .

4-2 Three-Dimensional Turbine

In this section the numerical setup is presented for the full 3D turbine as used in the numerical computation. First the geometry of the rotor blades, and the geometry of the complete domain will be discussed. Next the applied boundary conditions and flow characteristics used as input for the calculations will be described. At the end of this section the topology of the grid will be explained followed by the methods to post-process the required data.

The geometry of both the NREL 5MW and the MSWT blades, as discussed in section 2-1 are constructed from a series of foil sections. The exact non-dimensional geometry of both blade designs is presented in tables 4-3 and 4-4, where the x_p represents the location of the pitch axis, and β the pitch angle.

Table 4-3: Non-dimensional geometry of the MARIN Stock Wind Turbine 5MW turbine.

Section no.	Airfoil	r/R	c/D	β	t/c	x_p/c
1	Drela AG-04	0.046	0.035	42.712	0.128	0.375
2	Drela AG-04	0.132	0.041	23.109	0.128	0.375
3	Drela AG-04	0.252	0.046	11.475	0.128	0.375
4	Drela AG-04	0.382	0.042	6.523	0.128	0.375
5	Drela AG-04	0.512	0.037	3.878	0.128	0.375
6	Drela AG-04	0.642	0.032	2.216	0.128	0.375
7	Drela AG-04	0.772	0.027	1.245	0.128	0.375
8	Drela AG-04	0.892	0.023	0.497	0.128	0.375
9	Drela AG-04	0.978	0.014	0.064	0.128	0.375

During the model-scale experiments performed at MARIN, no hub was modeled for both the MSWT and NREL 5MW baseline turbine. For the numerical computations however a standard hub was modeled for both turbine geometries. The dimensions and geometry of

Table 4-4: Non-dimensional geometry of the NREL 5MW turbine.

Section no.	Airfoil	r/R	c/D	β	t/c	x_p/c
1	Cylinder1	0.024	0.028	13.308	1	0.5
2	Cylinder1	0.031	0.028	13.308	1	0.5
3	Cylinder2	0.054	0.029	13.302	0.93	0.478
4	Cylinder3	0.088	0.031	13.308	0.78	0.449
5	Cylinder4	0.137	0.033	13.308	0.61	0.423
6	DU-40	0.187	0.036	13.308	0.477	0.375
7	DU-35	0.252	0.037	11.48	0.383	0.375
8	DU-35	0.317	0.035	10.162	0.331	0.375
9	DU-30	0.382	0.034	9.011	0.29	0.375
10	DU-25	0.447	0.032	7.795	0.26	0.375
11	DU-25	0.512	0.03	6.544	0.238	0.375
12	DU-21	0.577	0.028	5.361	0.219	0.375
13	DU-21	0.642	0.026	4.188	0.202	0.375
14	NACA 64-618	0.707	0.024	3.125	0.18	0.375
15	NACA 64-618	0.772	0.022	2.319	0.18	0.375
16	NACA 64-618	0.837	0.02	1.526	0.18	0.375
17	NACA 64-618	0.892	0.018	0.863	0.18	0.375
18	NACA 64-618	0.935	0.017	0.37	0.18	0.375
19	NACA 64-618	0.978	0.011	0.106	0.18	0.375
20	NACA 64-618	0.983	0.01	0.082	0.18	0.375
21	NACA 64-618	0.988	0.009	0.06	0.18	0.375
22	NACA 64-618	0.992	0.008	0.04	0.18	0.375
23	NACA 64-618	0.995	0.006	0.023	0.18	0.375
24	NACA 64-618	0.998	0.005	0.01	0.18	0.375
25	NACA 64-618	0.999	0.003	0.003	0.18	0.375
26	NACA 64-618	1	0.002	0	0.18	0.375

the hub are presented in figure 4-7. The hub geometry is cylindrical shaped with spherically blunted tangent ogive shaped ends, in order to minimize the curvature variation which may induce flow separation.

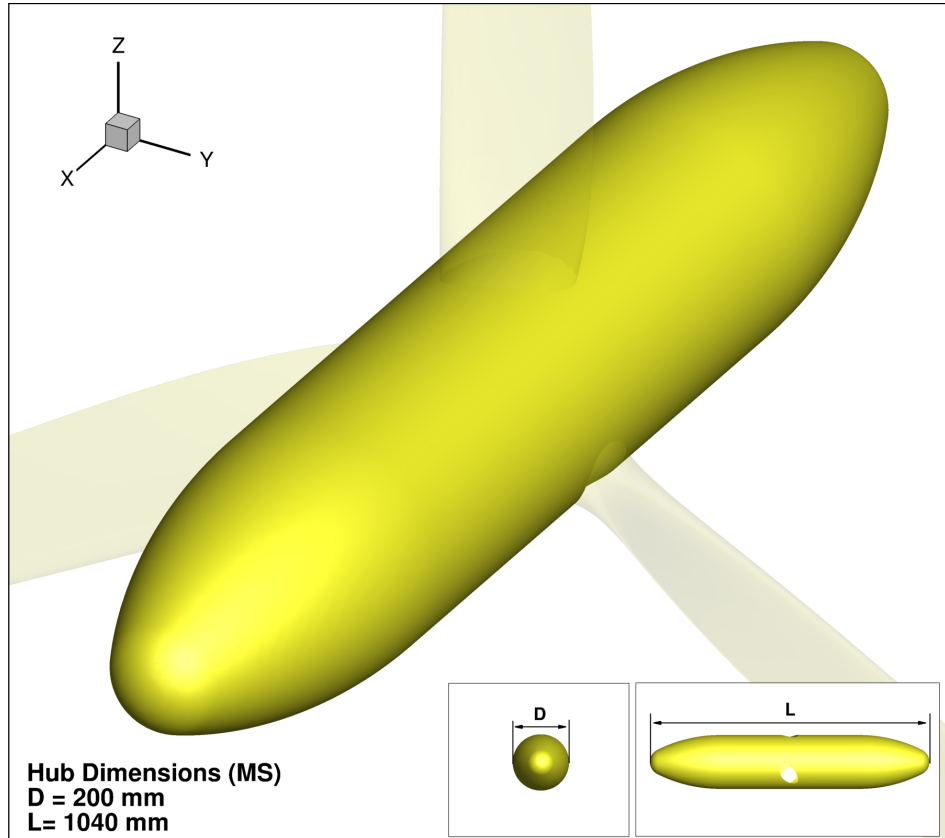


Figure 4-7: Dimensions of the hub at model-scale.

4-2-1 Domain Dimensions

The computational domain as used for the three-dimensional computations consists of a cylindrical volume in which the turbine is placed, as can be seen in figure 4-8.

The total length of the cylindrical domain, and its radius are defined by a multiple of the turbine diameter. The origin of the coordinate system and the location of the turbine is at $1/5$ the length of the cylinder as shown in figure 4-8.

4-2-2 Turbine motion modeling

Consider the origin \mathbf{x}_0 of a non-inertial body-fixed reference frame in which a particle position \mathbf{X} is given by,

$$\mathbf{X} = \mathbf{x} + \mathbf{x}_0, \quad (4-6)$$

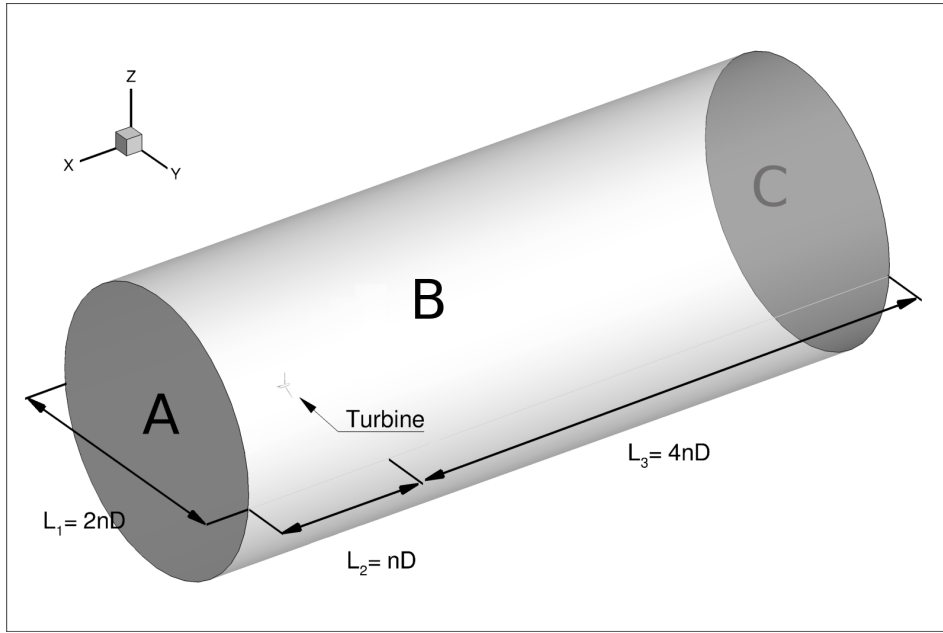


Figure 4-8: Dimensions of the 3D turbine domain.

where \mathbf{x} is the position of the particle in the body-fixed frame. By differentiation the velocities can be obtained,

$$\mathbf{V} = \mathbf{U} + \frac{d\mathbf{x}_0}{dt} + \boldsymbol{\Omega} \times \mathbf{x} = \mathbf{U} + \mathbf{V}_g, \quad (4-7)$$

Where \mathbf{U} represents the particle velocity relative to the body-fixed reference frame, $\frac{d\mathbf{x}_0}{dt}$ and $\boldsymbol{\Omega} \times \mathbf{x}$ the translation and rotation velocity of the body-fixed reference frame itself. The acceleration is given by the total derivative,

$$\frac{D\mathbf{V}}{Dt} = \frac{\mathbf{U}}{Dt} + \frac{d^2\mathbf{x}_0}{dt^2} + \frac{d\boldsymbol{\Omega}}{dt} \times \mathbf{x} + 2\boldsymbol{\Omega}\mathbf{U} + \boldsymbol{\Omega} \times (\boldsymbol{\Omega} \times \mathbf{x}),.. \quad (4-8)$$

Here four additional terms appear that now has to be accounted for in the conservation equations when a non-inertial reference frame is used. These terms represent the acceleration of origin of the non-inertial reference frame, the angular acceleration effect, the Coriolis acceleration, and the centripetal acceleration respectively [68].

To account for the rotative motion of the turbine several methods are available, based on either inertial or non-inertial reference frames [68];

- Relative-Formulation (RFM) or body-forces-approach: the RANS equations are written and solved in the moving or relative reference frame. Extra volumic terms, or body-forces, have to be considered,

- Absolute-Formulation (AFM): the RANS equations are solved in the moving reference frame but written in terms of absolute or inertial reference frame quantities,
- Moving-Grid-Formulation (MVG): the RANS equations are written and solved in the earth-fixed reference frame. Due to the motion of the objects, the equations are inherently unsteady, even for steady motions.

In this study the AFM formulation is used, therefore the additional velocity terms have to be included as well in the governing equations. The integral form of the mass conservation equation than becomes,

$$\int_{\mathcal{S}} (\mathbf{V} - \mathbf{V}_{x_0}) \cdot \mathbf{n} d\mathcal{S} = 0, \quad (4-9)$$

and the momentum equation,

$$\int_{\mathcal{S}} \frac{\partial \mathbf{V}}{\partial t} d\mathcal{V} + \int_{\mathcal{S}} [\rho \mathbf{V}(\mathbf{V} - \mathbf{V}_{x_0}) \cdot \mathbf{n}] d\mathcal{S} = \int_{\mathcal{S}} (\nu + \nu_t)[(\nabla \mathcal{V} + \nabla \mathcal{V}^T)] \cdot \mathbf{n} d\mathcal{S} + \dots \quad (4-10)$$

$$- \int_{\mathcal{V}} \nabla \left(p + \frac{2}{3} \rho k \right) d\mathcal{V} + \dots \quad (4-11)$$

$$- \int_{\mathcal{V}} \rho(\Omega \times \mathbf{V}) d\mathcal{V} + \dots \quad (4-12)$$

$$+ \int_{\mathcal{V}} \rho \mathbf{B} d\mathcal{V}, \quad (4-13)$$

Since all terms are expressed in the inertial reference frame, the boundary conditions are expressed in the inertial reference frame. E.g. for the no-slip condition at the moving body when using AFM is given by $V = V_{x_0}$. By using this method, the flow can be solved, in principle, using steady RANS. More information regarding this matter can be found in [68].

4-2-3 Boundary Conditions

For the three-dimensional computations a total of four boundary conditions are applied. At the surface of the turbine a wall boundary conditions (BCWALL) is applied, which is identical to the boundary condition applied at the surface of the two-dimensional airfoil (see section 4-1-2).

At the inflow region of the domain (**A** in figure 4-8) the velocity is prescribed as being the wind velocity, hence $\mathbf{V} = (v_{wind}, 0, 0)^T$. The inflow boundary conditions for the turbulence model variables are chosen similar to those of the two-dimensional computations.

At the outflow boundary (region **C** in figure 4-8) Neumann boundary conditions are applied, where the normal gradients for all quantities are zero, or;

$$\frac{\partial \mathbf{V}}{\partial \vec{n}} = \frac{\partial P}{\partial \vec{n}} = \frac{\partial \tilde{\nu}}{\partial \vec{n}} = \frac{\partial k}{\partial \vec{n}} = \frac{\partial \omega}{\partial \vec{n}} = 0, \quad (4-14)$$

where \vec{n} is the outward normal unit vector. Finally a boundary condition needs to be assigned at the wall of the cylindrical domain (region **B** in figure 4-8). At this wall a so-called pressure boundary condition is applied (**BCPRESSURE**), which requires the pressure to be constant at the boundary. For these computations the pressure at these boundaries is equal to the reference pressure as defined by the user, or;

$$P_{BC} = P_{ref}. \quad (4-15)$$

Additionally figure 4-9 shows the regions and their applied boundary conditions.

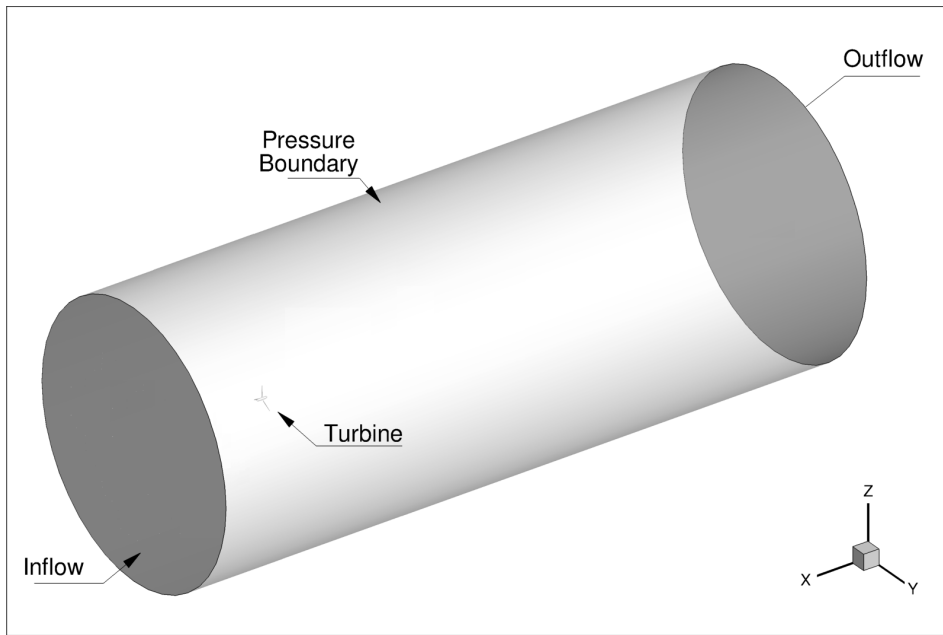
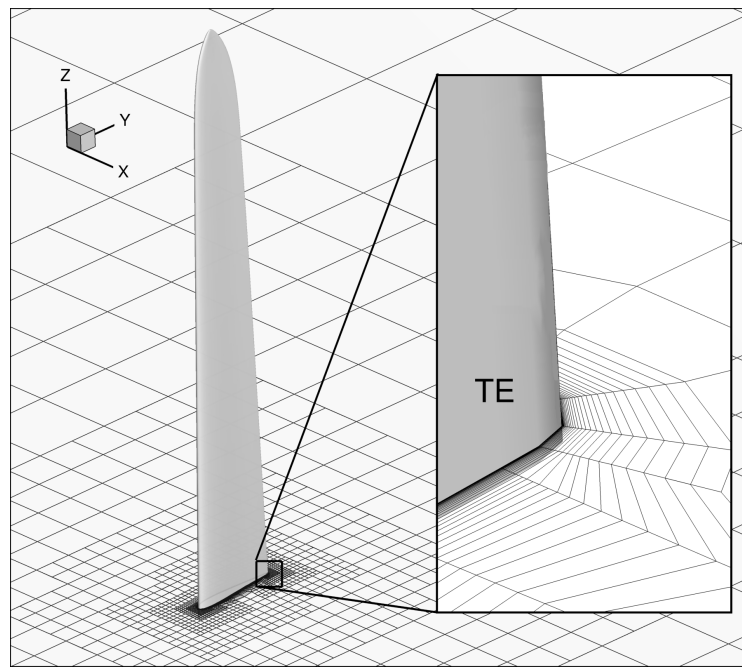


Figure 4-9: Boundary conditions on the 3D turbine domain.

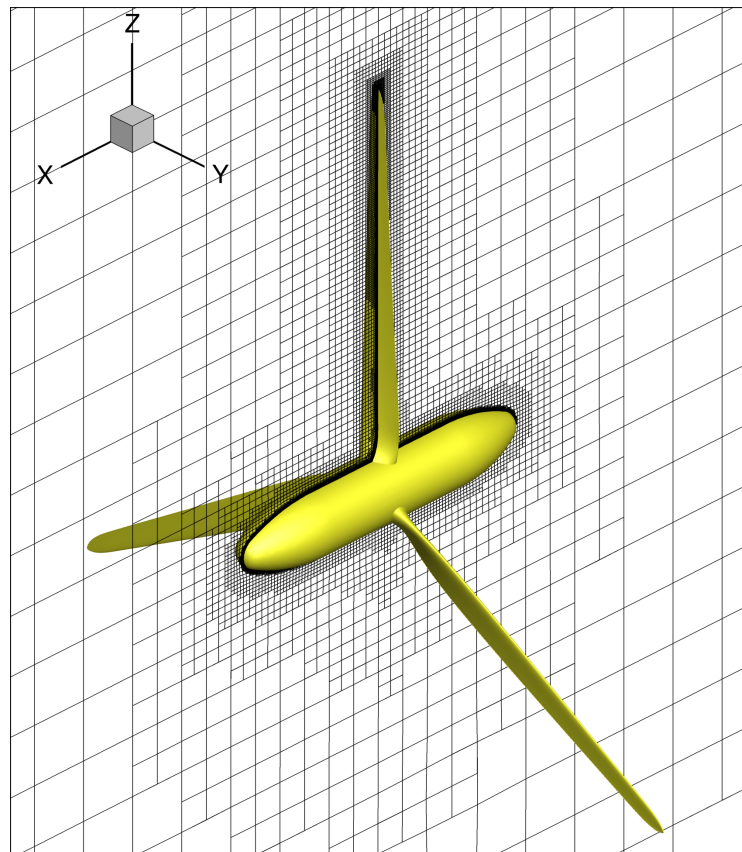
4-2-4 Grid Topology

As for the two-dimensional grid previously discussed, an initial cell size is defined based on the chord length. For the three-dimensional grid the initial cell size is defined by the turbine diameter. Next the initial grid is refined toward the geometry of the turbine until a sufficiently refined cell size is obtained at the surface of the turbine blade.

Additionally refinements are used near the surface of the turbine in order to properly model the viscous layer. The resolution of this refinement is based on the dimensionless wall distance y^+ , which is obtained according to the method described in section 4-1-3. To properly model the flow near the wall y^+ typically needs to be below one. In figure 4-10(a) the grid near the wall of the turbine blade is presented and a slice of the grid over the centerline of the turbine is shown in figure 4-10(b).



(a) Grid refinement near the wall of a turbine blade.



(b) Computational grid around the MSWT rotor at model-scale.

Figure 4-10: Detail of the 3D grid.

4-2-5 Calculation Overview

The performed calculations for the numerical study on the model- and full-scale MSWT and NREL 5MW baseline turbine are presented in table 4-5.

4-2-6 Post-Processing

The results of the three-dimensional computations consist of the flow field around the turbine including quantities such as velocity and pressure. In addition to these quantities both the forces and moments acting on the turbine blades are calculated. Both the thrust and power coefficients of the turbine can be computed by use of these forces and moments as follows:

$$C_T = \frac{F_x}{\frac{1}{2}\rho V^2 A}, \quad (4-16)$$

$$C_P = \frac{M_x \Omega}{\frac{1}{2}\rho V^3 A}, \quad (4-17)$$

where Ω is the angular velocity and A the swept area of the turbine given by $A = D^2\pi/4$.

The pressure distribution is expressed by means of the pressure coefficient C_{pn} given by,

$$C_{pn} = \frac{P - P_\infty}{\frac{1}{2}\rho(nD)^2}, \quad (4-18)$$

in which D is the diameter of the turbine and n the angular velocity of the turbine given in revolutions per second. Another useful derived quantity is the so-called Q -factor, which is used as an indication of the presence of vortices in the domain. The Q -factor is defined by [42],

$$\mathbf{Q} = \frac{1}{2} (\|\boldsymbol{\Omega}\|^2 - \|\mathbf{S}\|^2); \quad \bar{\mathbf{Q}} = \frac{1}{2} \left(\frac{\|\boldsymbol{\Omega}\|^2}{\|\mathbf{S}\|^2} - 1 \right); \quad \text{where,} \quad (4-19)$$

$$\boldsymbol{\Omega}_{ij} = \frac{1}{2} \left(\frac{\partial v_i}{\partial x_j} - \frac{\partial v_j}{\partial x_i} \right); \quad \mathbf{S}_{ij} = \frac{1}{2} \left(\frac{\partial v_i}{\partial x_j} + \frac{\partial v_j}{\partial x_i} \right). \quad (4-20)$$

In these equations $\boldsymbol{\Omega}$ and \mathbf{S} denote the anti- and symmetric part of the velocity gradient tensor $\nabla \mathbf{V}$ respectively.

Table 4-5: Overview of performed computations for the numerical study on the model- and full-scale MSWT and NREL 5MW baseline turbine.

V_{wind} (MS) [m/s]	V_{wind} (FS) [m/s]	TSR [-]	Domain [-]	N_{cells} [-]	Turbulence model [-]
Domain size study MSWT					
2.00	14.1	7.0	A	13.1M	$k - \omega$ SST (Standard)
2.00	14.1	7.0	B	13.3M	$k - \omega$ SST (Standard)
2.00	14.1	7.0	C	13.4M	$k - \omega$ SST (Standard)
Refinement size study MSWT					
2.47	17.4	7.0	C	8.4M	$k - \omega$ SST (Standard)
2.47	17.4	7.0	C	13.4M	$k - \omega$ SST (Standard)
2.47	17.4	7.0	C	18.6M	$k - \omega$ SST (Standard)
2.47	17.4	7.0	C	23.9M	$k - \omega$ SST (Standard)
2.47	17.4	7.0	C	29.6M	$k - \omega$ SST (Standard)
Turbulence modeling study MSWT					
2.00	14.1	7	C	29.6M	$k - \omega$ SST (Standard)
2.00	14.1	7	C	29.6M	$k - \omega$ SST (Standard)
MSWT full-scale					
1.61	11.4	3	C	51.9M	$k - \omega$ SST (Standard)
1.61	11.4	4	C	51.9M	$k - \omega$ SST (Standard)
1.61	11.4	5	C	51.9M	$k - \omega$ SST (Standard)
1.61	11.4	6	C	51.9M	$k - \omega$ SST (Standard)
1.61	11.4	7	C	51.9M	$k - \omega$ SST (Standard)
1.61	11.4	8	C	51.9M	$k - \omega$ SST (Standard)
NREL 5MW model-scale					
2.00	14.1	3	C	51.9M	$k - \omega$ SST (Standard)
2.00	14.1	4	C	51.9M	$k - \omega$ SST (Standard)
2.00	14.1	5	C	51.9M	$k - \omega$ SST (Standard)
2.00	14.1	6	C	51.9M	$k - \omega$ SST (Standard)
2.00	14.1	7	C	51.9M	$k - \omega$ SST (Standard)
2.00	14.1	8	C	51.9M	$k - \omega$ SST (Standard)
NREL 5MW full-scale					
1.61	11.4	3	C	46.6M	$k - \omega$ SST (Standard)
1.61	11.4	4	C	46.6M	$k - \omega$ SST (Standard)
1.61	11.4	5	C	46.6M	$k - \omega$ SST (Standard)
1.61	11.4	6	C	46.6M	$k - \omega$ SST (Standard)
1.61	11.4	7	C	46.6M	$k - \omega$ SST (Standard)
1.61	11.4	8	C	46.6M	$k - \omega$ SST (Standard)
Unsteady computation					
2.00	14.1	7	C	54.5M	$k - \omega$ SST (Standard)

Chapter 5

Numerical Study on a Two-Dimensional Wing Section

In this chapter the findings from all the numerical studies performed on the two-dimensional flow over the Drela-AG04 are presented. The general flow field is discussed in section 5-1. Next, the optimum dimensions of the computational domain is determined in section 5-2. Section 5-3 is devoted to the uncertainty studies on both the steady and unsteady flows. In section 5-4, a study is presented in which three turbulence models are compared for various flow cases.

5-1 General Results

In this section the main features of the flow are illustrated, the computations performed show a number of interesting phenomena. For the model-scale Reynolds number regime in the order of $Re = 10^4$, the flow field for zero angle of attack is presented in figure 5-1(a). It can be observed that for this Reynolds number regime there is a large amount of flow separation, even at zero angle of attack. Reynolds dissimilitude (see section 2-2) results in extremely low Reynolds numbers at model scale i.e. $Re = 10^4$. As explained in section 2-3-1 a consequence of the model-scale Reynolds number flows is a laminar character of the boundary layer which is less susceptible to turbulent transition.

In figure 5-1(b) the normalized turbulence viscosity $\bar{\mu}_t$ given by equation (5-1) is graphed for $\bar{\mu}_t \geq 1$, indicating the region in which eddy viscosity is dominant and the flow can be considered turbulent [18]. The magnitude of $\bar{\mu}_t$ in the wake-field is small relative to the magnitude present in the full-scale Reynolds number flow presented in figure 5-2(b).

$$\bar{\mu}_t = \frac{\mu_t}{\mu_{lam}} \quad (5-1)$$

Flow separation occurring at the pressure side of the airfoil as presented in figure 5-1(a), is recurring in figure 5-1(d) in terms of a negative wall shear stress (indicated by the letter *A*). At this point the negative wall shear stress indicates a negative flow velocity along the airfoil wall. This is in line with the recirculating streamlines in figure 5-1(a), indicating a separated flow region.

The wall shear stress for the full-scale Reynolds number flow is presented in figure 5-2(d). This graph shows a local minimum in the wall shear stress for both the pressure and suction side of the airfoil (indicated by *D*). The magnitude of wall shear stresses increase rapidly downstream of the location where these minima occur, which due to laminar/turbulent transition as seen in figure 5-2(b), indicating that there is a non-negligible laminar part even at $Re = 10^6$. Also note that the wall shear stress remains positive over the whole airfoil surface, indicating that no flow separation occurs, which is in line with the flow presented in figure 5-1(a).

The findings previously discussed on turbulence viscosity and wall shear stress (no local minima) show that the model-scale Reynolds number flow case is fully laminar, while for the full-scale Reynolds number case turbulence transition occurs near the leading edge of the foil. For the full-scale Reynolds number case the turbulent boundary layer will increase the ability of the flow to remain attached which is analogous to the theory presented in section 2-3-1.

Finally when the angle of attack is further increased, separation occurs for both full- and model-scale Reynolds numbers. The convergence plots of the L_∞ residual norms and C_l and C_d are presented for model- and full-scale computations in figure 5-3, which are representative for all two-dimensional calculations.

At these large angles of attack the flow is no longer able to stay attached to the foil surface, vortices start to shed at the suction side of the airfoil and unsteady RANS computations are needed.

The computed results for an angle of attack of 20 degrees are presented next, at which the flow is highly unsteady for both the full- and model-scale Reynolds number regimes. In figures 5-4 and 5-5 several snapshots are presented of roughly one shedding cycle for both $Re = 10^4$ and $Re = 10^6$. In these figures the non-dimensional vorticity $\bar{\omega}_z$ given by equation (5-2) is plotted.

$$\bar{\omega}_z = \frac{\omega_z c}{V_\infty} \quad (5-2)$$

The shedding of vortices is clearly visible in the wake-field for both the full- and model-scale Reynolds number flows. For $Re = 10^4$ a region of strong vorticity i.e. a vortex is located near the trailing edge at $T = 70.4 \text{ sec}$, indicated by the letter **A**. Consecutively the vortices are transported in flow direction as can be seen for the successive time steps in figures 5-4(b) to 5-4(h). Similar phenomena are observed for the full-scale Reynolds number Regime.

Additionally a time-trace is presented of the lift, drag and moment coefficient for both Reynolds number regimes in figures 5-6(a) and 5-6(b). These figures clearly show the cyclic behavior of c_l , c_d , and c_m caused by vortex shedding. The characteristics of the cyclic behavior for both Reynolds number regimes are presented in table 5-1.

The Strouhal numbers in this table are based on the projected frontal dimension of the airfoil given by equation (5-3), as used in [69–71]. In this equation f is the vortex shedding frequency of the airfoil, c the chord of the airfoil, and α the angle of attack.

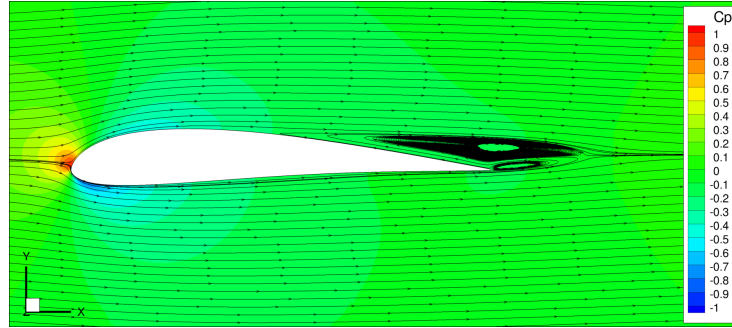
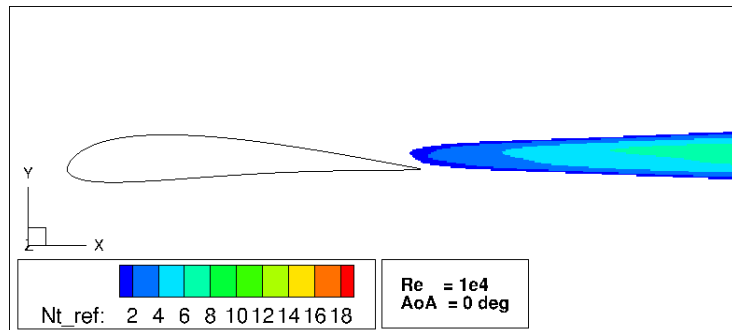
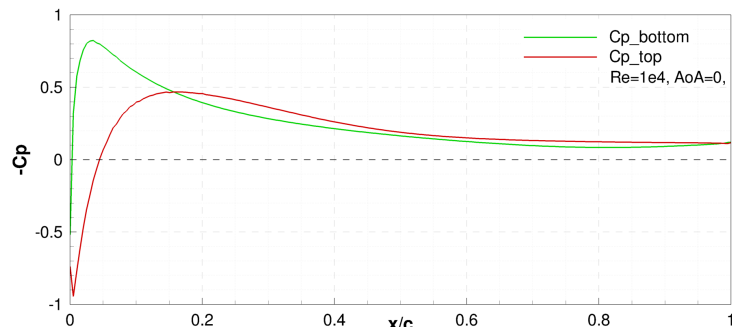
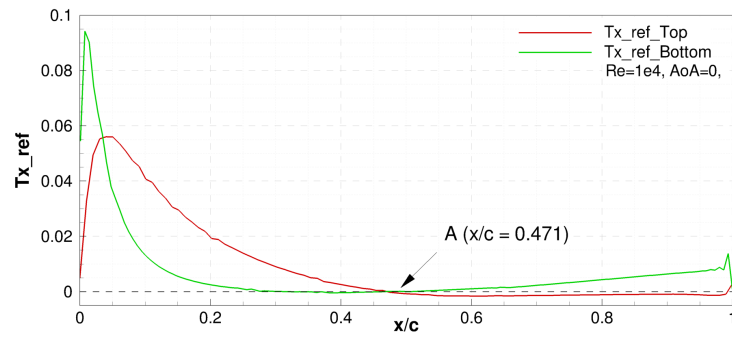
(a) Stream lines and normalized pressure C_p .(b) Normalized turbulence viscosity $\bar{\mu}_t = \mu_t / \mu_{lam}$.(c) Normalized pressure distribution C_p .(d) Normalized wall shear stress $\bar{\tau} = \tau_{wall} / q_\infty$.

Figure 5-1: Flow field characteristics for model-scale Reynolds number regime. $Re = 10^4$, $AoA = 0 \text{ deg}$.

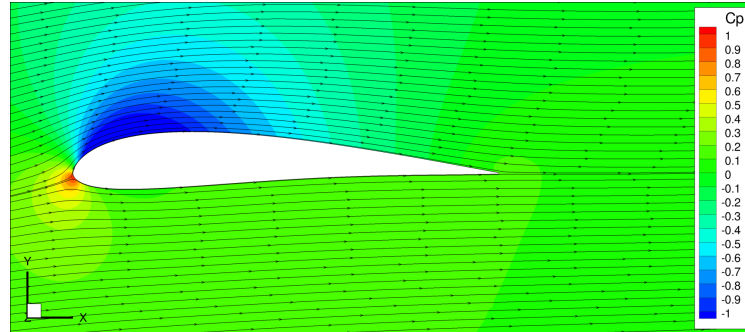
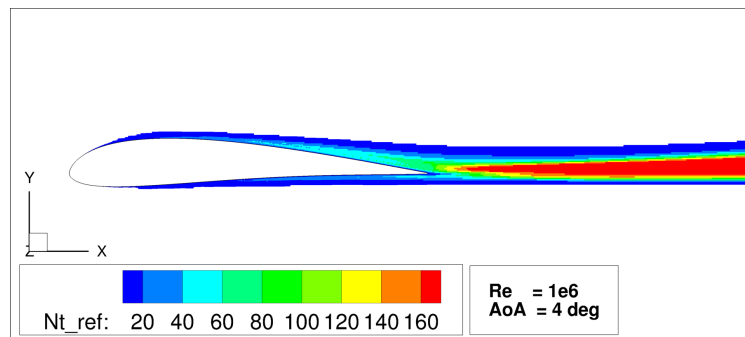
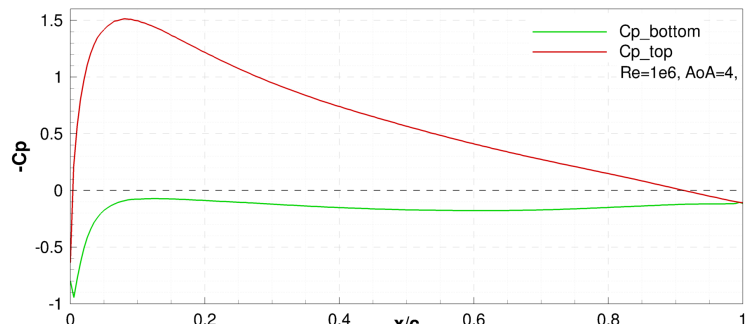
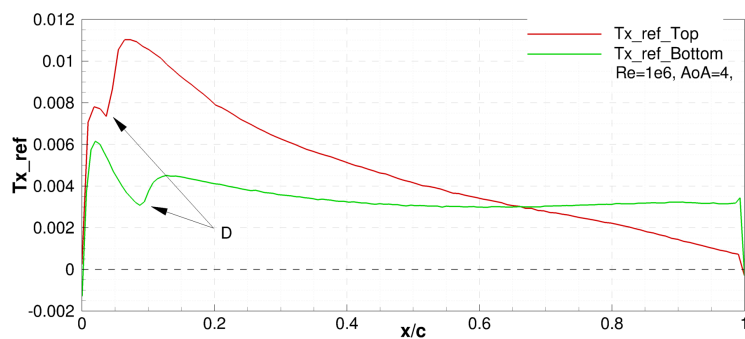
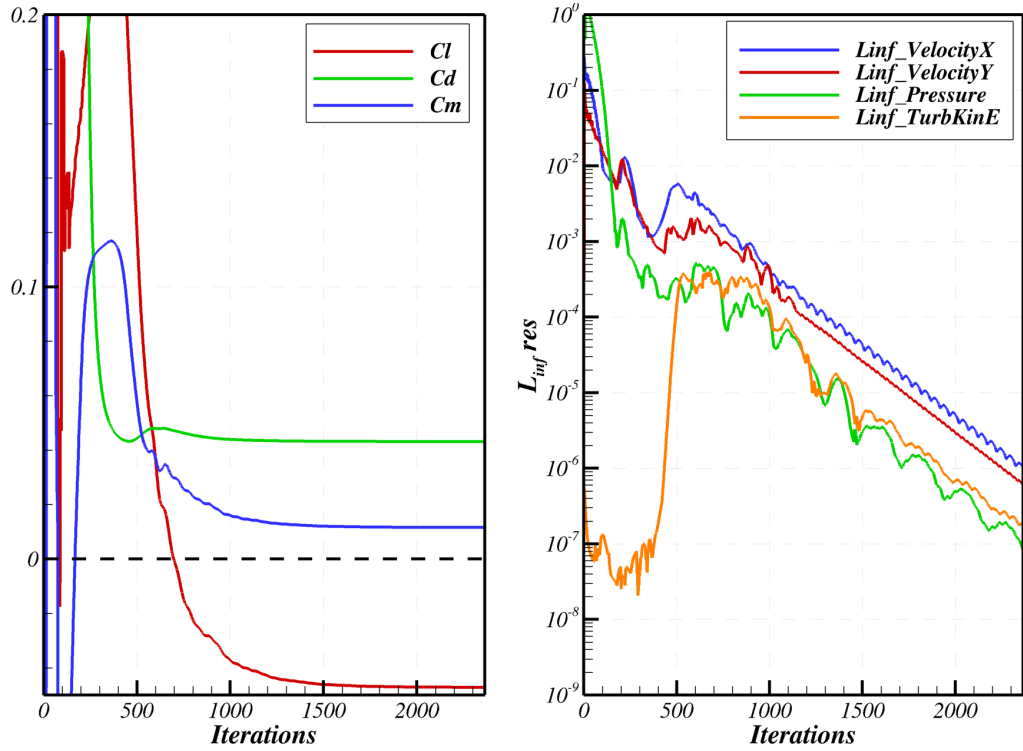
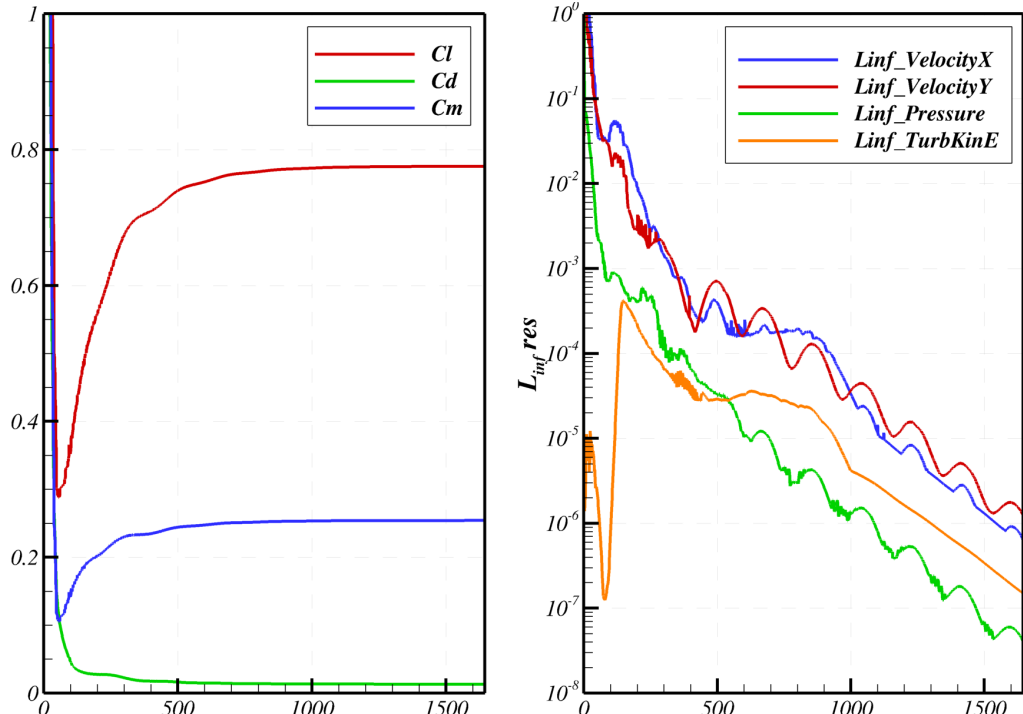
(a) Stream lines and normalized pressure C_p .(b) Normalized turbulence viscosity $\bar{\mu}_t = \mu_t / \mu_{lam}$.(c) Normalized pressure distribution C_p .(d) Normalized wall shear stress $\bar{\tau} = \tau_{wall} / q_\infty$.

Figure 5-2: Flow field characteristics for model-scale Reynolds number regime. $Re = 10^6$, $AoA = 0 \text{ deg}$.

(a) $Re = 10^4$, $AoA = 0$ deg, case.(b) $Re = 10^4$, $AoA = 0$ deg, case.**Figure 5-3:** TL_{∞} residual norms and C_l and C_d .

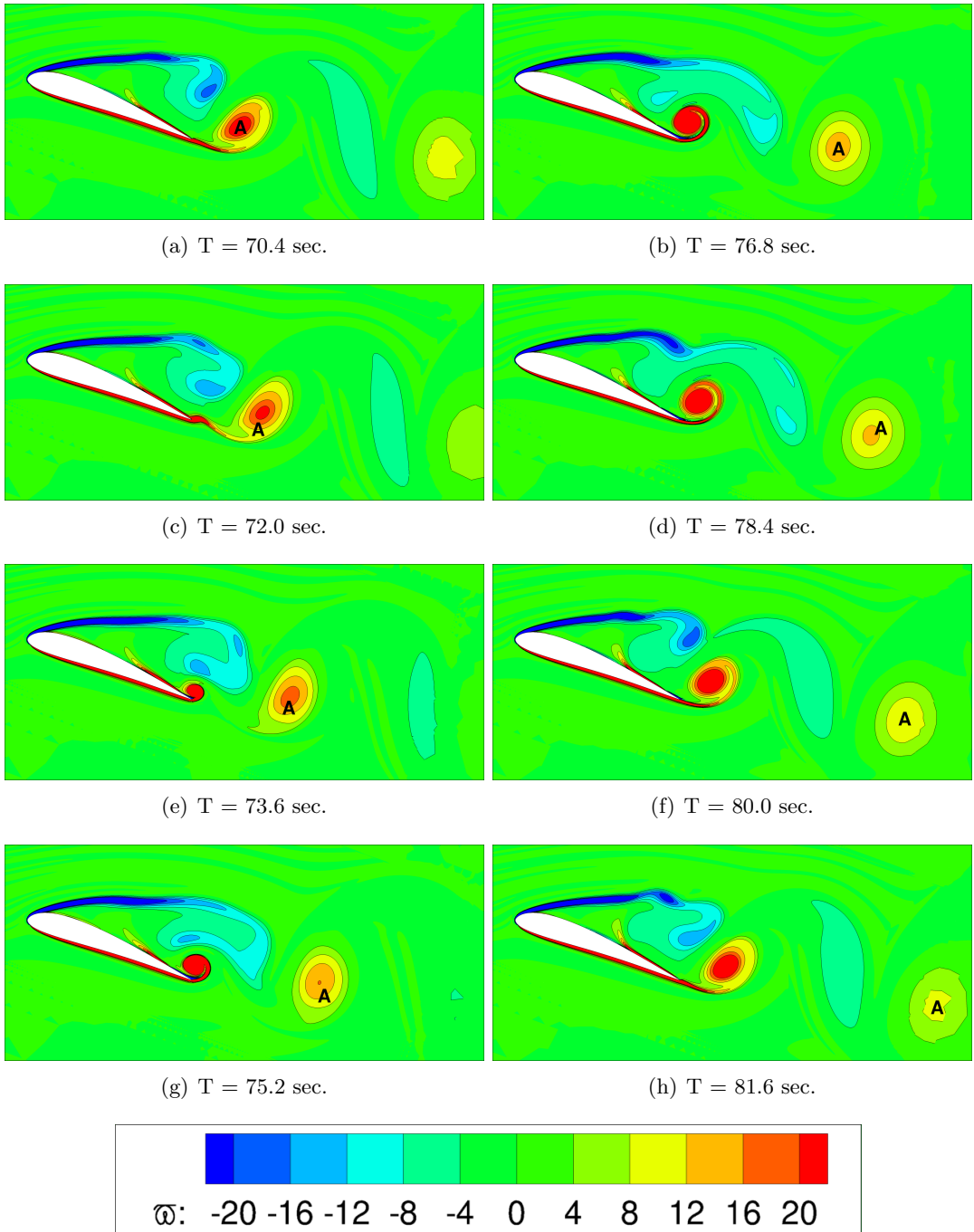


Figure 5-4: Vorticity $\bar{\omega}$ for $Re = 10^4$, $AoA = 20$ deg, for different time instants.

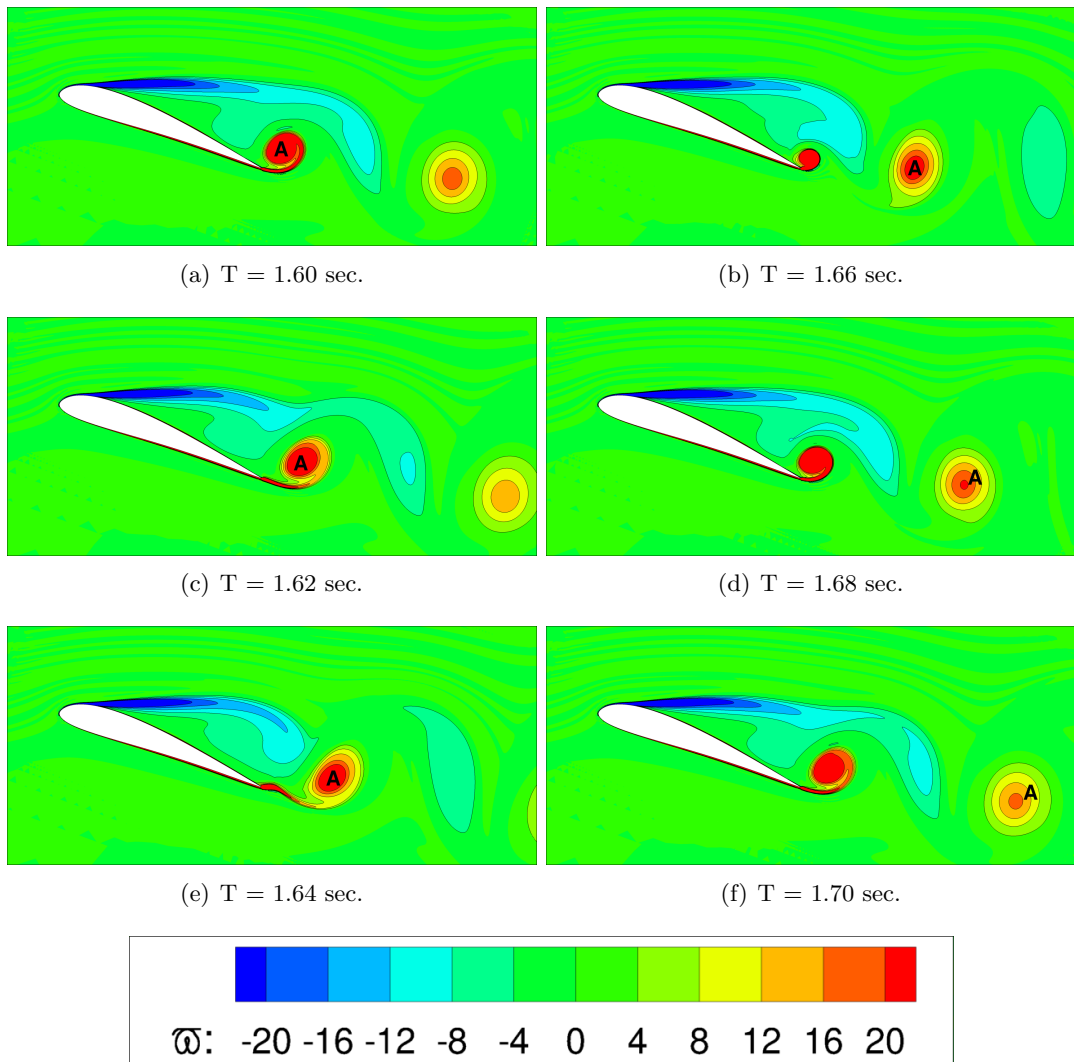


Figure 5-5: Vorticity $\bar{\omega}$ for $Re = 10^6$, $AoA = 20 \text{ deg}$, for different time instants.

$$St = \frac{fc \sin(\alpha)}{U_\infty}. \quad (5-3)$$

Table 5-1: Periodic characteristics at $AoA = 20 \text{ deg}$.

	Frequency [rad/s]	Period [s]	Strouhal no. [-]
$Re = 10^4$	0.087	11.44	0.198
$Re = 10^6$	11.00	0.09	0.251

For vortex shedding of cylinders Strouhal numbers (St) of $St = 0.20$ and $St = 0.267$ were found for Reynolds number regimes $Re < 10^5$ and $10^6 < Re < 3.5 \cdot 10^6$ respectively in [72]. Since these Strouhal numbers are not directly representative for airfoils, they are only used indicatively. Hence the results presented in table 5-1 are in reasonable agreement with these values (i.e. within 1.0 % and 6.5% for the $Re = 10^4$ and $Re = 10^6$ case respectively).

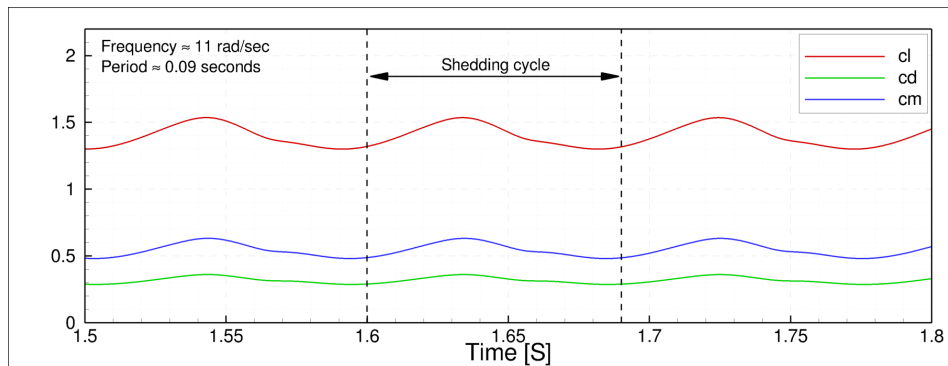
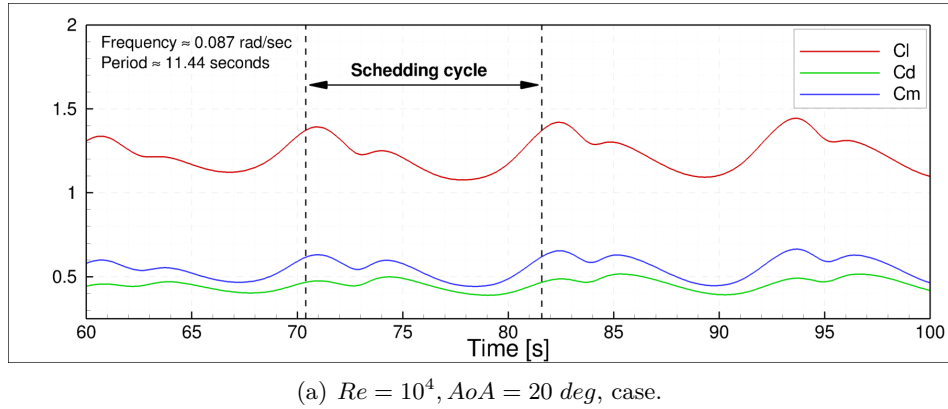


Figure 5-6: Time trace of lift, drag and moment coefficients for model- and full-scale Reynolds numbers.

A time-trace of C_l and C_d and a convergence plot of the L_∞ residual norms, both representative for the unsteady computations are presented in figure 5-7

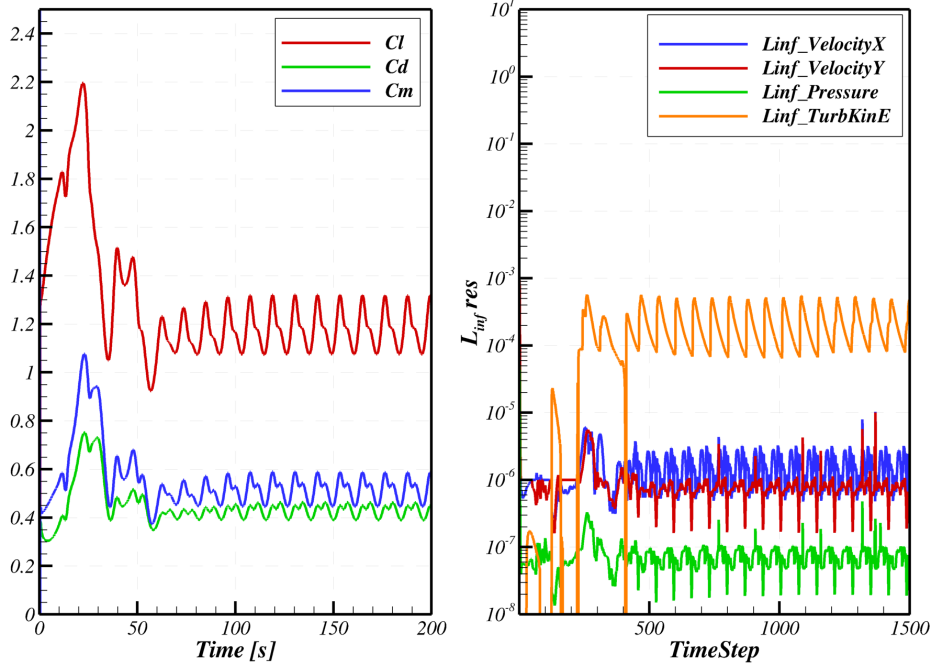


Figure 5-7: Time trace of lift, drag and moment coefficients for model-scale Reynolds number at $AoA = 20$ deg for $\Delta t = 1/6$ sec, and the L_∞ residual norms.

5-2 Domain Size Variation

After having shown the main characteristics of the flow field, a domain size study is performed in which various domain dimensions are compared in order to minimize the influence of the non-physical boundaries. A set of 15 domains have been analyzed with a radius ranging from 10 to 200 times the chord length. The following flow parameters have been analyzed for the set of domains,

- Reynolds numbers; 10^4 and 10^6 .
- Angles of attack; 0, 4, and 20 degrees.

For the extreme angles of attack, i.e. 20 degrees, the flow is fully separated and hence the Unsteady Reynolds Averaged Navier Stokes (URANS) solver of *ReFRESCO* is used. As a consequence of using the unsteady solver, the computations require large amounts of CPU power. Due to this requirement only three domains were analyzed for the 20 degree angle of attack case, i.e. domain radii of 10, 50 and 200 chord lengths.

The results of the steady computations will be discussed in section 5-2-1 followed by the unsteady results in section 5-2-2.

5-2-1 Steady Flow Calculations

The results of all the steady flow computations show a convergence of both C_l and C_d when the domain size is increased. An example is given for $AoA = 0$ degrees, $Re = 10^4$ in figure

5-8. The asymptotic behavior of the results for increasing domain radii presented in these graphs are representative for all cases analyzed.

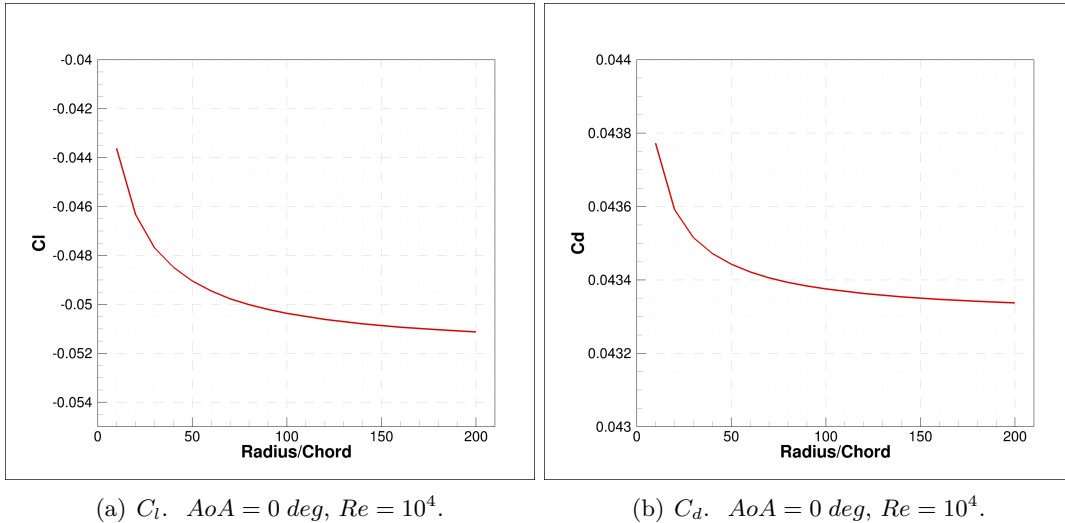


Figure 5-8: C_l and C_d for varying domain size and angle of attack.

The quantitative values (C_l and C_d) are presented in table 5-2. From this data it can be concluded that for the model-scale Reynolds number regime it is the lift coefficient that shows a high dependency on domain size, while for the full-scale Reynolds number it is the drag coefficient. This is also shown in figure 5-9, where C_l and C_d are plotted as a percentage of the C_l and C_d obtained for the largest domain.

The trend for the full-scale Reynolds number case is analogous to previous work presented in [67], where for a comparable Reynolds number a large domain dependence was found for C_d . This previous [67] work however does not cover model-scale Reynolds numbers used in the present study.

C_l at Model-Scale Reynolds Number ($Re = 10^4$) As observed before the flow at model-scale Reynolds numbers is sensitive to the size of the domain. This indicates that boundary conditions applied to the outer walls of the domain have a large influence on the solution.

For the flow at model-scale the influence of the boundary conditions is strongest for C_l (see table 5-2). To understand where this sensitivity originates from the lift coefficient is decomposed into a frictional and pressure part, $C_{l_{frict}}$ and $C_{l_{press}}$.

The result is presented in table 5-3. The decomposition in $C_{l_{frict}}$ and $C_{l_{press}}$ shows that the sensitivity in C_l is more severe at $Re = 10^4$ and originates mainly from the pressure component $C_{l_{press}}$, obviously. This can be explained by the more diffusive character at model-scale Reynolds numbers, which follows directly from the non-dimensional NS-equations (the diffusion terms contain Re^{-1}). As a consequence the flow disturbances are transported in all directions rather than in one main direction. The upper and lower pressure boundary will therefore have a larger influence on the airfoil surface when compared to the higher full-scale Reynolds number case.

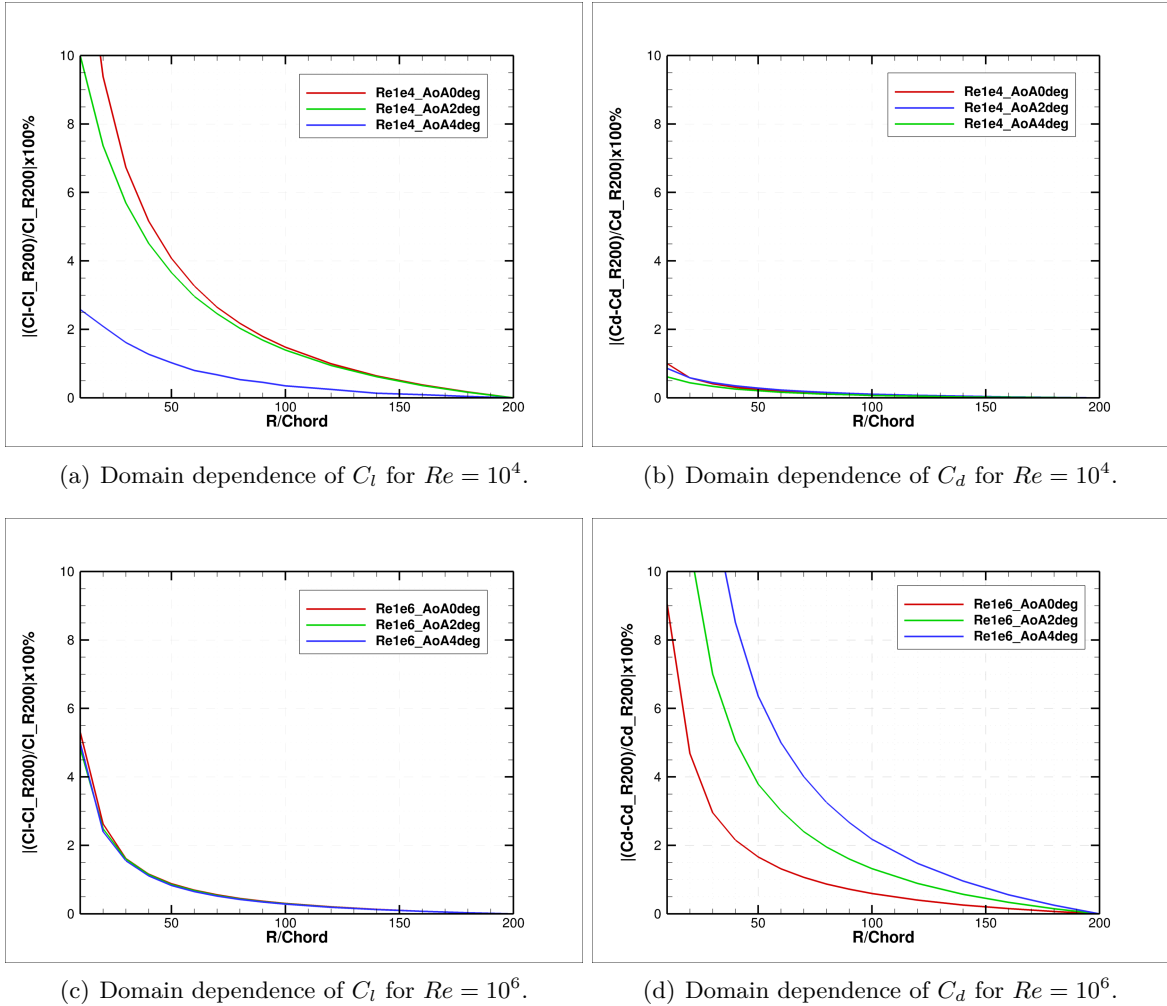


Figure 5-9: Domain dependence of C_l and C_d for varying Reynolds numbers and angles of attack.

Table 5-2: Domain size variation for various angles of attack and Reynolds number.

Domain $\frac{R}{c}$	C_l [-]	C_d [%]	C_l [-]	C_d [%]	Domain $\frac{R}{c}$	C_l [-]	C_d [%]	C_l [-]	C_d [%]
Flow case: $AoA = 0 \deg$ $Re = 10^4$									
10	-0.0436	14.68	0.0438	1.00	10	0.3263	5.30	0.0117	9.05
20	-0.0359	9.39	0.0436	0.59	20	0.3356	2.63	0.0112	4.69
30	-0.0477	6.73	0.0435	0.41	30	0.3390	1.62	0.0110	2.96
40	-0.0485	5.16	0.0435	0.31	40	0.3406	1.16	0.0109	2.16
60	-0.0494	3.27	0.0434	0.19	60	0.3422	0.69	0.0108	1.32
80	-0.0500	2.18	0.0434	0.13	80	0.3431	0.45	0.0108	0.87
100	-0.0504	1.48	0.0434	0.08	100	0.3436	0.30	0.0107	0.59
120	-0.0506	1.00	0.0434	0.06	120	0.3439	0.20	0.0107	0.40
160	-0.0509	0.38	0.0433	0.02	160	0.3444	0.07	0.0107	0.15
200	-0.0511	-	0.0433	-	200	0.3446	-	0.0107	-
Flow case: $AoA = 4 \deg$ $Re = 10^4$									
10	0.1791	2.58	0.0656	0.61	10	0.7352	4.98	0.0169	36.83
20	0.1782	2.09	0.0655	0.44	20	0.7552	2.40	0.0146	18.17
30	0.1774	1.62	0.0655	0.33	30	0.7618	1.55	0.0138	11.83
40	0.1768	1.27	0.0654	0.26	40	0.7652	1.11	0.0134	8.51
60	0.1760	0.80	0.0654	0.16	60	0.7687	0.65	0.0129	5.00
80	0.1755	0.53	0.0653	0.11	80	0.7705	0.42	0.0127	3.26
100	0.1759	0.35	0.0653	0.07	100	0.7716	0.28	0.0126	2.18
120	0.1748	0.25	0.0653	0.04	120	0.7723	0.19	0.0124	1.48
160	0.1747	0.09	0.0653	0.01	160	0.7732	0.07	0.0124	0.56
200	0.1746	-	0.0652	-	200	0.7738	-	0.0123	-
Flow case: $AoA = 4 \deg$ $Re = 10^6$									
10	0.3263	5.30	0.0117	9.05	10	0.7352	4.98	0.0169	36.83
20	0.3356	2.63	0.0112	4.69	20	0.7552	2.40	0.0146	18.17
30	0.3390	1.62	0.0110	2.96	30	0.7618	1.55	0.0138	11.83
40	0.3406	1.16	0.0109	2.16	40	0.7652	1.11	0.0134	8.51
60	0.3422	0.69	0.0108	1.32	60	0.7687	0.65	0.0129	5.00
80	0.3431	0.45	0.0108	0.87	80	0.7705	0.42	0.0127	3.26
100	0.3436	0.30	0.0107	0.59	100	0.7716	0.28	0.0126	2.18
120	0.3439	0.20	0.0107	0.40	120	0.7723	0.19	0.0124	1.48
160	0.3444	0.07	0.0107	0.15	160	0.7732	0.07	0.0124	0.56
200	0.3446	-	0.0107	-	200	0.7738	-	0.0123	-

As explained in section 2-3-1 the pressure over the airfoil surface is the main contribution to the lift. A slight change in pressure at the airfoil surface can therefore have a significant effect on the lift and thus C_l . Additionally this pressure change will alter the pressure gradient along the airfoil wall, which in turn can have a major effect on flow separation and the location of the separation point and therefore the lift coefficient.

The increased influence of the pressure boundary for model-scale Reynolds numbers results in a high domain size sensitivity for the lift coefficient, especially for separated flows.

Furthermore it must be noted that the magnitude of C_l is very small at these model-scale Reynolds numbers. A small variation in C_P will therefore result in a relatively large variation of C_l . This can also be observed in figure 5-9(a), where the dependence of C_l on the domain size will decrease for an increase in angle of attack.

This reduced dependence is a result of higher airfoil loadings and thus larger pressures. These large pressures at the airfoil are less sensitive to slight changes of the pressure due to the boundaries when changing the size of the domain.

C_d at Full-Scale Reynolds Number ($Re = 10^6$) Other than for the model-scale Reynolds number case, it is the drag coefficient that shows a strong dependence to domain size at higher Reynolds numbers. To get a better understanding of this sensitivity, the drag components i.e. frictional and pressure drag are presented non-dimensionally by, $C_{d_{frict}}$ and $C_{d_{press}}$ in table 5-4, as previously done in [67].

These results show that it is the frictional drag that is largely depending on domain size. This is also shown in figure 5-10, where the drag components are plotted as a function of domain size. In these graphs a large variation in $C_{d_{frict}}$ is only observed for the $Re = 10^6$ case.

For this condition there is no flow separation, the C_l values are larger, and for the larger Reynolds number convection becomes more important and therefore the character of the equations become less elliptical. Having in mind that $C_{d_{press}}$ barely changes with the domain size, the influence of the domain is mainly due to increase of the flow velocity V due to blockage: smaller domains, local $V \uparrow \Rightarrow C_{d_{frict}} \uparrow$.

5-2-2 Unsteady Flow

For the unsteady computations a suitable time step is chosen using the method described in section 3-4. In table 5-5 all the performed unsteady computations and corresponding flow characteristics are presented. In this table $\bar{\Delta t}$ represents the dimensionless time-step given by $\bar{\Delta t} = \Delta t V/c$. From these computations the time-averaged lift, drag and moment coefficients are obtained and compared.

As a result of the unsteady vortex shedding flow C_l , C_d , and C_m vary in time. In figure 5-11 the development in time of C_l , C_d , and C_m is presented. In this graph the effect of the initial conditions are clearly visible in the region indicated by **A**. In this region the flow field is developing until a steady cyclic behavior is reached (region **B**).

To make sure that the effects of the initial conditions have disappeared, several cycles are computed within region **B**. For the calculations used in this study a minimum of ten cycles in the cyclic region are computed. The final cycle is then used to compute the time average of the coefficients \bar{C}_l , \bar{C}_d , and \bar{C}_m .

Table 5-3: Lift components for domain size variation.

Domain $\frac{R}{c}$	C_l [-]	[%]	$C_{l_{frict}}$ [-]	[%]	$C_{l_{press}}$ [-]	[%]
$AoA = 0 \deg \quad Re = 10^4$						
10	$-4.36 \cdot 10^{-2}$	14.68	$3.58 \cdot 10^{-4}$	19.24	$-4.4 \cdot 10^{-2}$	14.8
20	$-3.59 \cdot 10^{-2}$	9.39	$3.36 \cdot 10^{-4}$	11.88	$-4.67 \cdot 10^{-2}$	9.26
30	$-4.77 \cdot 10^{-2}$	6.73	$3.25 \cdot 10^{-4}$	8.37	$-4.80 \cdot 10^{-2}$	6.65
40	$-4.85 \cdot 10^{-2}$	5.16	$3.19 \cdot 10^{-4}$	6.38	$-4.88 \cdot 10^{-2}$	5.10
60	$-4.94 \cdot 10^{-2}$	3.27	$3.12 \cdot 10^{-4}$	4.01	$-4.98 \cdot 10^{-2}$	3.23
80	$-5.00 \cdot 10^{-2}$	2.18	$3.08 \cdot 10^{-4}$	2.66	$-5.03 \cdot 10^{-2}$	2.15
100	$-5.04 \cdot 10^{-2}$	1.48	$3.07 \cdot 10^{-4}$	2.19	$-5.05 \cdot 10^{-2}$	1.71
120	$-5.06 \cdot 10^{-2}$	1.00	$3.04 \cdot 10^{-4}$	1.22	$-5.09 \cdot 10^{-2}$	0.98
160	$-5.09 \cdot 10^{-2}$	0.38	$3.01 \cdot 10^{-4}$	0.46	$-5.12 \cdot 10^{-2}$	0.38
200	$-5.11 \cdot 10^{-2}$	-	$3.00 \cdot 10^{-4}$	-	$-5.14 \cdot 10^{-2}$	-
$AoA = 4 \deg \quad Re = 10^6$						
10	$7.35 \cdot 10^{-1}$	4.98	$1.86 \cdot 10^{-4}$	19.86	$7.35 \cdot 10^{-1}$	4.98
20	$7.55 \cdot 10^{-1}$	2.40	$2.13 \cdot 10^{-4}$	7.99	$7.55 \cdot 10^{-1}$	2.40
30	$7.62 \cdot 10^{-1}$	1.55	$2.22 \cdot 10^{-4}$	4.42	$7.62 \cdot 10^{-1}$	1.55
40	$7.65 \cdot 10^{-1}$	1.11	$2.26 \cdot 10^{-4}$	2.74	$7.65 \cdot 10^{-1}$	1.11
60	$7.69 \cdot 10^{-1}$	0.65	$2.29 \cdot 10^{-4}$	1.15	$7.69 \cdot 10^{-1}$	0.65
80	$7.70 \cdot 10^{-1}$	0.42	$2.31 \cdot 10^{-4}$	0.50	$7.70 \cdot 10^{-1}$	0.42
100	$7.72 \cdot 10^{-2}$	0.28	$2.31 \cdot 10^{-4}$	0.22	$7.71 \cdot 10^{-1}$	0.28
120	$7.72 \cdot 10^{-1}$	0.19	$2.32 \cdot 10^{-4}$	0.10	$7.72 \cdot 10^{-1}$	0.19
160	$7.73 \cdot 10^{-1}$	0.07	$2.32 \cdot 10^{-4}$	0.01	$7.73 \cdot 10^{-1}$	0.07
200	$7.74 \cdot 10^{-1}$	-	$2.32 \cdot 10^{-4}$	-	$7.74 \cdot 10^{-1}$	-

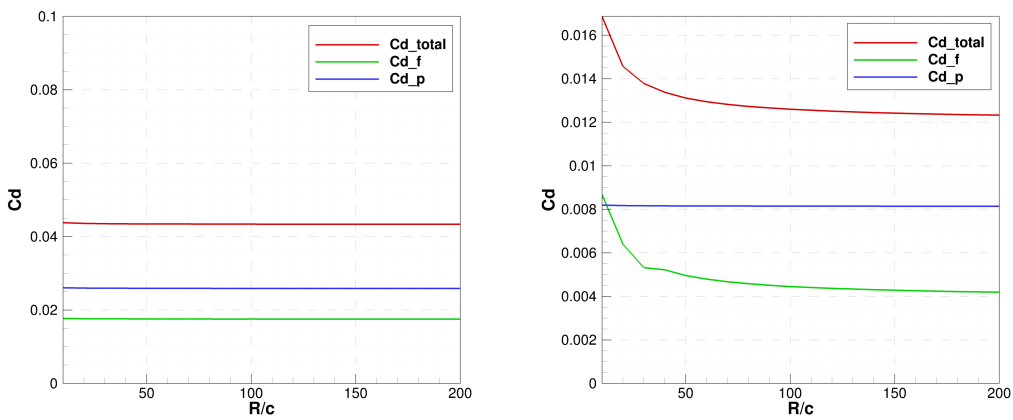
(a) Domain dependence of drag components for $AoA = 0, Re = 10^4$. (b) Domain dependence of drag components for $AoA = 4, Re = 10^6$.**Figure 5-10:** Domain dependence drag components for various flows.

Table 5-4: Drag components for domain size variation.

Domain $\frac{R}{c}$	C_d [-]	C_d [%]	$C_{d_{frict}}$ [-]	$C_{d_{frict}}$ [%]	$C_{d_{press}}$ [-]	$C_{d_{press}}$ [%]
<i>AoA = 0 deg Re = 10⁴</i>						
10	0.0438	1.00	0.0177	1.23	0.0261	0.85
20	0.0436	0.59	0.0176	0.73	0.0260	0.49
30	0.0435	0.41	0.0176	0.51	0.0259	0.34
40	0.0435	0.31	0.0176	0.39	0.0259	0.26
60	0.0434	0.19	0.0175	0.25	0.0259	0.16
80	0.0434	0.13	0.0175	0.16	0.0259	0.11
100	0.0434	0.08	0.0175	0.18	0.0259	0.07
120	0.0434	0.06	0.0175	0.08	0.0259	0.05
160	0.0433	0.02	0.0175	0.03	0.0258	0.02
200	0.0433	-	0.0175	-	0.0258	-
<i>AoA = 4 deg Re = 10⁶</i>						
10	0.0169	36.83	0.0087	107.17	0.0082	0.66
20	0.0146	18.17	0.0064	52.71	0.0082	0.39
30	0.0138	11.83	0.0053	27.09	0.0082	0.29
40	0.0134	8.51	0.0052	24.58	0.0082	0.23
60	0.0129	5.00	0.0048	14.40	0.0081	0.16
80	0.0127	3.26	0.0046	9.35	0.0081	0.12
100	0.0126	2.18	0.0044	6.24	0.0081	0.09
120	0.0124	1.48	0.0044	4.23	0.0081	0.06
160	0.0124	0.56	0.0043	1.59	0.0081	0.03
200	0.0123	-	0.0042	-	0.0081	-

Table 5-5: 2D unsteady domain size computations.

Domain size $\frac{R}{c}$	AoA [deg]	Reynolds number	Δt [s]	$\overline{\Delta t}$ [-]	CFL [-]
10	20,	10^4	$2.5 \cdot 10^{-1}$	0.0375	130
50	20,	10^4	$2.5 \cdot 10^{-1}$	0.0375	160
100	20,	10^4	$2.5 \cdot 10^{-1}$	0.0375	128
10	20,	10^6	$2 \cdot 10^{-4}$	0.003	54
50	20,	10^6	$2 \cdot 10^{-4}$	0.003	57
200	20,	10^6	$2 \cdot 10^{-4}$	0.003	57

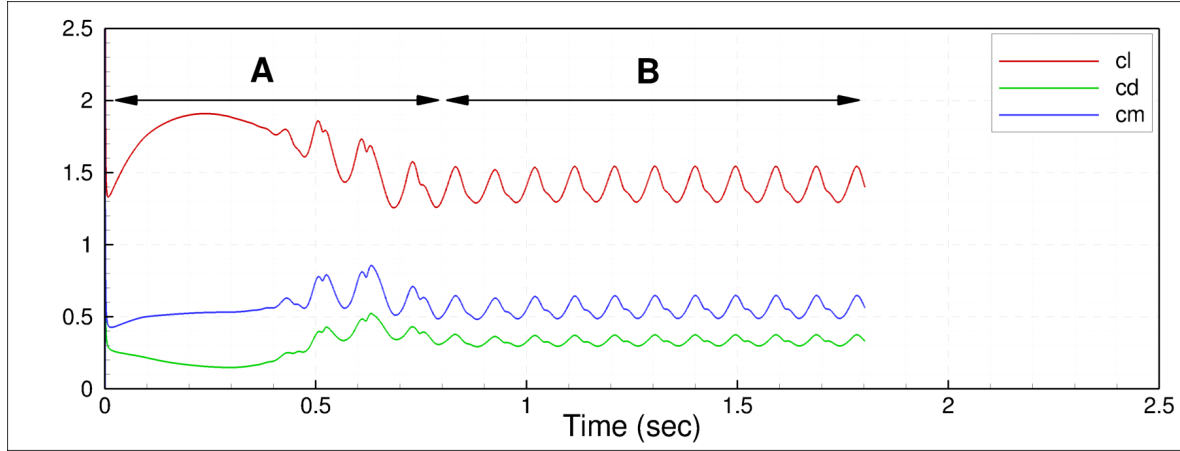


Figure 5-11: Development of lift, drag and moment coefficients for $Re = 10^6$, $AoA = 20 \text{ deg}$, $\Delta t = 2 \cdot 10^{-4} \text{ s}$.

Results The results for the unsteady domain size study are presented in table 5-6, where the average lift, drag and moment coefficients are given for three domains. These results show very little domain dependence, i.e. the results of the smallest domain differs from the $R = 200c$ results by a maximum of 3.13%. The trend of reduced domain size dependency for unsteady results presented in table 5-6 is in accordance with the steady computations, where the domain dependency is reduced for increasing angles of attack. Furthermore there are no extra dependency issues due to the unsteadiness of the flow.

Table 5-6: Average lift, drag and moment coefficients for the computed unsteady flow.

Domain Size $\frac{R}{c}$	\bar{C}_l [-]	\bar{C}_d [%]	\bar{C}_m [-]	\bar{C}_m [%]
Flow Case $AoA = 20 \text{ deg}$ and $Re = 10^4$				
10	1.236	0.53	0.457	1.37
50	1.235	0.41	0.454	0.77
200	1.230	-	0.450	-
Flow Case $AoA = 20 \text{ deg}$ and $Re = 10^6$				
10	1.401	0.38	0.319	-3.13
50	1.400	0.25	0.332	0.97
200	1.396	-	0.329	-

Additionally the lift, and drag coefficients for both the full- and model-scale Reynolds number regime are presented graphically in figure 5-12.

5-2-3 Final Remark

When the results of the domain size study are reviewed, it can be concluded that the influence of the domain size is most dominant for the steady flow computations.

The boundary conditions at model-scale Reynolds numbers mainly affect C_l of the airfoil,

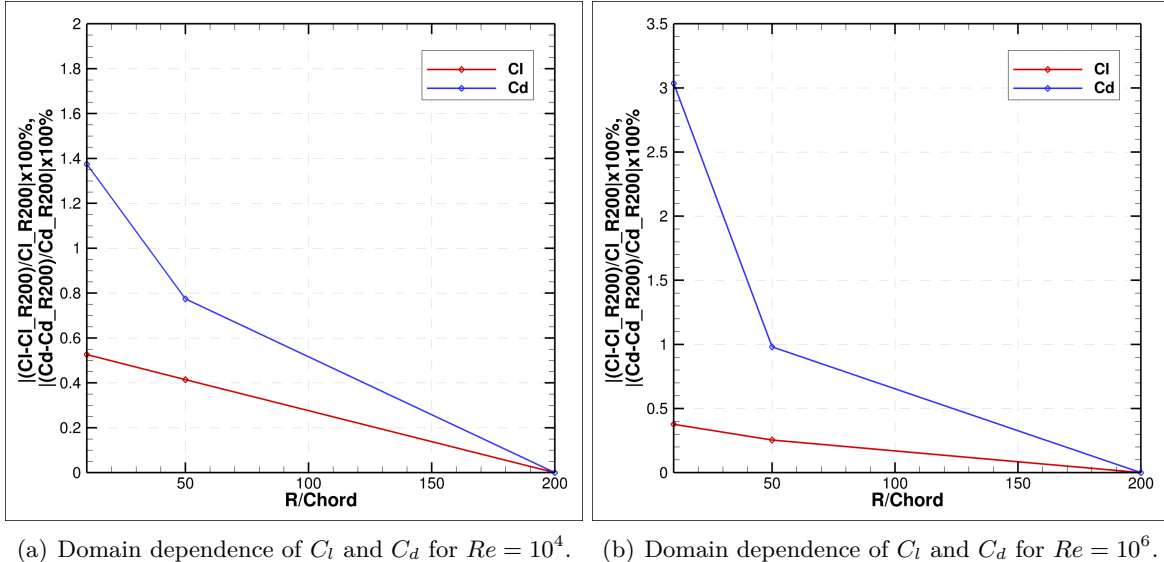


Figure 5-12: Domain dependence of Cl and Cd for unsteady computations.

while at full-scale Reynolds numbers it is mainly C_d that is affected, which was also shown in a previous study [67].

Following the observations a domain size of $100 c/R$ is selected for the remainder of this thesis. For this domain C_l and C_d typically differ less than 2.2 percent from the coefficients found for the $200 c/R$ domain for all conditions and the influence of the boundary conditions is considered negligible.

5-3 Numerical Uncertainty Study

In this study a set of seven grids are analyzed with a total number of cells varying between $363K$ and $1.43M$. The grids are analyzed using the following flow parameters,

- Reynolds numbers; 10^4 and 10^6 .
- Angles of attack; 0, 4, and 20 degrees.

Analogously to the domain size study, the 20 degree angle of attack case for the model-scale Reynolds numbers were computed using the URANS solver of *ReFRESCO*. For the unsteady calculations only four grids where computed due to the required CPU time for unsteady calculations.

5-3-1 Geometric Similarity

As explained in section 2-5 the grid uncertainty study requires geometrically similar grids. Generating a set of grids using *HEXPRESS* while maintaining geometric similarity is complicated, if not impossible. *HEXPRESS* implements a grid optimization procedure which

alters the grid geometry near domain walls to enhance the grid quality. As a consequence the geometric similarity between consecutive grid refinements is not maintained. In figures 5-13 and 5-14, a fine and coarse grid near the trailing edge of the airfoil section are presented. It can be seen from these figures that the grids are non-geometrically similar especially near the airfoil wall. Far away from the airfoil surface, e.g. at the top right corner of figure 5-13, both grids present better geometric similarity.

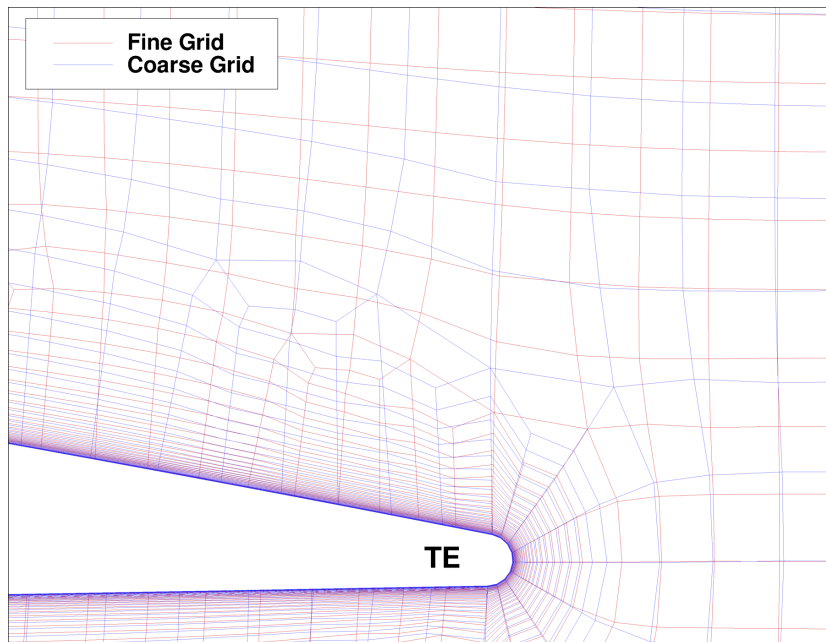


Figure 5-13: Coarse and fine grid at the airfoil trailing edge (TE).

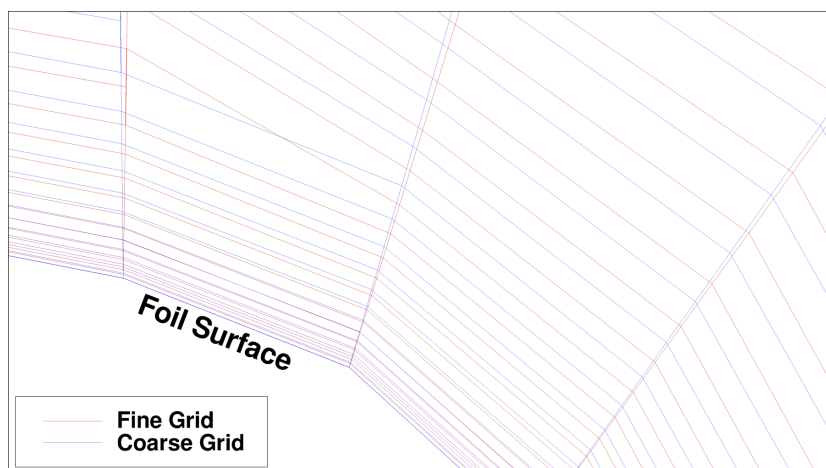


Figure 5-14: Coarse and fine grid at the viscous layer refinement.

5-3-2 Grid Characteristics

In table 5-7 the characteristics of the grid set is presented. Refining the grid is accomplished by increasing the initial cell size within *HEXEXPRESS*. The refinement zones located near the airfoil section as described in section 4-1 will automatically be refined according to the expressions,

$$c_i = \frac{C_i}{2^{n_i}}, \quad \frac{C_i}{c_i} = 2^{n_i}, \quad n_i = \frac{\ln(C_i/c_i)}{\ln(2)}, \quad (5-4)$$

where C_i is the initial cell size, c_i the refined cell size, and n_i the number of refinements applied to obtain the refined cells.

When refining the grids the viscous layer near the airfoil surface is also reduced in size, while maintaining the ratio between the initial cell size and the wall cell height. By doing so the geometric similarity between the grids is maintained "as much as possible". As a consequence the y^+ will, as expected, decrease when the grid is refined, as can be seen in figure 5-15, where the y^+ values of all grids are presented for $Re = 10^6$.

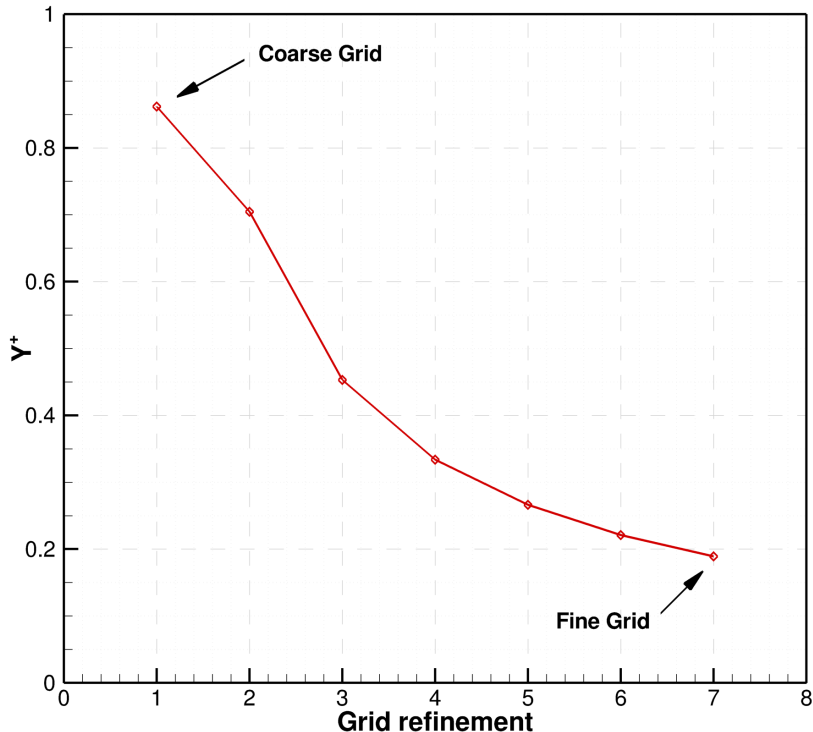


Figure 5-15: y^+ of the grid set for $Re = 10^6$.

As expected, the orthogonality and skewness properties presented in table 5-7 are improving when the grid resolution is increased (i.e. *orthogonality* $\rightarrow 90$ and *skewness* $\rightarrow 0$).

Table 5-7: Grid properties of grid refinement study.

Grid refinement	1	2	3	4	5	6	7
Total no. Cells	36339	128064	276016	479686	739454	1055265	1427023
Min. Orthogonality	37.938	36.247	38.718	39.248	39.347	37.212	37.812
Avg Orthogonality	89.199	89.616	89.733	89.805	89.845	89.866	89.887
Max. Skewness	0.6844	0.682	0.649	0.642	0.638	0.654	0.646
Ref. ratio	6.27	3.34	2.27	1.72	1.39	1.16	1.00

5-3-3 Iterative Error

Before starting with the analysis of the discretization error the iterative error is studied. For this study the method presented in section 2-5 is applied for all the grids presented in table 5-7. First the steady case is discussed followed by the unsteady case.

Steady computations The fluctuations of the lift, drag and moment coefficients of the last 200 iterations as well as the L_∞ -norm of the residuals are presented in table 5-8. Other than the computations marked in red the solutions are sufficiently converged such that the fluctuations of the integral quantities and the L_∞ -norm of the residuals are small. For the integral quantities the fluctuations are less than 10^{-3} percent, given by equation (2-80).

The computations marked in red did not converge to a steady solution. This is due to the fact that for finer grids highly separated flow tries to shed vortices and unsteady computations are needed. The computations for which convergence is not reached are for the least steady case i.e. $AoA = 4 \text{ deg}$ at $Re = 10^4$.

According to the theory, iterative errors can be neglected when they are at least two to three orders below the discretization error. This means that the iterative error for the data presented in table 5-8 can be assumed negligible when the numerical uncertainty is at least one percent. If this does not hold the maximum number of iterations must be increased.

Unsteady computations For the unsteady computations the integral quantities such as C_l , C_d , and C_m are varying in time. In this case the average values of these integral quantities need to be monitored. To make sure that the influence of the initial condition is negligibly small, a minimum of ten cycles in the cyclic range (indicated by **B** in figure 5-11) are computed. For the finest grid the average lift drag and moment coefficients of the last five cycles in the cyclic range are presented in table 5-9. The difference between the last 5 cycles is typically below one percent. The differences presented in 5-9 are representative for all computed grids.

Other than the cyclic behavior of C_l , C_d , and C_m the iterative errors need to be minimized. For the unsteady case the L_∞ norm of the residuals are all below 10^{-6} , for which the iterative error per time step can be assumed negligible.

5-3-4 Discretization Error

As previously mentioned an effort is made to generate a set of grids which resemble geometric similarity as much as possible. This is done in an attempt to use the numerical uncertainty

Table 5-8: Iterative convergence and error.

Grid no.	Grid ref. $\frac{h_i}{h_1}$	n_{iter}	L_2 residuals	L_∞ residuals	Fluctuations, last 200 iters		
			$\max(u.v, p)$	$\max(u.v, p)$	$100 \times \max(\phi_i - \phi_{end} / \phi_{end})$	C_l	C_d
Flow Case $AoA = 0$ deg and $Re = 10^4$							
1	6.27	1286	$1.5 \cdot 10^{-11}$	$9.9 \cdot 10^{-10}$	0.001	0.001	0.001
2	3.34	1200	$1.9 \cdot 10^{-10}$	$9.8 \cdot 10^{-9}$	0.001	0.001	0.001
3	2.27	1414	$4.5 \cdot 10^{-10}$	$9.9 \cdot 10^{-9}$	0.001	0.001	0.001
4	1.72	1872	$3.8 \cdot 10^{-10}$	$9.8 \cdot 10^{-9}$	0.001	0.001	0.001
5	1.39	2247	$3.9 \cdot 10^{-10}$	$9.9 \cdot 10^{-9}$	0.001	0.001	0.001
6	1.16	2766	$3.9 \cdot 10^{-10}$	$9.8 \cdot 10^{-9}$	0.001	0.001	0.001
7	1.00	3496	$2.8 \cdot 10^{-10}$	$9.9 \cdot 10^{-9}$	0.001	0.001	0.001
Flow Case $AoA = 4$ deg and $Re = 10^4$							
1	6.27	1861	$2.7 \cdot 10^{-11}$	$3.6 \cdot 10^{-9}$	0.001	0.001	0.001
2	3.34	1421	$1.6 \cdot 10^{-8}$	$9.8 \cdot 10^{-7}$	0.001	0.001	0.001
3	2.27	3823	$1.7 \cdot 10^{-8}$	$9.9 \cdot 10^{-7}$	0.001	0.001	0.001
4	1.72	2762	$4.3 \cdot 10^{-9}$	$9.9 \cdot 10^{-8}$	0.001	0.001	0.001
5	1.39	5000	$5.2 \cdot 10^{-10}$	$1.1 \cdot 10^{-8}$	0.001	0.001	0.001
6	1.16	8953	$1.0 \cdot 10^{-4}$	$1.6 \cdot 10^{-3}$	14.03	0.35	6.00
7	1.00	898	$1.7 \cdot 10^1$	$7.9 \cdot 10^3$	278.54	66.14	214.93
Flow Case $AoA = 0$ deg and $Re = 10^6$							
1	6.27	2236	$2.5 \cdot 10^{-10}$	$9.9 \cdot 10^{-9}$	0.001	0.001	0.001
2	3.34	2064	$7.6 \cdot 10^{-9}$	$9.9 \cdot 10^{-7}$	0.001	0.001	0.001
3	2.27	2687	$8.3 \cdot 10^{-9}$	$9.6 \cdot 10^{-7}$	0.001	0.001	0.001
4	1.72	2063	$8.0 \cdot 10^{-9}$	$9.9 \cdot 10^{-7}$	0.001	0.001	0.001
5	1.39	2126	$1.6 \cdot 10^{-10}$	$9.9 \cdot 10^{-9}$	0.001	0.001	0.001
6	1.16	2249	$1.2 \cdot 10^{-10}$	$1.1 \cdot 10^{-8}$	0.001	0.001	0.001
7	1.00	1994	$2.0 \cdot 10^{-9}$	$9.8 \cdot 10^{-8}$	0.001	0.001	0.001
Flow Case $AoA = 4$ deg and $Re = 10^6$							
1	6.27	1926	$4.0 \cdot 10^{-11}$	$3.6 \cdot 10^{-9}$	0.001	0.001	0.001
2	3.34	1841	$1.1 \cdot 10^{-8}$	$9.9 \cdot 10^{-7}$	0.001	0.001	0.001
3	2.27	2368	$8.5 \cdot 10^{-9}$	$9.9 \cdot 10^{-7}$	0.001	0.001	0.001
4	1.72	1521	$9.7 \cdot 10^{-11}$	$9.9 \cdot 10^{-9}$	0.001	0.001	0.001
5	1.39	1982	$9.4 \cdot 10^{-10}$	$9.8 \cdot 10^{-8}$	0.001	0.001	0.001
6	1.16	2316	$1.2 \cdot 10^{-10}$	$9.8 \cdot 10^{-9}$	0.001	0.001	0.001
7	1.00	2279	$4.5 \cdot 10^{-10}$	$2.2 \cdot 10^{-8}$	0.001	0.001	0.001

Table 5-9: Average lift of the final 5 cycles for $AoA = 20 \text{ deg}$ and $Re = 10^4$.

Shedding Cycle	\bar{C}_l	% Of last
Grid 5, $\Delta t = 0.08333 \text{ sec}$, $\bar{\Delta t} = 0.0125$		
1 (5^{th} to last)	1.23998	-0.624
2	1.21924	1.059
3	1.23021	0.169
4	1.23684	-0.369
5 (Last)	1.23229	-

theory presented in section 2-5. First, the standard definition for the typical grid cell size is used followed by the alternative methods, as presented in section 2-5. As explained the numerical uncertainty contains the round-off, iterative, and discretization error. In the two-dimensional case however the round-off and iterative errors are reduced such that they can be assumed negligible. The uncertainties presented in the following section are therefore only due to the discretization error.

Standard Method First the standard description for the typical cell size given by equation (2-88) is used. The numerical uncertainty is estimated for the lift, drag and moment coefficients. The resulting numerical uncertainty graphs for all steady computations are presented in figures 5-16 and 5-17. As expected for a set of unstructured grids the results of the uncertainty analysis show large variations in the numerical uncertainty of the specific flow cases. The following trends can be seen:

- The numerical uncertainty of C_l for the $AoA = 0 \text{ deg}$, $Re = 10^4$ flow case is 18.62% as compared to an uncertainty of only 6.64% for the $AoA = 4 \text{ deg}$, $Re = 10^4$ case. Furthermore large differences are observed for the uncertainty estimation of different quantities for a single flow case. For example the uncertainty of C_l for the $AoA = 0 \text{ deg}$, $Re = 10^4$ flow case is 18.62%, whereas 1.35% for C_d .
- To further investigate the effect of grid refinements on the C_l , C_d , and C_m , the magnitudes of these quantities are compared and presented in table 5-10 as the difference in percentage between the solution of the respective grid and the solution of the finest grid. Note that for the two finest grids no steady converged solution is obtained for the $AoA = 4 \text{ deg}$, $Re = 10^4$ flow case.
- The magnitude of all flow quantities show a converging trend when refining the grid. This is true for all flow cases. When the differences in C_l , C_d and C_m for the two finest grids are compared a maximum difference of less than 2% is found.
- Since the differences of C_l , C_d , and C_m are converging to a constant value, and the iterative errors being of small order (10^{-8} and below), it is expected that the large uncertainty estimations previously mentioned are caused by the implementation of unstructured grids combined with the unsteady separated flows, making the uncertainty estimation challenging. This is also observed in previous studies by others, e.g. [42].

- In addition, for the $AoA = 4\text{deg}$, $Re = 10^4$ flow case, convergence is not reached for the two finest grids. As a consequence the uncertainty estimation for this flow case is based on the five coarsest grids only, which affects the uncertainty estimation negatively.
- The general trend observed for all flow cases show the largest estimated uncertainty for integral quantity C_m , followed by C_l and finally the smallest uncertainties are estimated for C_d . Note however that this trend was not observed for the $AoA = 4\text{deg}$, $Re = 10^4$, which is likely caused by the unsteady, largely separated flow as previously explained.

Table 5-10: lift drag and moment coefficients for analyzed flow cases

Grid no.	$\frac{h_i}{h_1}$	C_l [-]	U_ϕ [%]	C_d [-]	U_ϕ [%]	C_m [-]	U_ϕ [%]
Flow Case $AoA = 0 \text{ deg}$ and $Re = 10^4$							
1	6.27	-0.0363	23.01	-	0.0445	3.10	-
2	3.34	-0.0343	27.35	128.32	0.0431	0.15	2.51
3	2.27	-0.0446	5.42	49.19	0.0432	0.08	1.45
4	1.72	-0.0472	0.19	29.10	0.0433	0.26	2.08
5	1.39	-0.0467	0.87	18.62	0.0433	0.26	1.35
6	1.16	-0.0479	1.67	13.45	0.0432	0.17	1.05
7	1.00	-0.0472	-	12.73	0.0431	-	1.82
Flow Case $AoA = 0 \text{ deg}$ and $Re = 10^6$							
1	6.27	0.5066	47.26	-	0.0104	6.85	-
2	3.34	0.3542	2.96	18.58	0.0116	3.99	12.67
3	2.27	0.3519	2.30	17.47	0.0113	1.29	6.27
4	1.72	0.3502	1.79	15.15	0.0112	0.64	3.59
5	1.39	0.3476	1.04	13.17	0.0112	0.26	2.40
6	1.16	0.3451	0.32	11.67	0.0112	0.13	1.75
7	1.00	0.3440	-	10.33	0.0112	-	1.35
Flow Case $AoA = 4 \text{ deg}$ and $Re = 10^4$							
1	4.51	0.2290	28.82	-	0.0677	5.16	-
2	2.40	0.1850	4.04	16.5	0.0641	0.44	15.51
3	1.64	0.1783	0.32	8.76	0.0637	1.10	17.44
4	1.24	0.1769	0.48	5.38	0.0641	0.42	15.83
5	1.00	0.1778	-	4.17	0.0644	-	13.97
6	-	-	-	-	-	-	-
7	-	-	-	-	-	-	-
Flow Case $AoA = 4 \text{ deg}$ and $Re = 10^6$							
1	6.27	0.7972	2.82	-	0.0148	13.13	-
2	3.34	0.7899	1.88	10.46	0.0136	3.46	11.42
3	2.27	0.7854	1.30	9.18	0.0133	1.06	5.61
4	1.72	0.7827	0.95	7.75	0.0132	0.36	3.34
5	1.39	0.7796	0.55	6.64	0.0131	0.04	2.24
6	1.16	0.7769	0.21	5.79	0.0131	0.05	1.56
7	1.00	0.7753	-	5.12	0.0131	-	1.36

Alternative Methods In an effort to improve the uncertainty estimation, the uncertainty analysis is performed using alternative methods to describe the typical grid cell size, as presented in section 2-5.

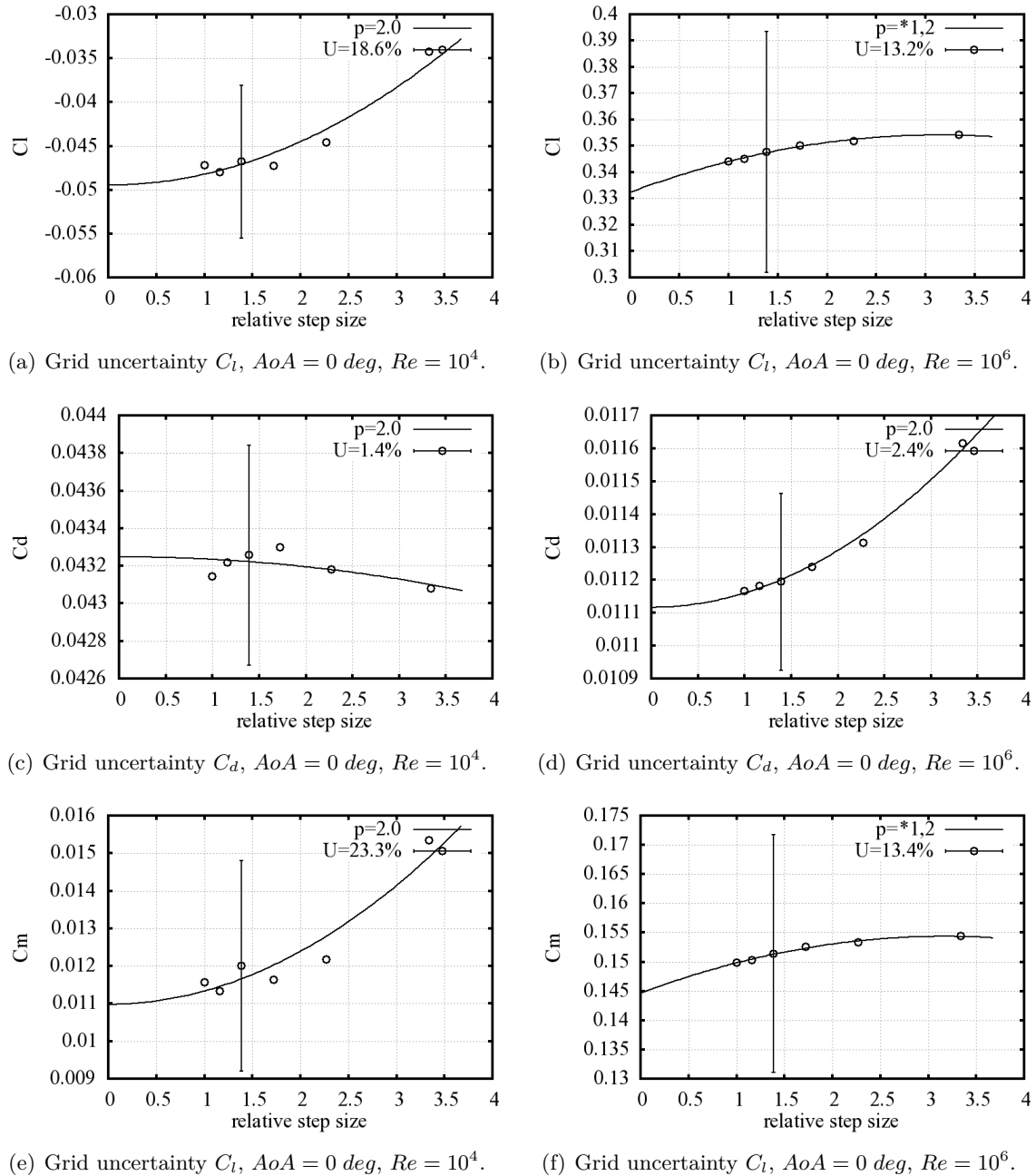


Figure 5-16: Grid uncertainty for the lift, drag, and moment coefficients, $AoA = 0 \text{ deg}$, $Re = 10^4, 10^6$.

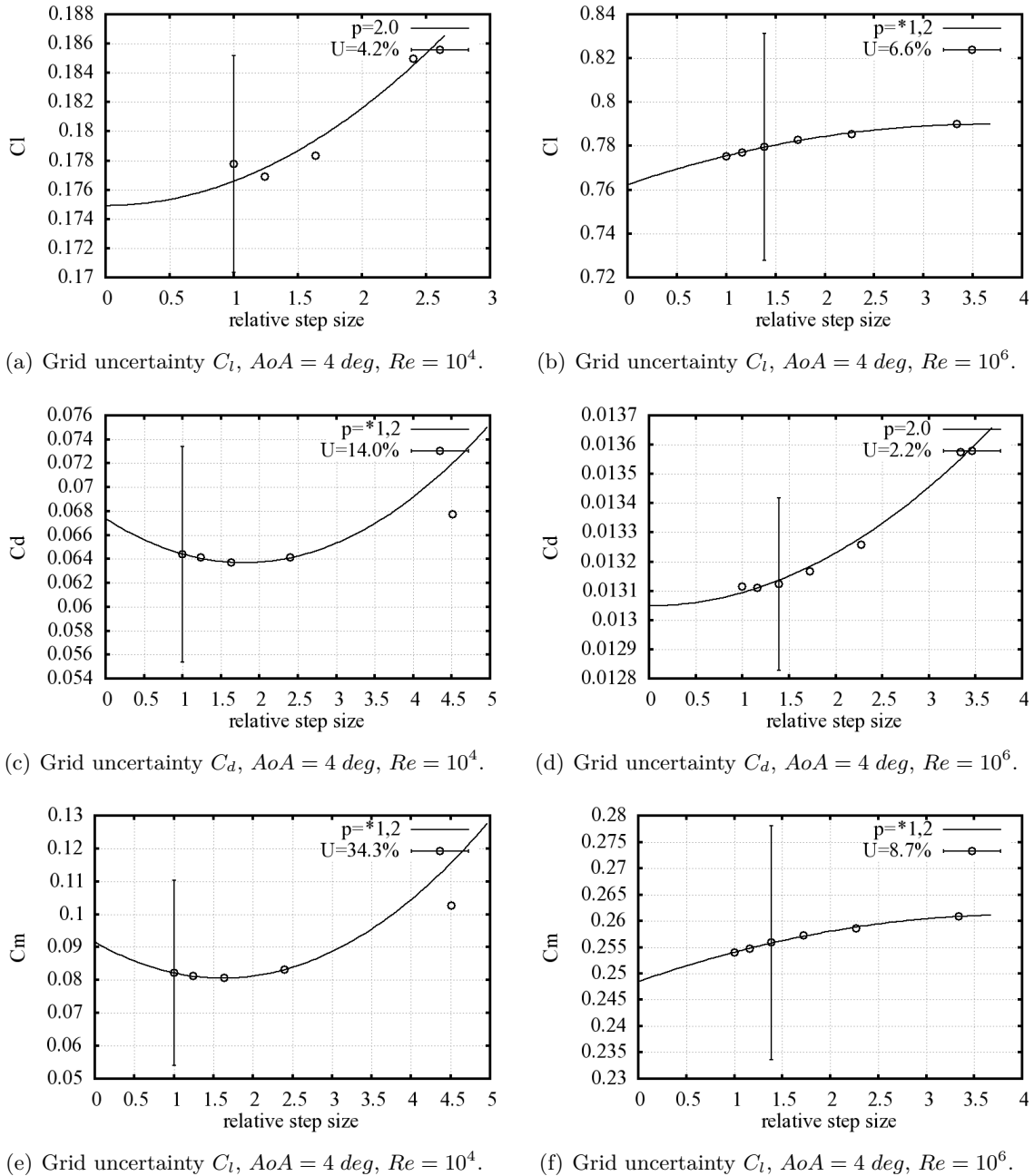
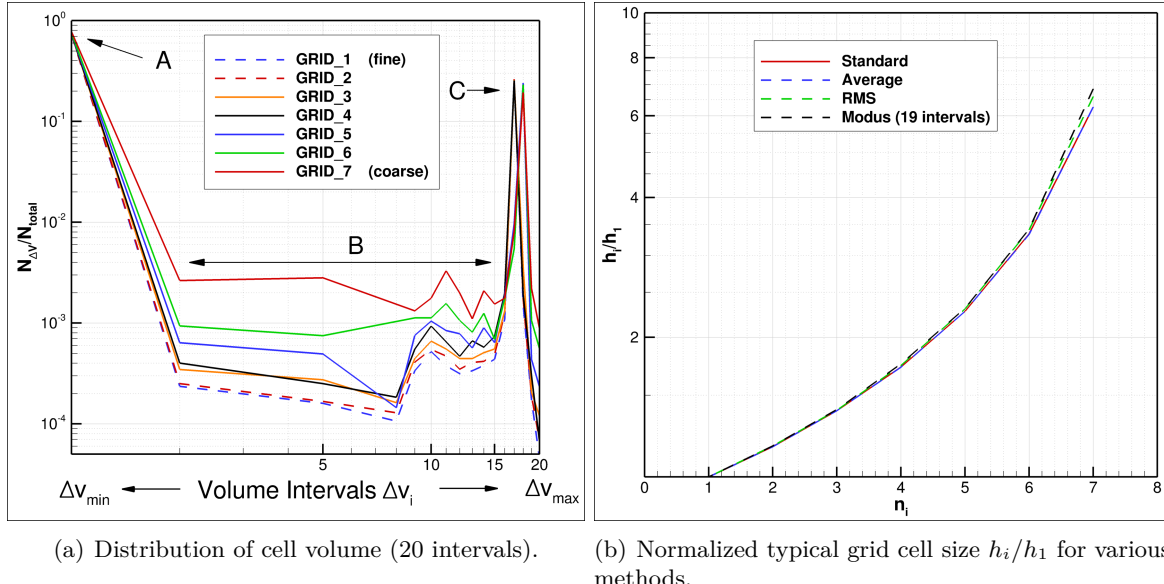


Figure 5-17: Grid uncertainty for the lift, drag, and moment coefficients, $AoA = 4 \text{ deg}$, $Re = 10^4, 10^6$.

The first two methods given by equations (2-92) and (2-93), are straight forward and not further discussed, the third method is based on the mode of the cell volumes and first requires an analysis of the grid cell volumes.

In figure 5-18(a) the cell volume distribution is presented for the complete set of grids. The graphs are obtained by subdividing the volume interval between the maximum and minimum cell volume (ΔV_{max} , ΔV_{min}) into 20 equidistant intervals. Subsequently the number of cells of the grid contained within the respective volume interval $N_{\Delta V}$ is plotted as a fraction of the total number of cells N_{Total} .



(a) Distribution of cell volume (20 intervals).

(b) Normalized typical grid cell size h_i/h_1 for various methods.

Figure 5-18: **Left:** Distributions of cell volumes in the computational domain. **Right:** Typical grid cell size based on various methods.

The distributions in 5-18(a) show three distinct regions for all grids, indicated by **A**, **B**, or **C**. The peaks at **A** indicate the presence of a large number cells with a cell volume equal or close to the smallest cell volume present in the domain. This peak represents the large number of cells located in the refinement box and near wall refinement region (see figure 4-5 and 5-13).

Furthermore the peaks marked by **C** indicate a large number of grid cells with a large cell volume. These peaks represent the large number of cells located outside the refinement box.

Finally region **B** contains a much smaller number of grid cells, having a volume larger than those in the refinement box yet smaller than the cells outside the refinement box, hence **B** represents the cells in the transition region between the refinement box and the unrefined region.

When the distributions of cell volumes for the various refinements given by figure 5-18(a) are compared, the modes are all within the smallest volume interval. This implies that the cells within the refinement box are representative for the typical grid cell size.

The effect of implementing the different methods of describing h_i is presented in figure 5-18(b), where h_i/h_1 is plotted for all grids. $n_i = 1$ and $n_i = 7$ represent the finest and coarsest grid respectively. The differences of h_i/h_1 between different methods, as presented in figure

5-18(b), are only small. The typical grid cell size ratio for various methods is also given in table 5-11.

Table 5-11: Typical grid cell size h_i/h_1 obtained using alternative methods.

Grid no.	Standard	Average	RMS	Mode
1	6.267	6.269	6.603	6.856
2	3.338	3.332	3.406	3.421
3	2.274	2.274	2.302	2.309
4	1.725	1.723	1.738	1.752
5	1.389	1.389	1.393	1.396
6	1.163	1.162	1.166	1.166
7	1.000	1.000	1.000	1.000

The corresponding uncertainty estimations for $AoA = 4 \deg$ $Re = 10^6$, using the alternative descriptions of h_i/h_1 are given in table 5-12. It can be seen that for the grid set considered the alternative definitions of the typical grid cell size result in uncertainty estimations close to the standard method. This trend is representative for all flow cases.

Despite the small differences between the proposed methods this approach could be useful for uncertainty estimations when using unstructured grids. The difference in estimated uncertainties between the various methods could perhaps be used in future studies as an indication of the geometric similarity of the computed grids.

Additionally the number of volume intervals used in the determination of the cell volume mode could have an influence on the uncertainty estimation when using this particular method. More research on this specific topic is however needed.

Table 5-12: Uncertainty estimation for various typical grid cell size definitions.

	Standard	Average	RMS	Mode
U_{C_l}	8.31%	8.31%	8.21%	8.03%
U_{C_d}	1.76%	1.76%	1.72%	1.70%
U_{C_m}	10.87%	10.87%	10.74%	10.50%

Unsteady computations For the unsteady computations an uncertainty estimation is performed according to the method described in section 2-5. In this case not only grid resolution but also the time-step size is varied. In total, 4 different grids and six time steps are used to compute the lift, drag, and moment coefficient for $AoA = 20 \deg$, $Re = 10^4$ (see table 5-13).

The uncertainty estimation is determined using both errors. The uncertainty plots corresponding to the unsteady calculations given in table 5-13 are presented in figure 5-19 for the lift, drag, and moment coefficients for the $AoA = 20 \deg$, $Re = 10^4$, flow case, with corresponding uncertainty estimations as given in table 5-14. Note that these uncertainties are for grid number five, as presented in table 5-7.

In this table ϕ_0 is the estimate of the exact solution (if $h_i/h_1, \tau_i/\tau_1 \rightarrow 0$). ϕ_1 is the solution of the finest grid and time step considered, in this case grid 5 in table 5-7 and $\Delta t = 1/50$.

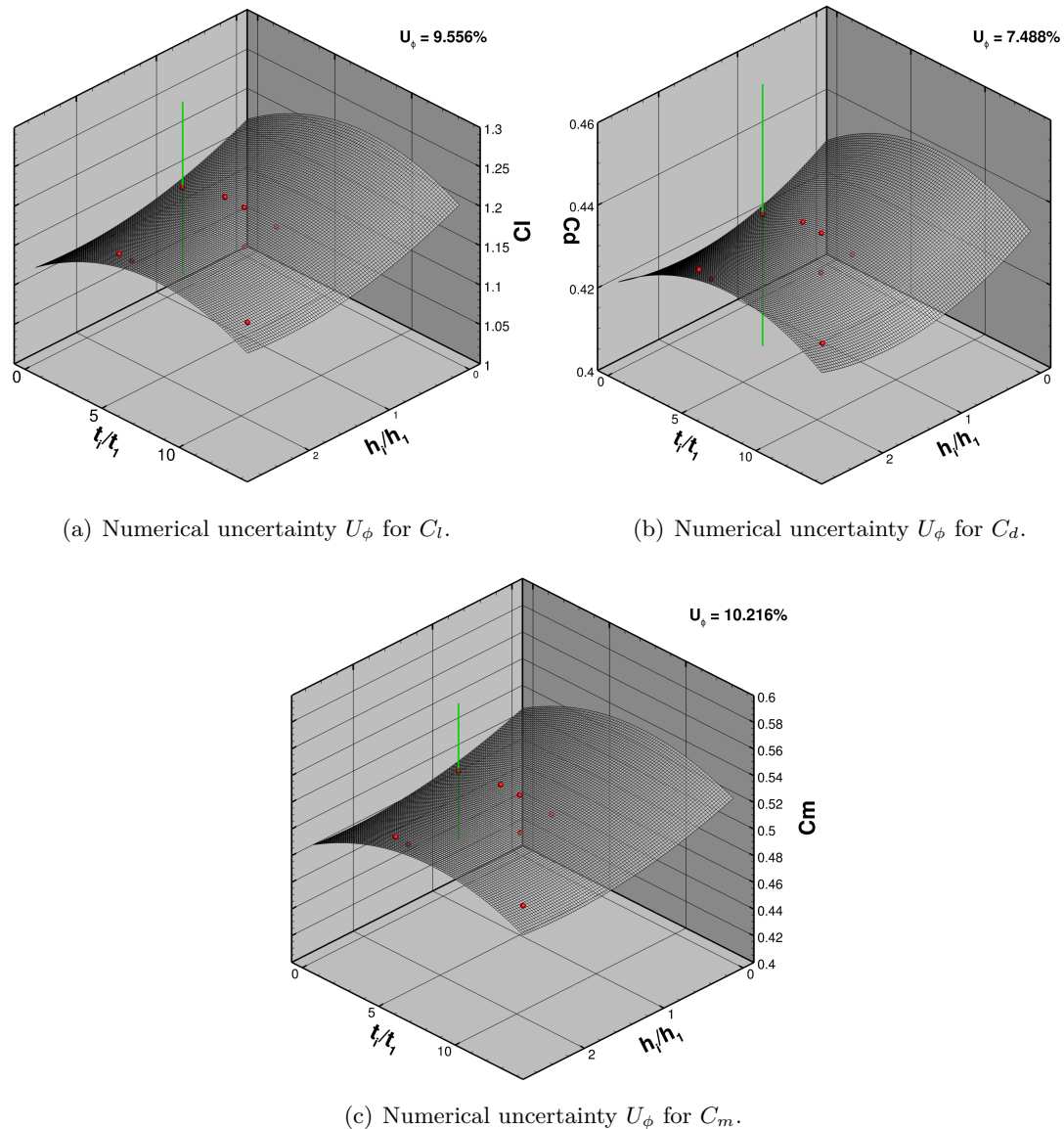


Figure 5-19: Numerical uncertainty estimation for unsteady flow $AoA = 20 \text{ deg}$ $Re = 10^4$ for grid 5 (see table 5-7).

Table 5-13: Grid set and timesteps used for unsteady uncertainty study.

Grid	h_i/h_1	$\Delta x/c$	τ_i/τ_1	$\Delta t [s]$	$\overline{\Delta t} [-]$	CFL [-]
2	2.403	1	12.500	1/4	0.0375	123
2	2.403	1	5.000	1/10	0.015	50
2	2.403	1	4.167	1/12	0.0125	42
3	1.637	2/3	8.333	1/6	0.025	81
4	1.412	1/2	8.333	1/6	0.025	90
4	1.412	1/2	6.250	1/8	0.01875	68
4	1.412	1/2	5.000	1/10	0.015	54
5	1.0	2/5	1.000	1/50	0.003	14

Table 5-14: Uncertainty estimation for $AoA = 20 \text{ deg}$, $Re = 10^4$ case.

	ϕ_0	ϕ_1	U_ϕ
C_l	1.176	1.148	9.6%
C_d	0.430	0.424	7.5%
C_m	0.511	0.499	10.2%

The unsteady uncertainty estimations given in table 5-14 show a similar trend when comparing with the steady results presented in table 5-10: integral quantity C_m shows the largest uncertainty followed by C_l , and finally the smallest uncertainty is found for C_d .

Although the inclusion of the time discretization error increases the complexity of the uncertainty estimation, for this particular flow problem the trend is in line with the uncertainty estimations presented previously for the steady flow cases studied. Note also that the uncertainties are overall smaller.

5-3-5 Final Remarks

As explained in section 2-5 the uncertainty estimation are very sensitive to perturbations in h_i , hence the results obtained from a set of non-geometrically similar grids must be used with great care. Additionally when unsteady computations are needed the estimation of the uncertainty becomes even more complicated because of the time discretization error that has to be considered. Despite the complexity the attempt made in this study to generate a grid set that resembles geometric similarity, and the implementation of an alternative description for the typical grid cell size can be valuable in analyzing the discretization error for unstructured grids. E.g. the graphs presented in figure 5-18 give insight in the geometric similarity of a grid set. This in turn could give some sort of degree of confidence for the uncertainty estimation.

The results presented in this section show that an uncertainty estimation of unsteady separated flows using unstructured grids is highly complex. Alternative methods have been applied to give more insight in the effect of the unstructured grid on the uncertainty estimation.

For both steady and unsteady flow, the uncertainty estimations and additionally the alternative methods applied, all show similar trends regarding the uncertainty estimation for the

various integral quantities. For this particular case this trend shows C_m having the largest uncertainty followed by C_l and finally the smallest uncertainty is found for C_d .

Based on all the results of the grid refinement study, grid number five was chosen for the remainder of the computations. For this grid the differences in C_l , C_d and C_m with the finest grid are less than four percent with a maximum uncertainty of 23.34 percent for the model-scale Reynolds number case at $AoA = 0 \text{ deg}$, and much less for all other cases.

Finally it must be mentioned that often the discretization error is analyzed solely by comparing the relative difference of the integral quantities obtained from a set of refined grids. In the present study an alternative method is used (least-squares based, see section 2-5) to asses the numerical uncertainty due to the discretization error.

5-4 Turbulence Modeling

In this section, three different turbulence models are use and compared: the Spalart-Allmaras one-equation model and the $k - \omega$ SST (Standard), and $k - \omega$ SST (2003) two-equation models. A detailed mathematical description of the three models is given in section 2-4-4. The computations are done for the full- and model-scale Reynolds numbers $Re = 10^6$ and $Re = 10^4$ respectively, as used in the previous studies.

Lift, drag, and moment coefficient The resulting C_l , C_d , and C_m for the analyzed turbulence models are presented quantitatively and as a percentage of the $k - \omega$ -SST (2003) solution in table 5-15. A clear distinction is made between the model-scale and full-scale Reynolds numbers.

For the model-scale Reynolds number case the C_l and C_m show a large difference of 650% between the one-equation Spalart-Allmaras model and both the two-equation $k - \omega$ SST models. This large difference is not observed for C_d , where a variation of only 1.6 % is observed between the one- and two-equation models. Furthermore the differences between the $k - \omega$ SST models are small, with a maximum difference of 0.19 % for C_m .

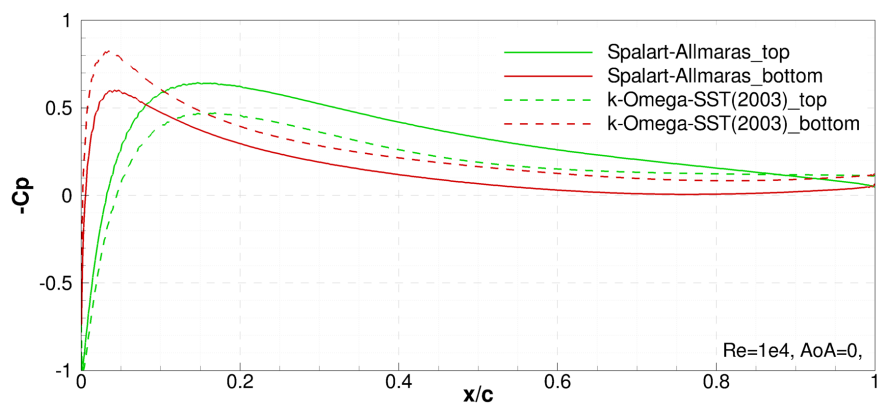
The large difference in lift coefficient between the Spalart-Allmaras and $k - \omega$ SST models reoccurs in the distribution of C_P over the airfoil as shown in figure 5-20. In this figure the computed pressures using the Spalart-Allmaras model are lower at the suction side while higher at the pressure side when compared to the $k - \omega$ SST models.

In the domain size study it is observed that the $AoA = 0 \text{ deg}$ and $Re = 10^4$ flow case is sensitive to small changes in the flow field by means of large domain size dependency. Similar trend is observed in this study, where the difference in flow quantities due to the applied turbulence models results in large variation of C_l and C_m . Additionally the magnitudes of C_l , C_d , and C_m are only small for this particular flow case, small changes in magnitude of the coefficients therefore results in large relative differences. Hence also the reduced difference of these quantities for the heavier loaded airfoil at $AoA = 4 \text{ deg}$.

For the full-scale Reynolds number regime the differences are much smaller compared to the model-scale case. Here a maximum difference between the one- and two-equation models of 1.45 % is observed for C_d . The difference between the $k - \omega$ -SST-Standard and $k - \omega$ -SST (2003) model is only 0.35 %.

Table 5-15: Lift drag and moment coefficients for three turbulence models

Turbulence model	C_l	[%]	C_d	[%]	C_m	[%]
Flow Case $AoA = 0 \deg$ and $Re = 10^4$						
Spalart-Allmaras	0.164349	451.41	0.043950	1.60	0.089965	649.34
$k - \omega$ SST (Standard)	-0.046824	0.12	0.043260	0.00	0.011983	0.19
$k - \omega$ SST (2003)	-0.046769	-	0.043258	-	0.012006	-
Flow Case $AoA = 4 \deg$ and $Re = 10^4$						
Spalart-Allmaras	0.482293	171.29	0.064533	0.23	0.184860	124.94
$k - \omega$ SST (Standard)	0.177139	0.36	0.064342	0.07	0.081910	0.33
$k - \omega$ SST (2003)	0.177775	-	0.064385	-	0.082183	-
Flow Case $AoA = 0 \deg$ and $Re = 10^6$						
Spalart-Allmaras	0.348169	0.16	0.011357	1.45	0.151660	0.18
$k - \omega$ SST (Standard)	0.347931	0.09	0.011167	0.25	0.151536	0.10
$k - \omega$ SST (2003)	0.347607	-	0.011195	-	0.151391	-
Flow Case $AoA = 4 \deg$ and $Re = 10^6$						
Spalart-Allmaras	0.783902	0.55	0.013263	1.06	0.257734	0.74
$k - \omega$ SST (Standard)	0.780397	0.10	0.013078	0.35	0.256191	0.13
$k - \omega$ SST (2003)	0.779613	-	0.013124	-	0.255853	-

**Figure 5-20:** Pressure coefficient along the surface of the airfoil at $AoA = 0 \deg$, $Re = 10^4$.

In addition to table 5-15 the lift and drag curves for the full-scale Reynolds number flow case are presented in figure 5-21.

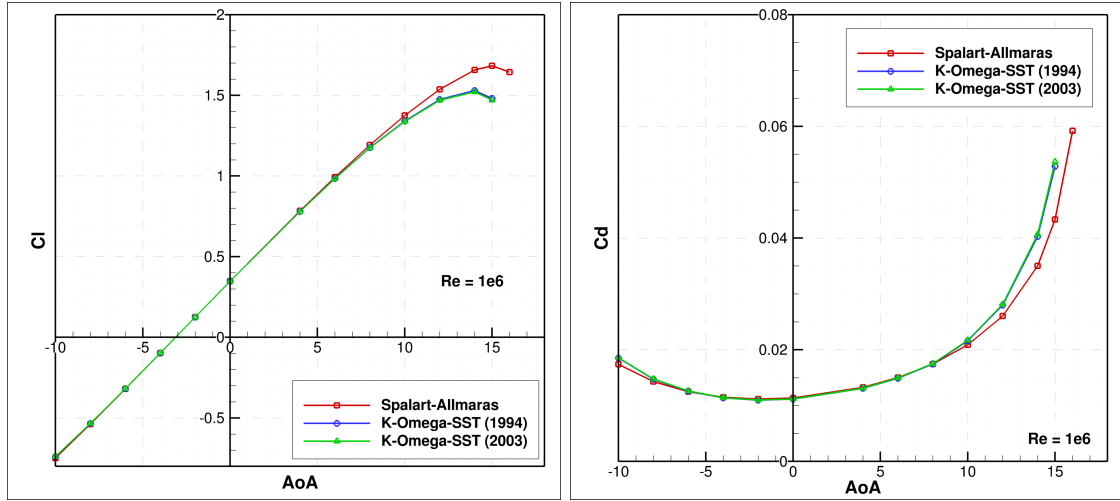


Figure 5-21: Lift and drag curves of the AG04 modified foil for various turbulence models ($Re = 10^6$).

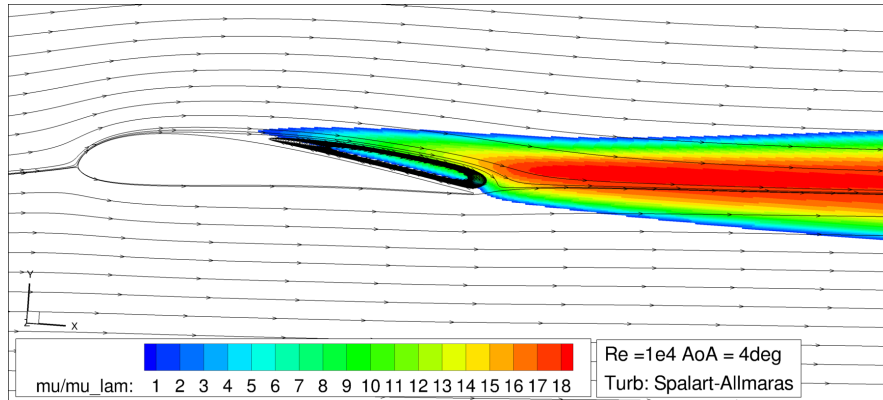
In these graphs the resulting C_l and C_d using the three turbulence models are plotted against the angle of attack. The models all show similar results for angles of attack between $-6 < \alpha < 6$. For larger angles of attack, i.e. $|\alpha| > 6$, the Spalart-Allmaras model over predicts C_l , and under predicts C_d when compared to the $k - \omega$ -SST models.

Furthermore the stall angle for the Spalart-Allmaras model is at $\alpha = 15 \text{ deg}$ while for the $k - \omega$ models a stall angle of $\alpha = 14 \text{ deg}$ is observed, indicating that the flow is able to remain attached longer for the Spalart-Allmaras model.

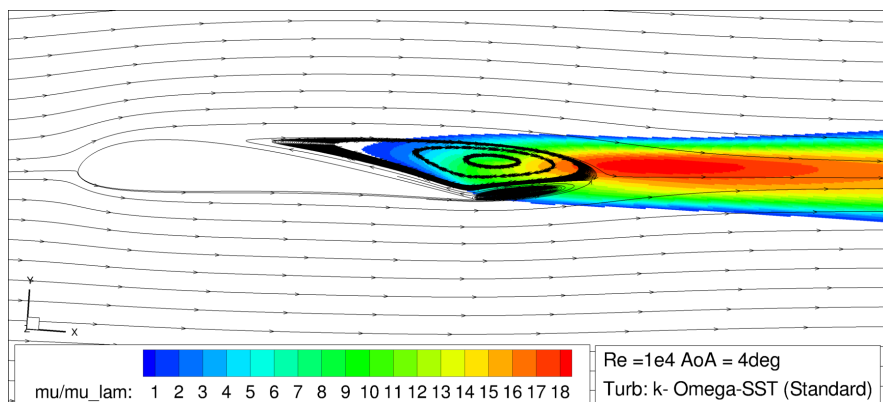
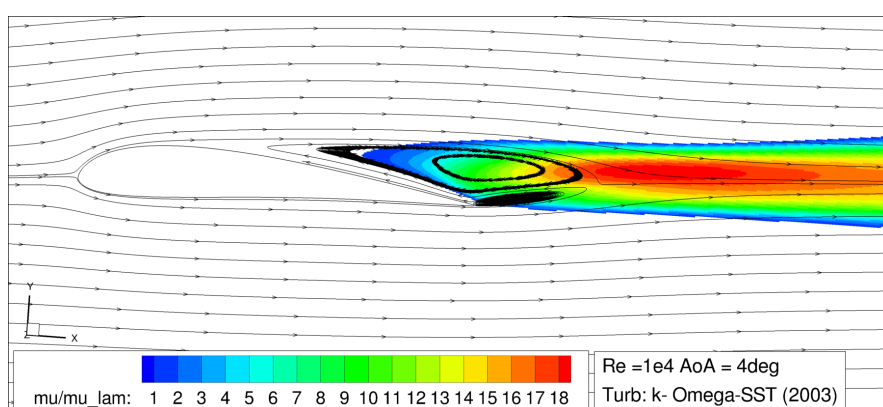
Flow characteristics Next the flow fields for the different turbulence models are compared. For the model-scale Reynolds number at $\alpha = 4 \text{ deg}$ the flow fields are presented in figure 5-22. In these figures the normalized turbulence viscosity and the streamlines are plotted. Note that blanking is applied in these figures for values $\bar{\mu}_t < 1$, indicating the region where turbulence viscosity is dominant and hence the flow can be considered turbulent.

In these plots a separation region is clearly visible at the trailing edge of the foil. It is known from previous studies that the Spalart-Allmaras model does not perform well for separated flows when compared to the $k - \omega$ -SST models [73]. Which could explain the large difference between the applied models.

In this particular case where separation is present, the difference between both the one- and two-equation models is significant. The region computed using the Spalart-Allmaras model is significantly smaller than the region obtained using the $k - \omega$ SST (Standard) and the $k - \omega$ SST (2003) model. Since flow separation has a major effect on airfoil performance, the difference in separation region between the two models explains the large differences in C_l and C_d observed in table 5-15 for the separated flow case. But contrary to what could be expected, the differences in C_d are minimal. This is the same trend as for the domain size study.



(a) Spalart-Allmaras.

(b) $k - \omega$ SST (Standard).(c) $k - \omega$ SST (2003).**Figure 5-22:** Normalized turbulence viscosity $\bar{\mu}_t = \mu_t/\mu$ for $\text{AoA} = 4\text{deg}$, $\text{Re} = 10^4$.

The effect is even larger for the zero angle of attack flow, as presented for the Spalart-Allmaras and $k - \omega$ SST (Standard) model in figures 5-23(a) and 5-23(b). In these figures the difference in separation zones is clearly visible. Additionally the shear stress over the foil is given in figure 5-23(c), this figure clearly shows the difference in location of the separation point. The location of the separation point has in turn a major effect on the lift performance of the airfoil, i.e. a separation point close to the leading edge results in a reduction of the produced lift whereas more lift is produced when the separation point is close to the trailing edge.

Note that the difference in drag coefficients observed in table 5-15 is also present in figure 5-23(c) by a difference in shear stress.

The differences between the turbulence models were also checked for the turbulence viscosity in the wake-field. The turbulence dominated regions in the wake obtained using the Spalart-Allmaras model, differ from the regions obtained using the $k - \omega$ SST models. When looking at the detailed view of the trailing edge in figure 5-24 it is observed that transition occurs further upstream for the Spalart-Allmaras model. Additionally the pressure coefficients in the flow domain are compared. Figure 5-25 shows the iso-curves of the pressure coefficient C_P in the flow domain for both the Spalart-Allmaras and the $k - \omega$ SST (2003) model. The differences between the latter are clearly visible. It must be mentioned that only one of the $k - \omega$ SST models is plotted since the differences between these models is negligible. This is in line with the results presented in table 5-15 for C_l , C_d , and C_m .

The normalized turbulence viscosity and the streamlines for the full-scale Reynolds number case are plotted in figure 5-27. Other than for the model-scale Reynolds number case presented in figure 5-22, the differences are small.

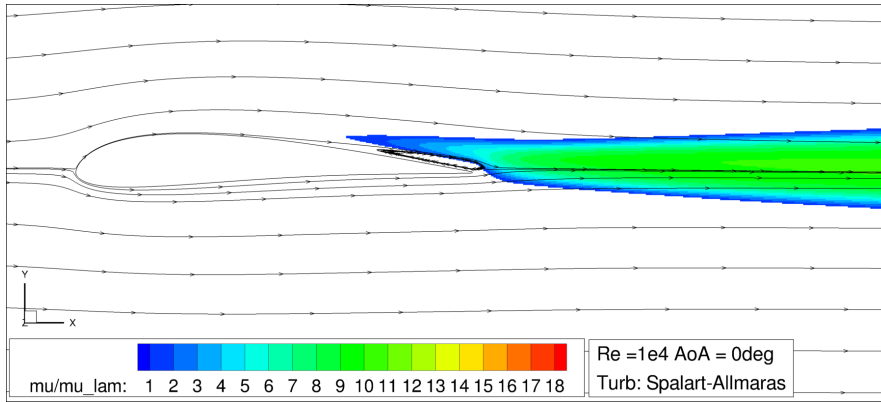
The streamlines for this case stay attached to the foil surface and no separation occurs. When looking at the normalized turbulence viscosity no significant difference is observed between the models. These observations are in accordance with the data presented in table 5-15, where a maximum difference of less than 1.6% between the two models is observed for the full-scale Reynolds number flow.

Figure 5-26 shows the iso-curves of C_P for both the Spalart-Allmaras and the $k - \omega$ SST (2003) model. When compared to the model-scale case the difference in the pressure field between the two models is small, which corroborates the data in table 5-15.

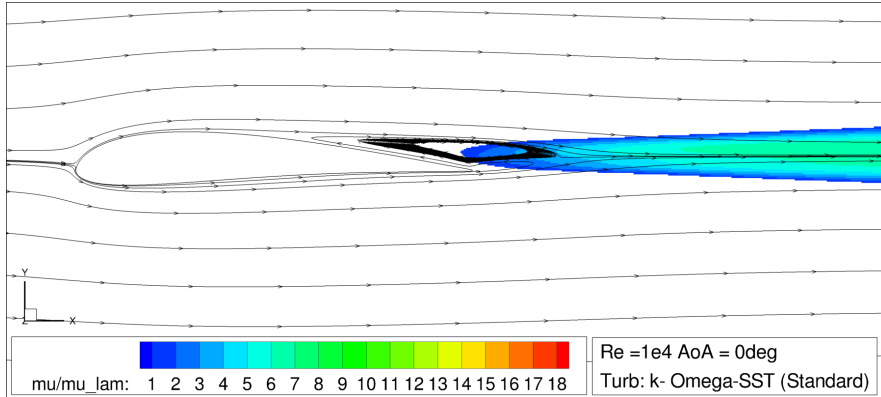
5-4-1 Final Remarks

The data presented in table 5-15 and figure 5-20 to 5-26 are all in agreement. For separated flow large differences between the Spalart-Allmaras and $k - \omega$ SST models are observed. For the fully attached flow at full-scale conditions the differences are small for both the flow field and for C_l , C_d , and C_m . The data presented are all in line with the work previously done in [73], where a comparison is made between the one- and two-equation models for a 2D-flow over various airfoils.

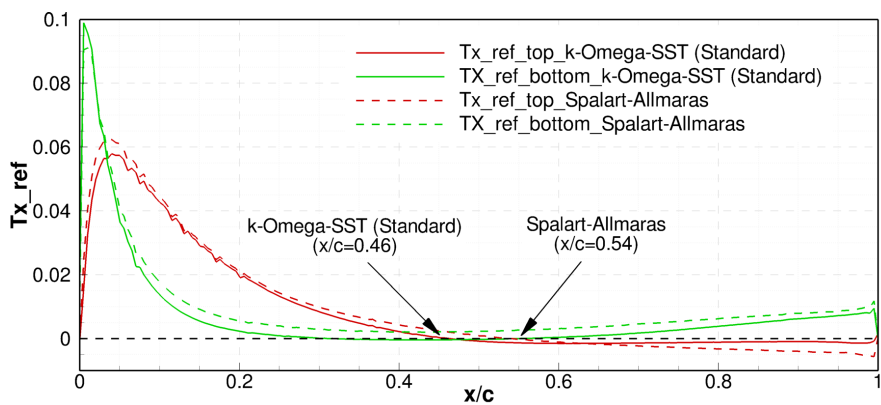
Since no experimental data is available for the modified Drela AG04 airfoil, a validation study can not be performed. However the work presented shows the importance of selecting a suitable turbulence model.



(a) Normalized turbulence viscosity $\bar{\mu}_t = \mu_t/\mu$ for $AoA = 0^\circ$, 10^4 using the Spalart-Allmaras model.

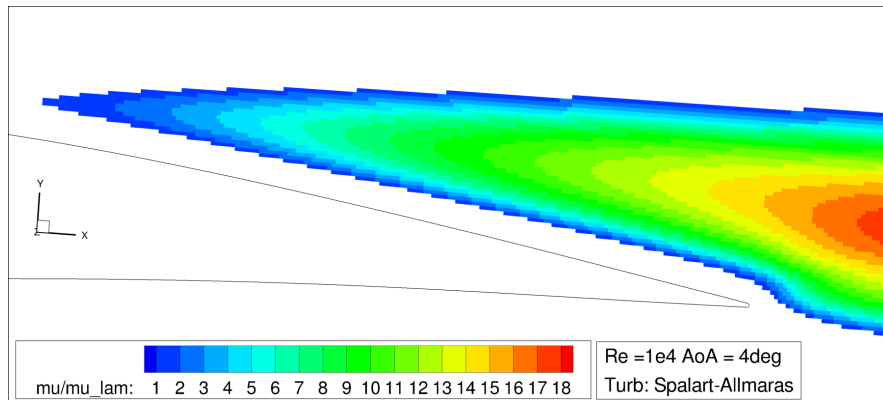


(b) Normalized turbulence viscosity $\bar{\mu}_t = \mu_t/\mu$ for $AoA = 0^\circ$, 10^4 using the $k - \omega$ SST (Standard) model.



(c) Normalized shear stress over the airfoil for $AoA = 0^\circ$, 10^4 . The wiggles present in this graphs are caused by the unstructured type grid, generated using Hexpress.

Figure 5-23: Flow field and shear stress over an airfoil for various turbulence models at $AoA = 0^\circ$, 10^4 .



(a) Spalart-Allmaras.

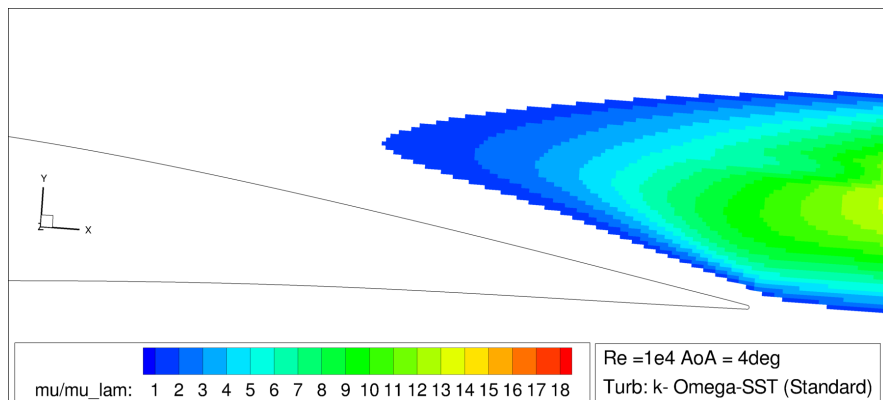
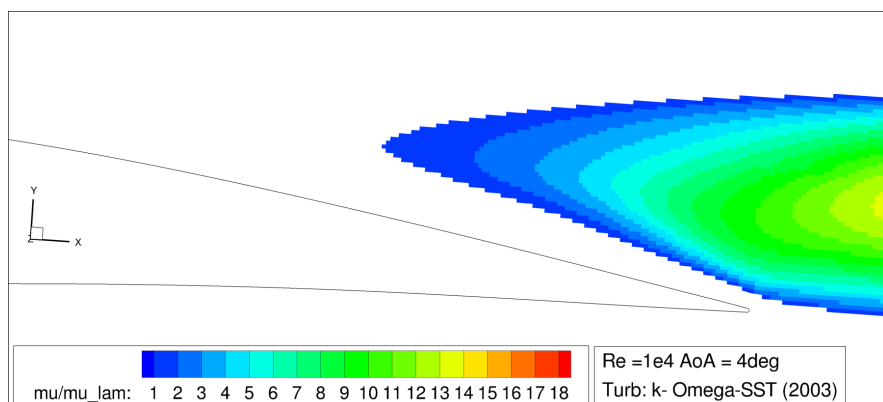
(b) $k - \omega$ SST (Standard).(c) $k - \omega$ SST (2003).

Figure 5-24: Trailing edge detail of the normalized turbulence viscosity $\bar{\mu}_t = \mu_t/\mu$ for $AoA = 4$, $Re = 10^4$.

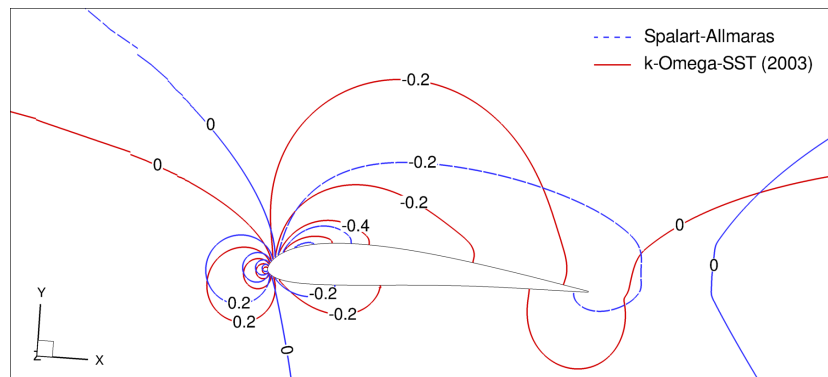


Figure 5-25: Effect of turbulence model choice on C_P in the flow domain for $AoA = 4$, $Re = 10^4$.

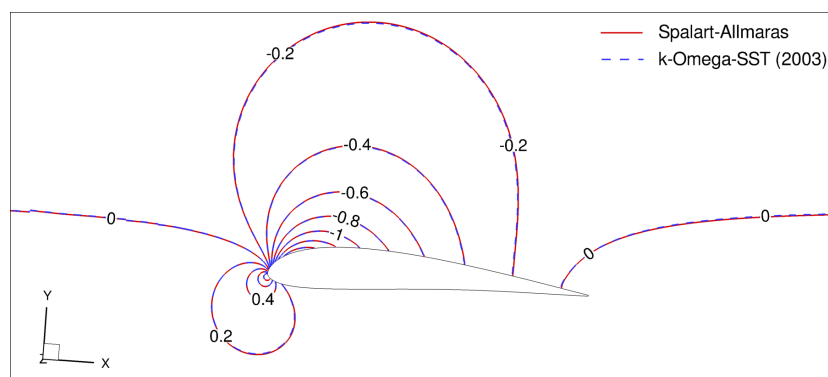
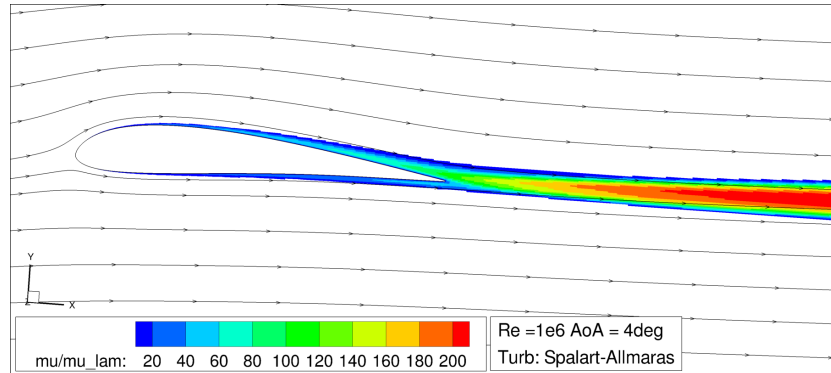
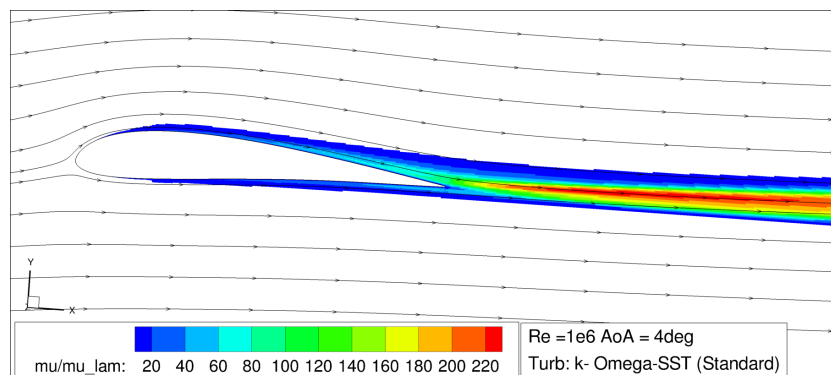
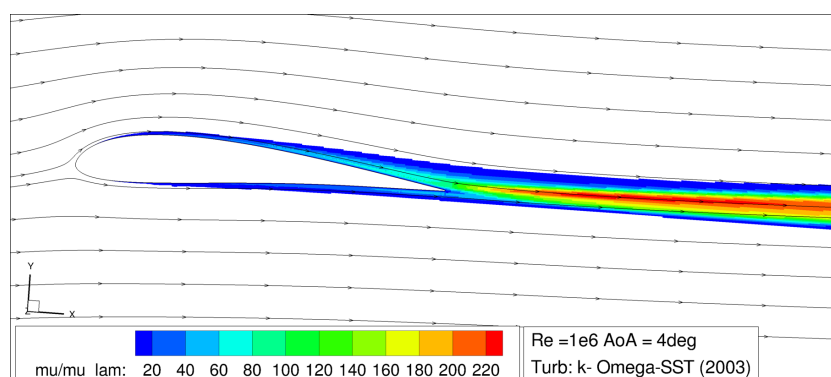


Figure 5-26: Effect of turbulence model choice on C_P in the flow domain for $AoA = 4$, $Re = 10^6$.



(a) Spalart-Allmaras.

(b) $k - \omega$ SST (Standard).(c) $k - \omega$ SST (2003).**Figure 5-27:** Normalized turbulence viscosity $\bar{\mu}_t = \mu_t/\mu$ for $AoA = 4$, $Re = 10^6$.

To gain more insight into where the differences between the three models originate from, a more in-depth study of the considered models is required. This is outside the scope of the present thesis work.

Chapter 6

Numerical Study on MARIN Stock Wind Turbine (MSWT) at Model-Scale

This chapter is devoted to several numerical studies focusing on the model-scale MARIN Stock Wind Turbine (MSWT). The knowledge here obtained will provide a solid foundation for the computations performed on the MSWT and NREL 5MW turbine in chapter 7. The present chapter starts with a domain size dependence study in section 6-1. Section 6-2 is devoted to a numerical uncertainty study, in which both the iterative and discretization error will be discussed. Two turbulence models are compared in section 6-3. In section 6-4 the MSWT model-scale computations are validated against experiments and finally in section 6-5, the general flow characteristics of the considered turbine will be discussed in detail. The calculations of the turbine are all done using the steady RANS solver ReFRESCO. Since the Absolute-Formulation (AFM) approach is used to model the turbine motion (see 4-2-2), steady RANS computations suffice.

6-1 Domain Size Variation

In order to obtain reliable flow data of the MSWT geometry it must be ensured that the influence of the domain on the solution is negligible. To do so a number of computations are performed in which the dimensions of the computational domain are varied (see section 4-2). In total three domains are analyzed, of which the dimensions are presented in table 6-1. Note that the dimensions are given as a multiple of the turbine diameter.

For each domain in table 6-1 a solution is obtain for a tip speed ratio of $TSR = 7$ and an inflow velocity of $V_{wind} = 2 \text{ m/s}$, which represents a full-scale wind speed of $V_{wind} = 14.1 \text{ m/s}$ for which model-scale experimental data is available.

In figure 6-1 the normalized axial velocity field for the computed domains and TSRs are presented. The velocities in this figure are normalized using the inflow velocity V_{wind} . The

Table 6-1: Overview domains used and corresponding dimensions.

Identifier	Upstream length: nD	Wake length: nD	Diameter nD
Domain A	5	20	10
Domain B	10	40	20
Domain C	15	60	30

region affected by the presence of the turbine is visualized by blanking the axial velocities which deviate less than 0.1% from the inflow velocity.

For the smallest domain **A** the affected axial velocity spreads outwards up to the boundaries of the domain (figure 6-1(a)). For both domain **B** and **C** the axial velocity is decelerated less than 0.1% of the inflow velocity near the external boundary. In this case it is assumed that the influence of the boundary conditions is negligible.

Note that at the region where the edges of the outflow and external domain boundary connect, the axial velocity differs more than 0.1% from the inflow velocity. This is caused by the interaction between the different boundary conditions imposed on the external and outflow boundary respectively. Since these corners of the domain are located in the far wake-field, they are assumed to have no influence on the solution in the vicinity of the turbine.

The thrust and power coefficients computed for the three domains are presented in table 6-2 and figure 6-2, in which the differences in C_P and C_T are presented relative to the largest domain (**C**).

Table 6-2: C_T and C_P for varying domain size.

Identifier	C_T		C_P	
	[−]	[%]	[−]	[%]
Domain A	0.7017	0.66	0.3026	2.77
Domain B	0.6975	0.05	0.2966	0.73
Domain C	0.6971	-	0.2944	-

For domain **B** the influence of the boundaries results in a difference of C_T and C_P less than one percent of the largest domain **C**. However it is expected that for lower tip speed ratios i.e. higher blade loading, the affected wake-field is larger and the dependency of the domain will increase. Additionally the increase of computation time between domain **B** and **C** is only 10 percent. Note also that domain dependence for the three-dimensional flow considered here is much smaller than previously observed for the two-dimensional flow (see section 5-2). The trends observed in this study are in line with previous studies regarding current turbines [18].

Considering the above results the dimensions of domain **C** are used for the remainder of the computations. For these domain dimensions the influence of the boundary conditions on the solutions are considered negligible.

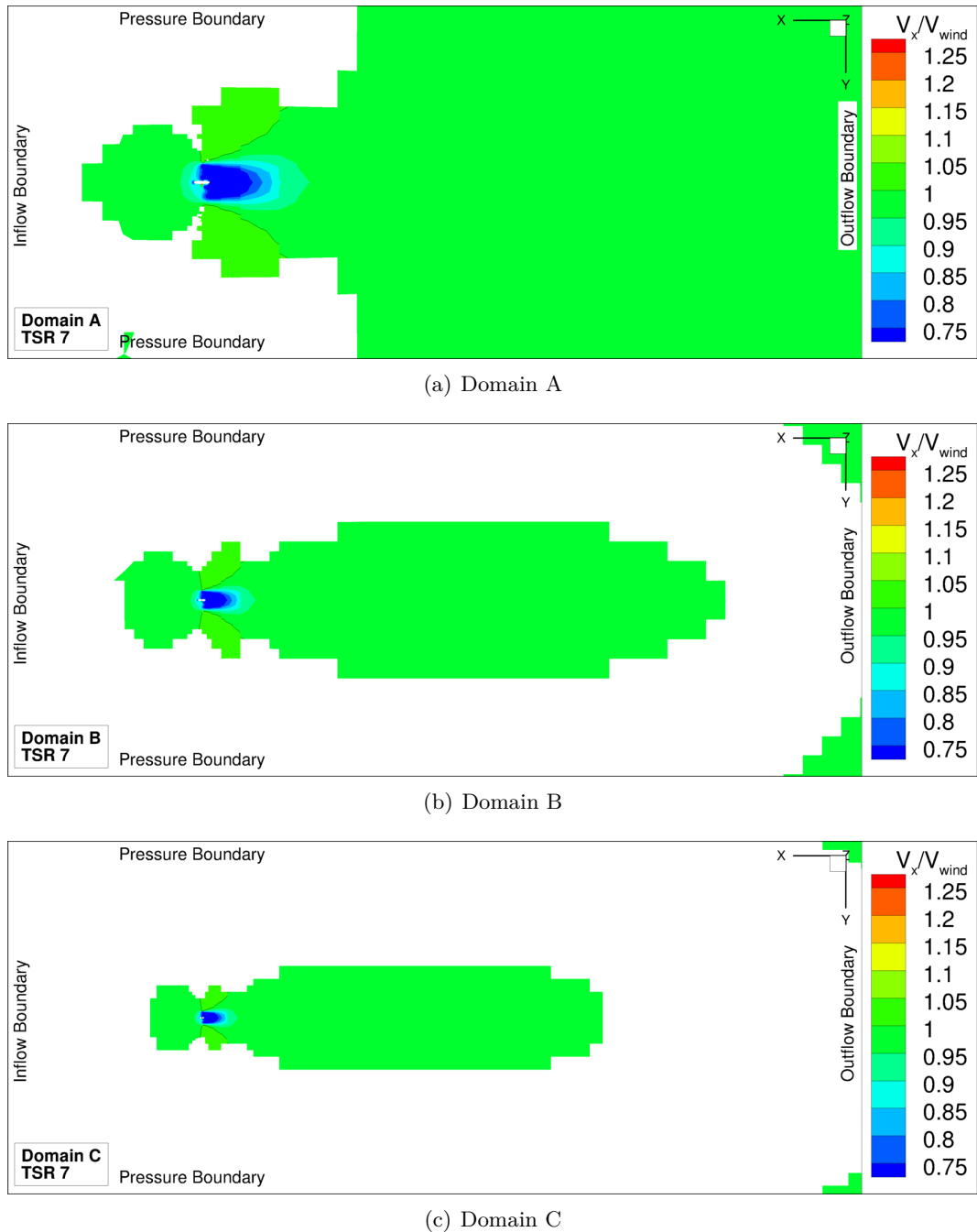


Figure 6-1: Normalized velocity fields for $TSR = 7.0$ at the $z = 0$ horizontal plane. Contour indicates the axial velocity, where values that differ less than 0.1% from the inflow velocity are blanked. The iso-curve indicates $V_x/V_{wind} = 1$, indicating the border of accelerated/decelerated flow.

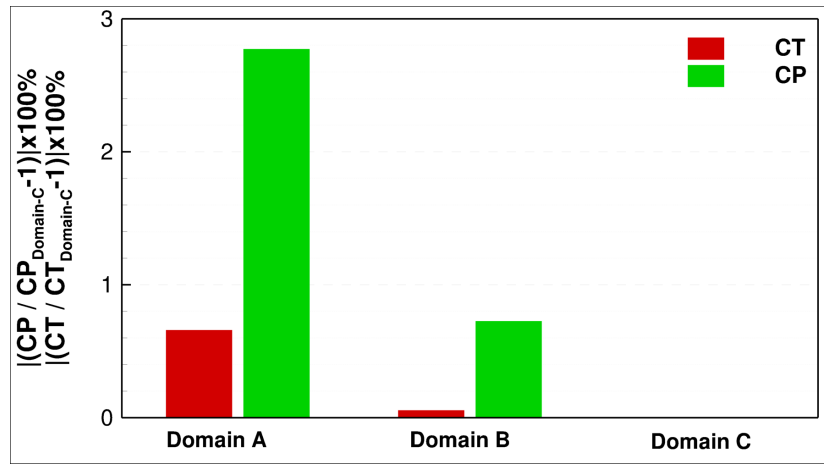


Figure 6-2: Domain size dependency of the model-scale MSWT at $TSR = 7$.

6-2 Numerical Uncertainty Study

To determine the numerical uncertainty of the considered computations, five grids are analyzed with a total number of cells varying between 8.4M and 29.5M. The properties of the grids are presented in table 6-3. The same method as for the two-dimensional study is used to generate the grids in an attempt to maintain geometric similarity as much as possible (see chapter 5).

Because of the laminar character of the flow at model-scale conditions combined with unexpected large amounts of flow separation and heavy blade loading, an iteratively converged numerical solution is not easily obtained. This is especially true for the finest grids, where vortices are trying to shed from the blade, as observed for the two-dimensional study.

To improve the convergence of the numerical solution, the wind speed is increased from $V_{wind} = 2.0 \text{ m/s}$ to $V_{wind} = 2.47 \text{ m/s}$, which resembles a full-scale wind speed of $V_{wind} = 17.4 \text{ m/s}$. By doing so the flow around the turbine is expected to be more stable with improved convergence characteristics as a result. Experimental data for the $V_{wind} = 17.4 \text{ m/s}$, $TSR = 7.0$ case is available for comparison.

Table 6-3: Grid properties of grid refinement study.

Grid refinement	1	2	3	4	5
Total no. Cells	8371928	13406225	18559122	23907087	29558234
Minimum Orthogonality	10.34	13.74	15.406	12.541	11.726
Average Orthogonality	77.871	78.197	78.420	78.157	77.966
Maximum Skewness	0.903	0.877	0.874	0.864	0.879
Grid ref. ratio	1.52	1.30	1.17	1.07	1.00

6-2-1 Iterative Error

Table 6-4 shows the iterative convergence obtained for the grid-set considered. The L_2 -norm of the residuals are of the order 10^{-5} , whereas a maximum order of 10^{-8} was previously shown for the two-dimensional case. The L_∞ -norm of the residuals are of the order 10^{-2} . For a verification study a minimal L_2 - and L_∞ -norm of the residuals of typically 10^{-6} and 10^{-3} is desirable.

The convergence plots of the L_2 -norms of the residuals and C_T / C_P , corresponding to the finest grid, are presented in figure 6-3. These convergence plots are representative for all computations performed in this chapter.

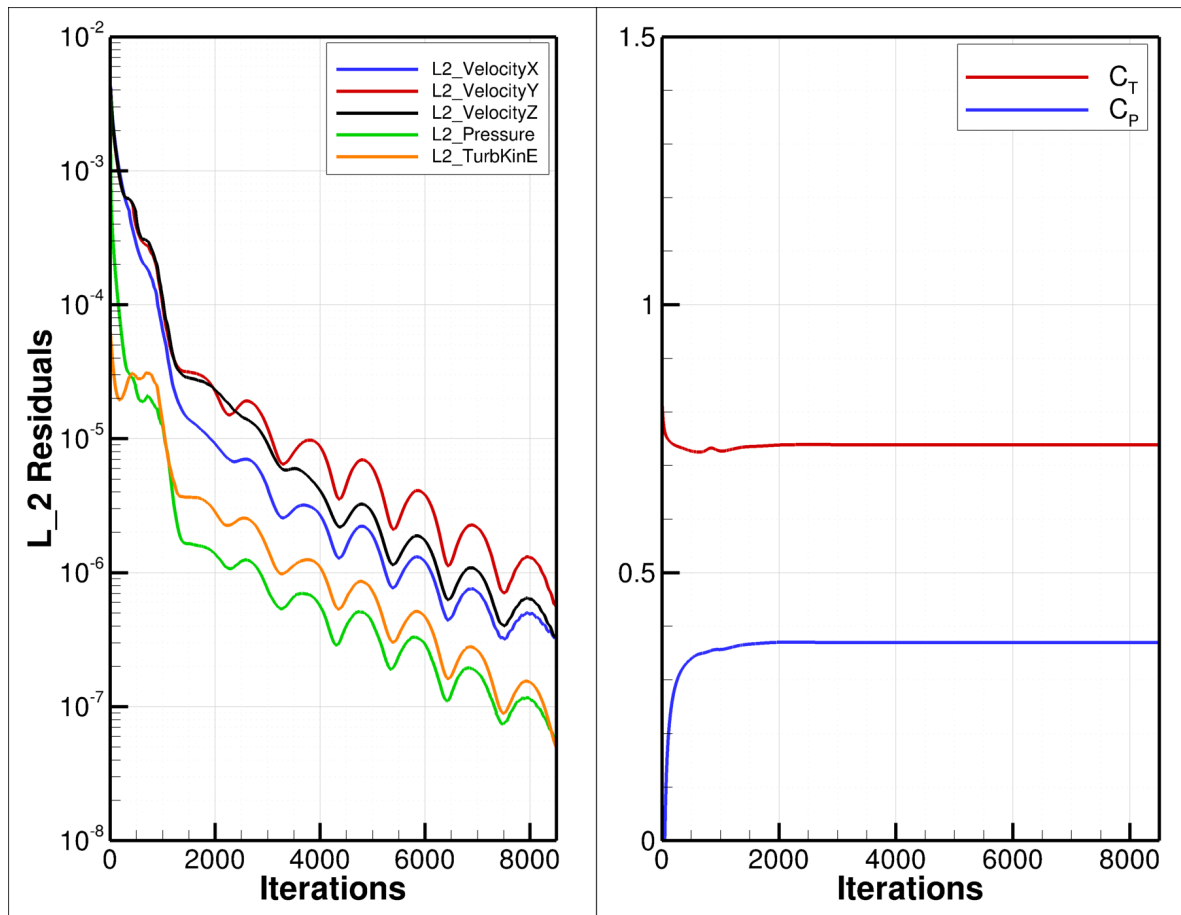


Figure 6-3: Iterative convergence plots of the L_2 -norm of the residuals and C_T and C_P for finest grid. $V_{wind} = 2.47 \text{ m/s}$ and $TSR = 7.0$.

The maximum residuals of the pressure are plotted in the flow domain of the finest grid in figure 6-4(a) for $|res_p| > 1 \cdot 10^{-6}$. It is clear that these residuals are a result of the unsteady flow present in the vortex of the blade root as can be observed in figure 6-4(b). In this figure the iso-surface of the dimensionless Q -factor is plotted. This unsteady flow is caused by the cylinder-like cross section of the turbine blade near the root. This effect is also observed previously by others [18]. Furthermore the local nature of the large residuals can also be explained by the difference between the L_2 - and L_∞ -norm of the residuals presented in table

6-4. A large difference in the latter, indicate that the residuals are large only locally.

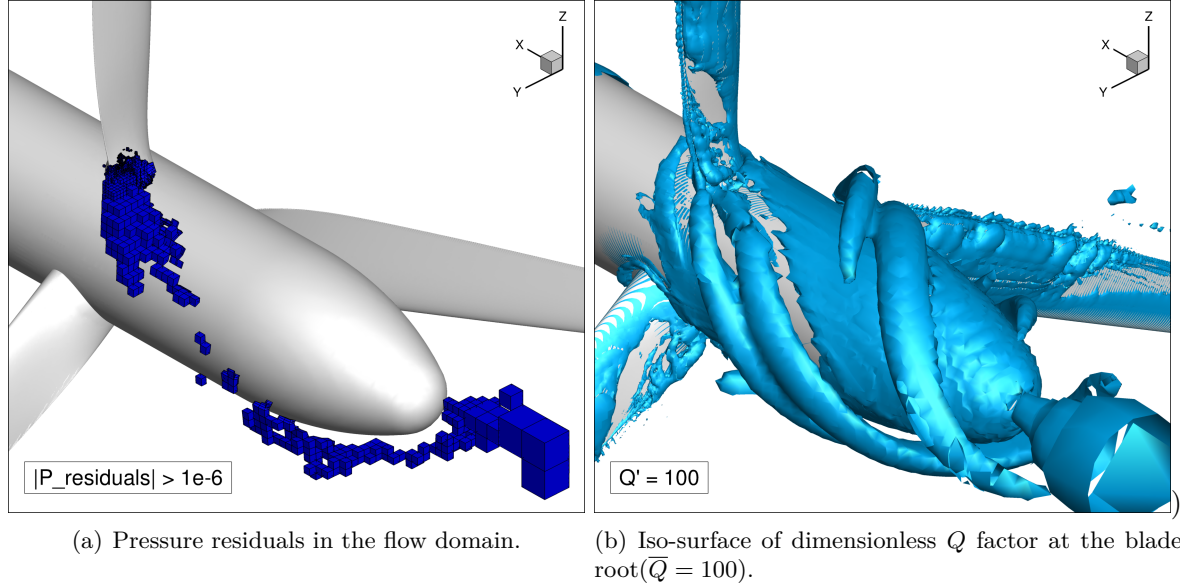


Figure 6-4: Pressure residuals in the wake of the blade root and root vortex.

Obtaining lower values for the residuals is challenging due to this unsteady behavior of the flow at the low model-scale Reynolds numbers. This is especially true for the low tip speed ratios, at which blade loading is high and the flow is fully separated.

When looking at the change of the integral quantities C_T and C_P of the last 200 iterations, the changes are all below 10^{-3} percent as shown in table 6-4, indicating that despite the relatively large values of the residuals the integral quantities do converge to a constant value. Note however that this does not mean the solution is converging to the correct values.

To be able to neglect the iterative error, the order of convergence must be two to three orders below the discretization error. The relatively large iterative error for this flow case (typically an L_∞ residual norm of 10^{-3}) must be kept in mind when evaluating the discretization error: it can be that the iterative error is too large to be neglected according to the theory presented in section 2-5.

Although not considered due to the required computational time, unsteady RANS computations would be desirable at model-scale conditions due to the unsteady behavior.

6-2-2 Discretization Error

Here the numerical uncertainty is estimated using the numerical uncertainty theory (see section 2-5). For this study a wind speed of $V_{\text{wind}} = 2.47 \text{ m/s}$ at $TSR = 7$, is used as explained before.

The resulting numerical uncertainty estimations are presented in table 6-5 for all grids at the specified flow condition. When looking at the estimated uncertainties presented, a large difference is observed between C_T and C_P . For C_T the estimated uncertainty of all grids is below 3.0 %, while for C_P the finest grid will obtain an uncertainty of 32.31 %.

Table 6-4: Iterative convergence and error.

Grid no.	Grid ref. $\frac{h_i}{h_1}$	n_{iter}	L_2 residuals $\max(u.v, w, p)$	L_∞ residuals $\max(u.v, w, p)$	Fluct. last 200 iters $100 \times \max(\phi_i - \phi_{end} / \phi_{end})$ C_T	Fluct. last 200 iters C_P
Flow Case $V_{wind} = 2.47 \text{ m/s}$ and $TSR = 7.0$						
1	1.52	8283	$1.4 \cdot 10^{-5}$	$1.24 \cdot 10^{-2}$	0.001	0.001
2	1.30	15000	$3.4 \cdot 10^{-5}$	$2.8 \cdot 10^{-2}$	0.001	0.001
3	1.17	15000	$7.9 \cdot 10^{-7}$	$1.6 \cdot 10^{-3}$	0.001	0.001
4	1.07	15000	$1.7 \cdot 10^{-5}$	$9.0 \cdot 10^{-3}$	0.001	0.001
5	1.00	15000	$1.7 \cdot 10^{-5}$	$9.1 \cdot 10^{-3}$	0.001	0.001

Table 6-5: Numerical uncertainty estimation for the MSWT model-scale computations.

Grid no.	Grid ref. $\frac{h_i}{h_1}$	C_T [-]	U_ϕ [%]	C_P [-]	U_ϕ [%]	C_P [-]
Flow Case $V_{wind} = 2.47 \text{ m/s}$ and $TSR = 7.0$						
1	1.52	0.7416	0.37	2.78%	0.3170	-14.27
2	1.30	0.7406	0.23	2.15%	0.3426	-7.37
3	1.17	0.7384	-0.06	1.78%	0.3551	-3.99
4	1.07	0.7375	-0.18	1.56%	0.3608	-2.44
5	1.00	0.7388	-	1.39%	0.3698	-
32.31%						

In addition to table 6-5, the graphs corresponding to the uncertainty estimation are shown in figure 6-5.

When only looking at magnitude of C_T and C_P , and the difference of these quantities for various grids, a similar trend is observed. The differences in C_T and C_P expressed as a percentage of the solution for the finest grid show a maximum difference in C_T of less than one percent, while for C_P a maximum difference of less than 15 percent for the coarsest grid.

The relative difference in C_T and C_P is also shown in figure 6-6. This figure clearly shows that the values of C_P converge to a constant value, while for C_T convergence is already reached.

The difference in C_T and C_P for the relative difference can be explained by the fact that C_P is much more sensitive to the change in attached flow region between the computed grids (see figure 6-7). This is due to the fact that C_P is computed by means of the moment about the rotating axis of the turbine. As a result of changes in C_l/C_d at the blade tip, C_P is altered significantly due to the incorporated distance from the rotating axis. C_T on the other hand is computed by means of the axial thrust force, hence changes in C_l/C_d along the blade-span contribute equally.

The even larger differences in the uncertainties between C_T and C_P are also partially caused by this phenomenon. Additionally the complex highly separated flow, the use of unstructured grids and, to some extend, the iterative error contribute to this observed difference.

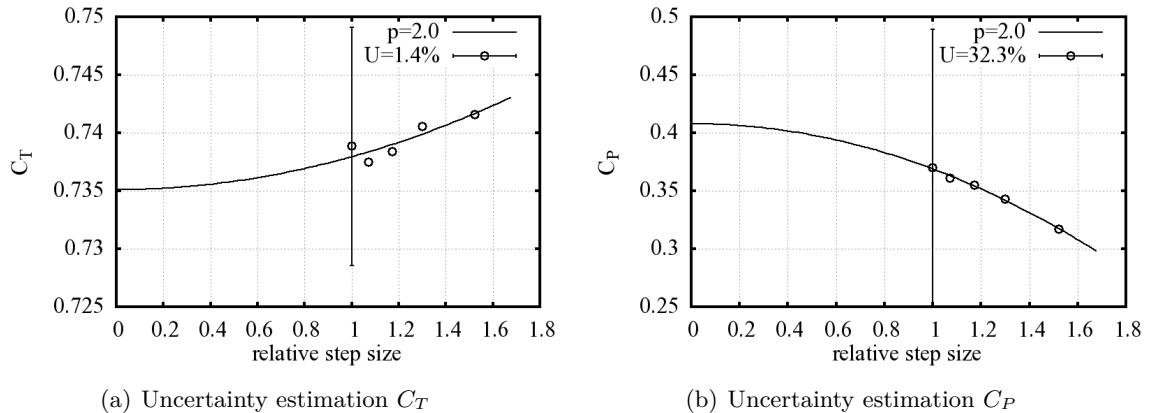


Figure 6-5: Numerical uncertainty estimation for flow case $V_{wind} = 2.47 \text{ m/s}$ and $TSR = 7.0$.

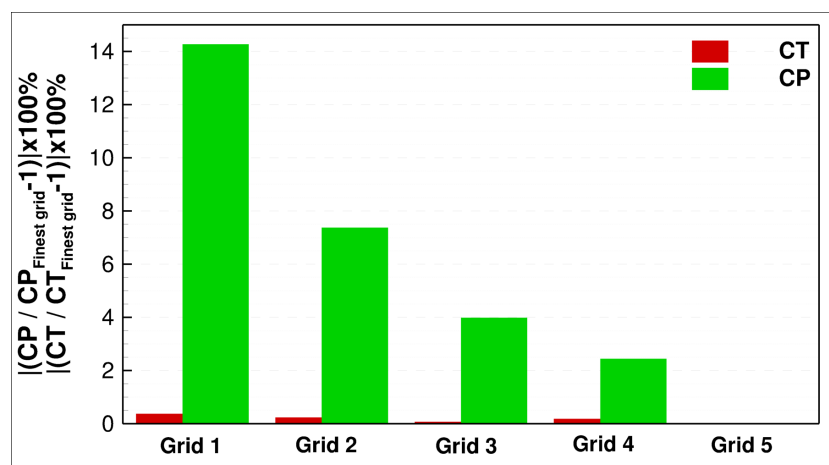


Figure 6-6: Power and thrust coefficient as percentage of the finest grid solution, at $V_{wind} = 2.47 \text{ m/s}$ and $TSR = 7.0$.

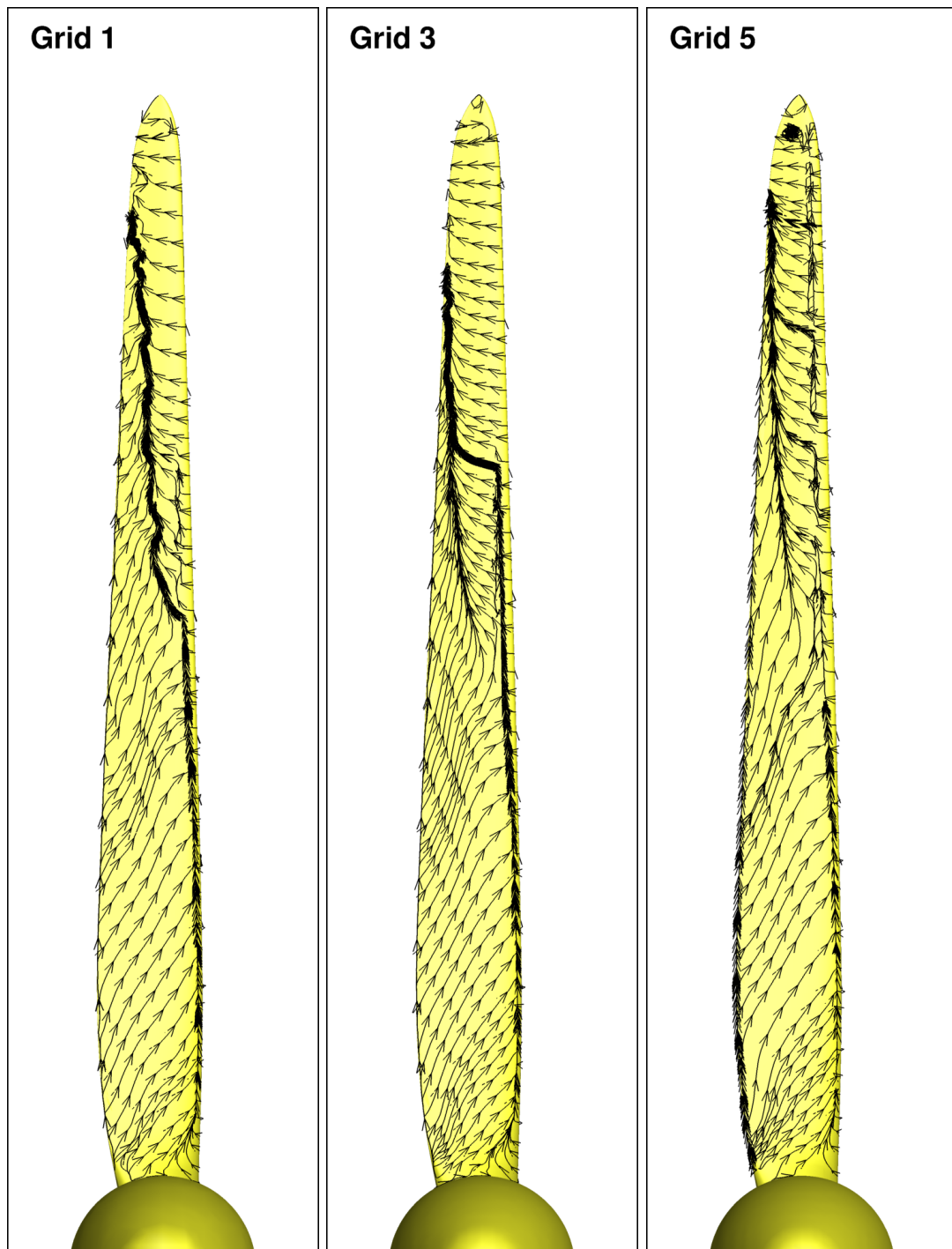


Figure 6-7: Limiting streamlines for model-scale MSWT at $TSR = 7.0$ for various grid refinements.

6-2-3 Final Remarks

From the previous studies it follows that obtaining a sufficiently iteratively converged solution is challenging when doing steady calculations. This, in combination with the use of unstructured grids, result in large uncertainties especially for the power coefficient C_P .

When looking at the differences in C_T and C_P between the grids and the estimated uncertainties, the finest grid is chosen for the remainder of the computations. For this grid an uncertainty of 1.39 and 32.31 percent is found for C_T and C_P . While the difference between C_T and C_P for the two finest grids are 0.18 and 2.44 percent respectively. It must be kept in mind however that the iterative error may have an effect on the uncertainty estimation and the obtained solution.

6-3 Turbulence Modeling

In this section two different turbulence models are used and compared. Since both $k - \omega$ -SST turbulence models show very comparable results for the two-dimensional flow problem, only the $k - \omega$ -SST-Standard and the Spalart-Allmaras model are used. A detailed description of the latter models can be found in section 2-4-4.

Power and thrust coefficient The numerical solutions using the two models are compared for a wind speed and tip speed ratio of $V_{wind} = 2.0 \text{ m/s}$ and $TSR = 7.0$. The resulting integral quantities C_T and C_P are presented in table 6-6.

Table 6-6: Power and thrust coefficients for two turbulence models

Turbulence model	C_T	[%]	C_P	[%]
Flow Case $V_{wind} = 2.0 \text{ m/s}$ and $TSR = 7.0$				
Spalart-Allmaras	0.7798	8.75	0.4048	28.22
$k - \omega$ -SST-Standard	0.7170	-	0.3157	-

Analogous to the refinement study the large differences in C_P can be explained to the sensitivity of this quantity with respect to the attached flow region, as it is shown next.

Flow characteristics In figure 6-8, the limiting streamlines over the suction side of the blades are presented for the Spalart-Allmaras and $k - \omega$ SST (Standard) model.

For both models the flow in the region near the blade tip remains attached. In this region the apparent angle of attack is much smaller than near the root of the blade and the local velocities are higher. As a result the flow is able to remain attached to the surface.

In the region of the blade near the root the apparent angle of attack is much larger and the flow is no longer able to stay attached to the blade surface. As a result the flow will separate from the blade surface, drastically degrading the performance of the blade locally. This phenomenon is clearly visible for both models. However, the size of the attached region is significantly smaller for the $k - \omega$ SST (Standard) model.

As explained in the grid refinement study, the size of this attached region has a significant effect on the performance of the turbine, especially when looking at C_P . For computing C_P the torque about the rotating x -axis is used, as can be seen in equation (4-17). A large attached flow region located near the blade tip will therefore contribute significantly to the total moment about the x -axis due to the large amount of lift generated in this region of the blade. Hence the large differences in C_P between the models, where the Spalart-Allmaras model show a larger attached flow region (figure 6-8), and C_P value (table 6-6) when compared to the $k - \omega$ SST model.

C_T on the other hand is computed by means of the axial force working on the turbine. As a result, the lift and drag coefficients over the complete turbine blade span contribute equally, in contrary to the increased contribution of the blade tip with regard to C_P . This leads to a reduction of the sensitivity to the size of the attached flow at the blade tip.

In figure 6-9 the normalized turbulence viscosity in the wake-field of the turbine blade at various radii is presented for both models. In this figure an iso-curve of the turbulence viscosity is shown for $\bar{\mu}_t = 1$, indicating the region where the turbulence viscosity is dominant and the flow can be considered turbulent. For all sections along the turbine blade the production of turbulence viscosity is much higher for the $k - \omega$ SST (Standard) model. Additionally it spreads out further away from the airfoil surface when compared to the wake-field of the Spalart-Allmaras solution. This is also shown in figure 6-10, where the turbulence viscosity is visualized by means of an iso-surface. Note that in this figure different levels are used for the iso-surfaces.

When looking at the wake-field of the two sections close to the hub ($r/R = 0.3, 0.5$) the separated region in which high values of turbulence viscosity is present is much larger for the $K - \omega$ -SST-Standard model. Clearly indicating the difference in turbulence viscosity production between the two models.

6-3-1 Result Summary

It is shown in this study that the Spalart-Allmaras and $K - \omega$ -SST-Standard model perform differently at model scale conditions. The size of the separated region at the suction side of the blade is sensitive to choice in turbulence model. The size of this region is in turn greatly affecting C_P . Hence large differences between the models is observed for C_P , while the differences are much smaller for C_T .

6-4 Validation procedure

In this section the numerical results are validated against the experimental data using the procedure presented in section 2-5. Following this procedure the validation uncertainty U_{val} is computed using equation (2-94), which is given again below for convenience ,

$$U_{val} = \sqrt{U_\phi^2 + U_{inp}^2 + U_{exp}^2}. \quad (2-94)$$

The numerical, input, and experimental uncertainties regarding the flow problem at hand are discussed next.

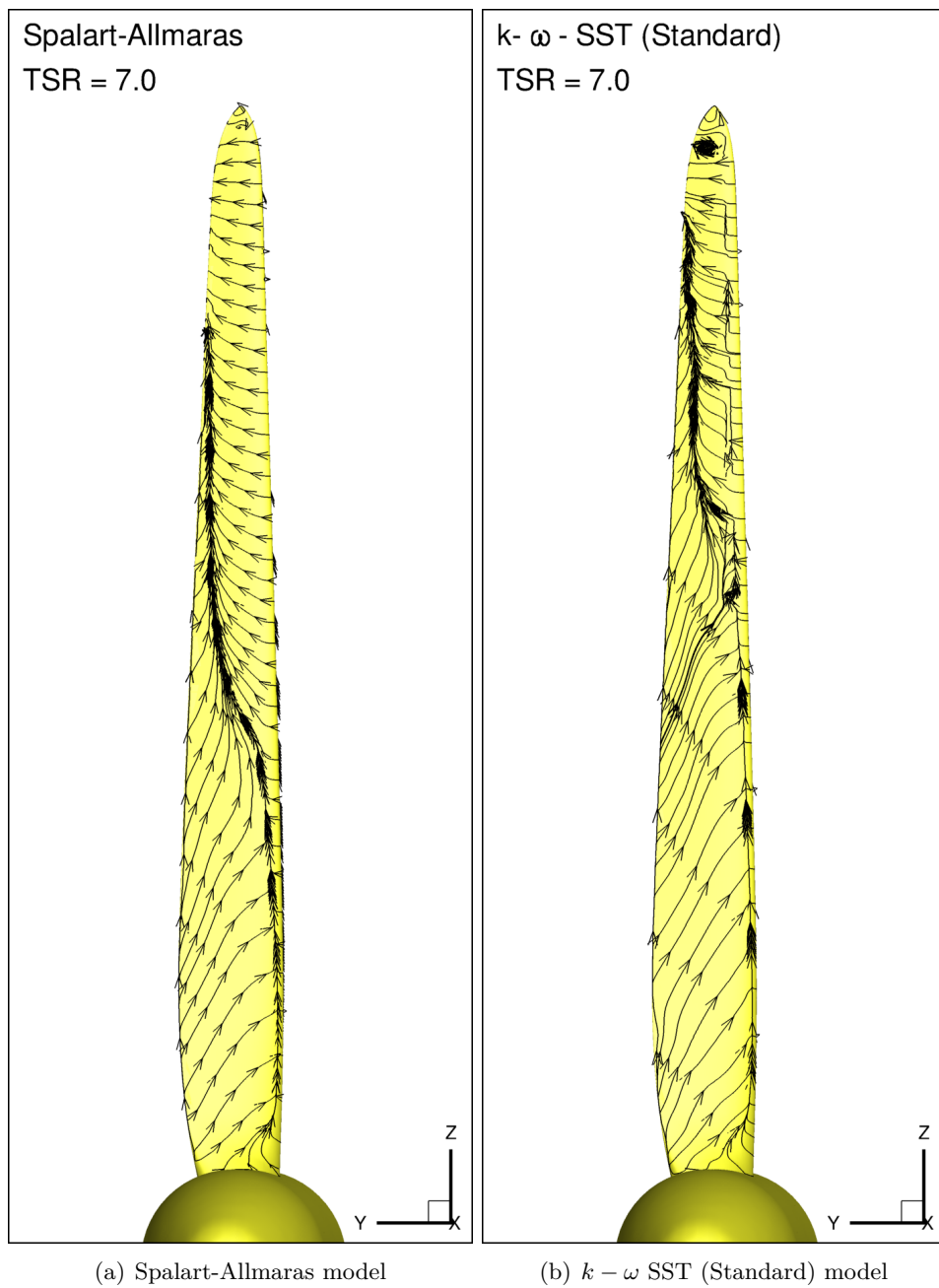


Figure 6-8: Limiting streamlines over the suction side of the turbine blades for two turbulence models at $V_{wind} = 2.0 \text{ m/s}$ and $TSR = 7.0$.

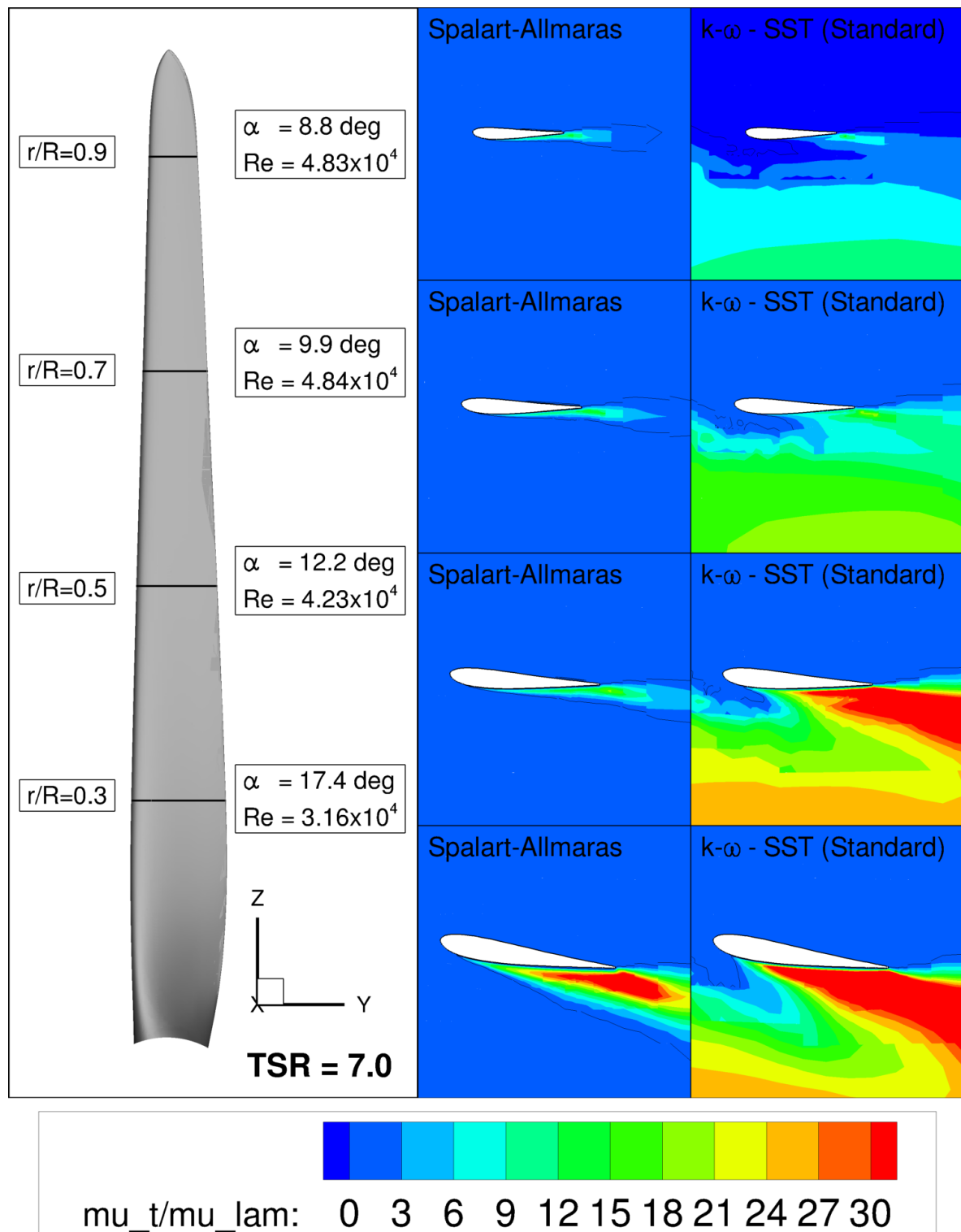
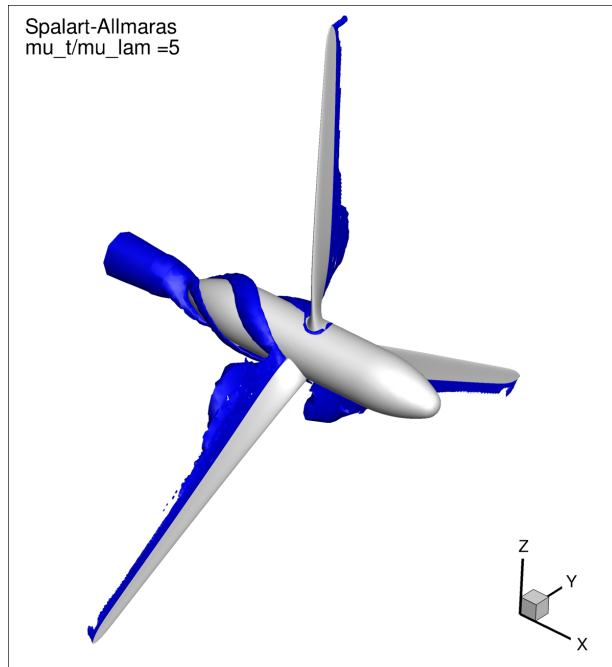


Figure 6-9: Normalized turbulence viscosity ($\bar{\mu}_t = \mu_t/\mu_{lam}$) in the wake-field of a turbine blade using Spalart-Allmaras and $K - \omega$ -SST-Standard turbulence models. Note that values below $\bar{\mu}_t < 1$ are blanked.



(a) Spalart-Allmaras model

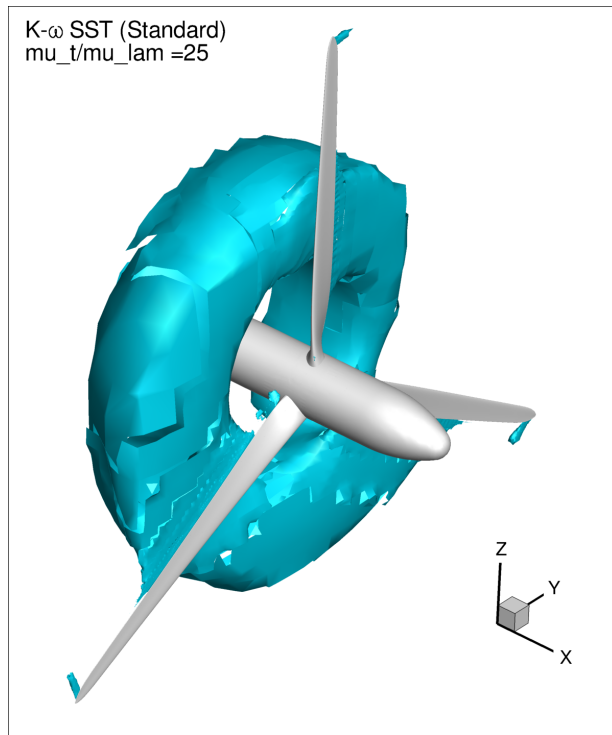
(b) $k - \omega$ SST (Standard) model

Figure 6-10: Iso-surface of the turbulence viscosity in the wakefield of the turbine for two turbulence models at $V_{wind} = 2.0 \text{ m/s}$ and $TSR = 7.0$.

Experimental Uncertainty As explained before the experimental uncertainty U_{exp} is set to 2.5% for both C_T and C_P over the full range of considered TSRs, taking into account reproducibility for different test runs, manufacturing tolerances and uncertainties of the measurement hardware. The experimental data and the absolute uncertainties are presented in table 6-7..

Table 6-7: MSWT model-scale experimental results including 2.5% uncertainty.

TSR	C_T	$\pm U_{exp}$	C_P	$\pm U_{exp}$
[–]	[–]	[–]	[–]	[–]
Flow Case $V_{wind} = 2.0 \text{ m/s}$				
1.32	0.124	3.11E-3	0.007	1.70E-4
2.64	0.214	5.35E-3	0.016	4.03E-4
3.96	0.320	8.01E-3	0.030	7.48E-4
5.28	0.437	1.09E-2	0.050	1.26E-3
6.60	0.636	1.59E-2	0.191	4.78E-3
7.92	0.787	1.97E-2	0.306	7.66E-3
9.24	0.850	2.13E-2	0.269	6.72E-3

Input Uncertainty The input uncertainty originates from a number of assumptions and simplifications made in the numerical model (see section 2-5). Blockage effects caused by the imposed boundary conditions are neglected, following the domain size study described in section 6-1. Furthermore, setting regarding initial turbulence, surface roughness and pitch angle accuracy are of great importance, especially for the unsteady low Reynolds number flow considered here. The remaining uncertainty due to simplifications such as the applied hub geometry and neglected turbine tower are extremely difficult to quantify. For simplicity the input uncertainty of $U_{inp} = 0$ is assumed.

Numerical Uncertainty The numerical uncertainty estimation presented in section 6-2 shows a large difference between the uncertainties of C_T and C_P , which are caused by a combination of the complex highly separated flow, the application of unstructured grids and, to some extend, the iterative convergence. Nevertheless the relative difference of the considered integral quantities show a converging trend when refining the grid.

To provide the best possible insight in the validity of the performed computations the validation procedure is performed using the estimated numerical uncertainty based on the least-squares method as proposed, as well as the uncertainty based on the relative difference between the two finest grids considered. For the relative difference method a safety factor of 3.0 is used, as suggested in [41].

Furthermore it must be noted that only one flow condition is used for the uncertainty estimation, i.e. $TSR = 7.0$. In principle, when following the validation procedure, only this specific flow conditions can be validated. Strictly speaking when a validation for all TSRs is desired the uncertainty study presented in section 6-2 must be performed for all TSRs separately. In this study however a uniform numerical uncertainty is assumed over the full range of TSRs.

The resulting numerical uncertainties are presented in table 6-8, where $U_{\phi_{LS}}$ and $U_{\phi_{rel}}$ represent the numerical uncertainty based on the least-squares method and relative difference of the finest grids respectively. Note that for $U_{\phi_{rel}}$ the safety factor of $F_s = 3.0$ is already included.

Table 6-8: MSWT model-scale numerical uncertainty obtained using relative difference of two finest grids and uncertainty estimation based on least-squares method.

	C_T	C_P
$U_{\phi_{LS}}$	1.39%	32.31%
$U_{\phi_{rel}} (F_s = 3.0)$	0.54%	7.32%

Validation uncertainty Using equation (2-94) and considering the assumptions mentioned above, the validation uncertainty U_{val} can be computed. The resulting values of U_{val} are presented in table 6-9, where $U_{val(LS)}$ represents the uncertainty based on the method using a least-squares fit of an error power law and $U_{val(rel)}$ the uncertainty based on the relative difference of the two finest grids.

Table 6-9: MSWT model-scale validation uncertainty obtained using relative difference of two finest grids and uncertainty estimation based on least-squares method.

	C_T	C_P
$U_{val(LS)}$	2.86 %	32.41 %
$U_{val(rel)}$	2.56 %	7.74 %

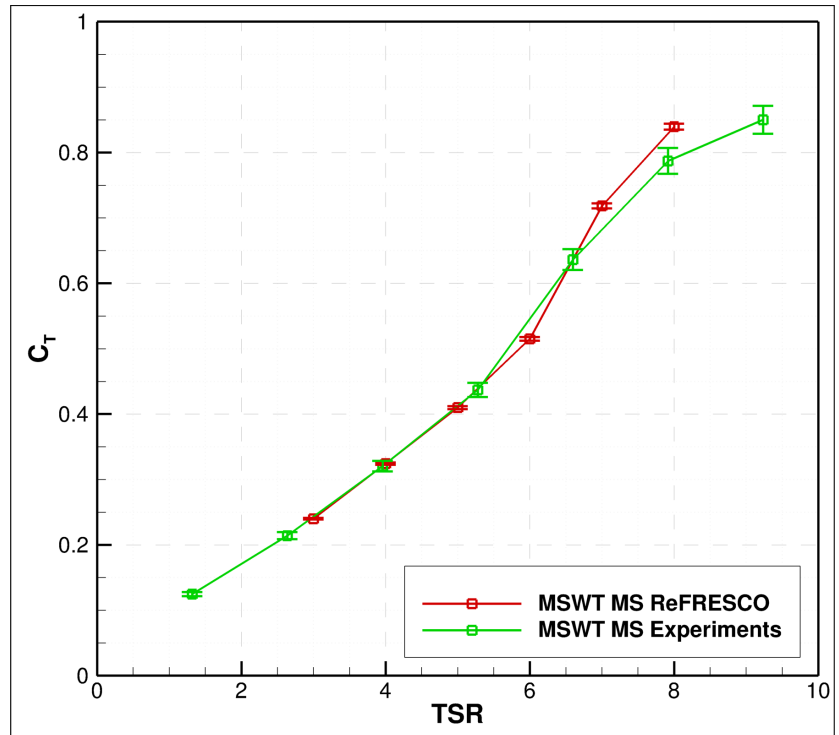
The C_T and C_P curves of both the experiments and numerical computations are presented in figures 6-11 and 6-12, in which the uncertainties presented in table 6-9 are also given. Both methods show similar uncertainties for C_T , while the differences for C_P are much larger.

Comparison Error and Validation The comparison error given by equation 2-95 can now be computed and compared with the validation uncertainties. The absolute comparison errors E and the validation uncertainties are given in table 6-10 for C_T and C_P . The comparison errors marked green are validated whereas the errors marked in red are not.

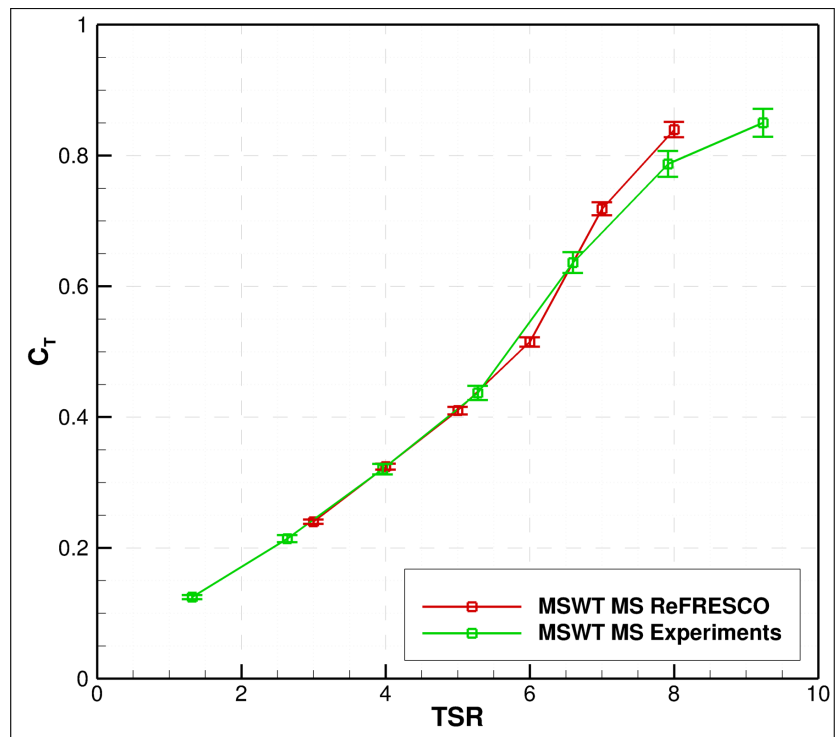
Although a large difference in validation uncertainty is observed between the two methods proposed (least-squares and relative difference), the validation results presented in table 6-10 are the same. Only the tip speed ratios 3 to 5 are validated with the experimental results whereas the tip speed ratios ranging from 6 to 8 are not.

The results which do not comply with the validation constraints are all for large TSRs, at which the numerical solutions are depending heavily on the numerical setup (grid resolutions and turbulence model). This is a direct result of the unsteady and partially separated flow regime in which the turbine is operating.

It must be mentioned that the experimental and numerical data used in this study are for different tip speed ratios, linear interpolation is used to obtain the intermediate values of C_T and C_P . Additionally the numerical and experimental uncertainties are assumed uniform for

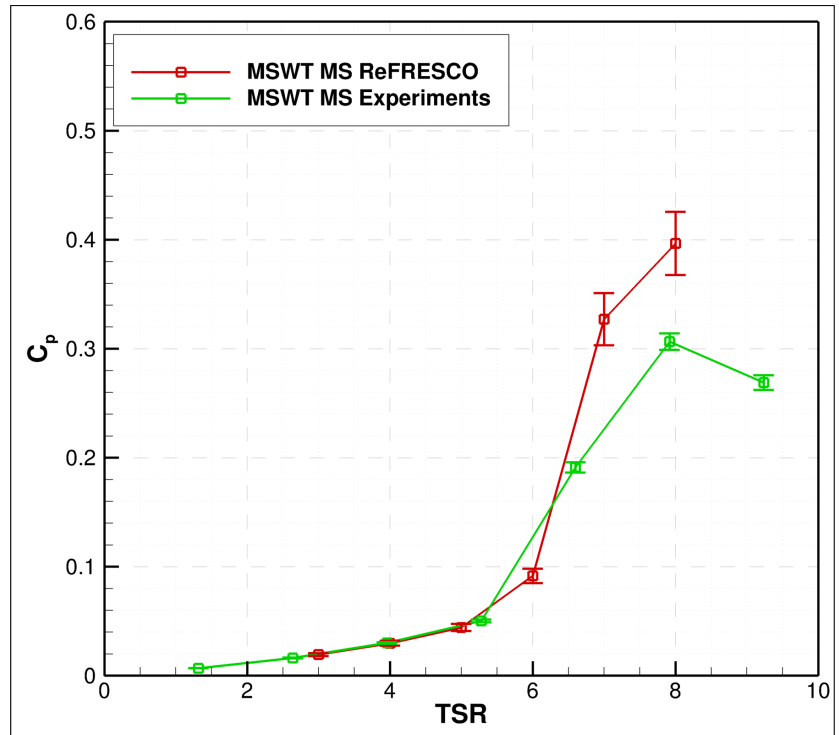


(a) Uncertainties based on relative difference between the two finest grids ($U_{\phi_{rel}}$).

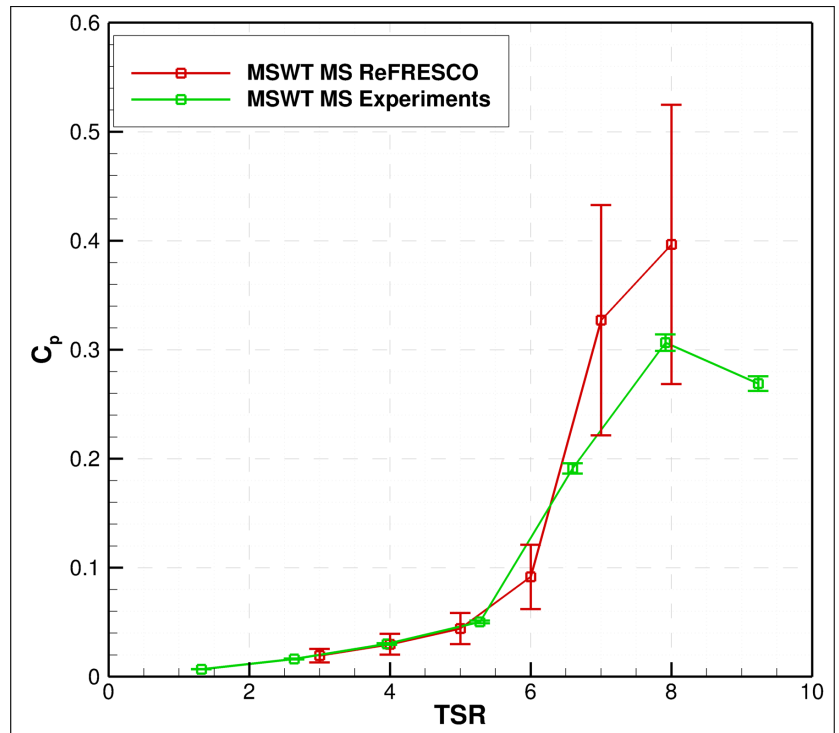


(b) Uncertainties based on least-squares approach ($U_{\phi_{LS}}$).

Figure 6-11: C_T curves of model-scale MSWT including uncertainties ($V_{wind} = 2.0 \text{ m/s}$).



(a) Uncertainties based on relative difference between the two finest grids ($U_{\phi_{rel}}$).



(b) Uncertainties based on least-squares approach ($U_{\phi_{LS}}$).

Figure 6-12: C_P curves of model-scale MSWT including uncertainties ($V_{wind} = 2.0 \text{ m/s}$).

Table 6-10: Absolute comparison error $|E|$ for both C_T and C_P .

TSR	$ E _{C_T}$	$ E _{C_P}$	$U_{val} (C_T)$	$U_{val} (C_P)$
least-squares based numerical uncertainty $U_{val(LS)}$				
3	1.35	3.41	2.86%	32.41%
4	0.03	2.97	2.86%	32.41%
5	0.62	4.09	2.86%	32.41%
6	5.70	28.19	2.86%	32.41%
7	5.30	44.47	2.86%	32.41%
8	6.13	30.43	2.86%	32.41%
relative difference based numerical uncertainty $U_{val(rel)}$				
3	1.35	3.41	2.56%	7.74%
4	0.03	2.97	2.56%	7.74%
5	0.62	4.09	2.56%	7.74%
6	5.70	28.19	2.56%	7.74%
7	5.30	44.47	2.56%	7.74%
8	6.13	30.43	2.56%	7.74%

the full range of TSRs. In order to improve the validation study, numerical and experimental uncertainties need to be determined over the full range of TSRs. Furthermore the tip speed ratios of the experimental and numerical results need to be matched such that interpolation is not needed.

6-5 General Flow Characteristics

The findings of the previous sections are now further analyzed for a range of tip speed ratios varying from $TSR = 3.0$ to $TSR = 8.0$. This range of TSRs is based on the condition close to the cut-in and operating condition of the turbine, at $TSR = 1.65$ and $TSR = 7.0$ respectively.

The wind speed is set to a constant value of $V_{wind} = 2.0 \text{ m/s}$ for which experimental data is available. The limiting streamlines over the suction side of the turbine blades are given in figure 6-13. $TSR = 3.0$ to $TSR = 6.0$ in this figure show a fully separated flow over the whole span of the blade. At this TSRs the turbine blades are subject to a large apparent angle of attack over the full radius, resulting in large adverse pressure gradients at the suction side of the blade near the trailing edge. Since the turbine at model-scale operates in the sub critical regime, the flow is not able to withstand these pressure gradients without separating from the blade surface, hence the turbine is fully stalled.

Although the apparent angle of attack is not directly computed, the geometrical angle of attack is a good alternative indicator for the exact apparent angle of attack. The geometrical angles of attack along the MSWT are given for the operating condition in table 4-1.

When the tip speed ratio is increased the apparent angle of attack over the foil is reduced, with the smallest angle of attack located at the tip of the blades, as shown in table 4-1. This is a direct result of the high radial velocity at the tip and the twist of the turbine blade.

Near the blade tip at these higher TSRs the angle of attack is small enough for the flow to

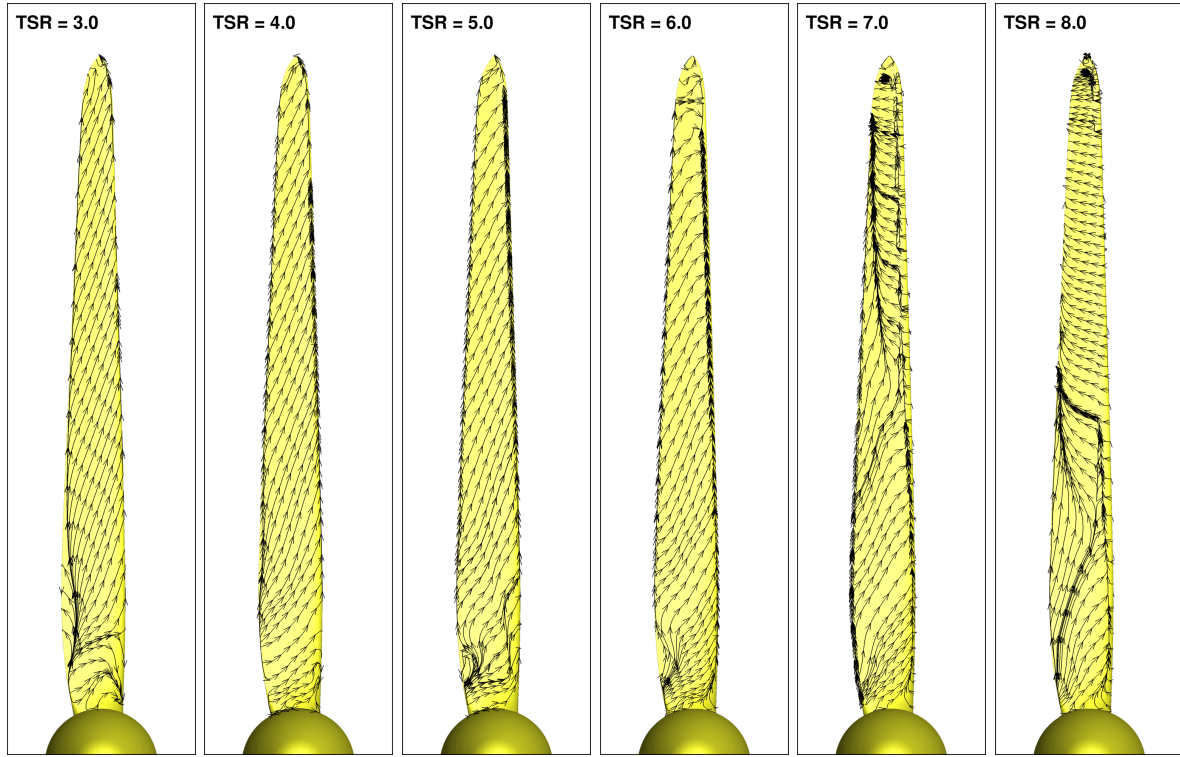


Figure 6-13: Limiting streamlines for model-scale MSWT at various TSR.

remain attached. This is also observed in 6-13, where the limiting streamlines show a fully attached region near the tip at $TSR = 7.0$ and $TSR = 8.0$.

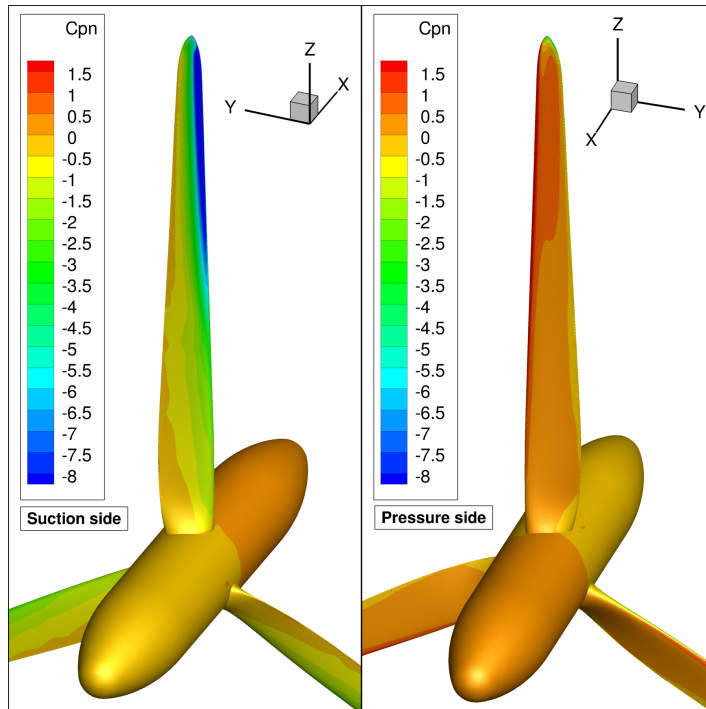
The pressure distribution over the turbine blades at the design condition is given for both the pressure and suction side in figure 6-14(a) by means of C_{pn} .

The region near the blade tips, where the flow is fully attached, show the largest difference between the pressure and suction side. It is this region where a large portion of the torque about the x -axis is generated. This is due to the attached flow which generates large amounts of lift, combined with a large distance from the center of rotation.

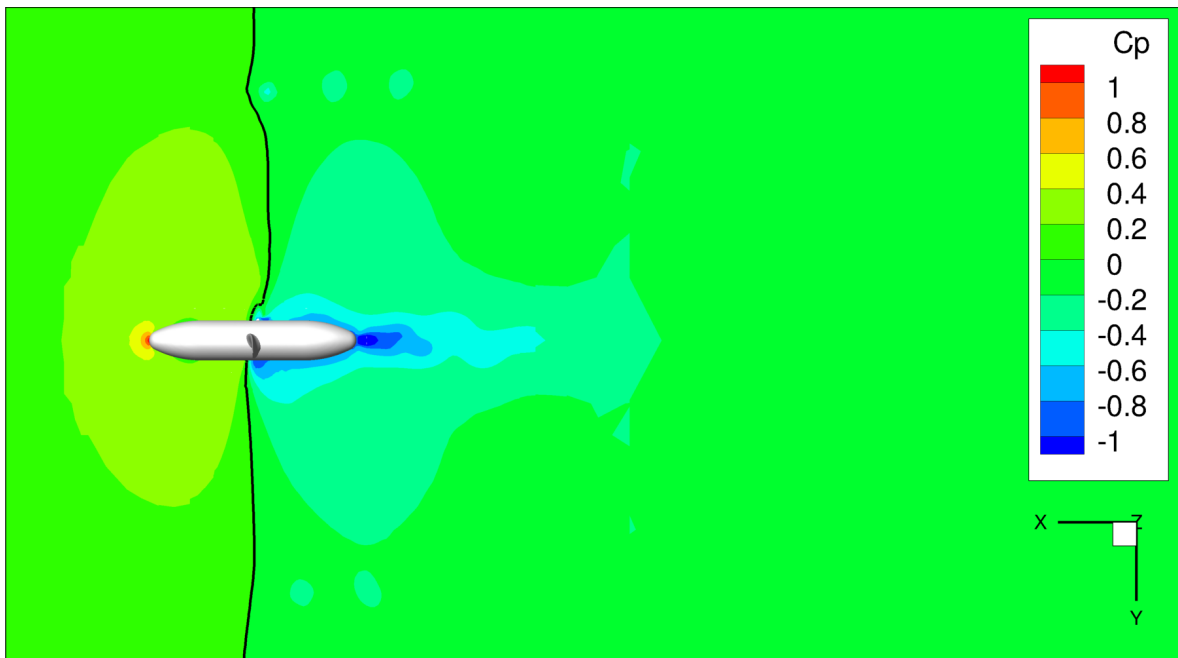
Near the blade roots the pressure difference between the pressure and suction side of the turbine is much smaller due to the separated flow in this region. As a result the lift generated in this stalled region is only small. The combination of a stalled condition and a small radial distance result in the fact that the torque contribution of the region near the root is only small.

Since torque is directly related to the production of power by means of equation (4-17), a fully attached flow over the full turbine blade is desirable. However a fully attached flow near the blade tip is crucial since its significant contribution to the total amount of torque produced.

The pressure field in the domain is presented in figure 6-14(b) by means of C_p . Here an iso-curve indicates the difference between the region with positive and negative pressure coefficients. In this figure the effect of the increased velocities in the tip vortices is clearly visible by means of a locally reduced C_p .



(a) Normalize pressure distribution on a turbine blade.



(b) Normalize pressure distribution in the domain.

Figure 6-14: Pressure distribution on a turbine blade and in the domain at $TSR = 7.0$.

The flow in the domain further away from the turbine is presented in figure 6-15, here the normalized axial and radial velocities $\bar{V}_{x,y} = V_{x,y}/V_{wind}$ are plotted in the xy -plane at the rotating axis of the turbine.

The iso-curves in figure 6-15(a) are set to one, representing the boundary between decelerated and undisturbed flow. The flow in the region directly in front and aft of the turbine are decelerated due to the energy being extracted from the wind by the turbine. This is also in line with the actuator disc theory discussed in section 2-3-2 (see figure 2-9).

Finally the deceleration of the flow in the wake-field is dissipated due to the reduction of the grid resolution in this region, as can be seen in figure 4-10(b). The wake-field of the turbine blades is clearly visible in figure 6-15(b) by the increased velocity magnitudes in the wake-field. To further visualize the vortices generated by the turbine, the normalized Q -factor and the normalized vorticity $\bar{\omega}_y = \omega D/V_{wind}$ are plotted in figure 6-16.

In these figures the tip vortex and root vortex are clearly visible. Due to the reduced grid resolution away from the turbine blade the vortices are dissipated, which is causing the iso-surface of the Q -factor to vanish in these regions.

When analysis of the wake-field is required a higher grid resolution is needed in this region to prevent the perturbations in the wake-field to dissipate due to poor grid resolution. This dissipating effect was also demonstrated in [42].

Finally the numerical results are compared to the experimental results in table 6-11, where C_T and C_P are given for the full range of TSRs.

Table 6-11: Thrust and power coefficients of both experiments and ReFRESCO calculations of the MSWT at model-scale

TSR	Experiments		ReFRESCO	
	C_T	C_P	C_T	C_P
MSWT at model-scale $V_{wind} = 2.0 \text{ m/s}$				
3.0	0.2432	0.0199	0.2399	0.0192
4.0	0.3241	0.0306	0.3242	0.0297
5.0	0.4124	0.0460	0.4098	0.0441
6.0	0.5460	0.1274	0.5149	0.0915
7.0	0.6823	0.2263	0.7185	0.3270
8.0	0.7911	0.3041	0.8396	0.3966

Note that for this table linear interpolation is used to match the experimental and numerical data for the desired TSRs. In addition to table 6-11, the results are plotted in figure 6-17

The numerical results presented in figure 6-17 show a good agreement with the experiments for C_T . The results of C_P show a good agreement in the low TSR range, however larger differences are found in the higher TSR range.

Above a TSR of 6.0 the flow is no longer fully separated and an attached region at the blade tip starts to develop, which will grow for an increasing TSR (see figure 6-13). As explained, the power coefficient is highly sensitive to the size of the attached flow region, since the majority of the power is produced in this region.

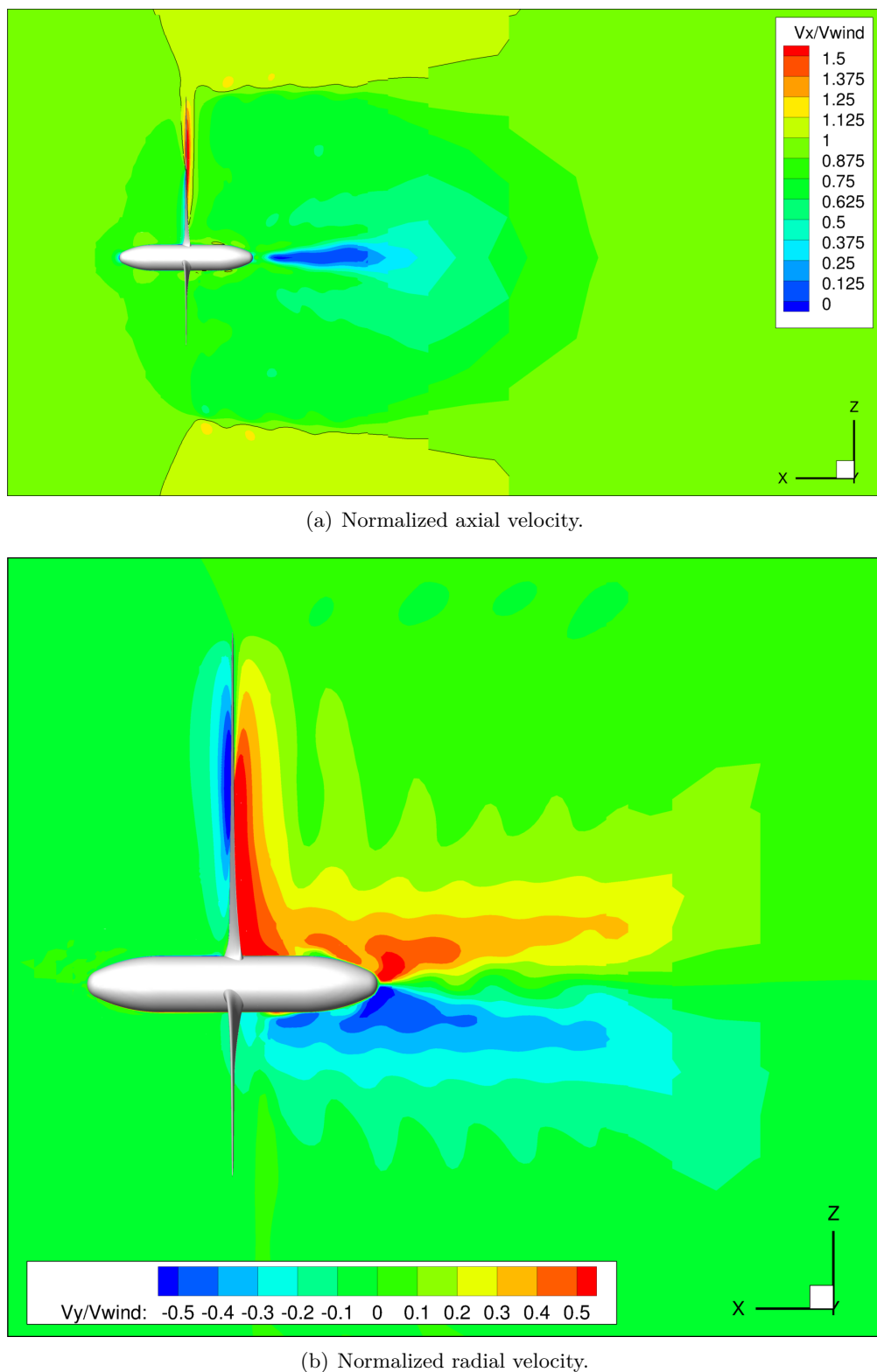


Figure 6-15: Normalized velocities over the turbine at $TSR = 7.0$.

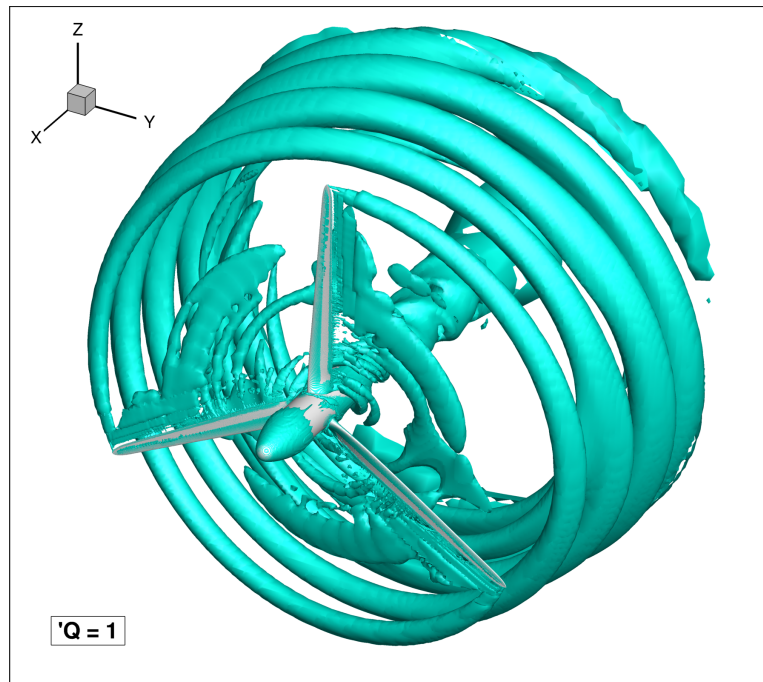
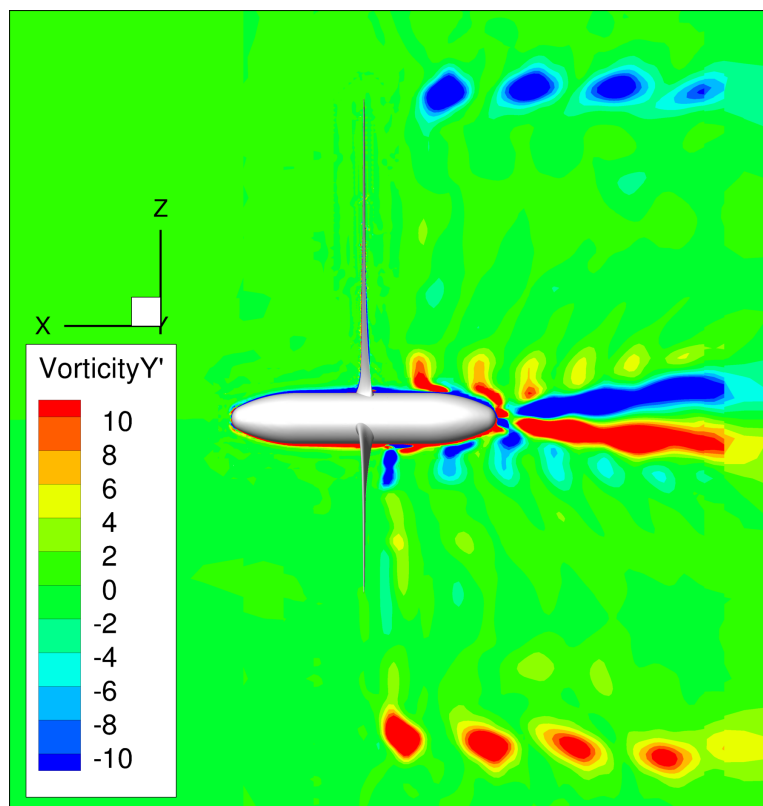
(a) Normalized Q -factor in the wake-field(b) Normalized vorticity about the y -axis in the wake-field

Figure 6-16: Normalized Q -factor and vorticity $\bar{\omega}_y$ in the wake-field at $TSR = 7.0$.

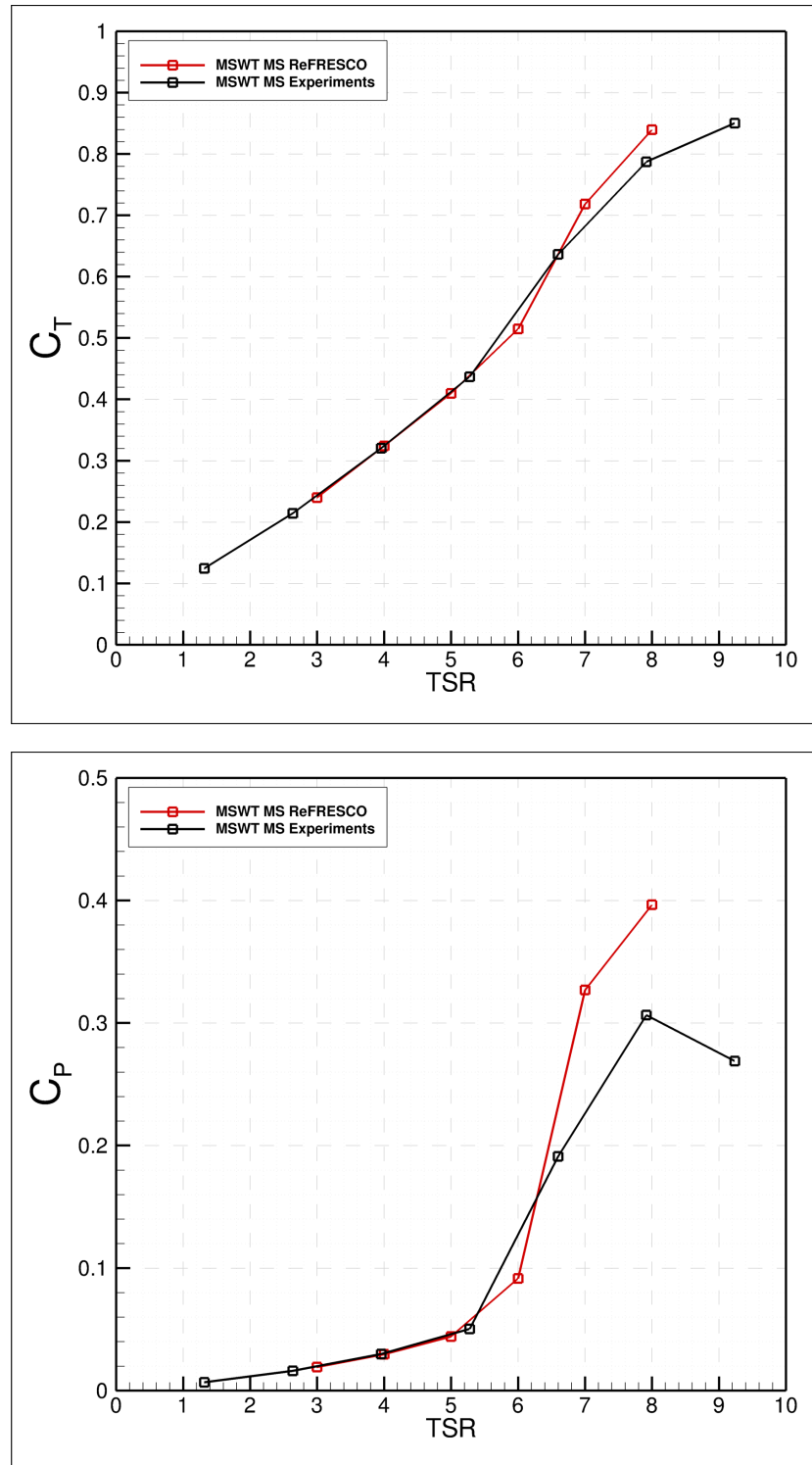


Figure 6-17: Thrust and power coefficient of MSWT experiments and numerical simulations at model-scale conditions as function of tip speed ratio ($V_{wind} = 2.0 \text{ m/s}$).

It can be concluded that there is a good match between numerically and experimentally obtained C_T and C_P curves, especially considering the unsteady highly separated low Reynolds number flow. Although the increased sensitivity of C_P results in a larger difference in the higher TSR-range, C_T shows good result over the full range of TSRs, which was the main goal of the performance-scaled turbine geometry.

Chapter 7

Comparison of NREL 5MW and MARIN Stock Wind Turbine (MSWT) Scaling Effects

In this chapter a comparison is made between the model-scale and full-scale NREL 5MW baseline turbine and the MSWT. First in section 7-1 the flow over the NREL 5MW baseline turbine is discussed and the relevant scaling effects presented. Similar topics concerning the MSWT are covered in section 7-2. In section 7-3 comparison is made between the flow over the full-scale NREL 5MW baseline turbine and the model-scale MSWT. Finally the C_T and C_P curves obtained from the RANS computations for the full-scale NREL 5MW baseline turbine are compared with the BEMT tool data in section 7-4.

7-1 Scaling Effects on the NREL 5MW Baseline Turbine

In this section the RANS computations on the model- and full-scale flow over the NREL 5MW baseline turbine are presented. As discussed the Froude-based scaling method is used to scale the wind velocity and the geometry is kept the same. For the model-scale conditions an inflow velocity of $V_{wind} = 2.0 \text{ m/s}$ is used whereas an inflow velocity of $V_{wind} = 11.4 \text{ m/s}$ is used to represent the full-scale conditions.

In figure 7-1 the turbulence viscosity is plotted at several sections along the blade span for both model- and full-scale conditions. This figure clearly shows the difference in turbulence intensity between the latter. At full-scale conditions transition occurs close to the leading edge, which enables the flow to remain attached to the surface when subject to large adverse pressure gradients. The opposite is true for the model-scale flow, hence the adverse pressure gradients cause the flow to separate after which transition occurs due to the unsteady nature of the flow in the wake-field, as can be seen in figure 7-1(a) by means of an increased production of turbulence viscosity.

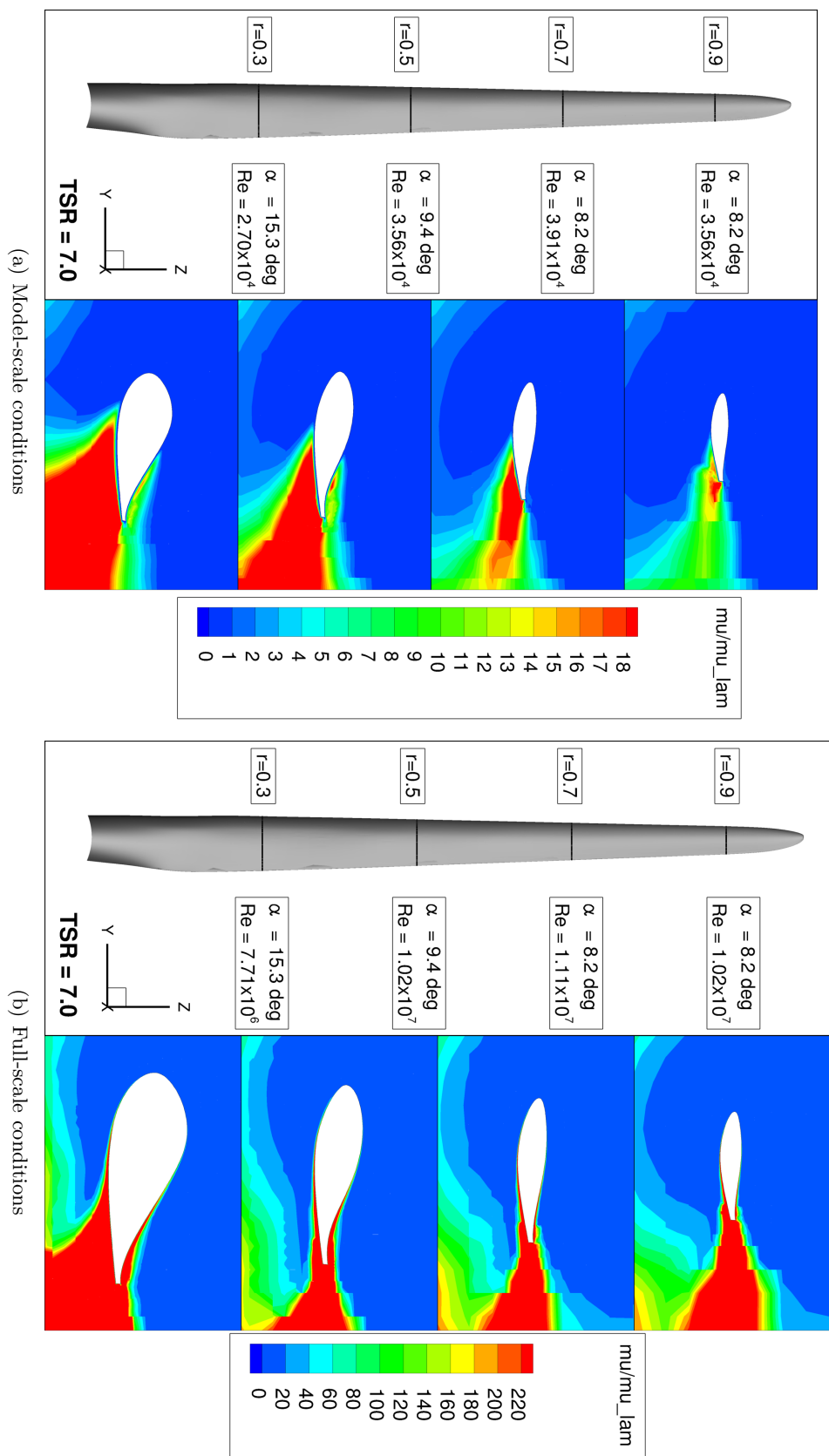


Figure 7-1: Turbulence viscosity at various sections along the blade span for NREL 5MW baseline turbine at model- and full-scale $TSR = 7.0$. Reynolds numbers presented are based on local chord length and velocity.

The limiting streamlines at the suction side of the blades are presented in figure 7-2 for model- and full-scale. Due to the laminar character of the flow at model-scale the foil is in stalled condition over the full range of $TSRs$, as can be seen in figures 7-2(a) to 7-2(f).

For the full-scale condition at which the flow can be considered fully turbulent, separation occurs at low $TSRs$ only due to heavily loaded blades and large local angles of attack. In the separated regions the local flow has a large radial velocity component, which contradicts the 2D flow assumption made in the previously discussed Blade Element Momentum Theory (BEMT). On the contrary for larger $TSRs$ the radial velocity components at the blades are indeed small, which justifies the BEMT assumptions (see figures 7-2(g) to 7-2(l)).

In addition to flow separation at the suction side of the thick cambered airfoil sections, a laminar separation bubble is observed at the pressure side of the blades at model-scale. The limiting streamlines in figure 7-3(b) clearly show the presence of this separation bubble near the trailing edge. Note that the bubble does not reach to the blade tip region, where the local velocities are higher and airfoil sections are much thinner.

The separation bubble can also be seen in figure 7-3(a) at $r = 0.3$ and $r = 0.5$. The separation bubble alters the local displacement thickness, reducing the effective camber of the airfoil. Which, as explained in section 2-3-1, has a negative influence on the amount of produced lift.

The fully separated flow in combination with the decambering effect of the separation bubble result in very poor C_T and C_P characteristics at model scale, which justifies the previous observations in [14, 17].

The C_T and C_P curves of the full-scale and model-scale RANS computations and the model-scale experiments are presented in figure 7-4. The experimental data published by H. R. Martin of the University of Maine [17] is presented in figure 7-4, along with the numerical RANS data of the model- and full-scale NREL 5MW turbine.

The experimental data available, uses a pitch angle of 6.4 degrees and a wind velocity of $V_{wind} = 2.94 \text{ m/s}$. Whereas for the RANS computations zero pitch angle was applied similar to the full-scale setup. This is done to avoid the need for an extra numerical grid to compute the 6.4 degrees pitch angle case. Additionally a model-scale wind velocity of $V_{wind} = 2.0 \text{ m/s}$ was used similar to that of the MSWT measurements. Although requested, by the time this thesis is written, only the measurement data above was provided, hence the presented model-scale measurement data is indicative only. The difference in the applied pitch angle and wind velocity results in the observed difference between the experimental and RANS data in figure 7-4.

7-2 Scaling Effects on the MARIN Stock Wind Turbine

Following the poor model-scale performance of the NREL 5MW baseline turbine [14, 17], the new low Reynolds-number MSWT was designed, built and tested. In this section the numerically obtained flow over the redesigned turbine is presented and discussed. For the model-scale conditions an inflow velocity of $V_{wind} = 2.0 \text{ m/s}$ is used whereas an inflow velocity of $V_{wind} = 11.4 \text{ m/s}$ is used to represent the full-scale conditions.

In figure 7-5 the turbulence viscosity is plotted at several sections along the blade span for both model- and full-scale conditions. This figure clearly shows the difference in turbulence

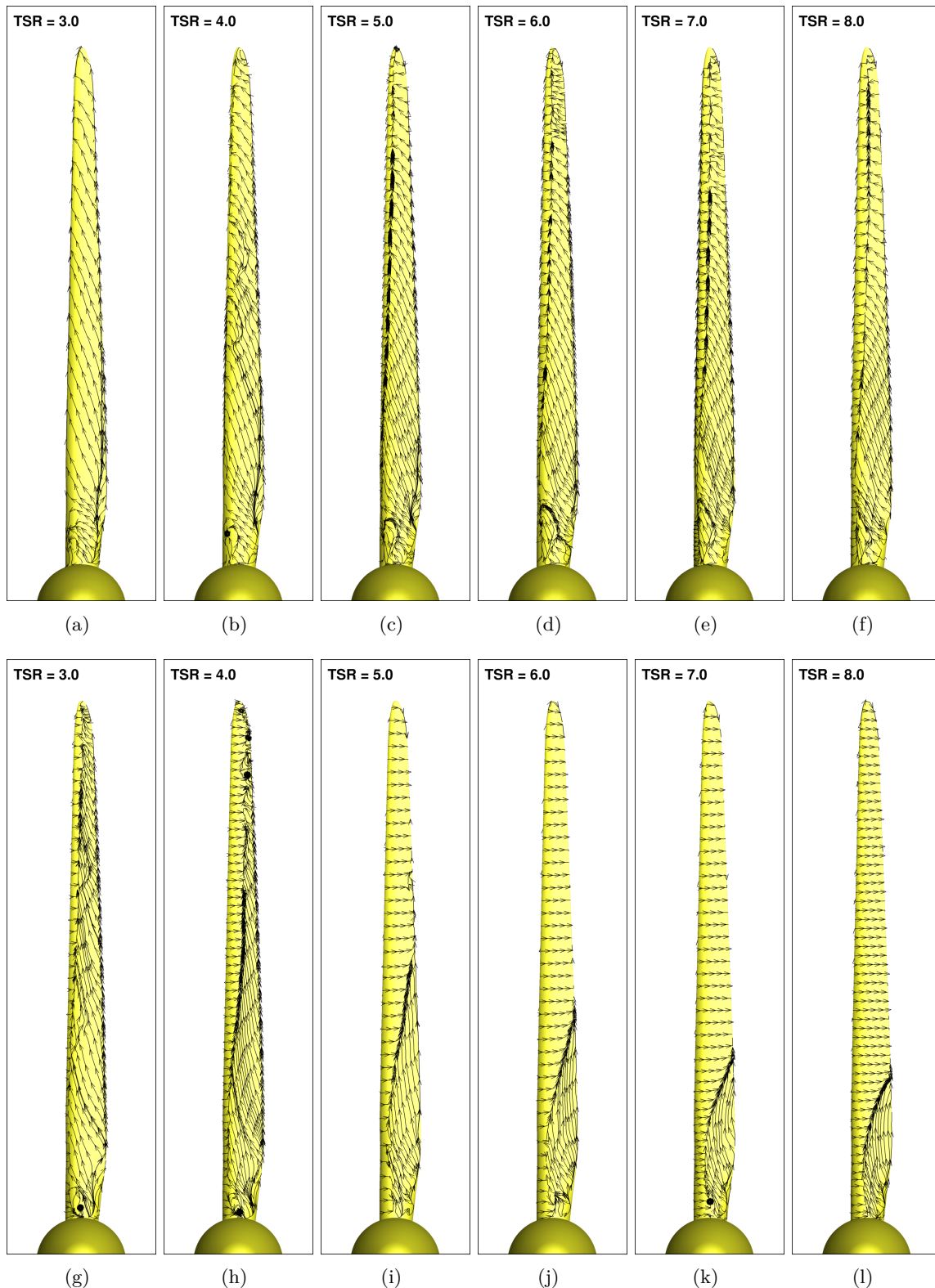


Figure 7-2: Limiting streamlines over the suction side of a turbine blade for model-scale (top) and full-scale (bottom) NREL 5MW wind turbine at various TSR.

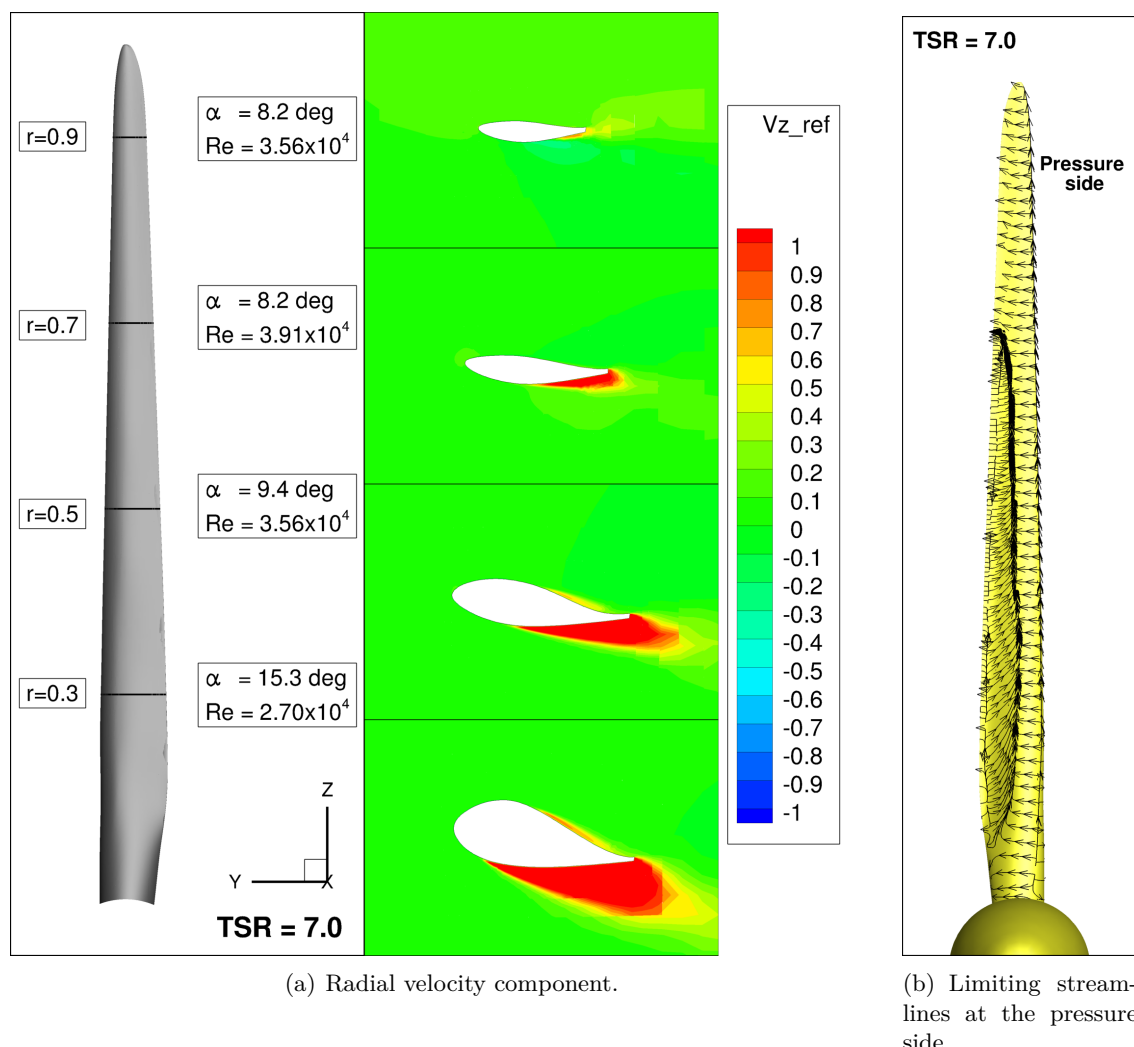
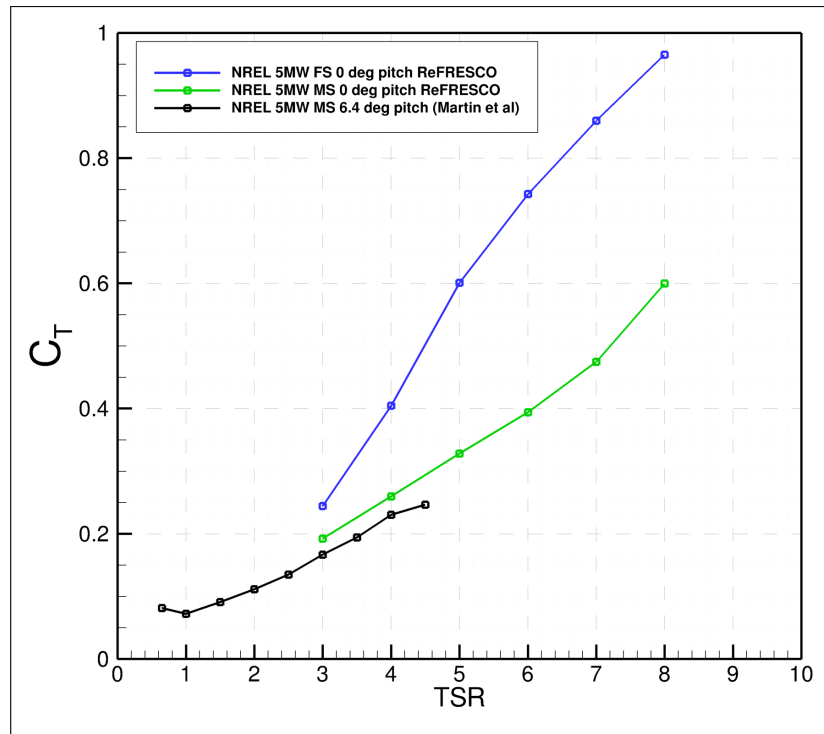
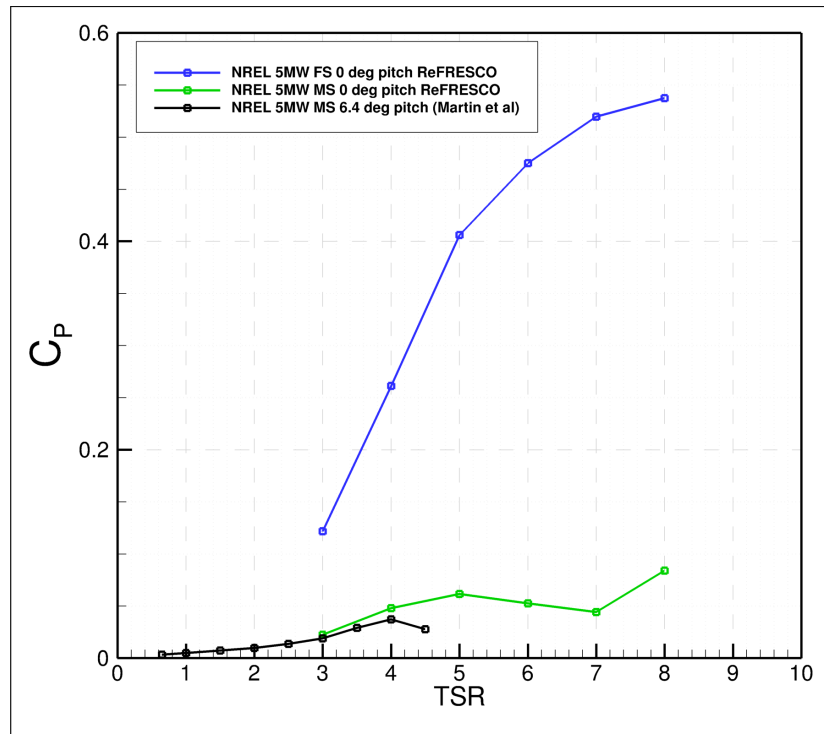


Figure 7-3: Radial velocity and limiting streamlines at the turbine blade for $TSR = 7.0$. Reynolds numbers presented are based on local chord length and velocity.



(a) Thrust coefficient



(b) Power coefficient

Figure 7-4: Thrust and power coefficient as function of TSR for both model- and full-scale NREL 5MW baseline wind turbine.

intensity between the model- and full-scale flow. At full-scale conditions transition occurs close to the leading edge, which enables the flow to remain attached to the surface when subject to large adverse pressure gradients. The opposite is true for the model-scale flow, where the adverse pressure gradients cause the flow to separate. After the flow has separated transition occurs due to the unsteady nature of the flow in the wake-field, as can be seen in figure 7-5(a) by means of an increased production of turbulence viscosity.

The limiting streamlines at the suction side of the blades are presented in figure 7-2 for model- and full-scale. Due to the laminar character of the flow at model-scale the foil is in stalled condition for $TSR = 3.0$ to $TSR = 6.0$, as can be seen in figures 7-6(a) to 7-6(d). For higher TSRs an attached region is located at the blade tip which will grow in size when the TSR is increased, as can be seen in figures 7-6(e) and 7-6(f). This is a direct result of the reduced angle of attack and increased local velocity when the TSR is increased. Furthermore, in addition to the improved aerodynamics by means of an attached flow region, a separation bubble does not exist and hence no decambering effects occur.

The separated region at the suction side of the blades have large radial velocity components, which contradicts the 2D-flow assumption made within the BEMT. At the attached flow regions for model- and full-scale, the radial velocity components along the blades are indeed small, justifying the BEMT assumed 2D flow (see figures 7-2(g) to 7-2(l)).

In figure 7-7 the thrust and power coefficients for the MSWT are plotted as a function of TSR. Here both model- and full-scale results are presented as obtained from experiments and RANS calculations. In these graphs the uncertainties for the model-scale MSWT are also plotted, in which the least-squares method was used for the numerical uncertainties.

Since both model- and full-scale turbines are in stalled condition at low TSRs, differences in C_T and C_P are only small. In the mid range TSRs an attached flow region starts to develop at full-scale while the flow remains separated at model-scale. As a result, the differences in C_T and C_P are larger. Finally when the attached region starts to develop at model-scale for the high TSRs, the differences are reduced.

7-3 Comparing the overall performance of the model-scale MSWT and full-scale NREL 5MW baseline turbine

Since the main goal of the MSWT design is to mimic the full-scale performance (C_T) of the NREL 5MW baseline turbine, a comparison is made between these two. In figure 7-8 the limiting streamlines over the suction side of both turbine geometries are presented. Furthermore the C_T and C_P curves of the latter models are presented in figure 7-9.

At low TSRs the flow over both turbines is fully separated as shown in figures 7-8(a) and 7-8(g). In the range of TSR 4.0 to 6.0 an attached flow region starts to develop over the blades of the NREL 5MW turbine whereas the flow over the model-scale MSWT is still fully separated, hence the increasing difference between the two flow cases. Finally for TSR 7.0 and above, an attached region is developing over the MSWT (figures 7-8(e) and 7-8(f)), which greatly increases the turbine's performance. This increased performance is also present in the figure 7-9 especially for C_P .

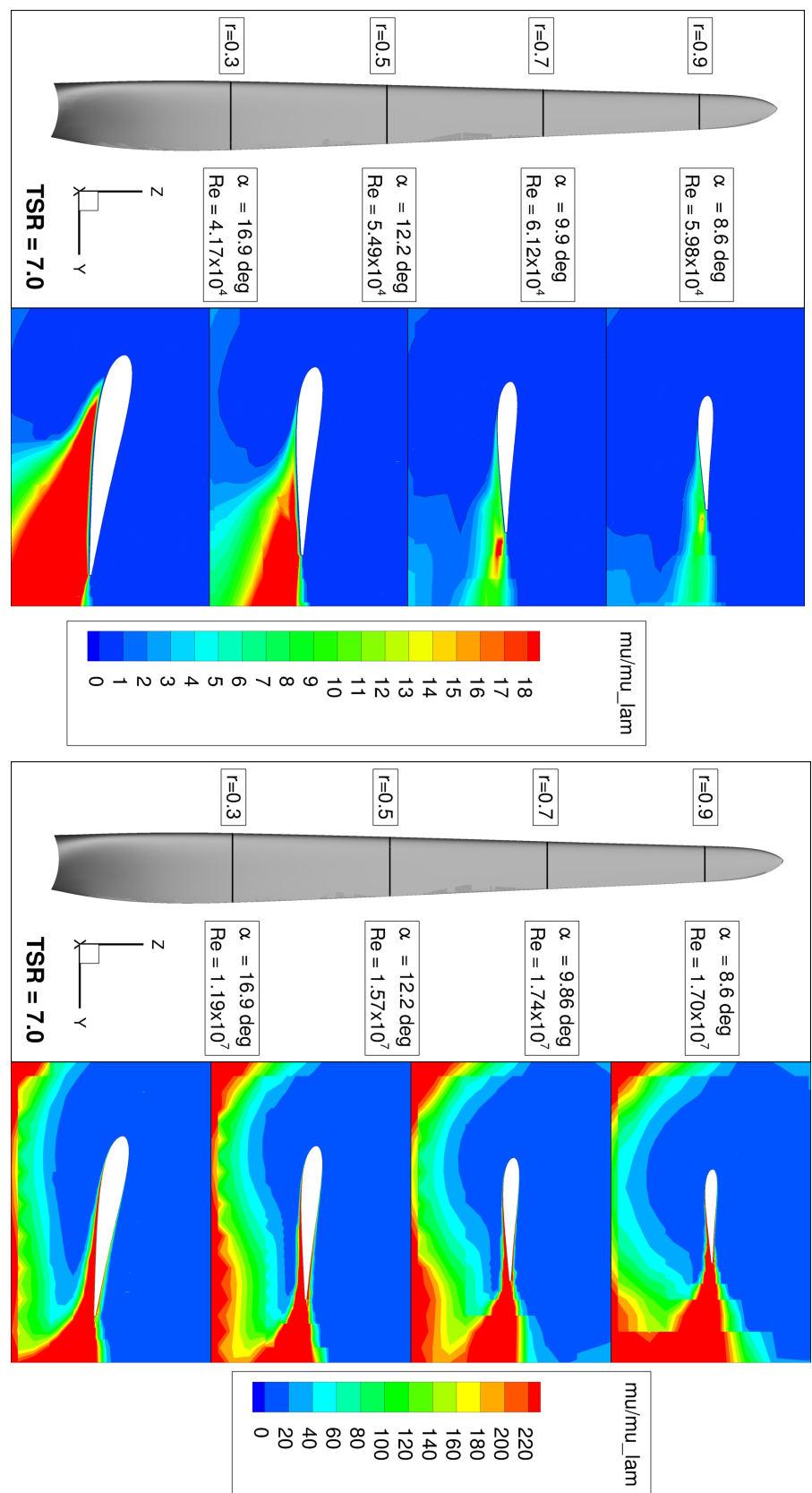


Figure 7-5: Turbulence viscosity at various sections along the blade span for MSWT at model- and full-scale $TSR = 7.0$.

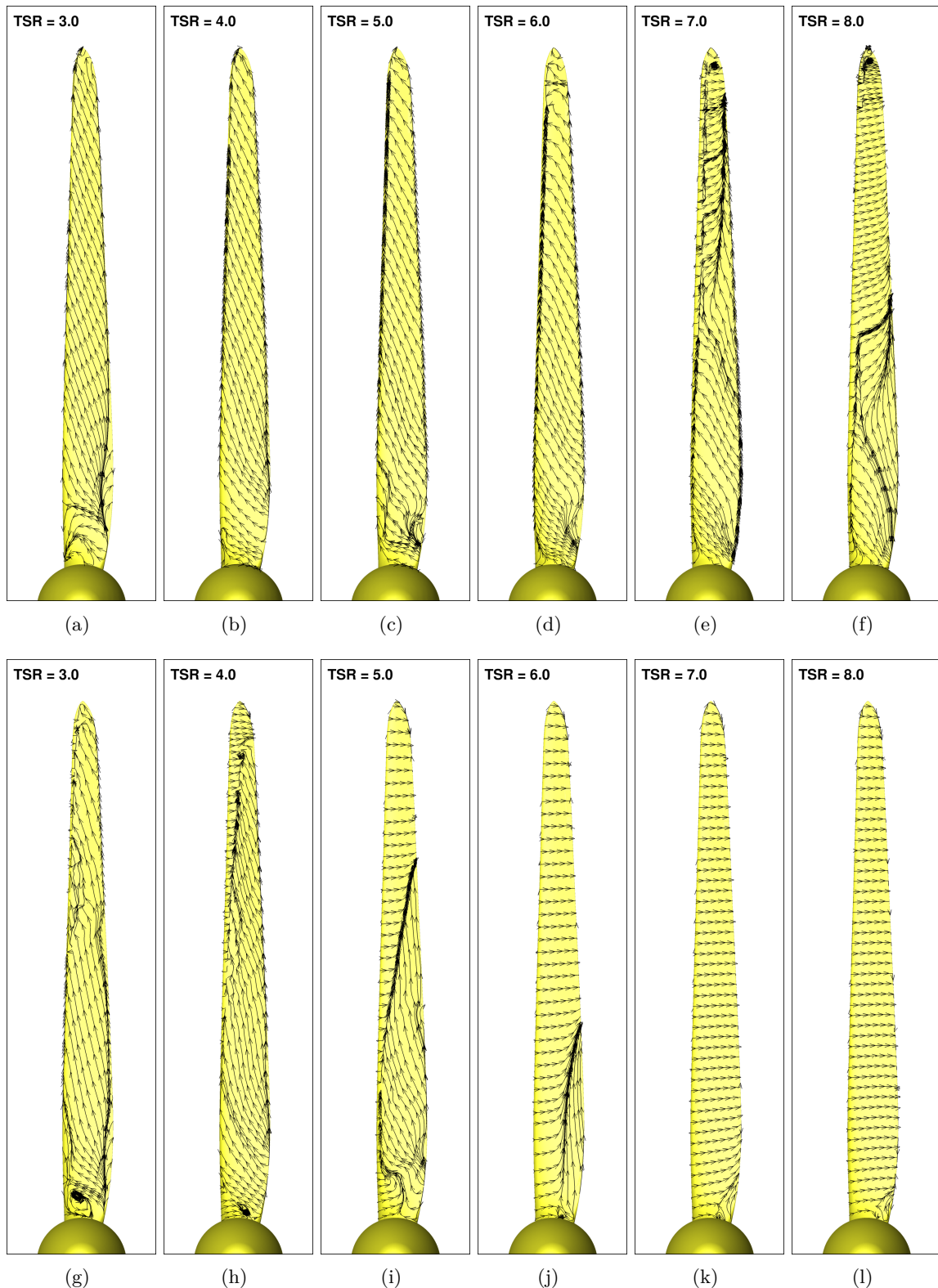
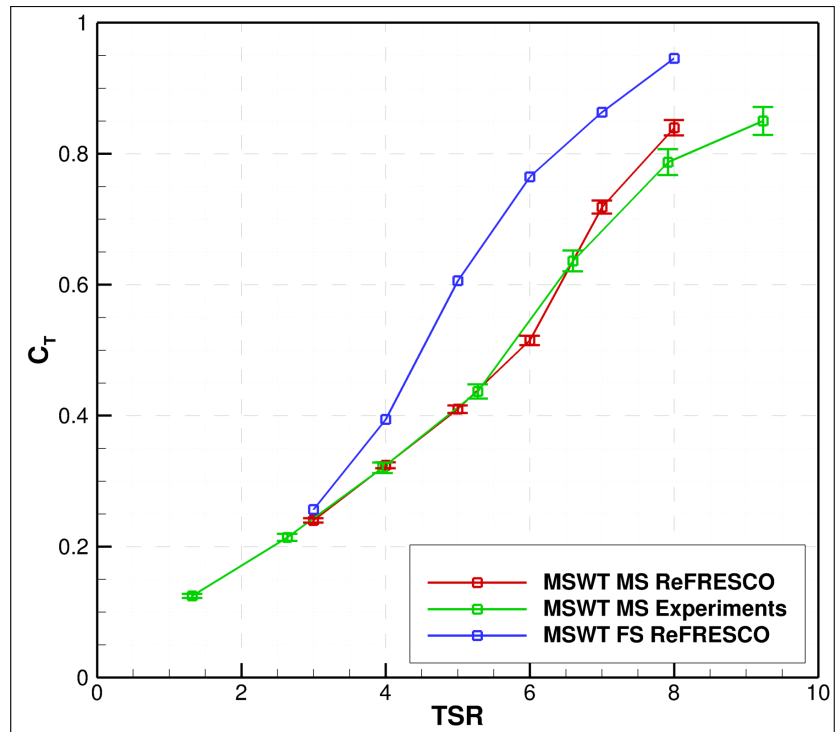
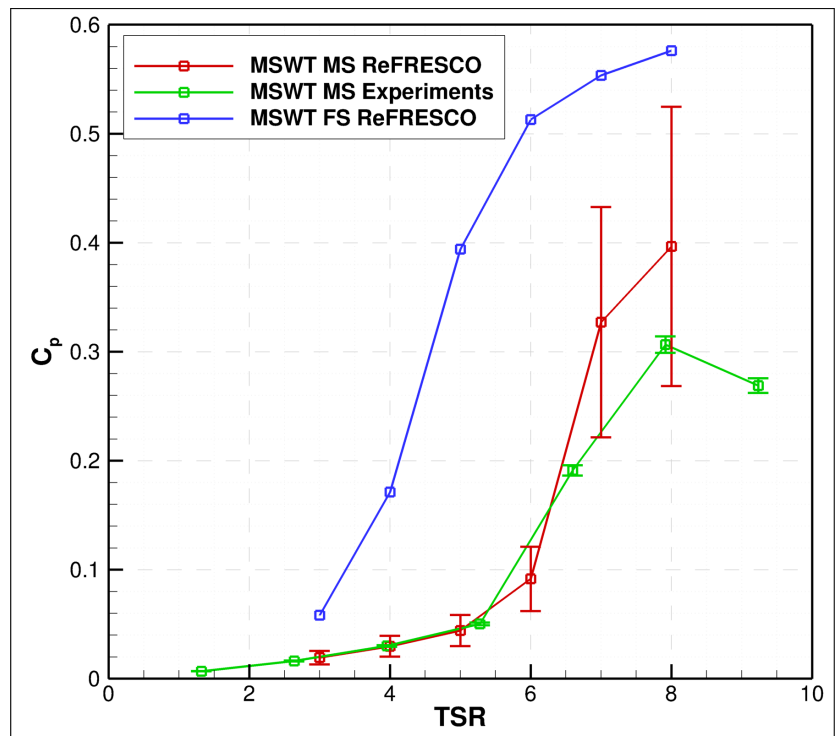


Figure 7-6: Limiting streamlines over the suction side of a turbine blade for model-scale (top) and full-scale (bottom) MSWT at various TSR.



(a) Thrust coefficient



(b) Power coefficient

Figure 7-7: Thrust and power coefficient as function of TSR for both model- and full-scale MARIN stock wind turbine.

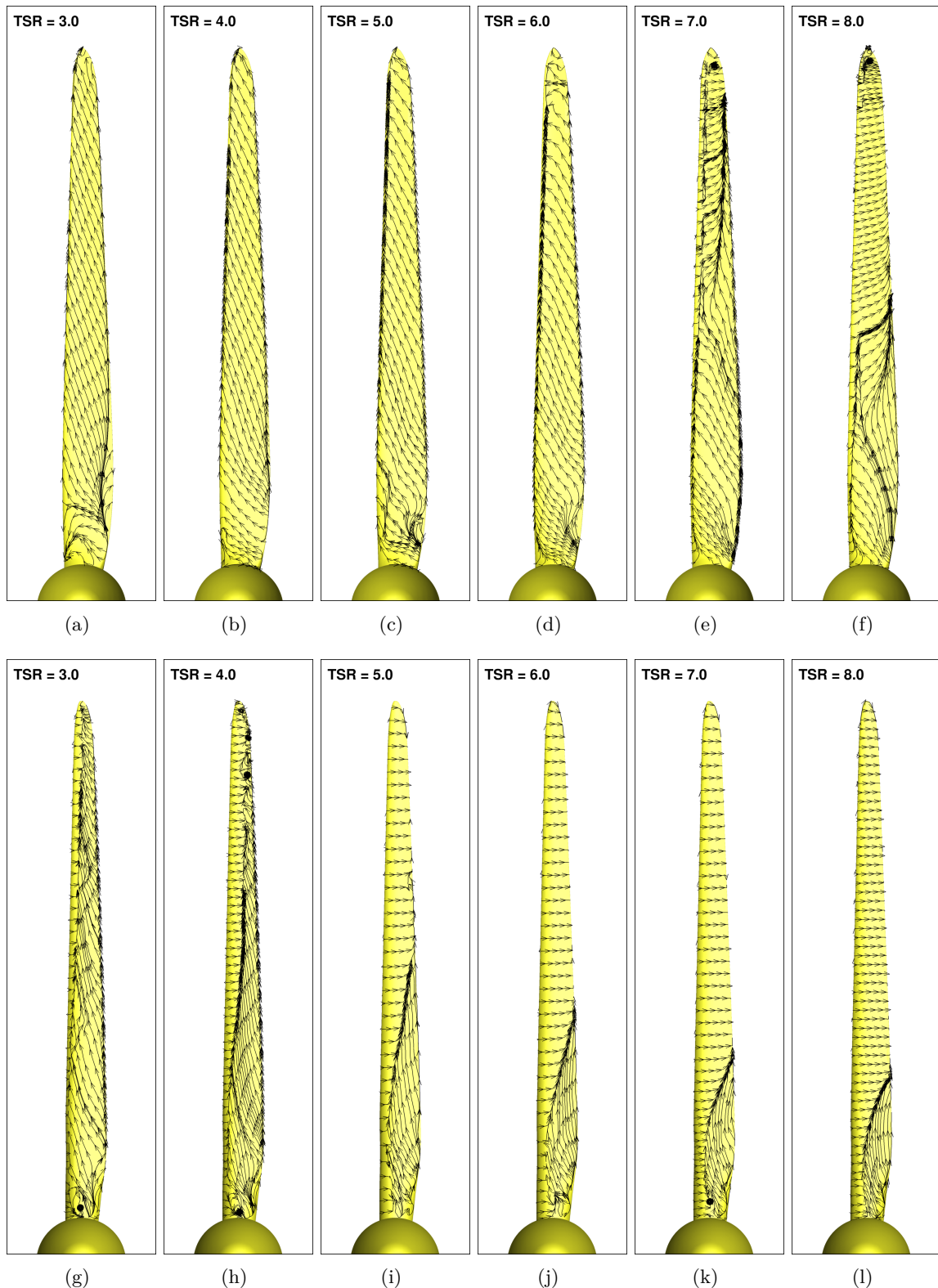


Figure 7-8: Limiting streamlines over the suction side of a turbine blade for model-scale MSWT (top) and full-scale NREL 5MW wind turbine (bottom) at various TSR.

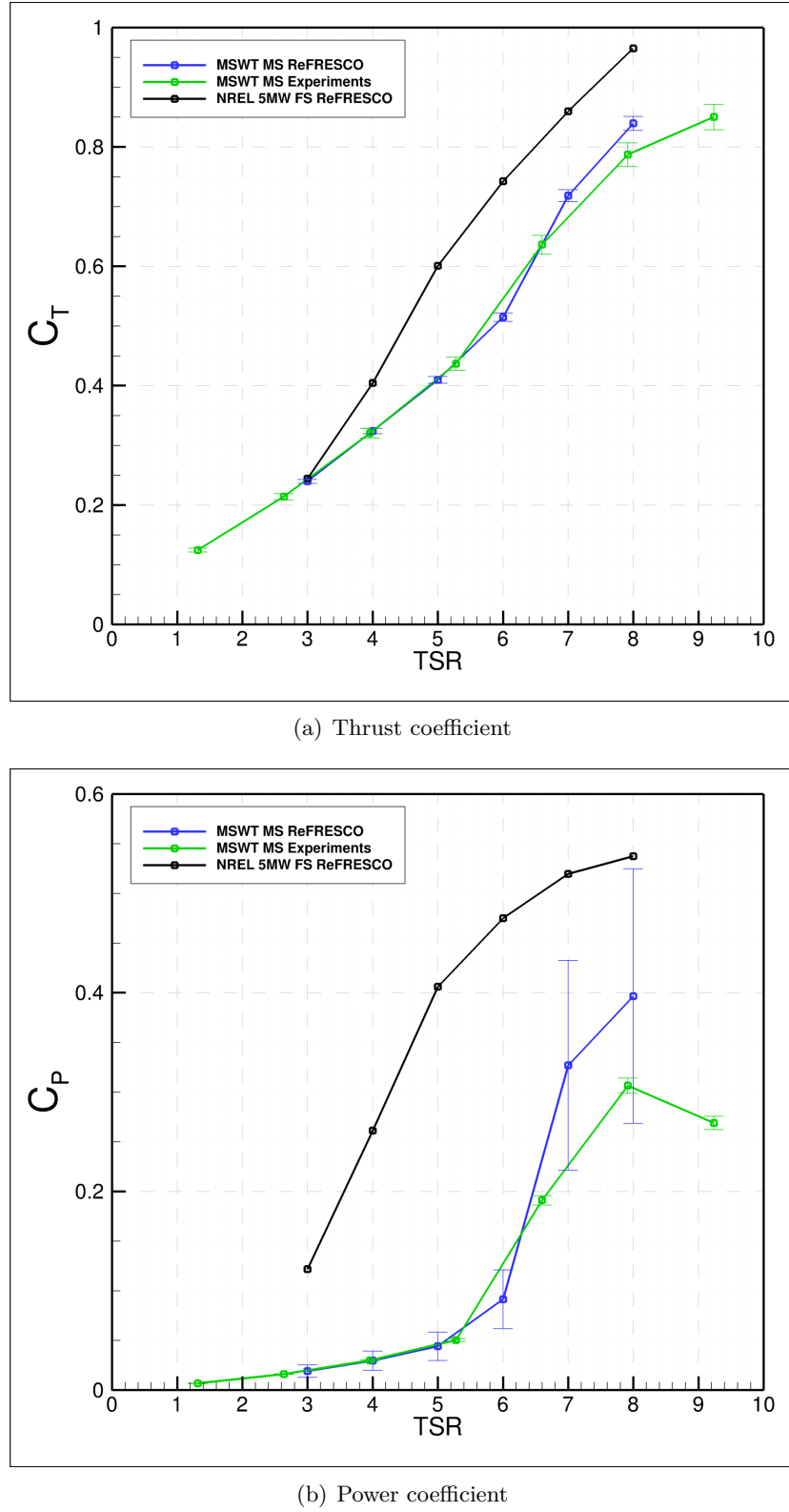


Figure 7-9: C_T and C_P as function of TSR for FS NREL 5MW baseline and MS MSWT.

According to the numerical results the C_T performance of the model-scale MSWT is different than that of the full-scale NREL 5MW. This difference was previously observed for the full-scale NREL 5MW BEMT results and the model-scale MSWT model experiments [19]. The differences however, are bigger according to the CFD computations. A similar trend is observed for the C_P values.

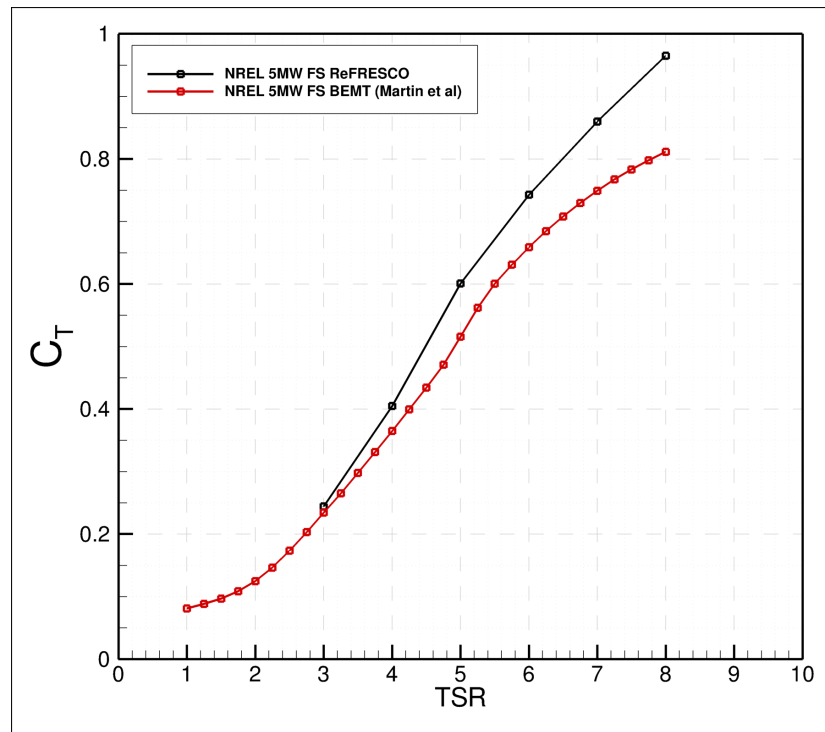
7-4 Comparing the full-scale BEMT and RANS results

The full-scale wind turbine performance data available in [14, 17], other than the RANS result presented in this study, are computed by BEMT-tools. In this section the BEMT tool data for the NREL 5MW baseline turbine are compared with the data obtained from the RANS computations as presented in section 7-1.

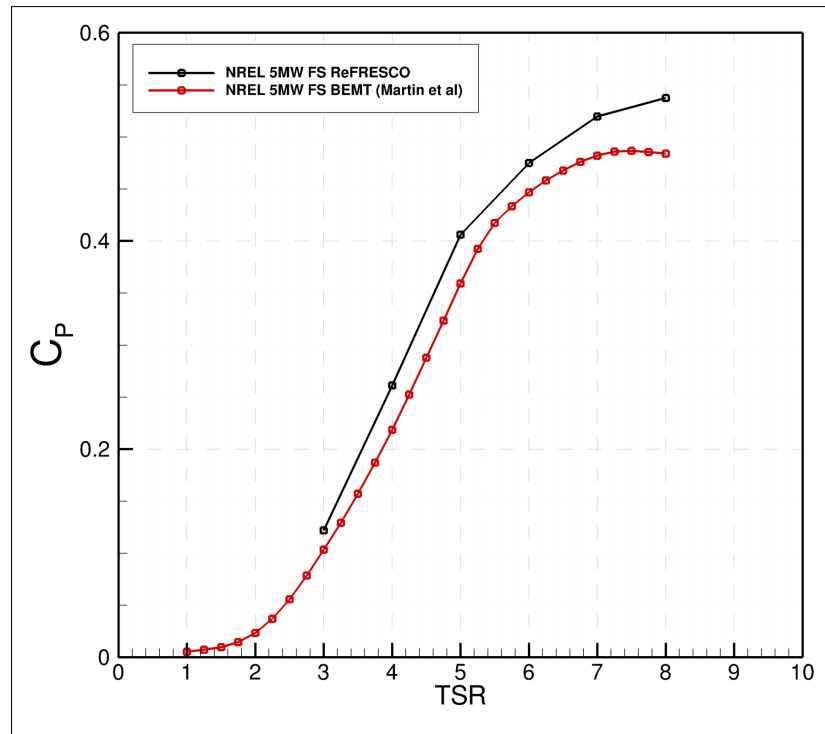
Both the C_T and C_P curve for the NREL 5MW baseline turbine are presented in figure 7-10. The BEMT results in this plot are taken from a publication by H. R. Martin of the University of Maine on the design of a similar scale model rotor [17]. These data were obtained using NREL's coupled aero-hydro-servo-elastic wind turbine simulator FAST (e.g. see [13]), in which the aerodynamics are computed by means of BEMT. Input coefficients needed for this tool are obtained from XFOIL computations, where a standard laminar to transition effect log factor, N_{crit} , of 9 was used [14, 17].

It is observed that over the full TSR range the ReFRESCO data predicts larger C_P and C_T values when compared to the BEMT data. The differences between both numerical tools increase for increasing TSR, especially for C_P . The BEMT tool predicts the maximum power coefficient to be at $TSR = 7.25$ while for the RANS computations the maximum is not yet reached.

Since no full-scale experimental data is available it is not possible to conclude which of the above methods predicts the turbine performance most accurately. Additionally it must be noted that the uncertainties of both the full-scale BEMT and RANS data are needed for proper judgment of the data presented. However it must be kept in mind that the BEMT-based modeling approach presented here, assumes a 2D flow over the blades with no radial interaction, which does not always hold. Especially for the heavily loaded turbine at low TSRs, where large amounts of separation occurs the radial components are large.



(a) Thrust coefficient



(b) Power coefficient

Figure 7-10: Thrust and power coefficient as function of TSR for full-scale NREL 5MW based on BEMT and RANS results.

Chapter 8

Conclusions and Recommendations

In this chapter the work presented in the previous chapters is summarized and recommendations are given regarding improvements of the study and future work. In section 8-1 and 8-2 the conclusions and recommendations of the two- and three-dimensional studies are presented. Section 8-3 is devoted to the scaling effects observed for the two analyzed turbine geometries.

8-1 Two-dimensional study

To improve input data for BEMT based tools, numerical simulations have been performed on 2D airfoils to study the Reynolds number effect due to Froude-scaled winds. Prior to these computations the influence of the numerics on the results were studied. Based on this numerical study a number of conclusions may be drawn.

- In order to reduce the influence of the boundary conditions extremely large domain dimensions are required. For this study a domain size of $R/c = 100$ is used, resulting in an influence of the domain on the solution of less than 2.2 percent, for all Reynolds numbers and angles of attack tested.

The influence of the domain was strong for C_l at model-scale Reynolds numbers while for full-scale Reynolds numbers the dependency was strong for C_d , which is in line with the work previously done by others.

For future computations an attempt to reduce the domain size dependency can be made by studying the influence of the α and β angle in the BCAUTODETECT settings, which determine the size of the pressure boundary.

- The iterative convergence of both steady and unsteady computations was very good for all tested cases.
- CPU times for steady computations were typically 2.5 hours on a standard workstation. For unsteady computations CPU times of typically 5 days using 32 cores on a six years old cluster.

- From the verification study it is found that the round-off and iterative-error are small enough to be considered negligible (typically L_∞ -norms of the residuals are below 10^{-6}). This holds for all cases analyzed, both steady and unsteady.

Performing an uncertainty study when using unstructured grids is shown to be challenging, especially for the unsteady case where a time-discretization error is introduced. Large uncertainty estimations up to 35 % for the extreme case are found for the steady computations performed. The trends found for the steady computations were also observed for verification study on unsteady computations.

To understand the effect of the unstructured grids on the numerical uncertainty estimation at low Reynolds numbers, it is desirable to perform more 2D computations on structured grids. By doing so it can be determined whether the large variation in the estimated numerical uncertainties are caused solely by the unstructured grids, the unsteady separated flow, or both. Furthermore these results can than be compared with the alternative methods of describing the typical grid cell size.

Additionally, to improve numerical uncertainty estimation using the alternative typical grid-cell definition based on the model of the cell volumes could be further studied. The number of cell volume intervals could be varied for the determination of the mode of the cell-volumes.

- A number of numerical computations are performed in which various turbulence models are implemented. At full-scale Reynolds numbers the differences between the various models are only small in both C_l , C_d , and C_m (typically less than 1.5%) as well as the flow characteristics.

At model-scale Reynolds numbers large difference are indeed observed. The numerical solutions of these separated flows show large variation in both size and geometry, which greatly affects the performance of the airfoil at hand.

Since no experimental data is available, validation can not be performed, however previous work done by others showed that the accuracy of the Spalart-Allmaras one-equation models is less when separated flow is modeled.

It can be said that at model-scale Reynolds number flows, choice of turbulence models plays an important role. The $k - \omega$ SST models are a good choice for numerical simulation of the separated low Reynolds number flows considered.

The sensitivity of the solution for domain size, grid density, and turbulence model show the complexity of these computations. More research is desired on the effect of other parameters such as for example the level of the inflow turbulence quantities. Newly developed turbulence/transition models can be used to study more the effect of transition on C_l/C_d . Additionally, to further corroborate the findings above, a similar study could be performed using a different airfoil type for which experimental data is available for validation.

8-2 Three-dimensional study

For the three-dimensional flow over the MSWT at model-scale, a numerical study comparable to the two-dimensional study is performed. The knowledge obtained in this study is summarized next.

- The influence of the domain is studied by analyzing the flow over the turbine using three domains with varying dimensions. For the largest domain of 30 times the turbine diameter, the influence of the boundary conditions are assumed negligible with less than one percent difference between the two largest domains.

To further study the influence of the domain size, additional computations should be performed for lower tip speed ratios. Since the affected wake-field is expected to be larger for the heavily loaded blades at low TSRs the domain size influence is likely to be larger.

- Reaching the desired iterative convergence using steady calculations is challenging due to the unsteady nature of the flow at model-scale conditions. Typical L_∞ - and L_2 - norms of the residuals in the order of 10^{-2} and 10^{-5} are found respectively in the wake-field of the blade root. The integral quantities C_T and C_P however do converge to a constant value. The magnitude of the iterative error in combination with the use of unstructured grids results in a large uncertainty. Using finer grids results in an uncertainty for C_T and C_P of 1.39 and 32.31 percent respectively. The absolute difference between the two finest grids, , is only 0.18 and 2.44 percent for C_T and C_P respectively. Because of the moderate iterative convergence and highly separated unsteady flow it is desirable to perform several URANS computations for comparison with the steady RANS computations. The results of this comparison could lead to more knowledge on the validity of using steady RANS solvers for low Reynolds number flows over wind turbines. The uncertainty estimation procedure based on the least squares method together with the more common approach based on the relative difference, as presented in this study, provide the engineer with an extra method to asses the reliability of the numerical computations. However the estimated uncertainties are merely indicative and should always be used with great care.
- A study has been preformed in which the Spalart-Allmaras and $k - \omega$ SST (Standard) model are compared. Since the turbine operates in the sub-critical regime large differences between the models are found mainly in C_P . From flow visualization it is observed that this large difference is related to the size of the separated region, which is different for both models. When comparing the obtained results with experimental data it is found that the $k - \omega$ -SST-Standard model is more accurate and the Spalart-Allmaras over predicts both C_T and C_P . Additionally as for the two-dimensional study, it might be of interest to study the effect of inflow turbulence levels. It is expected that this will significantly influence the solution because of the critical conditions in which the model-scale turbine operates.
- In the low TSR range (typically $TSR < 6$) the experimental and numerical data agree well for both C_T and C_P . In the $TSR > 6$ range the difference in C_P is larger, this is due to the sensitivity of C_P to the size of the attached flow region at the blade tips of the turbine. C_T is less sensitive to this effect and consequently the differences between the experimental and numerical data is much smaller for this quantity.
- With the numerical and experimental uncertainties known a validation study is performed for the MSWT at model-scale. Due to the large uncertainty estimations two methods are applied based on the least-squares method and the relative difference between the two finest grids.

Both methods however resulted in similar results, where only the lower TSR range ($TSR = 3.0$ to $TSR = 5.0$) is validated against the experimental data. The differences between the experimental and numerical data at higher TSRs are too large to be validated. This is caused by the critical flow in which the turbine operates.

8-3 Scaling effects of the MSWT and NREL 5MW

Overall it can be said that the results presented on the scaling effects are in line with the experimental observations previously described by others.

- The poor performance of the NREL 5MW baseline wind turbine at model-scale conditions is caused by Reynolds dissimilitude resulting in fully separated flows over the full range of computed TSRs. Additionally a pressure side separation bubble is present at model-scale, which further decreases the turbine performance due to its decambering effect. At full-scale conditions fully separated flow is only observed at the low TSRs and only partially in the higher TSRs near the blade root.
- For the flow over the MSWT at model-scale similar observations are made, where separation occurs over the full TSR range. However at higher TSRs an attached region is located at the blade tip resulting in increased C_T and C_P values when compared to the model-scale NREL 5MW baseline turbine. Additionally no separation bubble was observed on the pressured side of the blades.
- The attempt to improve the turbine performance by means of the altered geometry of the MSWT showed promising results. For the TSRs near the design conditions where an attached flow region is observed, the MSWT design shows great improvements in both C_T and C_P when compared to the NREL 5MW baseline in model-scale conditions. Although for C_P there is still a large difference is observed, the objective of scaling C_T was satisfactory. This is partially due to the increase of the blade chord length by 25% over the full blade span, and the attached flow region at the blade tip. For the lower TSR range the differences between the latter model are larger, due to the fully separated flow at model scale.

Despite the fact that the pitch distribution of the original NREL 5MW baseline turbine geometry is already altered for the MSWT, more improvements can be made. An altered pitch distribution such that the attached region at model scale resembles the full scale attached region is desired. Several initial CFD computations can be performed on this altered geometry using the best possible settings based on the findings presented in this study.

- For full-scale he differences between the BEMT and RANS computations of C_T and C_P where only small over the full range of TSRs. The RANS computations resulted in larger C_T and C_P values especially for higher tip speed ratios. No conclusions can be drawn on the accuracy of the methods due to the lack of available measurement data and uncertainty estimations. However it must be kept in mind that BEMT results rely on input data and certain assumptions with respect to the flow. E.g. the assumed two-dimensional flow over the blades does not hold for the highly separated flow at model scale.

To further investigate the validity of both full-scale BEMT and RANS computations a verification and validation study should be performed on both methods. For the BEMT computation input data based on both XFOIL and RANS data should be used and result compared. The fact remains however that no full-scale measurement data is available.

8-4 Wind Turbine Analysis Using CFD

As shown in this thesis, numerical analysis of floating offshore wind turbines using a RANS solver can be extremely valuable. However, when compared to the “less advanced” modeling tools such as BEMT codes, large amounts of CPU power is required. As an example: the amount of CPU time required for the present work is estimated to be roughly 60 years! It is obvious that without the available hardware (workstations/post-processing machines/HPC-clusters) and software (state of the art codes/unlimited licenses/unlimited cores), it is impossible to perform the amount of computations done in the present work.

Bibliography

- [1] United Nations, *World Population Prospects, the 2010 Revision*. United Nations, 2011.
- [2] International Energy Agency, *World Energy Outlook*. International Energy Agency, 2013.
- [3] Global Wind Energy Council, *Global Wind Report Anual Market Update 2012*. American Geophysical Union, 2012.
- [4] C. L. Archer and M. Z. Jacobson, “Evaluation of global wind power,” *Journal of Geophysical Research*, vol. 110, no. D12, 2005.
- [5] W. Musial and S. Butterfield, “Future for Offshore Wind Energy in the United States,” in *EnergyOcean 2004 Conference*, pp. 4–6, 2004.
- [6] European Wind Energy Association EWEA, *Deep Water, The Next Step for Offshore Wind Energy*. EWEA, 2013.
- [7] M. N. Schwartz, D. Heimiller, S. Haymes, and W. Musial, *Assessment of Offshore Wind Energy Resources for the United States*. Citeseer, 2010.
- [8] H. Dagher, “Making History With VolturnUS,” 2013. Webinar Slides University of Maine.
- [9] J. M. Jonkman and M. L. Buhl Jr, “Development and Verification of a Fully Coupled Simulator for Offshore Wind Turbines,” in *45th AIAA Aerospace Sciences Meeting and Exhibit, 8–11 January 2007, Reno, NV, AIAA Meeting Papers on Disc*, 2007.
- [10] Q. Wang, H. Zhou, and D. Wan, “Numerical Simulation of Wind Turbine Blade-Tower Interaction,” *Journal of Marine Science and Application*, vol. 11, no. 3, pp. 321–327, 2012.
- [11] J. M. Jonkman and P. D. Sclavounos, “Development of Fully Coupled Aeroelastic and Hydrodynamic Models for Offshore Wind Turbines,” in *44th AIAA Aerospace Sciences Meeting and Exhibit Meeting Papers*, 2006.
- [12] P. J. Moriarty and A. C. Hansen, *AeroDyn Theory Manual*. National Renewable Energy Laboratory, Golden, Colorado, USA, 2005.

- [13] J. Jonkman, “ NWTC Computer-Aided Engineering Tools.” <http://wind.nrel.gov/designcodes/simulators/fast/>, 2013. Accessed 23-August-2013.
- [14] H. R. Martin, “Development of a Scale Model Wind Turbine for Testing of Offshore Floating Wind Turbine Systems,” traineeship report, The University of Maine, 2011.
- [15] C. Cermelli, A. Aubault, D. Roddier, and T. Mc Coy, “Qualification of a Semi-Submersible Floating Foundation for Multi-Megawatt Wind Turbines,” in *Offshore Technology Conference*, 2010.
- [16] F. G. Nielsen, T. D. Hanson, B. Skaare, *et al.*, “Integrated Dynamic Analysis of Floating Offshore Wind Turbines,” in *Proceedings of OMAE2006 25th International Conference on Offshore Mechanics and Arctic Engineering, 4–9 June 2006, Hamburg, Germany*, 2006.
- [17] H. Martin, R. Kimball, A. Viselli, and A. Goupee, “Methodology for Wind/Wave Basin Testing of Floating Offshore Wind Turbines,” in *Proceedings of the 31st International Conference on Ocean, Offshore and Arctic Engineering Rio de Janeiro, Brazil June*, 2012.
- [18] W. Otto, D. Rijkema, and G. Vaz, “Viscous-Flow Calculations on an Axial Marine Current Turbine,” in *Proceedings of the 31st International Conference on Ocean, Offshore and Arctic Engineering Rio de Janeiro, Brazil June*, 2012.
- [19] E.-J. de Ridder, W. Otto, G.-J. Zondervan, F. Huijs, and G. Vaz, “Development of a Scaled-Down Floating Wind Turbine for Offshore Basin Testing,” *Proceedings of OMAE2014 33rd International Conference on Offshore Mechanics and Arctic Engineering, 8–13 June 2014, San Francisco, California, USA*, 2014.
- [20] D. M., “UIUC Airfoil Data Site. .” http://m-selig.ae.illinois.edu/ads/coord_database.html, 1995. Accessed 26-aug-2013.
- [21] M. S. Selig *et al.*, *PROPID User Manual: Aerodynamic Design Software for Horizontal Axis Wind Turbines*. UIUC Applied Aerodynamics Group, Department of Aerospace Engineering, University of Illinois, Urbana, Illinois, 2011. Version 5.3.1.
- [22] M. Drela and H. Youngren, “XFOIL Subsonic Airfoil Development System.” <http://web.mit.edu/drela/Public/web/xfoil/>, 2008. Accessed 01-November-2013.
- [23] G. Vaz, W. Otto, G.-J. Zondervan, and E.-J. Ridder, “Scale Effects on Floating-Wind and Current Turbines,” tech. rep., MARIN Report 70003-5-RD, 2013.
- [24] J. M. Jonkman, S. Butterfield, W. Musial, and G. Scott, *Definition of a 5-MW Reference Wind Turbine for Offshore System Development*. National Renewable Energy Laboratory Colorado, 2009.
- [25] S. Chakrabarti, “Physical Model Testing of Floating Offshore Structures,” in *Proc., Dynamic Positioning Conf. Model Testing*, pp. 1–33, 1998.
- [26] S. K. Chakrabarti, *Offshore structure modeling*. World Scientific River Edge, NJ, 1994.
- [27] T. Burton, N. Jenkins, D. Sharpe, and E. Bossanyi, *Wind Energy Handbook*. John Wiley & Sons, 2011.

- [28] J. D. Anderson, *Fundamentals of Aerodynamics*, vol. 5. McGraw-Hill New York, 2011.
- [29] S. J. Miley, *A Catalog of Low Reynolds Number Airfoil Data for Wind Turbine Applications*. NTIS, 1982.
- [30] P. Kunz and I. Kroo, “Analysis, Design, and Testing of Airfoils for Use at Ultra-Low Reynolds Numbers,” in *Proceedings of a Workshop on Fixed and Flapping Flight at Low Reynolds Numbers, Notre Dame*, 2000.
- [31] D. Marten, “ QBlade Guidelines.” <http://qblade.de.to/>. Accessed 24-April-2014.
- [32] A. Ning, “ CCBBlade.” <http://wind.nrel.gov/designcodes/simulators/ccblade/>. Last modified 13-January-2014; accessed 24-April-2014.
- [33] F. M. White, *Fluid Mechanics. 5th edition*. McGraw-Hill Book Company Boston, 2003.
- [34] S. B. Pope, *Turbulent Flows*. Cambridge university press, 2000.
- [35] F. T. M. Nieuwstadt, *Turbulentie: Inleiding in de Theorie en Toepassingen van Turbulente Stromingen*. Epsilon, 1992.
- [36] D. C. Wilcox, *Turbulence Modeling for CFD*, vol. 2. DCW industries La Canada, 1998.
- [37] P. Spalart and S. Allmaras, “A One-Equation Turbulence Model for Aerodynamic Flows,” *AIAA 30th Aerospacs Sciences Meeting, Reno, U.S.A.*, 1992.
- [38] W. Jones and B. Launder, “The Prediction of Laminarization with a Two-Equation Model of Turbulence,” *International Journal of Heat Mass Transfer*, pp. 301–314, 1972.
- [39] F. R. Menter, “Two-Equation Eddy-Viscosity Turbulence Models for Engineering Applications,” *AIAA journal*, vol. 32, no. 8, pp. 1598–1605, 1994.
- [40] F. Menter, M. Kuntz, and R. Langtry, “Ten Years of Industrial Experience with the SST Turbulence Model,” *Turbulence, heat and mass transfer*, vol. 4, pp. 625–632, 2003.
- [41] L. Eça, G. Vaz, and M. Hoekstra, “A Verification and Validation Exercise for the Flow over a Backward Facing Step,” in *European conference on computational fluid dynamics, ECCOMAS CFD*, 2010.
- [42] D. Rijpkema and G. Vaz, “Viscous flow computations on propulsors: verification, validation and scale effects,” in *RINA, Developments in Marine CFD*, (London, UK), RINA, 2011.
- [43] M. Bettle, S. L. Toxopeus, and A. Gerber, “Calculation of Bottom Clearance Effects on Walrus Submarine Hydrodynamics,” *International Shipbuilding Progress*, vol. 57, no. 3, pp. 101–125, 2010.
- [44] L. Eça, G. Vaz, and M. Hoekstra, “Code Verification, Solution Verification and Validation in RANS Solvers,” in *OMAE ASME 29th International Conference on Ocean, Offshore and Arctic Engineering, Shanghai*, 2010.

- [45] L. Eça, G. Vaz, and M. Hoekstra, “Code Verification of ReFRESCO with a statistically periodic manufactured solution,” *Proceedings of OMAE2014 33rd International Conference on Offshore Mechanics and Arctic Engineering, 8–13 June 2014, San Francisco, California, USA*, 2014.
- [46] L. Eça, M. Hoekstra, J. Beja Pedro, and J. Falcão de Campos, “On the Characterization of Grid Density in Grid Refinement Studies for Discretization Error Estimation.” Unpublished.
- [47] N. International, “HEXRESS Unstructured Full-Hexahedral Meshing.” <http://www.numeca.com/en/products/automeshtm/hexpressstm>, 2012. Accessed 22-April-2014.
- [48] NUMECA International, Numeca International, Brussels, *User Manual Hexpress*, 2012. Version 2.11d.
- [49] G. Vaz, F. Jaouen, and M. Hoekstra, “Free-surface viscous flow computations. Validation of URANS code fresco,” in *28th International Conference on Ocean, Offshore and Arctic Engineering (OMAE)*, (Honolulu, Hawaii), May 31–June 5 2009.
- [50] C. M. Klaij and C. Vuik, “Simple-type preconditioners for cell-centered, colocated finite volume discretization of incompressible reynolds-averaged navierâ€¢stokes equations,” *International Journal for Numerical Methods in Fluids*, vol. 71, no. 7, pp. 830–849, 2013.
- [51] L. Eça and M. Hoekstra, “Verification and validation for marine applications of cfd,” in *29th Symposium on Naval Hydrodynamics (ONR), Gothenburg, Sweden*, August 2012.
- [52] S. Toxopeus, C. Simonsen, E. Guilmeneau, M. Visonneau, T. Xing, and F. Stern, “Investigation of water depth and basin wall effects on kvlcc2 in manoeuvring motion using viscous-flow calculations,” *Journal of Marine Science and Technology*, vol. 18, no. 4, pp. 471–496, 2013.
- [53] A. Koop, C. Klaij, and G. Vaz, “Viscous-Flow Calculations for Model and Full-Scale Current Loads on Typical Offshore Structures,” in *Proceedings of MARINE 2011, IV International Conference on Computational Methods in Marine Engineering (Selected Papers), Computational Methods in Applied Sciences*,, 2013.
- [54] J. Windt, “Adaptive Mesh Refinement in Viscous Flow Solvers: Refinement in the Near-wall Region, Implementation and Verification,” in *Proceedings of NUTTS2013, Mulheim, Germany.*, 2013.
- [55] M. Kerkvliet, G. Vaz, N. Carette, and M. Gunsing, “Analysis of U-Type Anti-Roll Tanks using RANS. Sensitivity and Validation,” in *Proceedings of OMAE2014*, (San-Francisco, USA), June 2014.
- [56] B. Schuiling, “The Design and Numerical Demonstration of a New Energy Saving Device,” in *Proceedings of NUTTS2013*, (Mulheim, Germany), 2013.
- [57] F. Pereira, L. Eça, and G. Vaz, “On the Order of Grid Convergence of the Hybrid Convection Scheme for RANS Codes,” in *CMNI2013*, pp. 1–21, 2013.

- [58] G. F. Rosetti, G. Vaz, and A. L. C. Fujarra, “URANS Calculations for Smooth Circular Cylinder Flow in a Wide Range of Reynolds Numbers: Solution Verification and Validation,” in *Journal of Fluids Engineering*, p. 549, Asme, July 2012.
- [59] H. Bandringa, R. Verstappen, F. Wubbs, C. Klaij, and A. van der Ploeg, “On Novel Simulation Methods For Complex Flows In Maritime Applications,” in *Proceedings of NUTTS2012, Rome, Italy*, September 2012.
- [60] J. Hawkes, G. Vaz, S. Turnock, S. Cox, and A. Philips, “Software Performance Analysis of Massively-Parallel Hydrodynamics Simulations,” in *11th International Conference on Hydrodynamics (ICHD)*, October 2014.
- [61] D. R. Rijpkema, “Numerical Simulation of Single-Phase and Multi-Phase Flow over a NACA 0015 Hydrofoil,” master thesis, Technical University Delft, 2008.
- [62] J. D. Anderson, *Computational Fluid Dynamics*. McGraw-Hill New York, 1995.
- [63] F. M. S. Pereira, “Verification of ReFRESCO with the Method of Manufactured Solutions,” traineeship report, IST portugal, 2012.
- [64] J. H. Ferziger and M. Perić, *Computational Methods for Fluid Dynamics*, vol. 3. Springer Berlin, 2001.
- [65] M. M. Zdravkovich, *Flow around Circular Cylinders: Volume 1: Fundamentals*, vol. 1. Oxford University Press, 1997.
- [66] F. Jaouen, A. Koop, and G. Vaz, “Predicting Roll Added Mass and Damping of a Ship Hull Section Using CFD,” in *ASME 2011 30th International Conference on Ocean, Offshore and Arctic Engineering*, pp. 105–115, American Society of Mechanical Engineers, 2011.
- [67] G. Peyro, “Analysis of Flows on Stabilizer Fins using ReFRESCO: 2D, 3D, Static and Dynamic Effects,” traineeship report, ENSTA Bretagne, 2011.
- [68] G. Vaz and D. Rijpkema, “Non-Conformal and Sliding Interfaces in ReFRESCO,” tech. rep., MARIN Report 70015-13-RD, January 2013.
- [69] J. Katz, “A Discrete Vortex Method for the Non-Steady Separated Flow over an Airfoil,” *Journal of Fluid Mechanics*, vol. 102, pp. 315–328, 1981.
- [70] A. Fage and F. Johansen, “On the Flow of Air Behind an Inclined Flat Plate of Infinite Span,” *Proceedings of the Royal Society of London. Series A*, vol. 116, no. 773, pp. 170–197, 1927.
- [71] W. J. Olsman and T. Colonius, “Numerical Simulation of Flow Over an Airfoil With a Cavity,” *AIAA journal*, vol. 49, no. 1, pp. 143–149, 2011.
- [72] A. Roshko, “Experiments on the Flow Past a Circular Cylinder at Very High Reynolds Number,” *Journal of Fluid Mechanics*, vol. 10, no. 03, pp. 345–356, 1961.
- [73] P. Godin, D. Zingg, and T. Nelson, “High-lift Aerodynamic Computations with One- and Two-Equation turbulence Models,” *AIAA journal*, vol. 35, no. 2, pp. 237–243, 1997.

Glossary

List of Acronyms

NREL	National Renewable Energy Lab
EWEA	European Wind Energy Association
FOWT	Floating Offshore Wind Turbine
BEMT	Blade Element Momentum Theory
URANS	Unsteady Reynolds Averaged Navier Stokes
RANS	Reynolds Averaged Navier Stokes
TSR	Tip Speed Ratio
CFD	Computational Fluid Dynamics
MSWT	MARIN Stock Wind Turbine
LE	Leading Edge
TE	Trailing Edge
NS	Navier-Stokes
V&V	Verification and Validation
RMS	Root Mean Square
RE	Richardson extrapolation
QUICK	Quadratic Upstream Interpolation for Convective Kinetics
CDS	Central Difference Scheme
UDS	Upwind Difference Scheme
SIMPLE	Semi Implicit Method for Pressure Linked Equation

PDF	Probability Density Function
SA	Spalart-Allmaras
SST	Shear Stress Transport
RFM	Relative-Formulation
AFM	Absolute-Formulation
MVG	Moving-Grid-Formulation

List of Symbols

Latin Symbols

B	Body force vector	[N]
D	Deformation tensor	[−]
\mathbf{e}_f	Eccentricity vector	[−]
I	Identity matrix	[−]
T	Stress tensor for Newtonian fluids	[Nm ^{−2}]
V	Velocity vector (u, v, w) ^T	[ms ^{−1}]
\vec{n}	Outward normal unit vector	[−]
A	Area	[m ²]
c	Chord length / Speed of sound	[m]/[ms ^{−s}]
c_i	Refined cell size	[m]
C_i	Initial cell size	[m]
D	Circular domain diameter / Drag force	[m]/[N]
f	Shedding frequency	[s ^{−1}]
F_s	Safety factor for numerical uncertainty study	[−]
g	Gravitational constant	[ms ²]
h	Vertical distance (height)	[m]
k	Mean turbulence kinetic energy per unit mass	[m ² s ^{−2}]
L	Characteristic length / Lift force	[m]/[N]

M	Moment	[Nm]
N	Number of rotor blades	[−]
n_i	Number of refinements	[−]
n_p	Total number of grid cells	[−]
$N_{\Delta V}$	Number of cells within volume interval ΔV	[−]
N_{Total}	Total number of cell within a grid	[−]
P	Pressure	[Nm ^{−1}]
p_t	Observed order of accuracy of time discretization	[−]
q_ϕ	Source term in conservation equation	[ϕs^{-1}]
R	Resulting force / Blade tip radius	[N]/[M]
r	Radius	[m]
S	Planform area	[m ²]
T_i	Turbulence intensity	[−]
U_ϕ	Numerical uncertainty	[−]
U_{exp}	Experimental uncertainty	[−]
U_{inp}	Input uncertainty	[−]
V	Characteristic velocity	[ms ^{−1}]
V_{wind}	Wind velocity	[ms ^{−1}]
W	Relative velocity at rotor blade	[ms ^{−1}]
X_{cr}	Critical value along airfoil surface	[m]

Non-Dimensional Quantities

a	Axial induction factor	[−]
a'	Tangential induction factor	[−]
C_p	Pressure coefficient	[−]
$C_{d_{frict}}$	Frictional drag	[−]
$C_{d_{press}}$	Pressure drag	[−]
$C_{m_{LE}}$	Moment coefficient about the leading edge	[−]

C_{pn}	Angular pressure coefficient	[–]
L_2	RMS of the residuals of ϕ between iterations over the domain	[–]
L_∞	Norm of max. residual of ϕ between iterations over the domain	[–]
Re	Reynolds number	[–]
Re_x	Reynolds number at location x from the leading edge	[–]
$Re_{x_{cr}}$	Critical Reynolds number	[–]
St	Strouhal number	[–]
y^+	Non-dimensional wall distance	[–]
C_d	drag coefficient	[–]
C_l	lift coefficient	[–]
C_P	power coefficient	[–]
C_T	thrust coefficient	[–]
Fr	Froude number	[–]

Subscripts

∞	Far field location	[–]
ct	Flow property at the cell center	[–]
m	Model	[–]
p	Prototype	[–]

Greek Symbols

α	Angle of attack / Autodetect angle	[deg]
α_f	Interpolation factor	[deg]
α_t	Time discretization related constant	[–]
$\bar{\omega}_z$	Non-dimensional vorticity.	[–]
β	Blending coefficient / Autodetect angle	[deg]
Δt	Time step	[s]
δ	Boundary layer thickness	[m]

Γ	Diffusive coefficient in conservation equation	[−]
γ	Tip speed ratio	[−]
γ_r	Local tip speed ratio	[−]
λ	Scaling factor	[−]
μ	Dynamic viscosity	[$k\text{gm}^{-1}\text{s}^{-1}$]
μ_t	Turbulent viscosity	[$k\text{gm}^{-1}\text{s}^{-1}$]
$\mu_{t_{ref}}$	Normalized turbulence viscosity	[−]
Ω	Angular velocity	[s^{-1}]
ω	Turbulence dissipation rate	[s^{-s}]
ϕ	Numerical flow quantity	[−]
ϕ_0	Estimation of the exact solution	[−]
ϕ_i	Integral of local quantity for iteration i	[−]
ϕ_{exact}	Exact solution	[−]
ρ	Mass density	[kgrm^{-3}]
σ	Blade solidity	[−]
σ_r	Chord solidity	[−]
τ	Shear stress	[Nm^2]
τ_i	Time step of grid i	[−]
τ_w	Sheer stress on surface	[Nm^2]
$\tilde{\nu}$	Auxiliary viscosity	[$\text{kgrm}^{-1}\text{s}^{-1}$]
ε	Turbulence dissipation / Estimated discretization error	[m^2s^{-2}]/[−]
ζ	Non-dimensional radial position r/R	[−]
res_ϕ	Non-dimensional change of the residual of a given variable	[−]

